Microprocessor-controlled Brushless

DC Linear Stepping Motor

This thesis is submitted for the degree of Doctor of Philosophy

Adel Ismael

Wolfson Centre for Magnetics

Cardiff School of Engineering

Cardiff University

Wales, United Kingdom

March 2018

DECLARATION AND STATEMENTS

DECLARATION

This work has not previously been accepted in substance for any degree and is not concurrently submitted in candidature for any degree.

Signed ………………………….... (ADEL ISMAEL) Date……….……….

STATEMENT 1

This thesis is being submitted in partial fulfilment of the requirements for the degree of Doctor of Philosophy (PhD).

Signed … ……………………….. …. (ADEL ISMAEL) Date……….……….

STATEMENT 2

This thesis is the result of my own independent work/investigation, except where otherwise stated. Other sources are acknowledged by explicit references.

Signed … ………………………… (ADEL ISMAEL) Date……….……….

STATEMENT 3

I hereby give consent for my thesis, if accepted, to be available for photocopying and inter-library loan, and for the title and summary to be made available to outside organisations.

Signed … ………………………… (ADEL ISMAEL) Date……….……….

ACKNOWLEDGEMENTS

ABSTRACT

Presently, there is a rapidly growing research interest for an efficient, high thrust density and high thrust to input power electrical linear machine. However, only limited work has been carried out in terms of the development of brushless DC linear motors (BDCLM). Focusing on this research gap which presently exist in this field, this thesis makes the development of the BDCLM the research objective, in order to produce a large thrust to input power, compared to the already existing designs. The motor is designed in such way that the motor core accommodates twenty-four independent multi-layer coil sections wound with enamelled copper wire and each layer section has 470 turns without compromising the effective air-gap. Also, a design commutation algorithm to provide a smooth movement and a high thrust for the BDCLM is implemented.

The design, analysis and optimization of the BDCLM in applications that requires a high thrust to input current ratio is described in this project. The investigation includes; the analysis, design, and control of the BDCLM through appropriate modelling, construction and experimental validation of the modelled results, employing both the static and dynamic approaches. The BDCLM design was analysed from electrical, mechanical and magnetic perspectives.

A Finite Element Method (FEM) was used to predict the performance of the BDCLM and to optimise the motor parameters. Additional challenges such as force ripple and normal force are investigated and analysed. A Proportional Integral Derivative (PID) control system, based on an Arduino Mega board is used to control the motor speed and position. A graphical user interface (GUI) is built in LabVIEW environment to control the Arduino board.

The experimental results were within 8.9 %, 2 % and 3 % of the modelled results with respect to the motor thrust, speed and position. These results demonstrate a good agreement between the two approaches. This research work can be considered as an initial step to developing the BDCLM for commercial applications.

LIST OF ABBREVIATIONS AND NOMENCLATURES

Abbreviations

AC	Alternating Current
BLPMSM	Brushless permanent magnet synchronous motor
EMF	Electromotive force
FEM	Finite Element Method
IM	Induction Motor
NdFeB	Neodymium Iron Boron
SmCo	Samarium Cobalt
DC	Direct current
PWM	Pulse-Width Modulation
BLDCLM	Brushless direct current linear motor
LIM	Linear induction motor
LSM	Linear synchronous motor
DCLM	DC linear motor
ALNICO	Aluminium, Nickel and Cobalt alloys
PM	Permanent magnet
LPMBDCM	Linear permanent magnet brushless DC motor
EMF	Electrical magnetic field
EMCN	Equivalent magnetic circuit network
PMDCLM	Permanent magnet direct current linear motor

SMC	Sliding mode controller
ILC	Iterative Learning Control
ARC	Adaptive Robust Controller
PSO	Particle Swarm Optimizations
GA	Genetic Algorithm
LQR	Linear Quadratic Regulator
ACSA	Ant Colony Search Algorithm
PID	Proportional Integral Derivative
BSDCLM	Brushless and slotless direct current linear motor
LVDT	Linear Variable Differential Transformer
PC	Permeance Coefficient
NP	North Pole
SP	South Pole
DAEs	Differential algebraic equations
ODEs	Ordinary differential equations

Nomenclatures

H	Magnetic field strength
Φ_m	Magnetic flux
B_m	Magnetic flux density
B_s	Magnetic saturation flux density
B_i	Intrinsic magnetization
ψ	Flux linkage
Φ_l	Leakage flux
H_c	coercivity
B_r	Remanent magnetic flux density
BH_{max}	Maximum energy product
H_g	Air-gap magnetic field intensity
H_m	Permanent magnet field intensity
B_g	Air-gap magnetic field density
q	Leakage coefficient
P_m	Permeance of the magnet
F	Electromagnetic force
N	Number of coils in turns
E_{emf}	Electromotive force

E	Applied voltage
v	Motor speed
L	Inductance
T	Torque
D	Viscous coefficient
J	Moment of inertia
μ_0	Magnetic permeability of free space
μ_r	Relative permeability
M	Rotor mass
ω	Natural frequency
ξ	Damping ratio

TABLE OF CONTENTS

LIST OF FIGURES

LIST OF TABLES

Chapter 1   : Introduction and Objectives of the Project

1.1   Introduction

Rotary motors are the most common form of electrical machines in the market, and they are of different types such as, the DC motor, the synchronous motor and the induction motor. These machines are used when the need exists for converting electrical energy to rotational mechanical energy, and a corresponding range of linear machines exists for when the need to produce a linear output arises [1].

Recently, linear motors are widely used in industry applications. Many machine tools and industrial equipment are now utilizing linear machines in designs that require linear motion due to the advantages offered by this device. The simple structure of linear motor offers high flexibility to the machine in terms of size and space [2].

Electrical linear motors directly convert electrical energy into mechanical energy to produce linear motion without a need for gears, belts or other mechanisms. The absence of these features in the linear motors reduces the space taken up by the machine, weight, cost, and backlash of the systems [3].

The use of a microcontroller to control the switching of the power supply to the armature winding of a direct current linear motor, eliminates the need for brushes and commutators which is a major disadvantage of DC linear motors, because of the insecure contact, short live span of the brushes, and noise produced. Such control requires position and speed control of the motor with the help of a feedback circuit, by using position sensors. DC linear motor are used for short distances with precise control, whereas the AC linear motor is used where movements over long distances is required.

Although the linear electric motors were introduced almost a century ago, there was still limited research on the linear motors compared to the rotary counterparts, until the 1960s. Since then, linear motors could be found in many different applications [4].

1.2   Research background

Linear electric motors, in general, have a history going back to the early days of electromagnetic experimentation, with the first prototype built by Wheatstone in 1841, just 10 years after Faraday's discovery of the Law of Induction [5]. Wheatstone invented what we now call a linear reluctance motor. Since then, until the 1940's, there has been relatively little development in the field of linear motors compared to that of the rotary motor. This was mainly due to the perception of engineers, that rotary motion was the most efficient way to convert electrical energy to mechanical energy and vice versa [6]. In addition, linear motors are generally not able to achieve the same power rates and efficiencies compared to that produced by the rotary motors [7].

There was further interest on linear motors between the 1960s and 1970s, when Maglev transportation became a popular concept and numerous linear motor designs involving either superconductors or the newly available rare earth permanent magnets were developed [8].

Based on this historical development, linear electric motors can be grouped into four main categories: reluctance motors, DC motors, induction motors and synchronous motors. Reluctance motors generate a magnetic field using windings in one element of the motor and a force will be produced due to the interaction of this field and iron on the other element of the motor.

Induction motors use an alternating current in a set of coils on one element of the motor to induce a current in conductors in the other element. This produces a force based on the interaction of the magnetic field produced by these coils and the induced current.

However, DC and synchronous motors operate by generating a magnetic field on one element of the motor, using coils or permanent magnets. This produces a force in the coils on the other element of the motor, thereby the field generated by the current that interacts with the main field (permanent magnet or coils). Both of these motor types can use permanent magnets, which generates the much required field, thus, reducing the power consumption. This research will focus on DC linear motors, due to its ability to employ permanent magnets which offers simple structure and control [9].

1.3 Comparison of rotary-to-linear motors and linear motors

Most of linear motions are traditionally achieved by means of rotating machines and special transmission devices such as; ball rail, roller rail and ball screw systems. In mechanical rotary-to-linear transmission devices, a rotating motion is converted into linear motion. Such a conversion decreases the efficiency of the whole system [10].

These devices have limited thrust capability, poor position accuracy, very poor settling time, dynamic complexity and require a lot of maintenance. Different types of rotary-to-linear transmission devices are shown in figure 1.1.

In contrast, linear motors are electromagnetic devices which can produce linear motion without any intermediate gears, screws or crank shafts. Since there is no backlash or mechanical windup, the linear motors have great repeatability and high precision positioning. In addition, its positioning accuracy is dependent on the resolution of the

linear encoder and the stability of the machines. Since the load is directly connected to the mover, the settling time of the system is very short.

The reliability of the linear motors is much higher than the reliability of the rotary-to-linear transmission devices. A comparison of the properties of the rotary-to-linear transmission devices and linear actuator is shown in the table 1.1.

1.4   Advantages of linear motors

By providing a direct thrust force to a payload, linear motors offer numerous advantages over rotary-to-linear counterparts [11]. In application requiring linear motion, linear motors offer many advantages over the rotary motors. The main benefits of linear motors are its ability to achieve a high force density, the high positioning precision, mechanical simplicity, higher reliability, longer lifetime, accuracy associated with the mechanical simplicity of such systems and no backlash and less friction, thus, providing a very high accuracy [12].

1.5   Applications of Electrical Linear motors

Linear motors potentially have numerous applications. Some of these are listed below [12]:

- Material handling and storage.
- People movers (Elevators).
- Liquid metal pumping.
- Machine tools operation.
- Operation of sliding doors.

Table 1.1 The comparison of the properties of the rotary-to-linear devices and linear actuator [10].

Device property	Belt and pulley	Rack and pinion	Lead screw	Ball screw	Linear motor
Accuracy	--	-	++	+	++
Speed range	+	-	--	-	++
Travel range	-	+	--	--	++
Thrust	-	+	-	+	++
Friction	+	+	--	+	++
Maintenance	+	+	-	--	++
Life time	+	-	--	+	++
Price	+	++	++	+	-
Efficiency	+	-	--	-	++
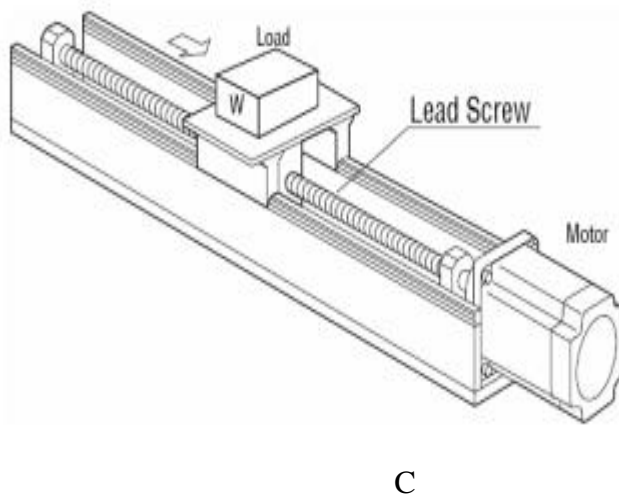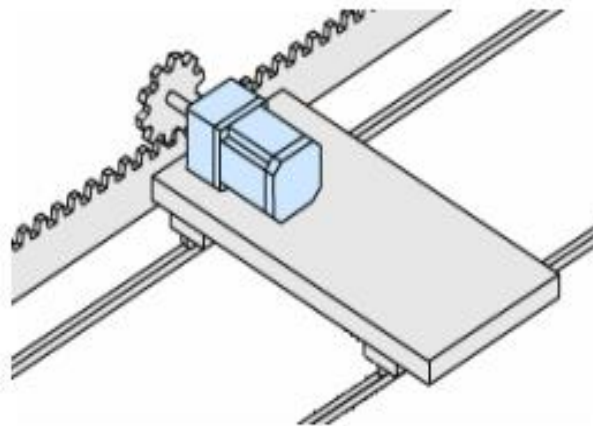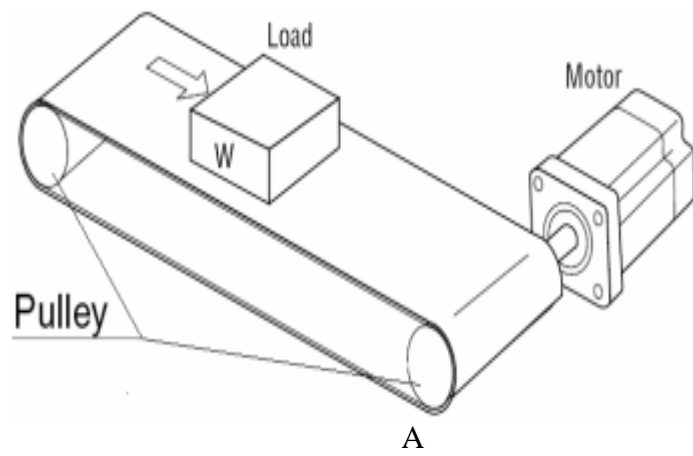
Figure 1.1 Deferent types of rotary-to-linear transmission devices (A) Belt and pulley system (B) Rack and pinion system(C) Lead screw system [10].

1.6   Thesis Objective

The key contributions of this thesis are based on analysis, modelling and PID control of a brushless DC linear motor supply, by a voltage controlled Pulse-Width Modulation (PWM) inverter to control the motor speed. The main objective of this thesis is to undertake a research towards improving the thrust to input current density compared to the present electrical machines. This project has four main research objectives, namely:

1. To design, construct and evaluate the Brushless DC Linear motor and assess its viability for use in linear movement systems.

2. To design the armature winding commutation algorithm for continuous linear movement and maximum developed thrust.

3. To develop and verify design optimisation criteria for the linear motor.

4. To design the PID controller and tune it using MATLAB/SIMULINK to control the motor speed and position.

5. To compare and analyse the simulation result (DC motor mathematical model in MATLAB/SIMULINK) and the experimental result.

6. To perform a thermal analysis of BDCLM in order to evaluate the heat radiation capability of this novel structure and guarantee secure applications.

To achieve these objectives the general methodology used for the machines follows the three steps outlined below:

1) Research Methodology.

- An in-depth literature review on the state of-the-art in the field of DC linear motors.

- Identification of key topologies and technologies to investigate.

- Building of finite element method (FEM) model to accurately perform analysis of the required models.

2) Design and optimisation

- Using the FEM technique to simulate different configurations.

- The configuration with the best performance is then optimized to achieve accurate results.

- Using the MATLAB/SIMULINK software to predict the performance of the motor under certain conditions.

3) Manufacture and construction

- The final design is used to build the prototypes of the machine.

1.7   Thesis Organisation

This thesis is divided into eight chapters. Chapter 2 gives an overview of classification of linear motors, in order to give a brief idea about the various possibilities to perform a linear movement. Also, a brief description of the different types of linear motors and their topologies are presented. Finally, the previous related work on the design of linear motors are reviewed.

In chapter 3, the electrical and mechanical design aspects of brushless DC linear motor (BLDC) from which a prototype design was created is described in details. The selection of the appropriate materials for the magnetic circuit and the reasons for their preference are all discussed.

Based on the preliminary geometry developed, an analysis using the FEM technique is performed in chapter 4. A comparison between the two proposed model designs is

carried out, in terms of the static thrust, air-gap flux density and magnetic flux distribution. Modelling of both the magnetic material properties and the permanent magnets is explained. The pre-processing operations involved mesh construction, specifying boundary conditions and excitation sources are also described in chapter 4. Furthermore, the post-processing operations to provide meaningful data from the field solutions are outlined, including flux linkage and force computations.

Chapter 5 outlines the experimental setup for real time implementation of open-loop velocity and position controllers. The static thrust was measured using load cell at different slider positions, to verify the algorithm which was designed to provide smooth motion and maximum thrust. A comparison was carried out between the measured static thrust and the computed thrust using FEM.

The dynamic behaviour of the motor, using a mathematical model in the form of a set of second-order differential equations that can be solved using numerical techniques is evaluated in chapter 6. To predict the performance of the motor under certain conditions, a model was created using MATLAB/SIMULINK. An experimental assessment of the motor is presented and compared with the simulated results, to illustrate the effectiveness of the dynamic modelling method.

Chapter 7 investigates the thermal behaviour of the BDCLM to analyse the temperature rising of the armature windings and irons of the motor, in order to provide a reference for the motor design and guarantee secure applications. It is very important to take temperature rising into account when designing such permanent magnet machines because the magnetic properties of permanent magnets may change, leading to demagnetization, which can deteriorate their electromagnetic performance and limit their thrust output.

Chapter 8 summaries the conclusion of each chapter, and suggests the route for future work, in order to expand the scope of this research.

Chapter 2 ： Classification, Topology and Related work

This chapter provides a general overview of linear motor classification in order to provide an overview of the various ways to perform a linear movement. Several types of linear motors and their topologies are briefly discussed in this thesis. This chapter also presents the characteristics of permanent magnet materials and their behaviours in magnetic circuit. Finally, previous related work on linear motor designs are also reviewed.

2.1   Introduction

Recently, linear motors have been widely used in industrial applications. Many machine tools and industrial equipment are now adopting linear machine in designs that require linear motion due to the advantages offered by such device. The simplicity of linear motor structure offers high flexibility to the machine, in terms of size and space [2]. Electrical linear motors directly convert electrical energy into mechanical energy to produce linear motion without a need for gears, belts or other mechanisms. The absence of these components in the linear motors reduces its weight, cost and backlash of the system [3].

Figure 2.1 illustrates the concept of linear motor; the idea behind the linear motor is simple enough. It is a conventional rotary motor split open and rolled out flat, the result is a flat single sided linear motor. The original stator becomes the forcer and the rotor becomes the mover [13]. Therefore, instead of producing a torque (rotation), it produces a linear force along its length. In linear motor design, the load is coupled directly to the

motor, hence, a direct linear motion is achieved without a need for any rotary to linear transmission devices [14].
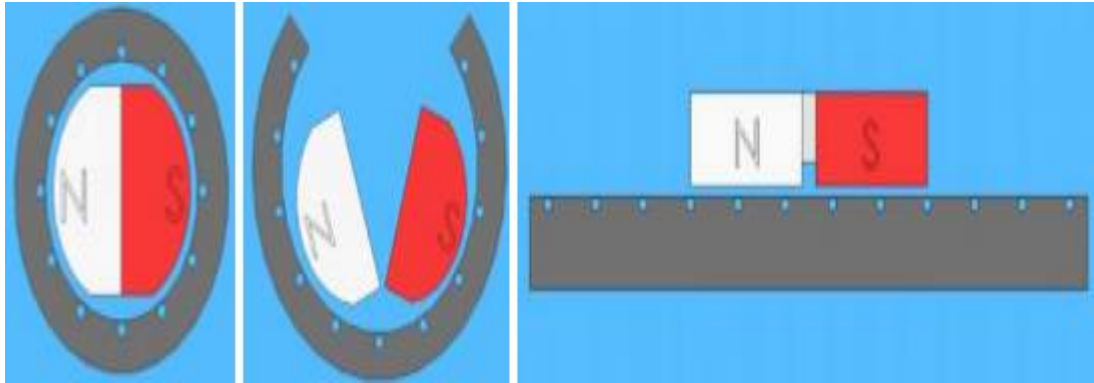
Figure 2.1 Illustrating the Imaginary Process of Unrolling a Rotary Motor [15].

Because linear motors do not have the luxury of 360 degree rotation, they must either keep a short moving secondary (magnet assembly) and increase the length of the primary (coil assembly), or increase the length of the secondary and keep a short moving primary [15], as illustrated in figure 2.2.

(a   (b
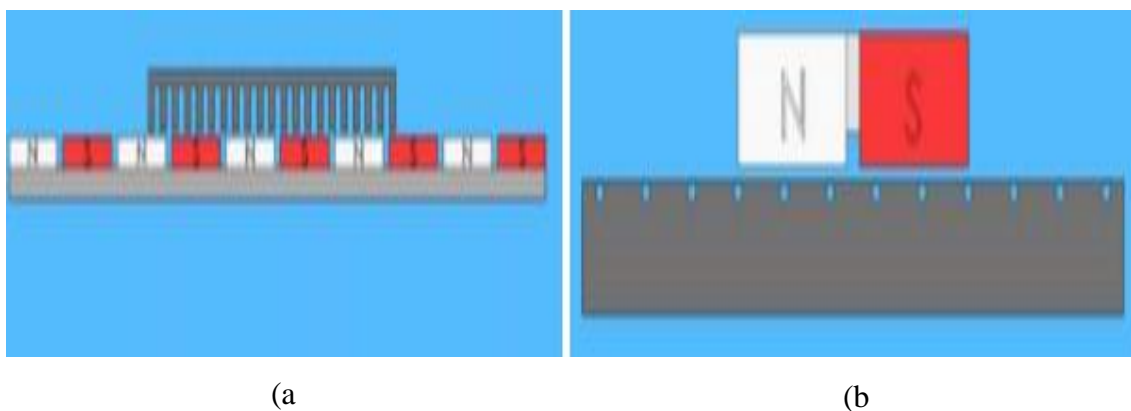
Figure 2.2 Illustrating the Differences between a) Moving Primary and b) Moving Secondary [15].

2.2 Linear motor classification and topology

There is no new technology inherited in the linear motors, with respect to their rotary counterparts, but merely designed with a different structure. However, its shape and pattern of movement is different [16]. A slight variation exists with respect to the output force of the linear motor and the rotary motor. That is, for the linear motor the force acts on the same direction with the armature winding, whereas the acting force is circumferential (radial) in the case of the rotary machines.

Several structures and topologies of linear motor exist in literature. Each type exhibits its own inherent benefits to the user. They can be either induction, synchronous or DC motors, with a transverse or a longitudinal flux. Figure 2.3 illustrates all the possible classifications of linear motor.

In terms of the linear motor topology, two different structures exist which are the tubular or flat. These two structures can have a long or short secondary and can be either double or single sided. All these structure variations may be combined to give many possibilities to implement a linear movement. Figure 2.4 illustrates all the possible topologies of the linear motor.
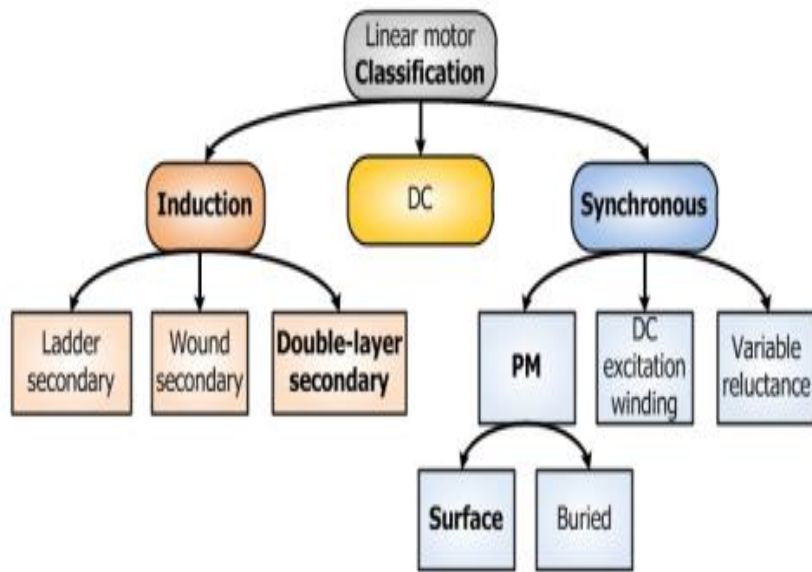
Figure 2.3 Classification of the linear motor [17]
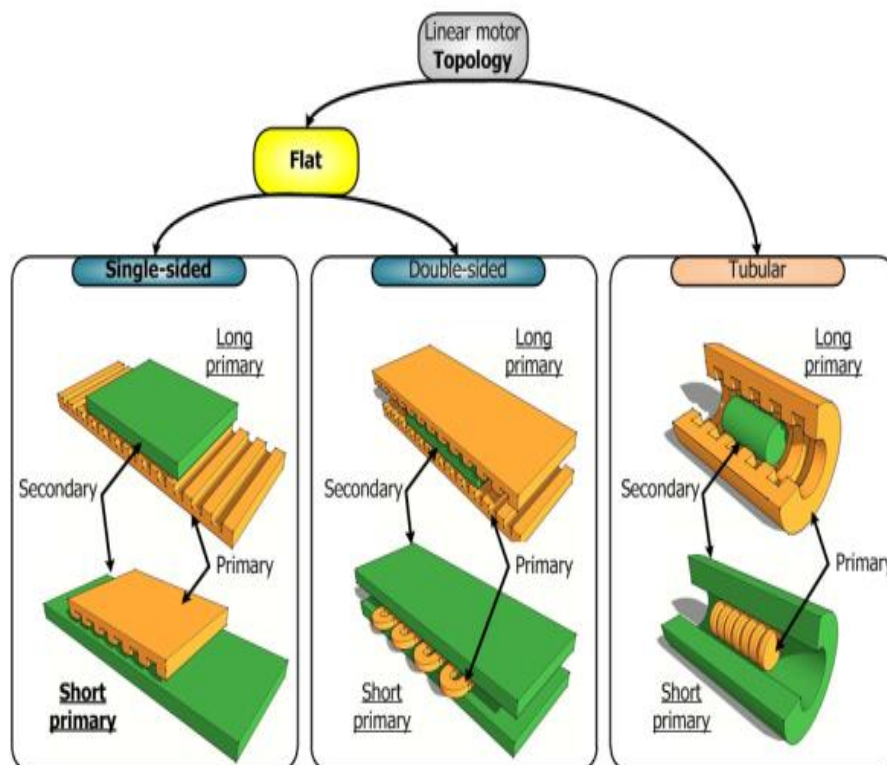
Figure 2.4 Topologies of the linear motor [17].

The rotary motors and linear motors can be divided into three main groups, which are: the induction motors, the synchronous motors and the DC motors, as shown in Figure 2.3.

- Linear induction motor (LIM): The LIM is a motor in which the excitation is induced by the primary in a conduction layer. The primary generates a magnetic field in the air-gap, which induces a voltage in the secondary. The electromagnetic thrust is produced by the interaction between the generated magnetic field and the induced secondary currents. The LIM construction is very simple, thus, it is less expensive than the LSM.

- Linear synchronous motor (LSM): The LSM is a motor in which the linear motion is produced in synchronism with the generated magnetic field in the air-gap. The thrust is generated due to the interaction of the magnetic field produced by the primary and the magnetic field produced by the PM. The thrust density of the LSM is higher than that of the LIM.

- DC linear motor (DCLM): The DCLM uses a DC as the excitation current. The thrust is generated by the interacting magnetic field which is generated by the switched DC current and the magnetic field produced by the PM. DC linear motors are generally made up of two main units; the permanent magnet unit which provides the main air gap flux and the armature unit. Either of the two can be the moving part while the other is fixed, the moving part is usually shorter, while the length of the static part determines the track length of the motor.

The motor part that contains the windings in which the current flows, in order to generate electromagnetic flux is called active, and the magnet part across the air gap is called passive. The stationary part (active or passive) is called the stator and the moving part (active or passive) of the motor is called the translator or the mover [6]. In this thesis, the terms rotor and mover both refer to the permanent magnet which produces the main magnetic field. The terms stator will be used for the motor armature which contains the winding, and refers to the stator part of the motor.

2.2.1 Slotted Linear Motor

This type of linear motors has a moving winding assembly, which is shorter than the stator, and coils wound around the teeth. The stator consists of a long group of magnets mounted on a magnetically permeable surface [3]. Figure 2.5 illustrates the construction of slotted linear motor. The iron core guides the magnetic field generated in the coil, hence significantly increasing the output force produced. This type of linear motor has a strong magnetic attraction force between the magnet assembly and the stator laminations.

Slotted linear motors are very powerful and compact. Unfortunately, these motors suffer a high cogging force due to the mutual attraction between the magnets and the iron cores of the mover. The cogging force depends on the relative position of mover and magnets, and exists even when there is no current. A robust mechanical guidance system is required to guide the moving part and to keep the air gap precise [7].
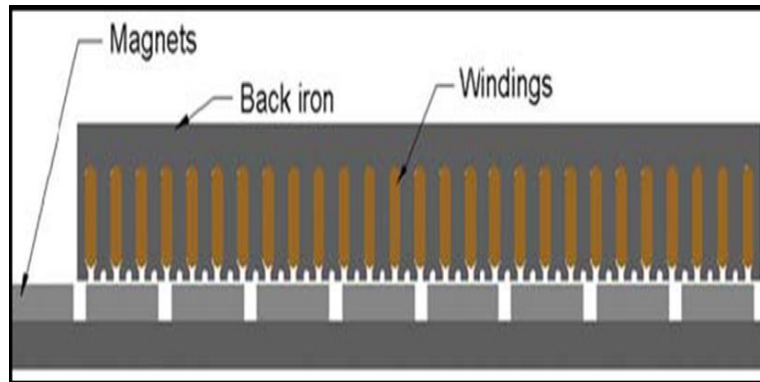
Figure 2.5 Slotted Linear Motor [15]

2.2.2 Slotless Linear Motor

Figure 2.6 illustrates the construction of slotless linear motor. Slotless linear motors have the armature winding without teeth and therefore, the tooth ripple component of the cogging force is eliminated. However, there is a disadvantage associated with the design, which is; slotless linear motors suffer from a lower magnetic flux crossing the air gap [18]. Hence, a thicker magnet is required in order to overcome the reduction of magnetic flux density in the slotless motor, due to the absence of teeth.
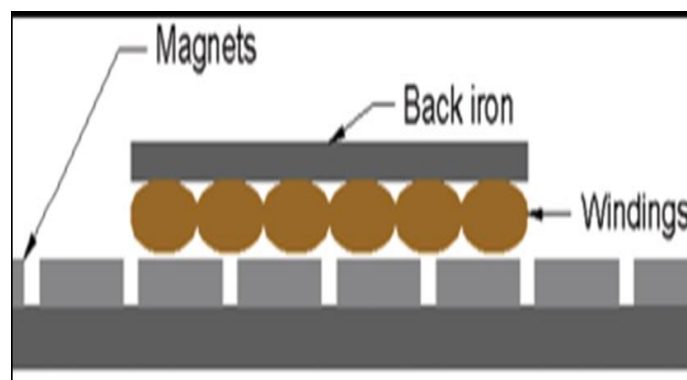
Figure 2.6 Slotless Linear [15].

2.2.3 Ironless Linear Motor

This type of motor is also called an air-core motor and as its name implies, an ironless linear motor has no iron core inside. The mover is constructed with coils wound and held together with epoxy. Figure 2.7 illustrates the structure of the Ironless motor. Compared with the other types, the moving coil motor have a light weight armature and possesses the highest force to inertia ratio. The main advantage of this motor the elimination of the cogging force. The ironless armature improves the power density of the motor since it has a very light weight [3].
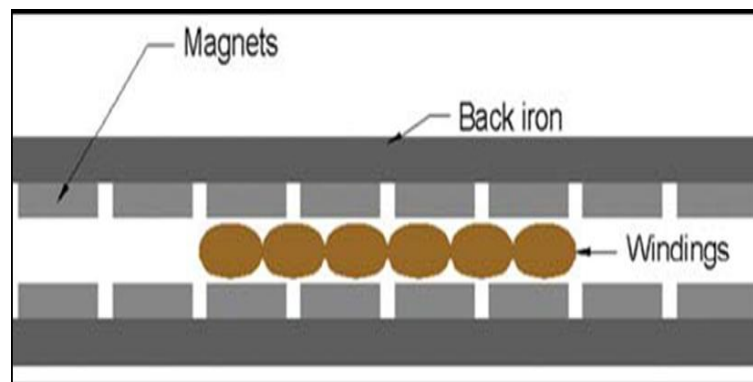
Figure 2.7 Ironless Core Linear Motor [15].

Furthermore, there is no attraction force between the coil assembly and the permanent magnets, which make it ideal for applications requiring high acceleration of lighter loads. However, moving coil motors have a lower efficiency compared with the slotted and slotless types, because of their high magnetic air-gap, which is the sum of the coil height and magnet height. In this case, thicker magnets are required [3]. Figure 2.8 shows the effective air gap in the slotted and slotless core design.

The ironless core type is preferred to avoid problems associated with the saturation of the magnetic circuit and the interaction between moving magnets and magnetic fixed

parts. Generally, due to their light weight, ironless PM linear motors are often used for applications that requires a high dynamic as well as precise motion control [18, 19, 20]. Comparison between different types of linear motors is listed in table 2.1.
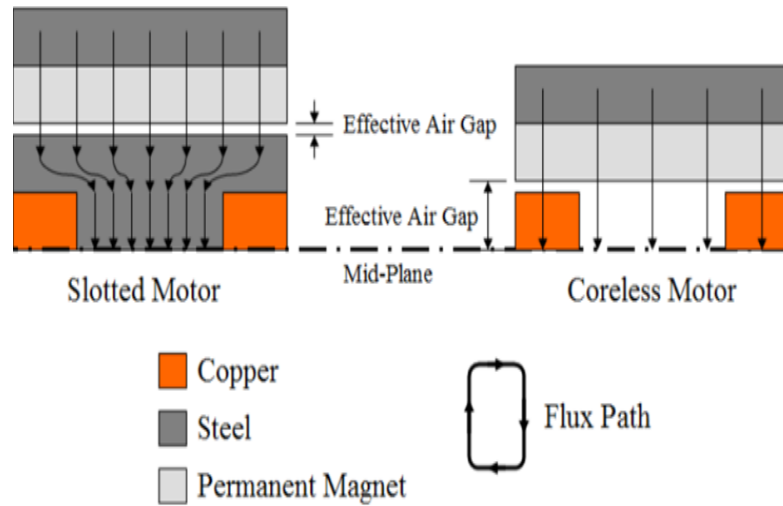
Figure 2.8 Effective air gap in slotted and slotless core design [20].

Table 2.1 Linear Motor Type Comparison [19]

Feature	Iron core	Ironless	Slotless
Attraction force	Most	None	Moderate
Force cogging	Medium	high	lowest
Power density	Highest	Medium	Medium
Force weight	Heaviest	Lightest	Moderate

2.3   Classification of Magnetic Materials

Magnetic materials are classified according to their relative permeability (μ_r), which are; ferromagnetic materials, electrical conductor materials (Diamagnetic) and electrical insulator (Paramagnetic) materials. Paramagnetic materials such as air and aluminium have a relative permeability slightly higher than unity ($\boldsymbol{\mu_r} > 1$). Diamagnetic materials such as copper has a relative permeability slightly less than unity ($\boldsymbol{\mu_r} < 1$). Both of these materials has a linear relationship with an applied magnetic field (**H**). Ferromagnetic materials such as iron have a relative permeability much greater than unity ($\boldsymbol{\mu_r} \gg 1$) and does not have a linear relationship with an applied magnetic field (**H**).

The magnetic properties of magnetic materials are defined based on the hysteresis loop, which can be classified into two categories [21]:

Soft Magnetic Materials: These materials have a narrow hysteresis loop, low remanence flux density and small coercive field; hence they can be magnetised and demagnetised easily.

Hard Magnetic Materials: These materials have wide hysteresis loop, high remanence flux density and high coercive field. They are usually used as permanent magnets. The hysteresis loops for soft and hard magnetic materials are shown in Figure 2.9.
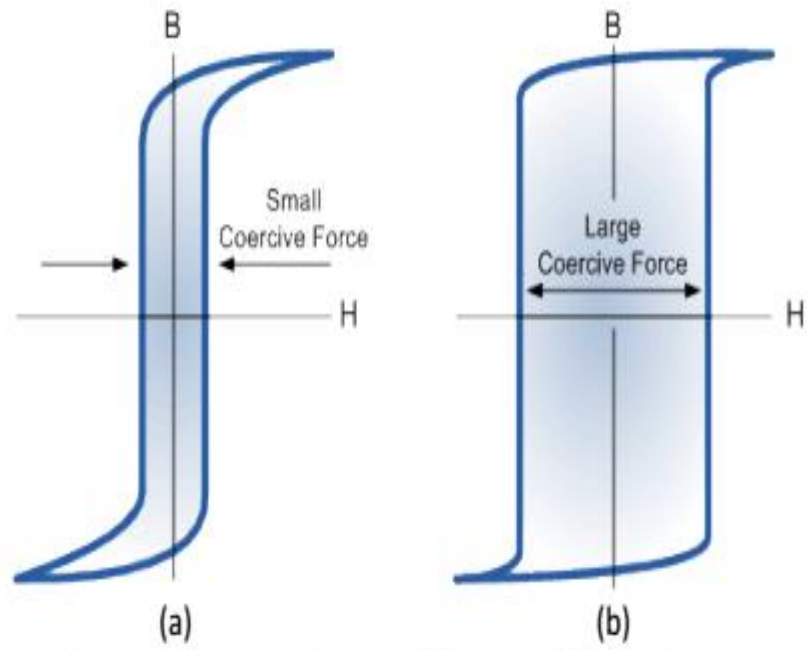
Figure 2.9 Comparison between hysteresis loops of (a) soft and (b) hard magnetic materials [21].

2.3.1 B-H curve and magnetic hysteresis loop

The basic characteristic of a magnetic material is its hysteresis loop, which is also called the B-H curve. The B-H curve illustrates the relationship between flux density (B) and magnetic field strength (H) in a given material. The hysteresis loop can be obtained by changing the magnetic field and measuring the magnetic flux density in the magnetic circuit [94]. In ferromagnetic materials, the ratio of the magnetic flux density to magnetic field strength (B/H) is nonlinear. All magnetic materials possess its own magnetic hysteresis curve.

The nonlinear relationship between B and H reflects the behaviour of ferromagnetic core as shown in Fig 2.11. Starting from zero point (0) which represents a general un-magnetised condition, where *B* and H are zero. When the field strength H is gradually increased, the flux density B also increases. The B-H curve follows the path from point 0 along the dotted line to point a, which is known as the "initial magnetisation curve" of the material. At point a, any additional increase in the magnetic field leads to very little increase in the magnetic flux density. This is known as the "magnetic saturation region". This point determines the maximum level of the magnetic flux that can be achieved by the material [21].

 When the magnetising field is decreased to zero, the flux will not be decreased to zero but attains point b called remanence (+Br) state, due the residual flux that remains in the core even when there is no magnetic field. In order to reduce Br to zero at point c, a negative field strength Hc must be applied. The magnetic field to force the flux density to return to zero, at point c, is known as the coercive field or the coercivity of the material [21].

If the intensity is further increased in the negative direction, a reversal saturation flux density B_s is achieved at point d.

 Similarly, if the magnetising field is decreased to zero, the flux will not be decreased to zero but will attain a negative residual flux at point e (−Br). Increasing the field strength causes the coercive force to demagnetise the core again at point f. The flux then increases with increase in magnetising current until the saturation point is reached again at point a where the path ends. The complete path (a-b-c-d-e-f-a) which forms a closed loop is called magnetic hysteresis loop [22]. This thesis concerns about designing a brushless DC linear motor, hence there is no effect of hysteresis loses on the motor response.
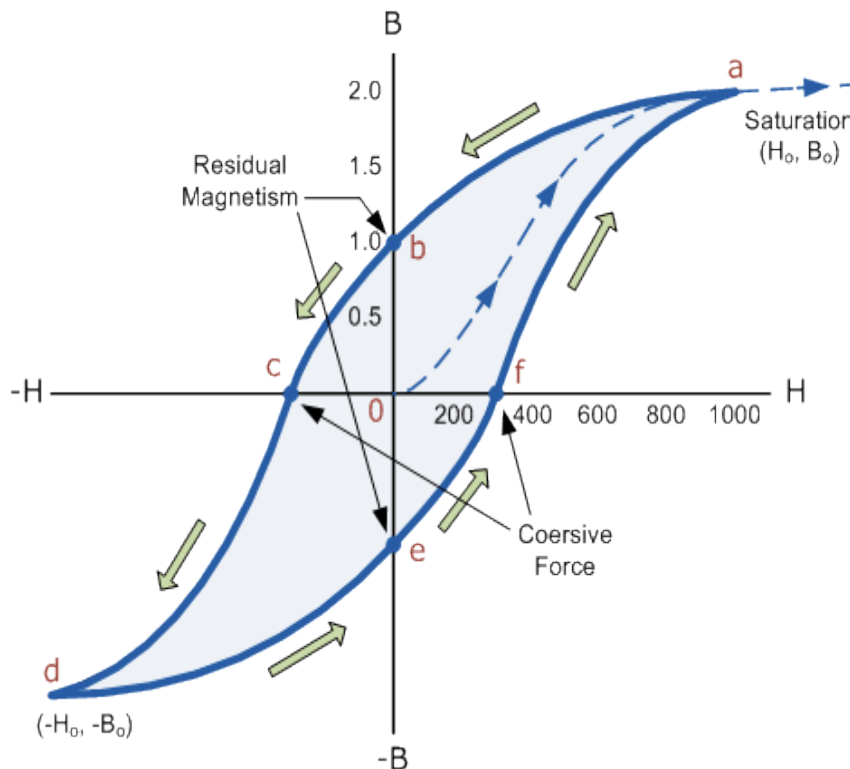
Figure 2.10 Magnetic hysteresis loop [22].

Figure 2.10 shows the B-H curve for three different materials; air, iron and steel. It can be seen that an increase in the magnetic field strength (H) leads to a proportional increase in the magnetic flux density (B) until a certain level is reached where the flux density level becomes almost constant as the field strength continues to increase. At this point all the magnetic moments within domains in the core are perfectly aligned with one another. This region is known as the "magnetic saturation of the core".
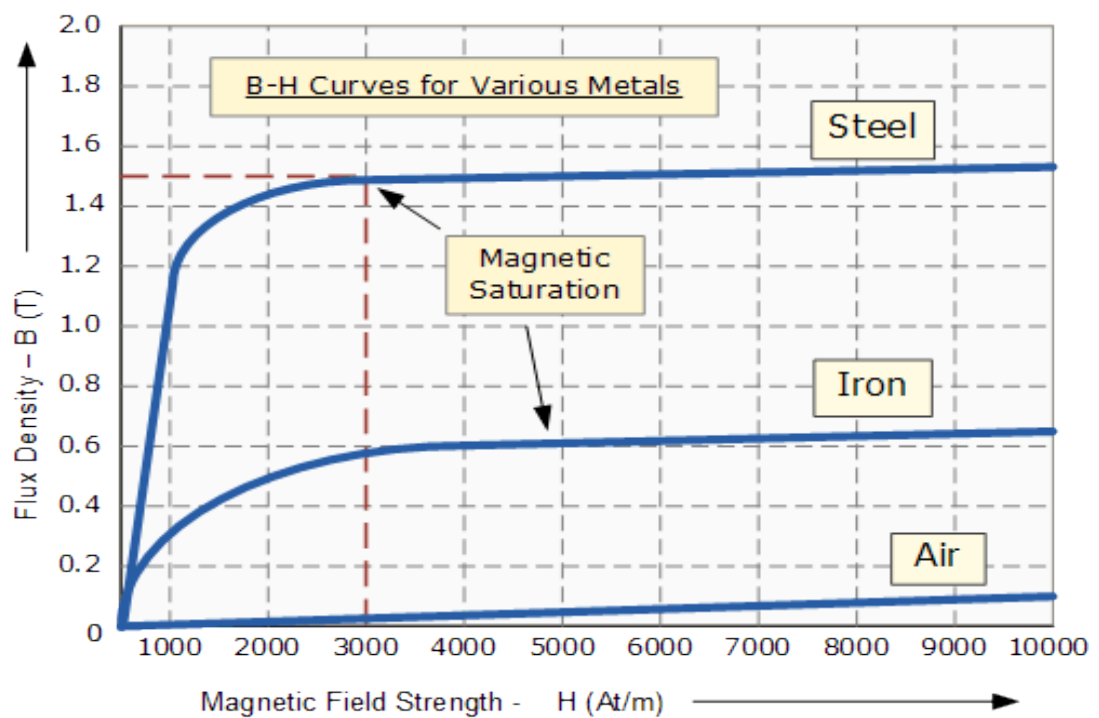
Figure 2.11 Magnetisation Curve of different type of material [22].

2.3.2 Common Types of Permanent Magnets

The permanent magnet properties affect the performance of the motor. Hence, a proper knowledge is required in order to select the appropriate material and to acquire a good understanding of PM motors [23]. Permanent magnet materials are characterized using three specific parameters which are [24]:

• Residual Flux, (B$_r$).

• Coercive Force, (H$_c$).

• Maximum Energy Product, (BH) $_{max}$.

Residual flux is the maximum flux density that can be retained by the magnet at a specified temperature. Coercive force is the value of magnetic flux intensity when the magnetic flux density is zero [24].

The maximum energy product is considered as one of the important properties of the permanent magnet. It represents the maximum energy available per unit volume (kJ/m^3) which is the multiplication of residual flux density (B_r) and coercive force (H_c). The larger the value of (BH) $_{max}$, the smaller the magnet material required to produce the same force [4].

A variety of magnet materials are available in the market which vary with respect to their characteristic and cost. The design criteria for choosing a permanent magnet in a brushless DC linear motor are [25]:

1- High coercivity to resist demagnetisation.

2- High energy product to give minimum magnet volume.

3- Low temperature coefficient to give stable performance under all conditions and to resist demagnetisation.

4- Low cost.

There is a general trade-off between (1) to (4). A comparison between the different available permanent magnet materials will be discussed in the next paragraph.

The earliest manufactured magnet materials were hardened steel. Magnets made from steel were easily magnetised. However, they could hold very low energy and it was easy to demagnetise. Today, there are different types of PM materials available in the market. The types available include; Aluminium, Nickel and Cobalt alloys (ALNICO), Strontium Ferrite or Barium Ferrite (Ferrite). However; Ferrite magnets are considered the most popular choices for low-cost motors because they are cheap [23].

It is important to choose a proper permanent magnet material in an electric machine, because it influences the thrust and power density. The future of permanent magnet motor technology changed after the discovery of the rare-earth magnets where magnetic flux density can be increased up to 1.5 T levels. Amongst the permanent magnet materials, the rare-earth permanent magnets; Samarium Cobalt (SmCo) and Neodymium Iron Boron (NdFeB) are considered to be the best grades. This is due to the capability of these materials to store large amounts of magnetic energy needed to operate, as well as their high coercivity which allows for small size application [88]. SmCo magnets have higher flux density levels but they are very expensive. NdFeB is replacing samarium cobalt (SmCo) and alnico in many applications. However, for very high-temperature applications, SmCo is more suitable than NdFeB [23], [26].

 NdFeB magnets are the most common rare-earth magnets used by manufacturers worldwide. They give higher power-to-weight ratio [3]. The high remanence and

coercivity allows for reduction in motor frame size, for the same output compared with motors using ferrite magnets. However, the size reduction is at the expense of an increased cost of the magnets [23], [27]. A brief comparison of the different magnets used in PM motors is illustrated in Table 2.2.

Furthermore, all these magnets have a linear characteristic throughout the second quadrant of B-H carve, and they are classified as hard magnets because of their high resistance to demagnetisation. Figure 2.12 illustrates the demagnetisation curves for the different permanent magnet materials [28].
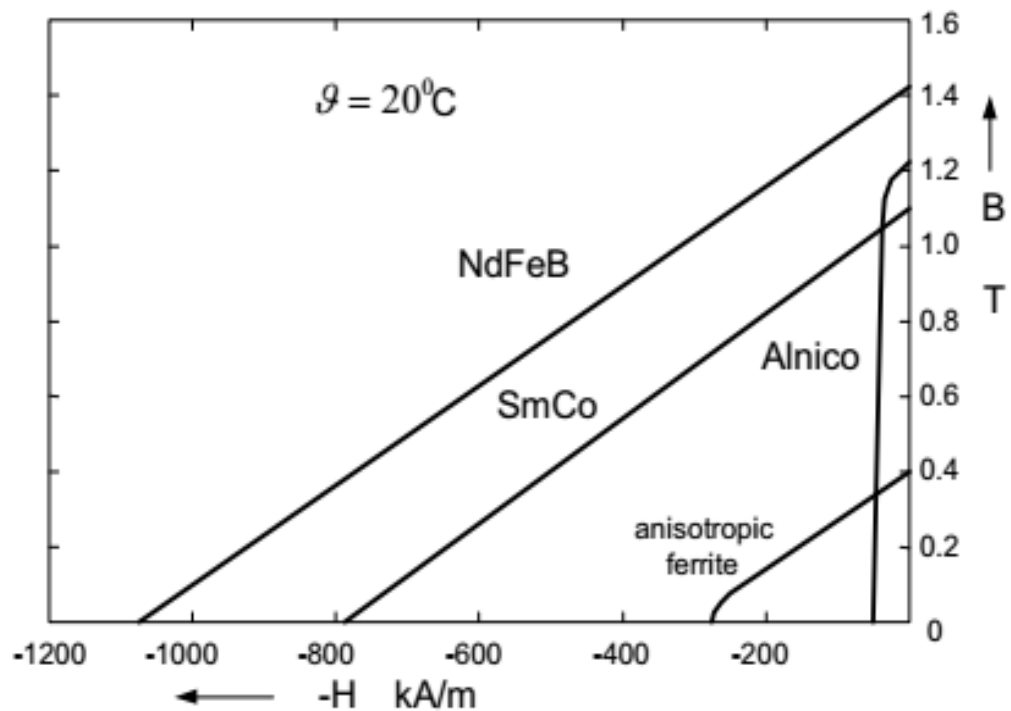
Figure 2.12 Flux Density versus Magnetising Field of Permanent Magnetic Materials [29].

Table 2.2 Typical permanent magnet material magnetic properties [14].

Materials	B_r[T]	H_c[kA/m]	$(BH)_{max}$[kJ/m^3]	T_c[°C]	T_{w-max}[°C]	Resistance to demagnetisation
Alninco	1.2	10	6	500	500	Very high
Ferrite	0.43	10	5	300	300	Very high
SmCo	Up to 1.1	Up to 820	Up to 240	Up to 820	Up to 350	Low
NdFeB	Up to 1.5	Up to 1033	Up to 422	Up to 380	Up to 200	Moderate

2.4 Magnetic Circuit Analysis

The fast development of permanent-magnet material and its influence on the industrial market has led to the replacement of induction motors with permanent-magnet machines, which has a smaller size and higher efficiency compared to the induction motors. Therefore, prior to the analysis of the magnetic circuit for the PM, it is necessary to acquire a good understanding of the characteristic of the PM material [25].

2.4.1 Demagnetization curve of a PM

Figure 2.13 explains the permanent magnet operation, its ability to produce a flux and magnetomotive force under different service conditions. A PM can produce a magnetic field in an air-gap without an excitation winding and no dissipation of electric power. Similar to other ferromagnetic materials, a PM can be evaluated according to its B-H curve. However, the upper left-hand quadrant known as the demagnetization curve is the region of interest [29]. Figure 2.13 shows the demagnetization curve of a PM material. The graph provides specific information on how a given material with specific dimension can operate under magnetic loading conditions [25].

When no current is applied to the armature winding, the PM operates with remanent magnetic flux density (B_r) and intrinsic coactivity (H_c). If a reverse magnetic field intensity is applied, the magnetic flux density decreases to point K. The operating point of magnetic material K is the intersection of the load line with demagnetization curve of PM, which is known as the Permeance Coefficient (PC) [25].

When the reversal magnetic flux density is removed, the flux density returns to point L according to a minor hysteresis loop. The minor hysteresis loop is usually replaced by a straight line called the recoil line [29].

The general relationship between the magnetic flux density (B_m), intrinsic magnetization(B_i) and magnetic field intensity (H_m) in a ferromagnetic material may be expressed as:

$$B_m = \mu_0 H + B_i \quad (2.3)$$

Where μ_0, is the magnetic permeability of free space $\mu_0 = 4\pi \times 10^{-7}$ H/m.

When $H = 0$ the intrinsic magnetic flux density $B_i = B_r$.
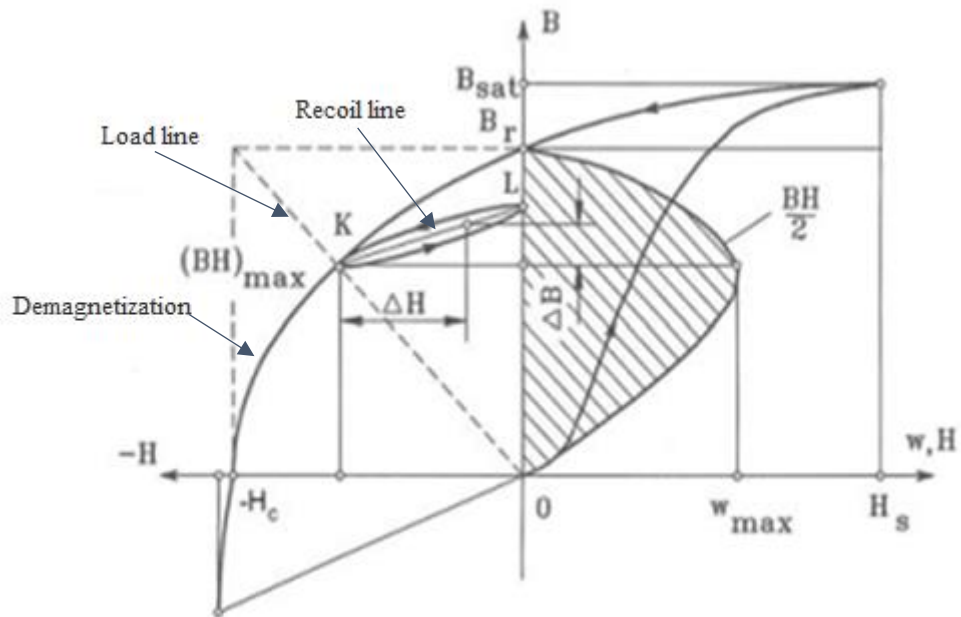
Figure 2.13 Demagnetization curve, recoil loop of a PM [29].

2.5   Magnetic circuit analysis in PM motor

In an analogy to a magnetic circuit, the magnetic circuit is equivalent to an electrical circuit. The flux generated in the magnetic circuit is equivalent to the current generated in an electrical circuit, the magnetomotive force is equivalent to the voltage, and the reluctance is equivalent to the resistance in an electrical circuit. Table 2.3 shows the magmatic circuit parameter equivalence with respect to the electrical circuit parameters.

The design of a PM is mainly concerned with determining the basic dimensions and the material specifications required to produce a sufficient magnetomotive force (MMF), in order to overcome the reluctance of the magnetic circuit and to produce the desired flux in the air gap [25].

Table 2.3 Equivalent of electrical and magmatic circuit parameters.

Electrical circuit	Unit	Magnetic circuit	Unit
Current (I)	Ampere	Flux (Φ)	Weber
Resistance (R)	Ohm	Reluctance (Ɍ)	A /Wb
Voltage (V)	Volts	Magnetomotive force (MMF)	A

A magnetic circuit in linear motors basically consists of three elements; the permanent magnet, the air gap, and the iron path for the flux. The MMF which is produced by the PM determines the total flux generated in the external circuit as expressed in equation 2.4 [3]:

$$MMF = \Phi.\,Ɍ \qquad (2.4)$$

Where Φ is the flux, MMF is magnetomotive force and $Ɍ$ is the reluctance. Figure 2.14 shows a simple magnetic circuit with a permanent magnet. The magnetic flux generated by the permanent magnet travels from the North Pole (NP) to the South Pole (SP) through the air-gap.
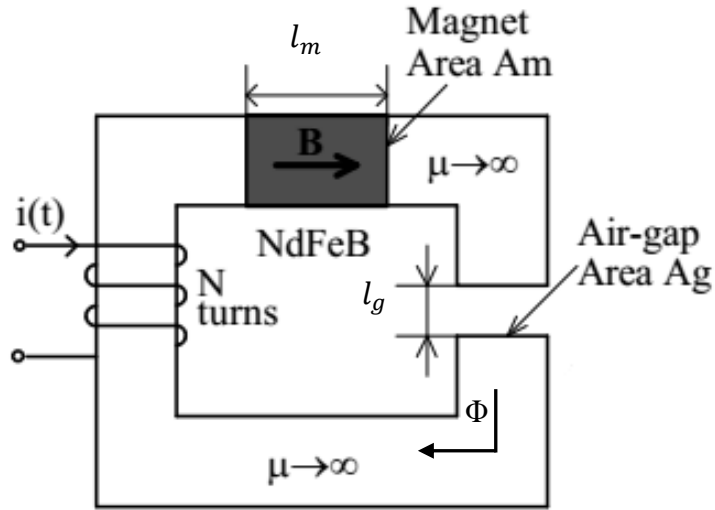
Figure 2.14 A schematic diagram showing a simple magnetic circuit with permanent magnet [25].

Assuming there is no flux leakage in the magnetic circuit and the magnetic permeability of the steel is infinite, therefore, the total flux passing through the magnet must be equal to the total flux through the air-gap and the drop in MMF around the magnetic circuit is equal to 0 when current is equal to zero (I=0).

$$\text{MMF} = \text{NI} = k_r H_g l_g + H_m l_m \qquad (2.5)$$

$$H_g = \frac{H_m l_m}{k_r l_g} \qquad (2.6)$$

Where H_g and H_m are magnatic field intensities in the air-gap and in the permanent magnet respectively. k_r is the reluctance factor. The value of the reluctance factor varies between (1.0 –1.2) depends on the machine [25].

$$B_m . A_m = q . B_g . A_g \qquad (2.7)$$

$$B_m = \frac{q . B_g . A_g}{A_m} \qquad (2.8)$$

Where B_g and B_m are the magnetic field densities in the air-gap and in the permanent magnet respectively. **q** is the leakage factor, the leakage factor has a typical value range between (0.9 - 1.0)[25].

$$B_g = \mu_0 . H_g \qquad (2.9)$$

$$B_m = \frac{q . \mu_0 . H_g . A_g}{A_m} \qquad (2.10)$$

$$B_m = \frac{q . \mu_0 . A_g}{A_m} \frac{l_m H_m}{k_r . l_g} \qquad (2.11)$$

In equation 2.11, it can be seen that there is a linear relationship between the magnetic field densities (B_m) and magnetic field intensity (H_m). This linear relationship is called the load line, as shown in figure 2.15.
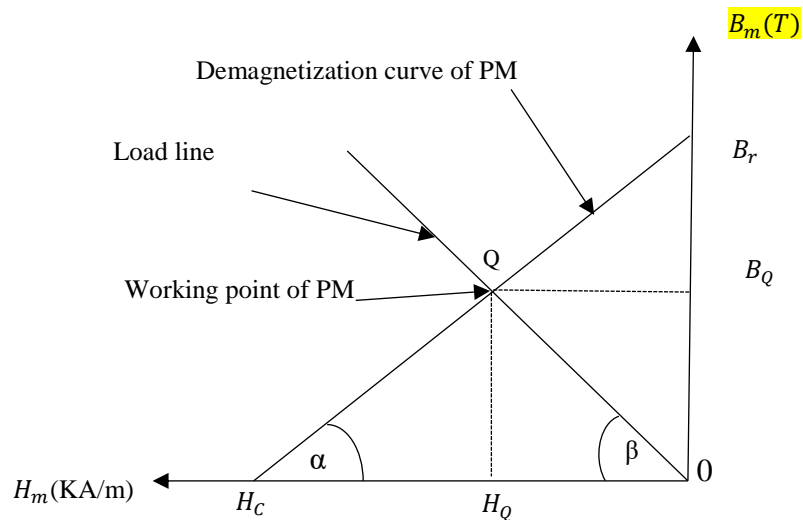
Figure 2.15 Demagnetization curve and load line of PM.

As can be seen in figure 2.15, there are two intersecting lines, which are; the load line and the demagnetization curve of the permanent magnet. The equation of the demagnetization curve is given by:

$$B_m = tan\alpha . H_m + B_r \quad (2.12)$$

The slope of the demagnetization curve is:

$$tan\alpha = \frac{B_r}{H_c} \quad (2.13)$$

$$B_m = \frac{B_r}{H_c} . H_m + B_r \quad (2.14)$$

The point Q in the graph where the load line and the demagnetization curve intersect represents the operating point of the permanent magnet.

2.5.1   Equivalent Magnetic Circuit of Permanent Magnet Motor

Figure 2.16 shows a schematic diagram of the magnetic flux distribution in one-pole section of permanent magnet motor (half N pole and half S-pole). In an electric machine, the permanent magnet is considered as a flux source. As shown in the graph, the flux produced by the permanent magnet (Φ_m) consists of two parts;

 a) The flux produced by the permanent magnet travels from the N-pole through the air-gap to stator core teeth across the air-gap before going back to the S-pole and then to the rotor steel to complete the closed-loop circuit. This flux is called the useful flux.

 b) The other flux generated passes through the air-gap without linking with the phase winding, this flux is called the leakage flux (Φ_l).

$$\Phi_m = \Phi_g + \Phi_l \quad (2.15)$$
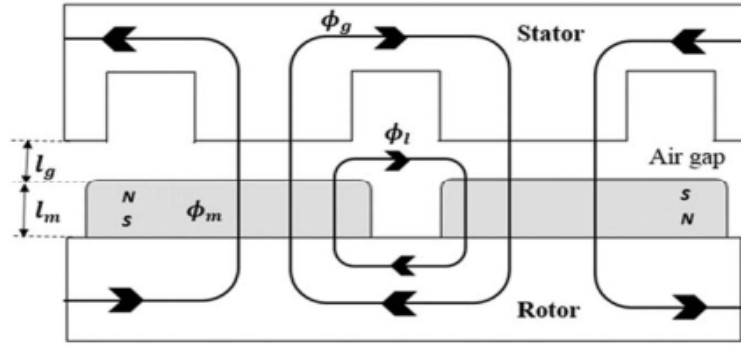
Figure 2.16 Schematic diagram of the magnetic flux path for PM motor [25].

Figure 2.17 shows the equivalent magnetic circuit for the schematic diagram displayed in figure 2.16, where R_m, R_g, R_l, R_s and R_r are the equivalent reluctances of permanent magnet, air-gap, leakage flux, stator and rotor steel respectively.

$$\Phi_m = \frac{4R_m}{4R_m + 4R_g + R_l + R_s + R_r} . \Phi_r \quad (2.16)$$

The magnetic permeability for steel material is a thousand times greater than that of air. Therefore, the reluctance for steel is comparatively very small and can be ignored. Thus, the equation (2.16) can be simplified as:

$$\Phi_m = \frac{4R_m}{4R_m + 4R_g + R_l} . \Phi_r \quad (2.17)$$

The leakage flux coefficient (q) can be considered as the ratio of the flux generated from the permanent magnet to that passing through the air-gap can be expressed mathematically as:

$$q = \frac{\Phi_m}{\Phi_g} = \frac{\Phi_g + \Phi_l}{\Phi_g} \qquad (2.18)$$

The equation (2.17) can be simplified as [25]:

$$\Phi_m = \frac{\Phi_r}{1 + q.P_m.R_g} \qquad (2.19)$$

Where (P_m) is the internal magnet permeance and can be expressed a shown in equation 2.20 [25]:

$$P_m = \frac{\mu_0 \mu_r A_m}{h_m} \qquad (2.20)$$

From equation (2.18), Φ_g can be expressed as:

$$\Phi_g = \frac{\Phi_m}{q} \qquad (2.21)$$

Substitute equation (2.19) in equation (2.21) yields

$$\Phi_g = \frac{q.\Phi_r}{1 + q.P_m.R_g} \qquad (2.22)$$

Given that

$$\Phi_g = B_g . A_g \qquad (2.23)$$

And

$$\Phi_r = B_r . A_g \qquad (2.24)$$

Equation (2.22) an be rearranged to

$$B_g = \frac{q.\frac{A_m}{A_g}\Phi_r}{1 + q.P_m.R_g} \qquad (2.25)$$
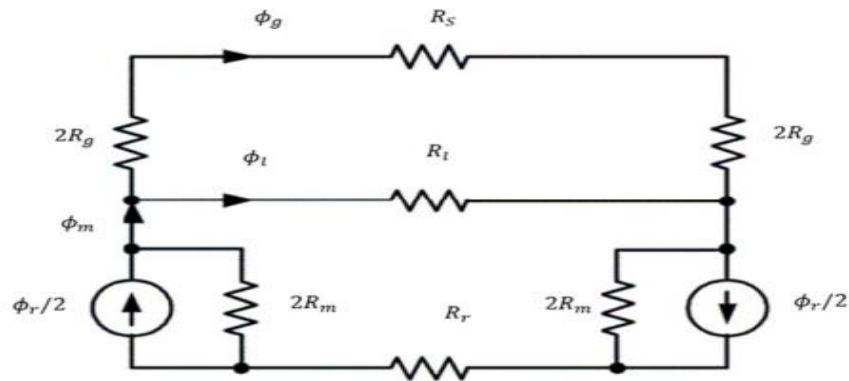
Figure 2.17 Complete magnetic equivalent circuit for one pole of PM motor [25].

2.5.2 Different types of permanent magnet configuration

There are different configurations for producing the air-gap flux density in permanent magnet machines. The PM is the magnetic source and can be either surface (mounted) or inserted (buried) in a magnetic yoke or combined to form a Halbach array. However, for this project the mounted PM configuration is used due to their simple structure and low manufacturing cost [25].

Figure 2.18a shows a single-sided surface PMs where PMs are magnetised perpendicular to the direction of the traveling magnetic field and the yoke of the reaction rail is ferromagnetic. Figure 2.18b shows a single-sided buried-type PMs where PMs are magnetised in the direction of the traveling magnetic field and the yoke of the reaction rail is non-ferromagnetic (e.g. Aluminium). Figure 2.18c shows a Halbach

array where magnetisation vector should rotate as a function of distance along the array. The Halbach array does not require any ferromagnetic yoke [30].

a)   Single sided mounted magnets

b) Single sided insert magnets

c)   Single sided Halbach array
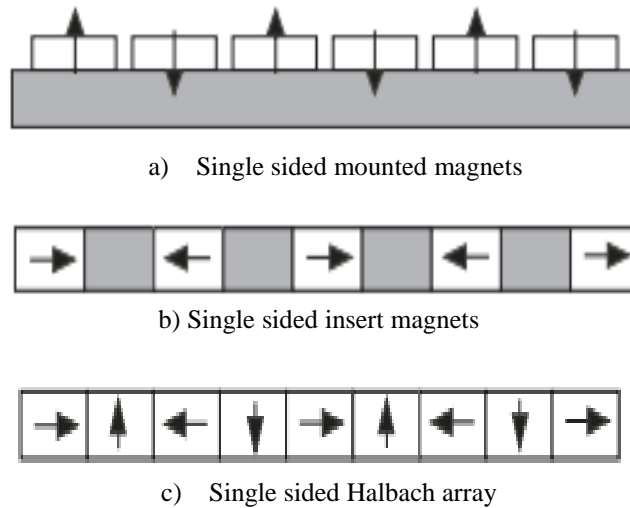
Figure 2.18 Different magnetic ways [30].

2.6   Linear Motor Forces

In conventional rotary machines there are two forces acting on the rotor surface. One is the tangential force which produces the torque and the other is a radial force acting perpendicularly to the rotor surface. The radial force sums to zero around the circumference due to the cylindrical shape of the motor [31]. For the linear motor, the main forces involved are the thrust, normal and lateral forces.

Figure 2.19 illustrates the forces associated with linear motors. This thesis will concentrate more on the thrust force. The thrust results from the interaction between the armature current and the magnetic flux provided by the permanent magnet, which is directly proportional to the amount of current flowing in the motor armature. The higher the current magnitude, the higher the thrust produced by the motor.
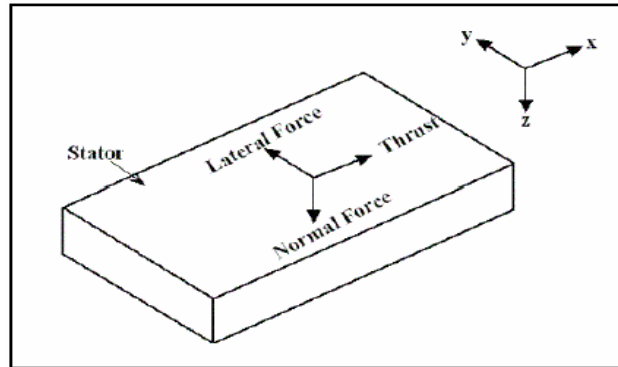
Figure 2.19 Forces associated with Linear motors [32].

The normal force is perpendicular to the stator in the Z-direction. The normal force is generated due to the attraction between the permanent magnets and the iron core of the stator. The normal force problem associated with the single-sided DC linear motor configuration affects its operating characteristics, stability and control strategy [33].

In a double-sided DC linear motor configuration, when the armature core is centrally located between two sets of permanent magnets, the normal force between the armature core and one side of the permanent magnet is equal and opposite to that on the other side of the permanent magnet. Therefore, the net normal force is zero. A net normal force will only occur if there is no symmetry between the stator and the mover. Lateral force is a side force that is undesirable due to the orientation of the stator and it only exists in induction motors [32].

2.7   Forces and Effects associated with Linear Motor

There are several nonlinear effects associated with linear brushless DC motor, due to its magnetic structure and other physical imperfections. These effects influence the

performance of the motor. The significant effects are the force ripple, the end effect and air-gap effects. A brief discussion of all the effects are discussed below [33].

2.7.1 Force ripple

The two main sources of force ripple are the cogging force (or detent force) and the reluctance force [34]. Generally, cogging force can be divided into core cogging force and teeth cogging force. Core cogging force which occurs in every pole pitch (occurs periodically) happens as a result of the mutual attraction between the magnets and the back iron. Whereas, teeth cogging force is generated due to the attraction force between the permanent magnet and the teeth structure [35]. Figure 2.20 shows the cogging force and the end effect.

Moreover, even in the case were there is no winding current, the cogging force still exists and exhibits a periodic relationship with respect to the position of the translator relative to the magnets. The detent force is the summation of two components, which are the cogging force caused by the interaction between the permanent magnet (PM) and the iron core and the end effect caused by the finite mover length [32].

$$F_{\text{Detent}} = F_{\text{Cogging}} + F_{\text{End effect}} \quad (2.26)$$
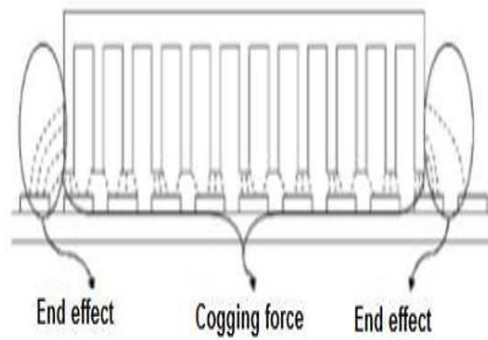
Figure 2.20 End effect forces in linear motor [32].

The reluctance force is created due to the variation of the self-inductance of the windings with respect to the relative position between the magnets and the translator. Thus, the reluctance force also has a periodic relationship with the translator-magnet position.

The force ripple has a significant effect on the positioning accuracy achievable and it could also produce oscillations. Hence, the force ripple affects the stability of the system, especially at low velocities or with a light load. Also, as long as a ferromagnetic core is used for the motor armature core, the ripple force exists in almost all variations of PMLM (flat, tubular, moving-magnet) [36].

2.7.2   End effects

The fundamental difference between a rotary motor and a linear motor is the finite length of the linear motor which causes the magnetic field to interact with the end of the armature winding and permanent magnet [19, 37]. Figure 2.20 shows the end effect forces in linear motors. The finite length of a linear motor has a major impact on its

performance. A linear motor has an open ended air gap with an entry end and an exit end, while a rotary motor has a closed air gap.

The most significant drawback caused by the end effect is the reduction of magnetic flux density near the ends of the motor mover, which spreads out into the adjoining air. This means that the traveling magnetic field cannot join up on its own, thereby introducing an end effect. The end effect is clearly exhibited in the form of a non-uniform flux density distribution along the length of the motor [38].

2.7.3 Air gap affect

The main difference between a linear motor and a rotary motor is the variation in the air gap. The length of air gap is the most critical aspect which determines the characteristics of the machine. Basically, an increase in the length of the air-gap causes a drop in the magnitude of the flux density and hence, a drop in developed thrust. Therefore, to obtain a high thrust, a minimal value has to be chosen for the air-gap length [33].

Nevertheless, in practice, the air-gap cannot be designed with a short length due to some mechanical limitations. In this project, a mechanical clearance of 5 mm (the length of the air-gap) is set between the motor mover and the armature core.

2.7.4 Effect of armature reaction

In linear machines where the effective length of the air-gap is relatively large and the average flux density of the air-gap is small, more stator current will be required to produce the rated thrust. As a result of the larger stator current requirement, a significantly larger armature reaction magnetic field is induced [25]. This magnetic field

tends to oppose and weaken the main flux which is produced by the permanent magnet. This higher armature reaction magnetic field could cause two problems [39]:

- The risk of demagnetisation damages to the permanent magnets and should be avoided under all machine operating conditions.

- Magnetic saturation in the stator teeth of armature core.

If the fringing effect is neglected, the maximum flux density in the stator teeth will be the linear sum of the magnetic field produced by the permanent magnet and the armature field which is given by [25]:

$$B_{max} = B_g + B_{arm} \qquad (2.27)$$

Where B_g air-gap flux density and B_{arm} is the flux density produced by armature reaction and this can be determined by equation 2.28 [88]:

$$B_{arm} = \frac{\mu_0 \mu_r MMF_{arm}}{g} \qquad (2.28)$$

Where, $\boldsymbol{F_{arm}}$ is the magnetomotive force produced in the armature and g is the equivalent air-gap length. To ensure that the armature core (B_{Core}) is unsaturated the equation 2.29 has to be satisfied:

$$B_{Core} \leq B_{max} \qquad (2.29)$$

For mild steel, the typical saturation flux density value is 1.8 T.

2.8 Machine design features

The design features for electrical machines can be classified into four categories, which are; electric, magnetic, thermal, and mechanical designs. All four categories are strongly related when designing any electrical machine [39]:

• **Electrical design;** this represents the supply voltage, frequency, number of phases of the machine, winding layouts, turns per phase and wire sizes.

• **Magnetic design**; this represents the air-gap length, properties of permanent magnet material (demagnetization curve and mass density) and the motor core material properties (B-H curve and core loss).

• **Thermal design;** this involves calculating the motor loss, temperature distribution and the cooling system of the motor. Depending on the application or power level, various types of cooling are used.

• **Mechanical design;** this represents the machine length and size, slot height, core height, noise, bearing design, inertia calculation and forces on the motor rotor.

2.9   Direct current linear motors

There are different types of DC linear motors in literature. They are categorised according to their principles and mode of operation. As a result of the rapidly growing power electronics and microcontrollers, the mechanical carbon brush commutators in the conventional DC linear motor is been replaced with electronic commutators. Hence, noise and electrical interference caused by the carbon brushes are eliminated. Generally, a DC motor is made up of two main units, which are the field and armature units. Either of the two can be the mobile part while the other is the stationary part. In the case of the DC linear motor, the mobile part is usually shorter than the stationary part. The length of the stationary part determines the length of the motor.

2.9.1 Permanent magnet DC linear motors

Permanent magnet DC linear motors is the type which employs permanent magnet as the field unit, instead of the winding field. The conventional motor uses two field windings, one on the stator acting as the main filed unit and the other on the moving part. The replacement of the field winding by a set of permanent magnets offers a considerable reduction in the power loss of the excitation circuit.

In comparison with electromagnetic motors, permanent magnets have the following properties [40]:

- No electrical energy is absorbed by the field excitation system, hence, no excitation losses.

- Higher thrust and higher output power per volume.

- Better dynamic performance, by reducing the weight of the moving part.

- Higher magnetic flux density in the air-gap.

- Simple construction and easier maintenance.

2.9.2 Principle of Operation

DC linear motors have similar operating principle compared to the conventional DC rotary motor. In the DC linear motors, the permanent magnet sets up the main field flux. The radial component of the flux cuts at right angle the flux generated in the armature winding. This gives rise to an axial force on the magnet mover unit which produces a linear motion.

Since the output force is dependent on both the magnetic flux and the armature current, a very high force can be produced by injecting a high current into the armature winding

and by maximizing the air-gap magnetic flux density between the permanent magnet and armature winding.

One advantage of the DC linear motor is its capability to control the force and speed characteristic, by changing the current in the armature winding. To produce a bi-directional displacement, the current in the armature windings must be reversed. The mechanical commutation parts of the motor could be replaced with an electronic commutator to obtain brushless DC linear motors [1].

2.10 Power Switching Circuit

In the brushless DC linear motor, the power switching H-bridge acts as an electronic commutator, which switches the DC current between the armature windings according to the instantaneous mover position. H-bridge is a circuit that can connect a supply voltage to a load in either direction.

The characteristic of the current waveform obtained in our motor design is dependent on switching of three devices out of the nine H-bridge devices at a given time. Thus, reducing the power consumption of the system.

The DC supply voltage is connected across nine armature winding with one winding carrying a positive current and the other two carrying a negative current, according to the commutation algorithm which has been designed to provide a smooth movement.

It is also possible to use the power-switching bridge to control the level of the current supplied to the armature windings, by using pulse width modulation (PWM). In PWM method, power is controlled by applying pulses of variable width by changing the pulse width of the power supply. When the pulse width is small, the average voltage applied onto the motor winding is low. While, if the pulse width is wide, the average voltage is

higher. The selection of the appropriate devices required is determined by the combination of switching frequency, power handling capability and cost [25].

Figure 2.21 illustrates the three operation principles of the H-bridge circuit, which are; a) when switches 1 and 4 are closed, current will flow in the forward direction, b) when switches 2 and 3 are closed, current will flow in the reverse direction and c) when switches are off, no current will flow in the armature windings. In the H-bridge circuit, MOSFETs are used for the switches, and the MOSFETs are turned on and off by the microcontroller.
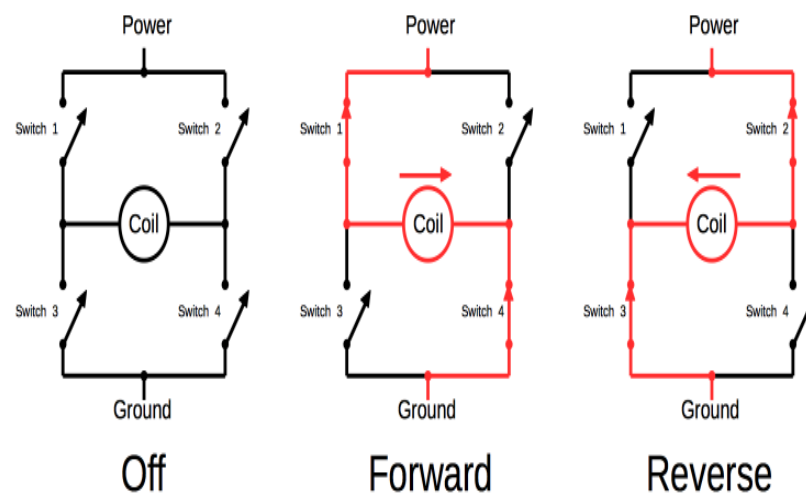
Figure 2.21. Operation principles of the H-bridge circuit [41].

2.11 Mathematical Modelling of BLDC Linear Motor

Like any DC motor, the electromagnetic force is based on Lorentz's law which states that the amount of force generated is equal to the cross product of the magnetic flux density and the amount of current flowing through a current carrying conductor:

$$F = N.B_g.L.i \qquad (2.30)$$

Where F is the electromagnetic force vector, N is number of coils in turns, L is the length of the conductor, i is the armature current vector and B_g is the air-gap magnetic flux density victor.

The force is proportional to the magnitude and direction of the current, as well as the magnetic flux density. Since the flux density of the permanent magnet and the number of turns are fixed, the direction of the magnitude and direction of the force will depend on the magnitude and polarity of input current. Hence;

$$T(t) = K_t.i(t) \qquad (2.31)$$

Where K_t , is the motor torque constant.

The back (induced) electromotive force E_{emf} , is a voltage proportional to the motor velocity;

$$E_{emf}(t) = K_b.v \qquad (2.32)$$

Where K_b , is the back electromotive force constant.

The dynamic characteristic of BLDC motor is similar to that of the permanent magnet rotary DC motor. The characteristic equations for the BLDC motor can be expressed as:

$$E(t) = L\frac{di(t)}{dt} + R \cdot i(t) + E_{emf}(t) \qquad (2.33)$$

$$T(t) = J\frac{dv(t)}{dt} + D \cdot v(t) \qquad (2.34)$$

Where $E(t)$ is the applied voltage, $v(t)$ is the motor speed, L is the inductance of the stator, $i(t)$ is the current of the circuit, R is the resistance of the stator, T is the motor torque, D is the viscous coefficient and J is the moment of inertia.

Combining equations (2.21), (2.32), (2.33) and (2.34) yields;

$$E(t) = L\frac{di(t)}{dt} + R \cdot i(t) + K_b \cdot v(t) \qquad (2.35)$$

$$K_t \cdot i(t) = J\frac{dv(t)}{dt} + D \cdot v(t) \qquad (2.36)$$

Using the Laplace transform, equations (2.33) and (2.34) can be written as:

$$E(s) = L \cdot s \cdot i(s) + R \cdot i(s) + K_b \cdot v(s) \qquad (2.37)$$

$$K_t \cdot i(s) = J \cdot v(s) \cdot s + D \cdot v(s) \qquad (2.38)$$

Where s denotes the Laplace transform. From (2.35), $i(s)$ can be expressed as

$$i(s) = \frac{E(s) - K_b \cdot v(s)}{L \cdot s + R} \qquad (2.39)$$

Substituting equation (2.39) in (2.38), equation 2.40 is obtained as

$$K_t \cdot \left(\frac{E(s) - K_b \cdot v(s)}{L \cdot s + R}\right) = J \cdot s \cdot v(s) + D \cdot v(s) \qquad (2.40)$$

$$K_t \cdot E(s) - K_t K_b \cdot v(s) = (Ls + R)(J \cdot s \cdot v(s) + D \cdot v(s)) \qquad (2.41)$$

$$K_t \cdot E(s) = (Ls + R)(Js \cdot v(s) + D \cdot v(s)) + K_t K_b \cdot v(s) \qquad (2.42)$$

$$K_t \cdot E(s) = (Ls + R)v(s)\ (Js + D) + K_t K_b \cdot v(s) \qquad (2.43)$$

$$K_t \cdot E(s) = v(s)[(Ls + R)\ (Js + D) + K_t K_b] \qquad (2.44)$$

From equation (2.44), the transfer function can be expressed as:

$$\frac{v(s)}{E(s)} = \frac{K_t}{(R + LS)(JS + D) + K_t K_b} \qquad (2.45)$$
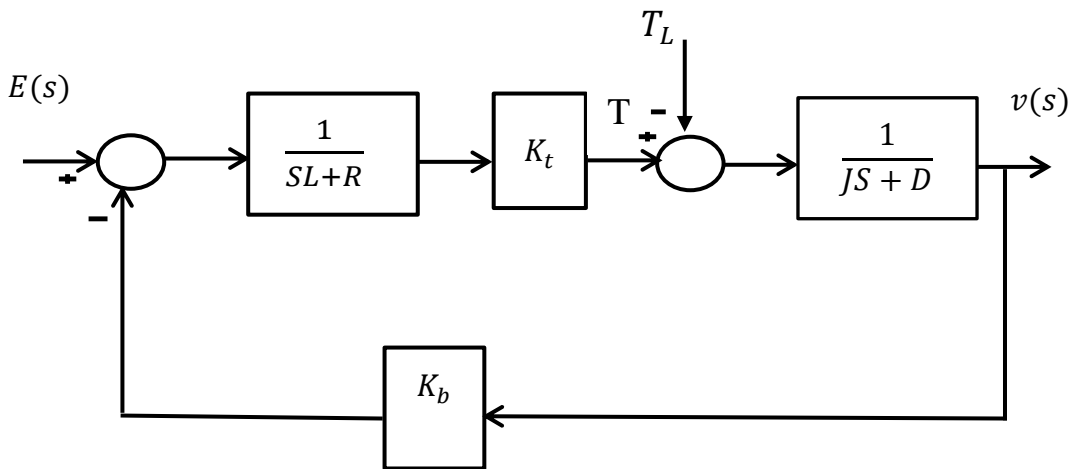
Figure 2.14. Block diagram of the BLDC motor.

2.12   State of the art

Recent improvements in the rare-earth permanent magnet (PM) materials and power electronics have generated new opportunities in the design, construction, and application of permanent magnet motors [28]. In the last few decades, many theoretical and experimental developments with respect to the field of low power applications of linear motors have been proposed. A few of them were related to the development of the DC linear motors. The BDCLM in this thesis is considered as a continuous work of in the field of DC linear motors for low speed and larger thrust to input current ratio. The proposed motor in this project was designed to produce the larger thrust to input power ratio, compared to the existing designs in the literature.

The literature review of DC linear motors is generally divided into two main areas, which are the wounded field DC linear motor and the permanent magnet DC linear motor [42].

2.12.1   Wound field DC linear motors

Although the linear electric motors were introduced centuries ago, there was still limited research on the linear motors compared to the rotary motors up until the 1960s. Since then, linear motors could be found in many different applications [5].

In 1964, a novel type of brushed DC linear motor was developed by Ratcliff and Griffiths [43]. The motor had a moving field unit and four brushes. The armature core was made of mild steel and was wounded with a copper conductor along its entire length. Also, the field unit coils were wounded on the carriage as shown in figure 2.15. The broken lines in figure 2.15 shows the direction of the magnetic flux in the motor. Four brushes were fixed to the carriage to supply a DC current to the armature windings.

In 1969, Jones [44] developed the brushed DC linear motor, which was introduced by Ratcliff and Griffiths. He modified the pole shape and reduced the number of brushes from four to three as shown in figure 2.16. Similar to figure 2.15, the broken lines in figure 2.16 also shows the direction of the magnetic flux in the motor. The motor had a fixed armature winding and a moving field unit. The armature voltage was supplied through three brushes.
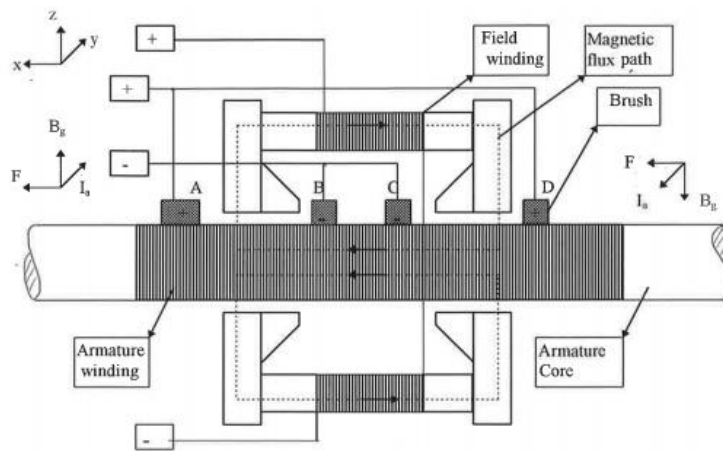
Figure 2.15 Cut section of wound field two pole linear motor was design by Ratcliff and Griffiths [43].
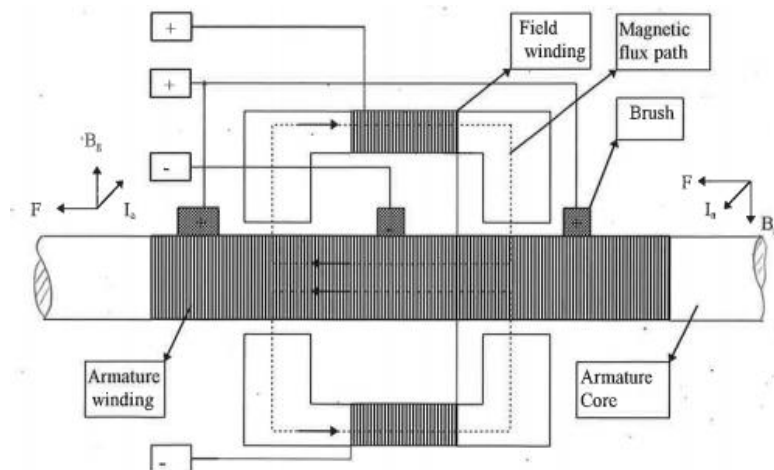
Figure 2.16 Cut section of wound field two pole linear motor was design by Jones [44].

Also, in 1969, Griffiths and Jones [45] introduced two types of wound field DC linear motor, with two poles as shown in figure 2.17 and four poles wound field as shown in figure 2.18. These linear motors have a fixed armature winding and a moving field unit. The armature voltage was supplied through brushes which were fixed to the carriage of the linear motor. In 1971 Warnett [46] developed a wound field DC linear motor similar to motor introduced by Griffiths and Jones, but with cylindrical field winding.
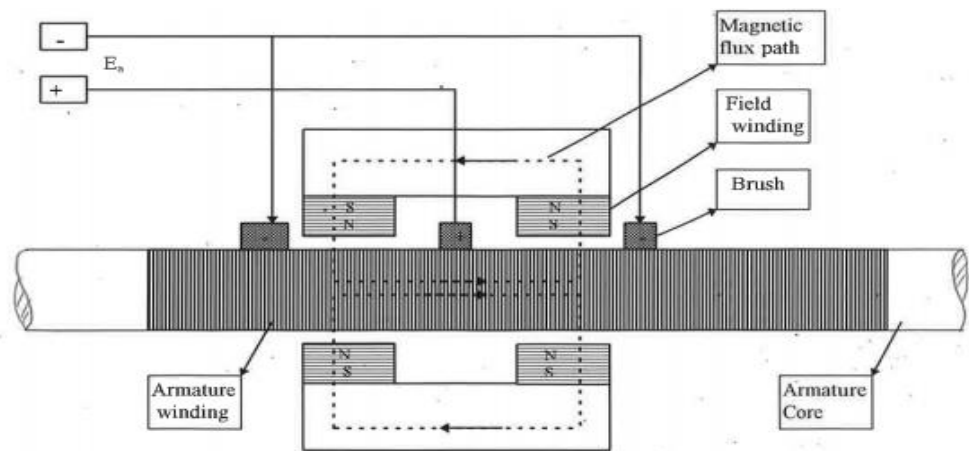
Figure 2.17 Cut section of wound field two pole linear motor was design by Griffiths and Jones [45].
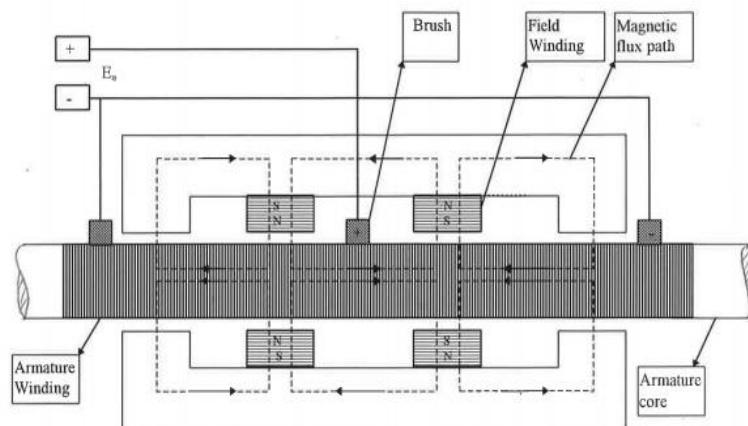
Figure 2.18 Cut section of wound field of four pole linear motor was design by Griffiths and Jones [45].

In 1969, Green and Paul [47] introduced another type of DC linear motor for short-stroke and static applications. Figure 2.29 shows two pole linear motor where the motor was designed such that the field unit is fixed and the armature was free to move over a limited distance. A single layer winding was wound around the circular mild steel core and the direction of the winding was reversed at the center of the core. Therefore, the need of using brushes to reverse the polarity of the supply current was elleminated. This type of motor design is called the brushless wound DC linear motor. The flux pattern for the motor is illustrated in figure 2.20.
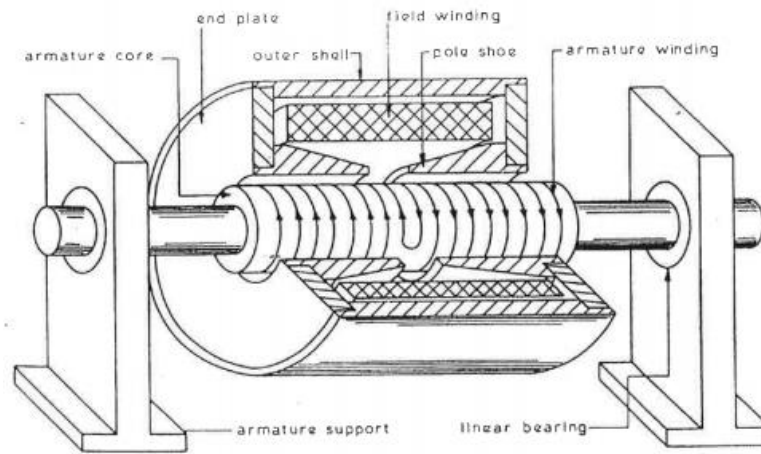
Figure 2.19 Two pole wound field linear motor was design by Green and Paul [47].
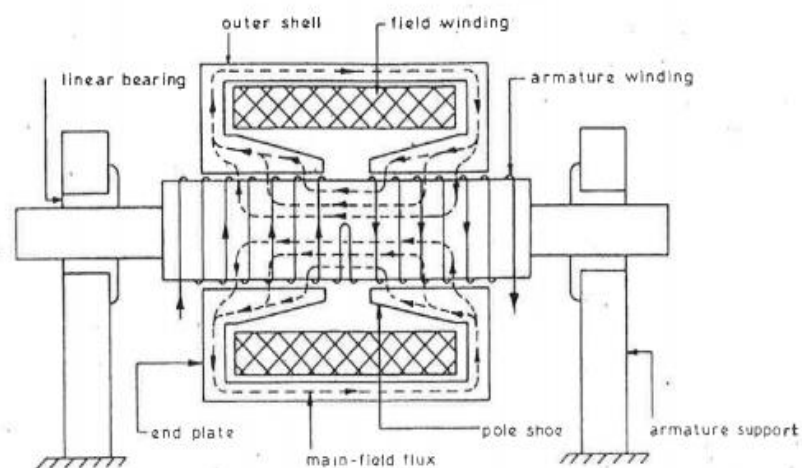
Figure 2.20 Flux pattern of two pole wound field linear motor [47].

2.12.2 Permanent magnet DC linear motors

The recent improvements in the rare-earth permanent magnet (PM) materials and in power electronics have created new opportunities for the design, construction, and application of permanent magnet motors [28]. In the 1970s, the wound field unit was replaced by permanent magnets in the DC linear machines, which increased their performance and efficiency.

Two ferrite permanent magnet DC linear motors were constructed by Basak [48] in 1975. The two motors designed were similar to the linear motor design that was developed by Jones and Griffiths, except that the field winding was replaced by a ferrite permanent magnet. By using a permanent magnet field source, the performance of the motor was improved because of the need for just one power supply.

Figure 2.21 shows the ferrite DC linear motor with four poles, while figure 2.22 shows the ferrite DC linear motor with two pole, with broken lines in both designs demonstrating the magnetic flux path. The two motors had a long circular mild steel bar and an armature coil wound around it. Since a ferrite magnet with a low maximum energy product was used to generate the air-gap flux density, the maximum thrust produced was 3 N with a current of 2 A. A side elevation of the motor is shown in figure 2.24.

Dascalescu [49] designed a permanent magnet DC linear motor for position control of the corona electrodes in electrostatic separation. The motor was similar to the linear motor, which was developed by Basak. The motor was designed as a moving field and a stationary armature system. The field system consists of ferrite permanent magnets attached to a laminated silicon-iron yokes. The armature core was made of a mild steel with a single layer of enamelled wire wound around it as shown in figure 2.24.
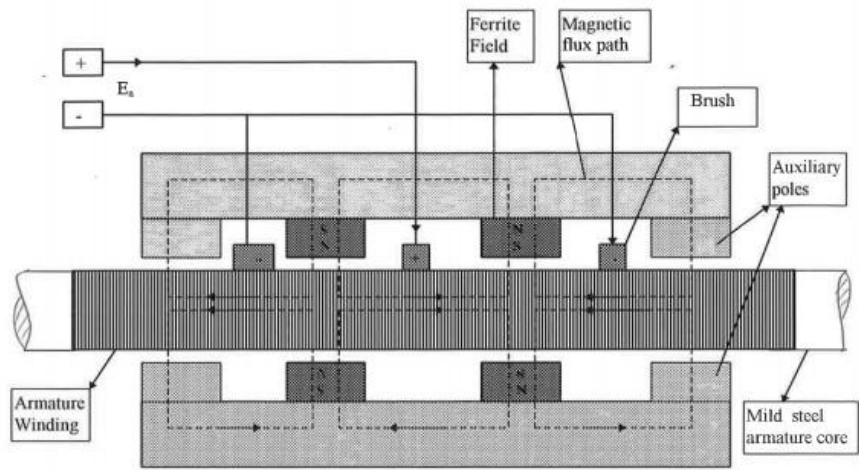
Figure 2.21 Cut section of a ferrite four pole DC linear motor [48].
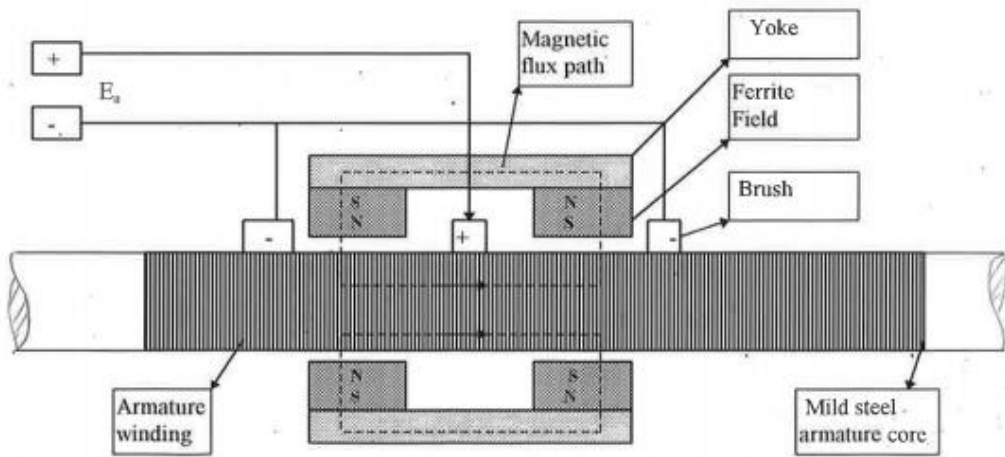
Figure 2.22 Cut section of a ferrite field two pole DC linear motor [48].
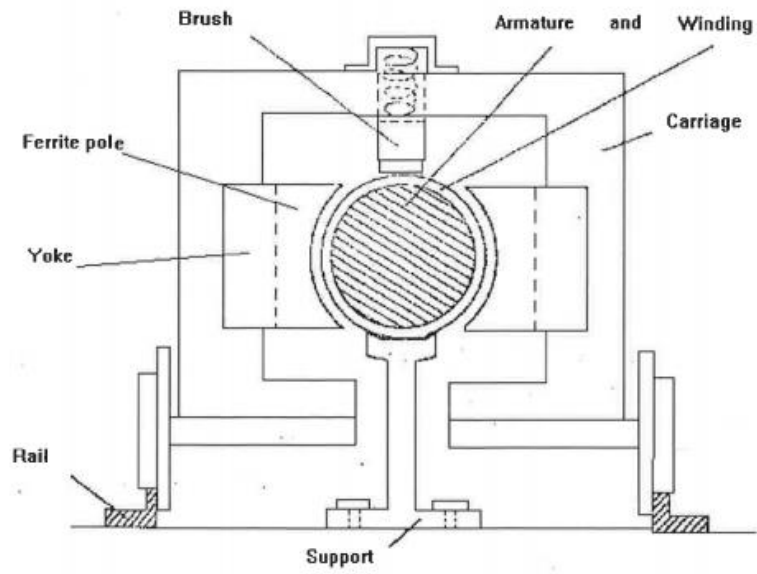
Figure 2.23 The elevation view of the motor [48].
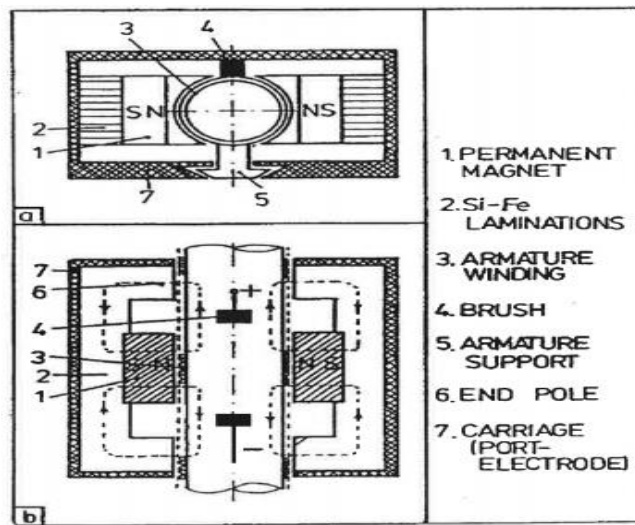
Figure 2.24 DC linear motor designed by Dascalescu for electro-stators [49].

With the improvement in the rare-earth permanent magnet in 1985, a high energy Neodymium-iron-born permanent magnet was used as the field unit for both the rotary and linear motor applications. Two flat permanent magnet linear motors for long-stoke application were investigated by Akmes [50]; in the first design, Neodymium-iron-born (NdFeB) permanent magnet was used as the field unit while the second design made use of a ferrite magnet as the field unit. He compared the experimental and FEM results for both motors. The results showed that the NdFeB permanent magnet motor had better efficiency.

A brushless DC linear motor with square cross-section armature core and NdFeB permanent magnet was developed and tested by Anayi in 1995 [51]. Figure 2.25 shows the cross-section of the motor design. The motor slider which accommodates four permanent magnets was guided by a linear bearing and two fixed bars. Sixty-four winding sections were wound on the armature core and a microprocessor controlled switching circuit was implemented to energise the winding sections in sequence. Anayi measured and computed the static thrust, axial flux and flux density of the linear motor, as a function of the linear motor slider position. The rectangular shape of the permanent magnet provides a uniform air-gap. FEM was employed to compute the flux distributions throughout the entire cross-section of the motor.

In 1996, Filho [52] designed two brushless DC linear motors with two parallel armature cores. The first motor design had a continuous armature winding as shown in figure 2.26, while other design had a multi-sectioned armature winding as shown in figure 2.27, which can be used as stepper motor. Both motors had seven blocks of NdFeB permanent magnets used as the magnetic field source. Two long square section bars of mild steel were employed as fixed armature core. In this design each winding section

could be energised individually or simultaneously. Also, each section must be energised in time with synchronisation with the position of the moving unit.
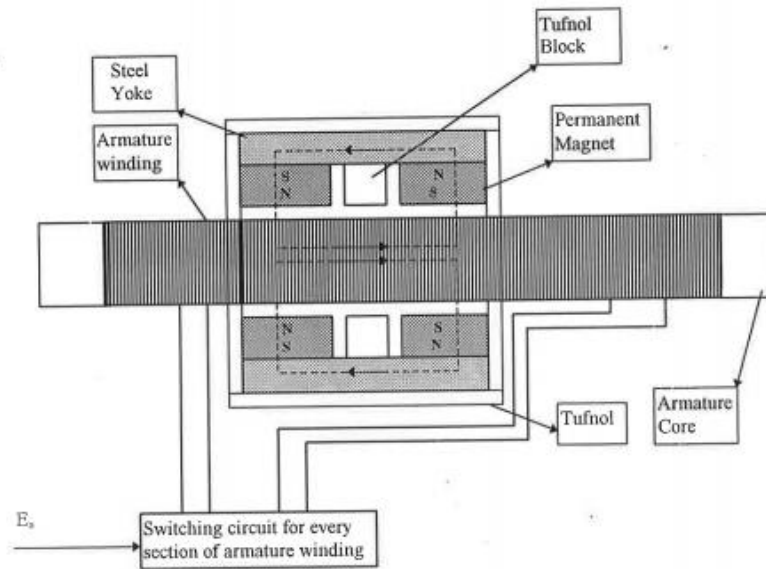
Figure 2.25 A brushless DC permanent magnet linear motor designed by Anayi [51].
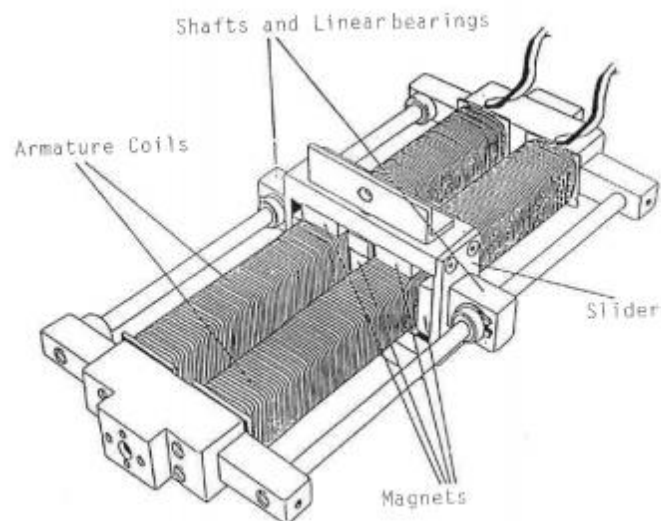
Figure 2.26 Double armature brushless DC linear motor with continuous winding [52].
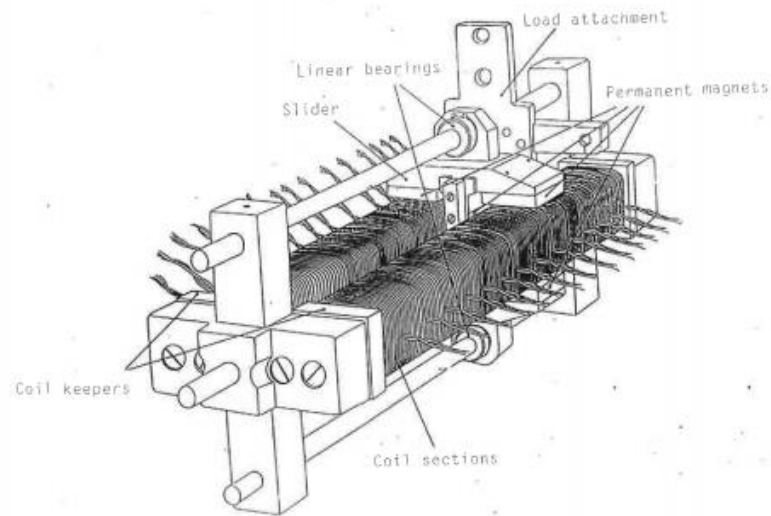
Figure 2.27 Double armature brushless DC linear motor with multi-sections of armature windings winding [52].

A DC linear stepping motor was constructed by Basak [31] using sections of triple layer of armature windings, which uses a movable field unit housing NdFeB rare-earth permanent magnet, as well as a long stator comprising of a mild steel bar. The performance of this motor was compared with another motor with a similar configuration but with a single layer of armature windings.

Basak highlighted that one way of increasing the thrust is to use a multi-layered armature winding. The experimental result showed that the difference in the air-gap between the single and triple layer configuration had a little effect on the useful flux. The experimental result showed that the thrust developed in the multi-layered (triple) armature winding motor is about three times larger than that developed in the single layer design, for a given current and useful flux [31].

The design and optimization of the DC linear motor systems employing the FEM and MATLAB techniques have gained a considerable amount of attention in literature. Three dimensional electromagnetic and dynamic FEM was utilized by Basak [53] to analyse the dynamic characteristics of a square-armature DC linear motor for material handling systems. The analysis of the result was done with respect to velocity as a function of time by varying the current applied. Also the output force and power as a fuction of velocity was analysed.

In-Soung Jung, et al [54] analysed and compared the static thrust, detent force and the normal force of two types of short primary and short secondary permanent magnet of linear synchronous motor using FEM. The authors developed an FEM magnetic field model to illustrate that detent force ripple can be reduced by changing the magnet width-slot pitch in a short secondary linear motor whereas detent force ripple is larger in a short primary type linear motor.

A simulation method using MATLAB/SIMULINK was introduced by Junyong LU [55] to analyse the performance of the speed-controlled system of linear permanent magnet brushless DC motor. In the close loop model, a dual loop rate control scheme is employed. The current loop adopts P (proportiona1) controller as an inner loop, which has fast tracking performance. While the velocity loop adopts PI (proportional integral) controller as the outer loop in order to make the whole system error-free at steady state. The simulation results showed the effectiveness of the control method and the high performance of the closed-loop system.

Okonkwo [12] highlighted the effects of armature reaction and saturation of the permeable members of a prototype double armature PMDCLM. The design concepts based on using sectional excitation of the armature winding as a function of the

permanent magnet position and armature flux compensation. The results obtained from simulations and measurements showed that the effects of the problems of armature reaction and saturation of the permeable members of the motor are reduced and compared to the model with the entire armature winding excited at a time.

Aboulnaga and Emadi [56] presented a high performance linear brushless DC (BLDC) motor for very low power applications. The motor is designed in such way that the core is slotless and ironless. This ironless core eliminates the attraction force between the rail and the forcer as well as it reduces the magnetic losses. The motor is a moving magnet brushless motor and the slotless ironless rectangular armature is made from aluminium which offers lightweight, better heat dissipation and maximum strength. The result showed better dynamic performance is achieved because of the lower winding inductance.

Skewing the permanent magnet and PM shaping technique to reduce the cogging force was criticised by Shuhua Wang [57]. Shuhua Wang emphasised that these techniques yield a complex and expensive PM shape, especially for tubular topologies. Shuhua Wang presented a finite element based method for minimizing the detent force in a slotted linear brushless permanent magnet motor. These methods are applied to an eight pole, forty-eight slot, surface mounted short secondary type PMLBDC machine. The minimizing of detent force is done by combination of the methods of magnet shifting and optimizing the magnet width, the detent force could theoretically be nearly eliminated without compromising the back EMF and the average thrust force.

Gyu-Hong Kang [58] presents a novel design technique and characteristic analysis of an air core type Permanent Magnet (PM) linear motor based on Space Harmonics Field analysis methodology. The proposed analysis and design process is verified against the

2-D finite element analysis. Magnet skewing and variation of pole ratio (magnet width / pole pitch) are applied to the design in order to minimize electromagnetic force ripple. The result showed that the thrust ripple is slightly influenced by skewed magnet whereas variation of pole ratio is severely affected and Space Harmonics Field analysis is found reliable methodology for air core type PM linear brushless motor.

Nicola et al [59] presented a simple technique based on shift of PMs to reduce both the cogging force and the harmonic content in the back EMF of the tubular permanent magnet linear synchronise motor without a current harmonic compensation. The technique consists of a proper shift of PMs, in order to compensate the harmonics of the flux density waveform among the PMs of the structure to achieve a smooth force.

Huang [60] proposed a simple but effective method of optimizing the mover structure (length of the armature coil) based on using Maxwell method to minimise the end force for permanent magnet DC linear motor (PMDCLM) and the accuracy of optimized structure was tested and verified based on finite element method.

Myung J et al [34] presented optimal design using sequential quadratic programming (SQP) method for minimization of force ripple and maximization of thrust force in brushless permanent magnet linear motor. The optimal design technique was based on two steps; one step is for reducing the force ripples by choosing optimise variable parameters such as armature length, magnet width and pole shift length which considered as initial value in step two. The second Step two is achieved by choosing the optimise variable (coil diameter, slot depth and magnet thickness) for maximising the thrust. The result showed that magnet width has main effect on tooth ripple component of cogging force, and armature length has a main effect on end effect component of

cogging force, whereas magnet pole length has small effect on both cogging and mutual force ripple.

Control system design and analysis of linear motor systems has also received some attention in the literature. Many researches considering optimise the geometry parameter of the motor such as; skewing of magnet, shifting of magnet pole pair, etc. However, motor optimal design reduces ripple force to a certain degree but does not completely eliminate it. Moreover, special machine design increases the complexity in production process, which results in higher machine cost as well as reduces the motor performance. Therefor many research works have been carried out towards more advanced position control to overcome nonlinearities and uncertainties that associated with BDCLM drive systems.

Lim at al [62] highlighted that a simple PID controller alone is not sufficient to attain high-accuracy precision positioning with the presence of nonlinearities and uncertainties in the linear DC motors. Lim proposed a hybrid control scheme consisting of a linear conventional PID position controller together with a plug-in Iterative Learning Control (ILC) to improve the tracking performance for periodic time-varying trajectory. The plug-in Iterative Learning Control improves the system tracking performance by using the information from the previous cycle in the next cycle.

Tan and Panda [14] proposed a robust nonlinear Sliding Mode Controller (SMC) for position control of the linear brushless direct current motor (LBLDCM). Nonlinear Sliding-mode insensitive to parameter variations and external disturbances as compared to PID controller. Tan and S.K. Panda stated that for periodic position tracking, the tracking performance can be further improved by supplementing a plug-in Iterative Learning Control (ILC) to the SMC. The periodic tracking error has been reduced to as

close as possible to the encoder resolution, thus providing very precise tracking for the motor.

Imen and Shakeri [62] presented feedforward adaptive learning controller with feedback controller for a prototype linear brushless permanent magnet DC motor. The feedback controller based on PID controller is designed to improve stability and efficiency of the system while the feedforward which is based on a neural network adaptive controller is designed to retrieve the unknown knowledge of the feedback controller, and usage of these data to improve the controller efficiency.

Li Xu and Bin Yao [8] developed an output feedback Adaptive Robust Controller (ARC) scheme based on discontinuous projection method for high performance robust motion control of epoxy core linear motors. The proposed controllers take into account the effect of model uncertainties coming from the inertia load, friction force, force ripple and the external disturbances. The proposed controller uses on-line parameter adaptation to compensate the effect of nonlinear disturbances.

Tan, Lee and Zhao [36] presented the design and realization of an adaptive controller to reduce the force ripple in an iron-core permanent magnet linear motor (PMLM). A composite control structure, consisting of three components: a simple feedforward component, a PID feedback component and an adaptive feedforward compensator (AFC). The PID parameters are tuned using a Linear Quadratic Regulator (LQR) design technique to achieve optimal motion trajectory tracking. The AFC generates a controller signal to eliminate the inherent force ripple, hence facilitating smooth precise motion without compromising the maximum force achievable.

Particle Swarm Optimizations (PSO) technique was utilised by Nasri [63] to optimally tune the PID gains parameters. The proposed technique is modelled in Simulink and the

PSO algorithm is implemented in MATLAB. To show the effectiveness of the proposed technique, a comparison is made with the designed PID controller with Genetic Algorithm (GA) and Linear quadratic regulator (LQR) methods. The results showed that the proposed controller can perform an efficient search for the optimal PID controller, and can improve the dynamic performance of the system in a better way.

A novel Ant Colony Search Algorithm (ACSA) method was utilised by Navidi, Bavafa and Hesami [9] for determining the optimal proportional- integral derivative (PID) controller parameters, for speed control of a linear brushless DC motor. The authors comparing the novel ACSA method with GA method and LQR method. The result showed that the proposed method was more efficient in improving the step response characteristics such as, reducing the steady-states error; rise time, settling time and maximum overshoot in speed control of a linear brushless DC motor.

2.13   Conclusion

An overall comparison among different classification and topologies of linear machines has been well reviewed. Classification of the magnetic materials which have been used in the linear motors were discussed. A comparison of common types of permanent magnets was carried out to choose suitable for our motor. Advantages of linear motors over rotary to linear system was highlighted.

 A full analysis of a magnetic circuit in a permanent magnet machine and the determination of air-gap flux density value have been illustrated by the means of "Equivalent Magnetic Circuit". Forces associated with Linear motors and nonlinear effects associated with the design which influence the motor performance are discussed. Finally, previous related work on design linear motors are reviewed.

Chapter 3   : Electromechanical Motor Design

This chapter describes in detail the electrical and mechanical design of the brushless DC linear motor (BDCLM), from which the prototype design used in this project is proposed. The selection of the appropriate materials for the magnetic circuit and the permanent magnets as well as the reasons for their preference are also discussed.

3.1   Selection of materials

The selection of the appropriate materials, used for the proposed BDCLM prototype design is discussed in this section. Several factors were taken into consideration in designing the BDCLM, including the thickness of the armature winding in other to avoid the problem of overheating, thus preventing the breakdown of the insulation between wires. Another factor which was taken into account the dimension of the armature core which accommodates all the magnetic flux without getting saturated.

3.1.1   Magnetic material properties

The choice of the magnetic material used for the motor design is crucial. The magnetic material to be used for the construction of the motor armature should have a high saturation flux density, a high permeability and a low hysteresis loss [1].

In an electric motor, the magnetic flux which is produced by the permanent magnet is guided by elements made of alloys of iron in order to close the magnetic circuit. If the magnetic flux to be guided has only a DC component, then the magnetic material used can be a non-laminate iron alloy. However, if the magnetic flux has a high amplitude AC component and a high frequency, the magnetic material must be laminated in order to decrease as much Eddy current losses as possible. The flux densities in the teeth and

cores are usually selected around the knee point of the **B-H** curve. The material used for the construction of the traditional armature core is silicon iron, with a knee flux density around 1.4 T. However, with the improvement in magnetic material over the past few years, core materials with saturation flux densities as high as 2.2 T is employed [39]. The motor core is usually made from mild steel with its saturation curve is illustrated in Figure 3.1.
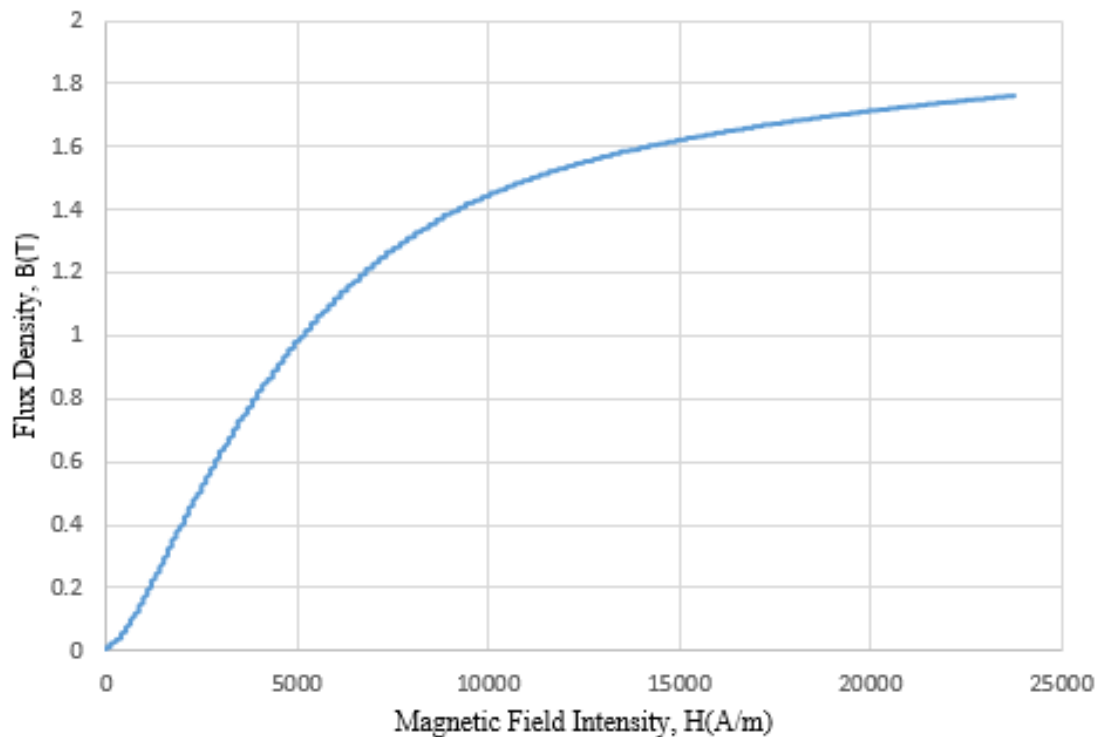
3.1 Mild steel and its saturation curve.

3.1.2 Permanent Magnet Material

The choice of PM materials used is an important factor to consider in motor design. A permanent magnet with; high remanence, high coercivity, wide range of temperature and low cost is highly desirable in the design of electromechanical energy converters

[12]. Rare-earth permanent magnets are usually used for electrical motor design. The strength of the magnet makes it more practical to use, since it requires less space within an electric motor. The quality of the permanent magnet is judged based on its demagnetization curve, which is the part of the hysteresis loop that lies in the second quadrant between the residual flux density and the coercive force.

An important parameter to be considered when choosing a permanent magnet material is the point on the demagnetization curve where the B-H product is maximum. At this point the volume of the magnetic material required will be at its minimum. Magnet technology over the recent years has progressed rapidly due to the introduction of rare-earth materials, which have a high coercive force, a high flux density and large energy product [12].

A compromise between cost and performance was made in choosing the rare-earth magnet used. Samarium cobalt magnets (SmCo5) are most desirable, However, they are more expensive. NdFeB magnets are more expensive than ferrite and alinco, but have high energy product density which provide an advantage of a compact size and efficiency.

For the motor design used in this project, the armature windings were excited for a very short period of time in other to eliminate the thermal effects. Therefore, the temperature requirement of permanent magnets is not strict. A comparison between NdFeB and SmCo magnets are shown in Table 3.1. The magnets chosen were rectangular neodymium iron boron (NdFeB) magnets. The two major advantages of NdFeB magnets are that they can produce a higher energy product and are cheaper than Samarium cobalt magnets.

Table 3.1 Comparison between NdFeB and SmCo magnets [12].

Material	NdFeB	SmCo
Energy Products	10 to 48	15 to 32
Mechanical Strength	medium	low
Corrosion Resistance	low	medium
Temp Stability	low to medium	high
Cost	lower	higher

3.2 Mechanical design

The mechanical design of the linear motor requires careful analysis of the specifications, that is; the material, dimension and size. The principal objective was to achieve a high thrust and an accurate positioning of the mover. Furthermore, due to its topology, it can be used as a brushless linear stepping motor. The main physical constraints originate from the permanent magnets, mild steel used for the armature core and the copper windings.

The top and side view of the BDCLM model prototype is presented as shown in figure 3.2. Based on its construction, the motor is a double-sided moving magnet DC linear motor. Twenty-four armature coils were set in the stator side, and 8 permanent magnets were put in the movable side called carriage. A constant magnetic field is produced by a radially magnetised rectangular NdFeB permanent magnet.
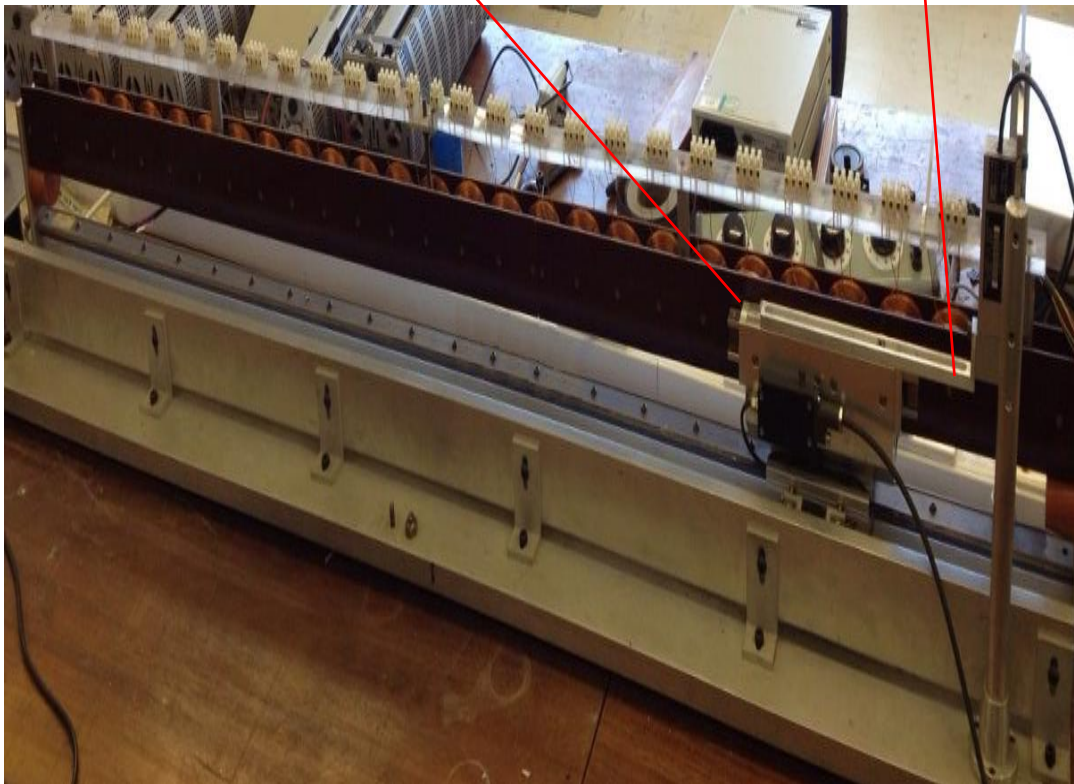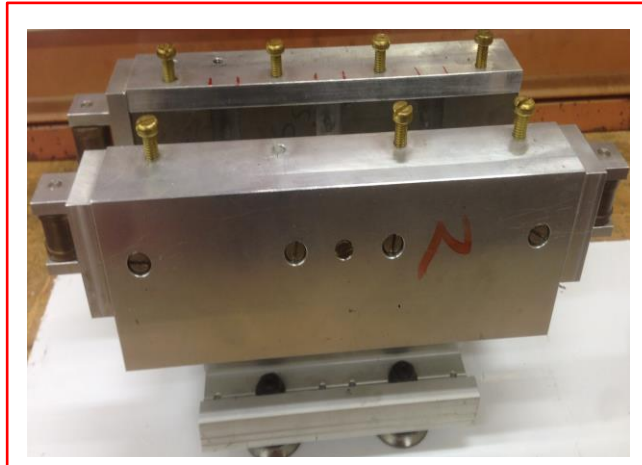
Figure 3.2. Physical prototype of BDCLM.

From the motor setup shown in Figure 3.2, it can be observed that there are two sources of magnetic field, which are; the permanent magnet which provides the main magnetic flux, and the armature windings which carries the DC current. When the position of the moving magnet unit is detected by Linear Variable Differential Transformer (LVDT) position sensor, the driver circuits of the related armature coils directly under the magnets, turns on and the current flows into the armature coils. Then, the moving magnet unit moves according to Fleming's left-hand rule. The direction of the armature current is dependent on the polarity of the moving magnet. Although the stator of the BDCLM consists of 24 armature coils, only 3 coils facing the moving magnet are in the on-state in order to provide a smooth movement.

The field system was mounted inside the carriage made from aluminium. The carriage was supported and guided by a rail of the same length as the armature, which positioned parallel to the armature and under it. There are four wheels attached to the carriage in order to balance the air-gap on both sides of the magnet.

3.2.1   Permanent magnet arrangement

The permanent magnet which represents the field system was mounted inside the carriage and was used as the moving part of the BDCLM. Figure 3.3 shows the configuration of permanent magnet moving unit. The length of the slider is 213 mm and it consists of 4 permanent magnet (NdFeB) blocks on each side of the slider. The permanent magnets used have a dimensions of 42 mm x25 mm x 30 mm and were arranged as N-S-N-S polarities in order to generate a radial magnetic flux density. The permanent magnets were separated by 3 Tufnol blocks as magnetic isolators with dimensions of 15 mm x 30 mm x 30 mm to help separate the magnets.
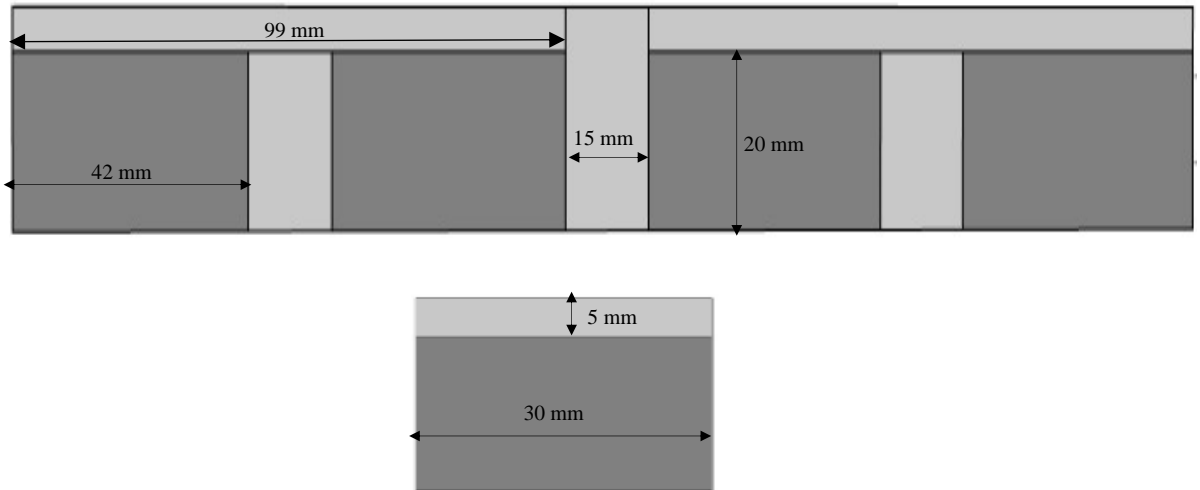
Figure 3.3 Configuration of permanent magnet moving unit.

Two back iron with a dimensions of 99 mm x 5 mm x 30 mm were attached to the back of the magnets in the field housing one each side, in order to close the magnetic circuit generated by the PMs.

The armature windings were designed while taking the power of the motor, the current carrying capability of the armature windings and the track length into consideration. The armature core was designed with a 1.8-metre-long mild steel bar with a cross-sectional area of 25 mm x 30 mm, which determines the travelling distance of the motor.

3.2.2   Coil arrangement

Figure 3.4 shows the configuration of the armature windings which were distributed along the armature core. There are twenty-four independent multi-layer coil sections distributed along each side of the armature core with enameled copper wire of 0.5 mm in diameter, which is equivalent to the standard wire size of 24 AWG. This allows for a maximum DC current of 29 A to flow. In addition, the armature windings are electrically independent from each other.

The smaller the diameter of the wire, the greater the number of turns per-metre length for a given length of armature winding section, hence, the greater the force produced and the less the current carrying capability of the wire. Therefore, using 24 AWG enamelled copper wire, a compromise was made between the force produced and the maximum current that can pass through the windings without causing any damage.

The ends of the copper wires terminate at the connector blocks which were fixed to a rail directly above the armature and connected to the power supply through switching circuits. The current density in the armature winding was relatively high. However, there was no need to cool the armature winding since it was subjected to large current

for a short period of time.

The armature winding was wound around the teeth with a dimensions of 30 mm x 24 mm x 7 mm. Each coil section has 470 turns and was fed with a DC current. A thin layer of glass cloth tape (150°C rated) was wound over the core teeth to provide additional insulation. Commutation is achieved by energizing the armature sections in a sequence with the aid of a microcontroller.

A linear movement occurs when the armature windings located under the permanent magnets are properly fed with currents. A magnetic thrust force will be created on the mover and hence, the latter moves accordingly. The developed thrust depends on the air-gap magnetic flux density which is produced by the permanent magnet and the current density vector in the armature windings [62].

The resistance R of the coil was calculated from equation (3.1):

$$R \ = \frac{\rho_c \, l_c}{A_c} \quad\quad\quad (3.1)$$

Where ρ_c the resistivity of the copper, A_c is the wire cross-section and l_c is the total length of the copper wire.

The resistance of 5.89 Ω was calculated, which was in good agreement with the measured resistance of 6.1Ω. The resistance of the armature winding was measured by means of a digital multimeter and was used in the Matlab modelling presented in chapter 7.
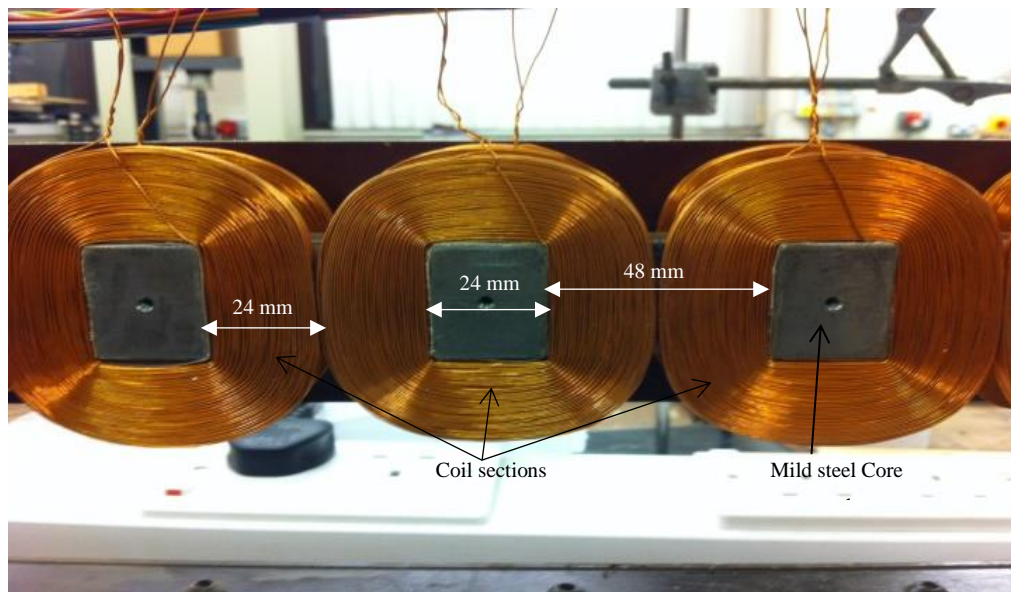
Figure 3.4 Configuration of the armature windings sections.

The inductance of the armature winding was measured using a precision Impedance Analyzer (model 4294A) produced by Agilent technologies Ltd. Figure 3.5 shows the inductance of the armature winding measurement set-up. The parameters of the BDCLM are listed in table 3.2.

Table 3.2 Motor measurement parameters.

Armature resistance (R)	6.1Ω
Armature inductance (L)	7.8 mH
Moving unit weight (M)	6.4 Kg
Weight of the rod of LVDT	135 g
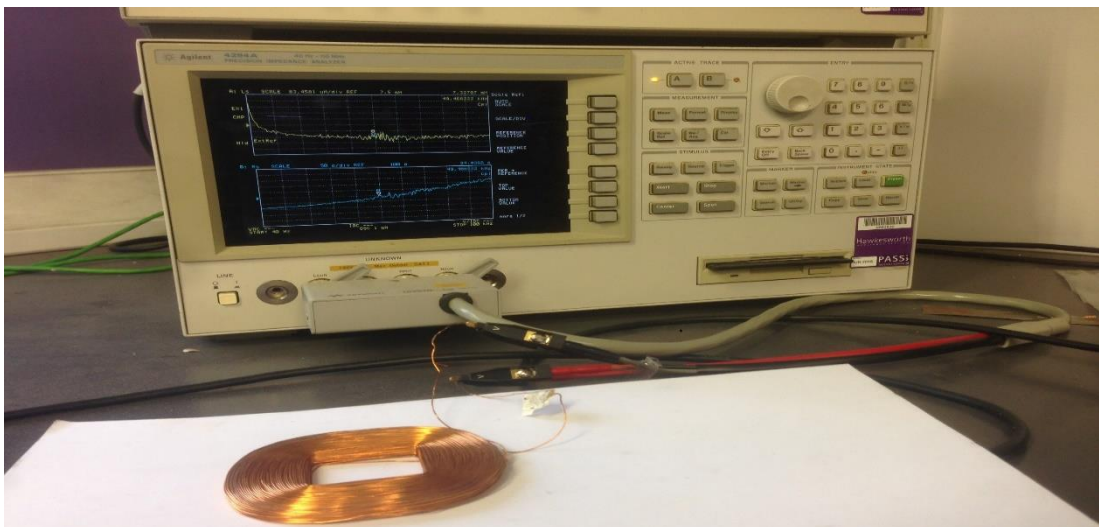
Figure 3.5 Inductance of the armature winding measurement
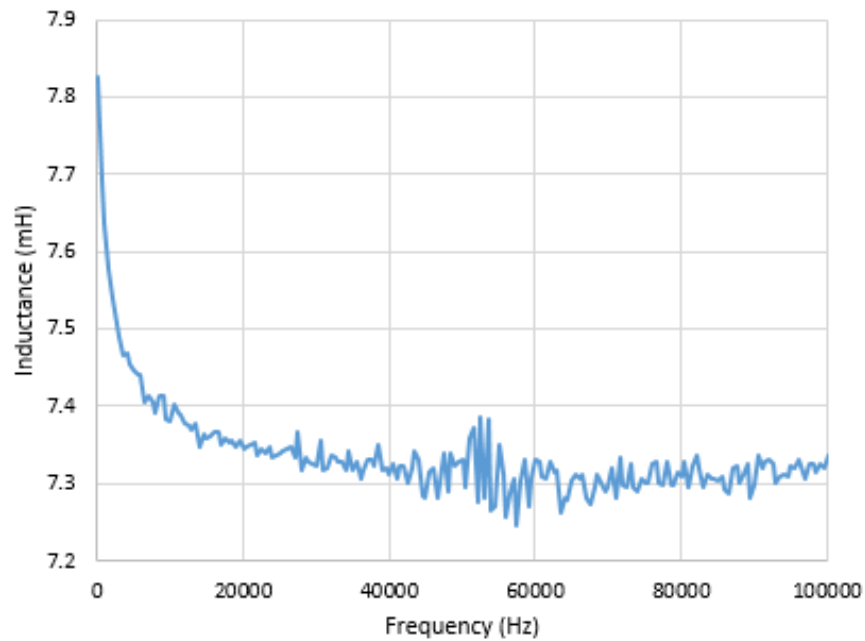
Figure 3.6 Inductance of the armature winding.

3.3   Instrumentation

This section gives an overview of all the measurement equipment used to control the motor and its electrical parameters.

3.3.1   Linear Variable Differential Transformer (LVDT)

The linear variable differential transformer (LVDT) consisted of a single primary coil of wire with secondary coils placed on either side of the primary coil. The voltage generated in the secondary coils changes with respect to the core position. The value of output voltage was varied from +5V and -5V across a length of 40 cm. The core of the LVDT is mechanically attached to the slider of the BDCLM. The electrical specifications of the LVDT DCT series from "RDP Electronics Ltd" are listed in table 3.3.

Table 3.3 The electrical specification of the LVDT

Input requirements	+10 to +20 DC volte
Linearity	0.5% of full range
Output voltage	-5 to +5 DC volt
Output load	2K ohms
Operating temp range	-50 C to +70 C

3.3.2 Motor Driver Board

To drive the BDCLM each armature winding was energised independently by a power control board. These boards were the core part of a current controller. The important components of the power control boards are the MOSFETs switches due to their; high voltage rating, high current rating and fast turning on and off capability.

The driver board uses a 20 A dual DC motor driver (H-Bridge circuit) from "Robokits" to control the switching of four transistors, in order to control the voltage applied to each winding of the BDCLM. This board directly controls the power going into the motor, based on the PWM commands from the controller board.

The driver board supplies the DC voltage and enables the motors to move in both directions, that is; clockwise (CW) for forward or counter-clockwise (CCW) for reverse movements, by reversing the polarity of the motor supply voltage. The motor driver board is ideal in applications where the armature winding requires up to 20 A during the start-up and during the normal operation of the motor. The driver motor board has the following features:

- DIR – Pulled down to GND Forward by default and Backward when 5V (logic high)

- PWM – Pulse Width Modulation input to control speed of motor (recommended freq 20Hz to 400Hz).

- BRK – Breaking input to halt the motor in operations when 5V (logic high).

- 5V – Regulated 5V output from motor driver board (maximum 50mA supply).
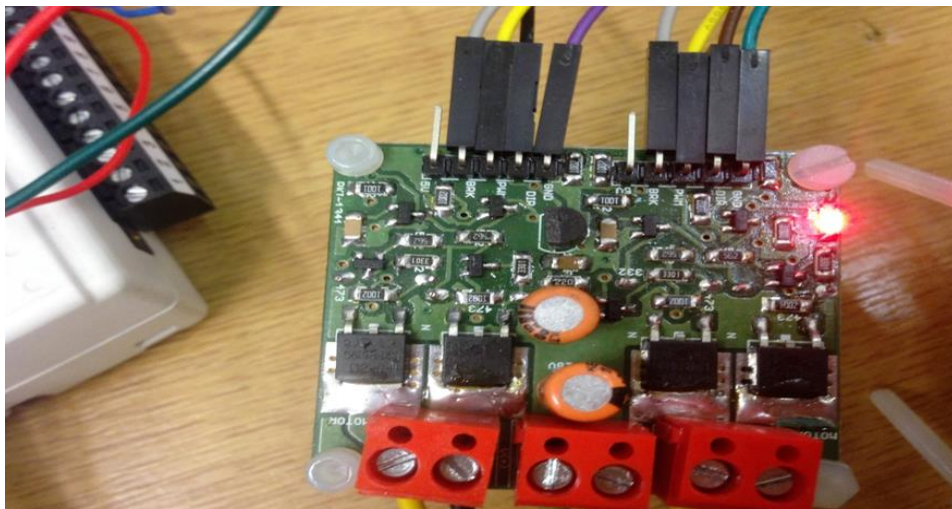
Figure 3.7 Motor driver Board.

3.3.3 Pulse Width Modulation (PWM)

The controller unit is used to provide a PWM signal to the H-Bridge unit. PWM is a digital signal used to control analogue circuits by repeating series of on and off pulses. The on-time is the time when the DC supply is applied to the load (H-Bridge circuit), and the off-time is the period of time when the supply is switch off. The two important variables for generating PWM signal are listed below [43];

- The frequency which determines how fast the switching turns on and off.

- The duty cycle which is the ratio of on period as a percentage of total switching time.

3.3.4 Controller Board

The microcontroller chosen for this project was an "Arduino Mega" which is a low-cost and an easy to use microcontroller designed to develop interactive sensor applications. It is based on "Atmel ATmega 328" microcontroller chip (8-bit) which runs at 16 MHz and it has 54 digital input/output pins (of which 14 can be used as PWM outputs), 16 analogue inputs, 4 UARTs (hardware serial ports), a 16 MHz crystal oscillator and a USB connection. The microcontroller provides the interface between the controller and the motor. The specifications of the Arduino Mega is shown in table 3.4.

Table 3.4 Specification of the Arduino Mega

Microcontroller	ATmega1280
Operating Voltage	5V
Input Voltage (recommended)	7-12V
Input Voltage (limits)	6-20V
Digital I/O Pins	54 (of which 15 provide PWM output)
Analogue Input Pins	16
DC Current per I/O Pin	40 mA
DC Current for 3.3V Pin	50 mA
Flash Memory	128 KB
Clock Speed	16 MHz
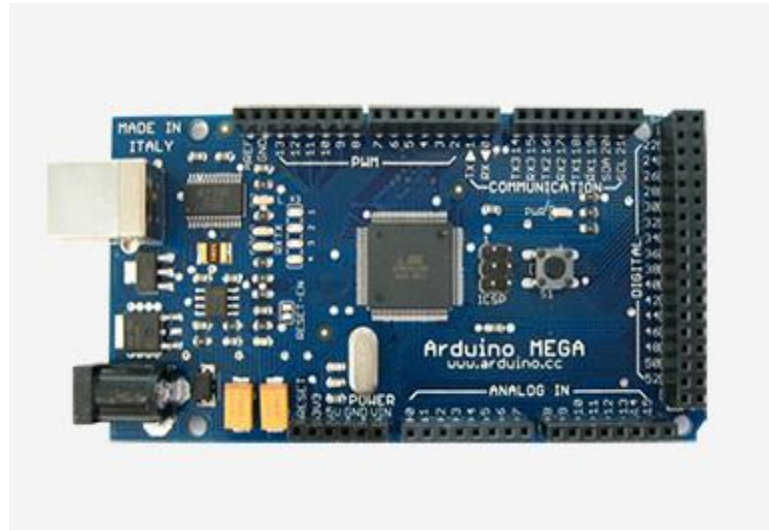
Figure 3.8. Arduino Mega is a microcontroller board.

3.3.5 Data acquisition card

Data acquisition hardware acts as the interface between the computer and the outside world. It is also used to communicate between the motor circuit and the LabVIEW program. The data acquisition presented in this project was a USB-6211 from "National Instruments" as shown in figure 3.9. The USB-6211 is a bus-powered USB M Series multifunction data acquisition (DAQ) module optimized for superior accuracy with a fast sampling rate. It offers 16 analogue inputs; 250 kS/s single-channel sampling rate; two analogue outputs, four digital input lines, four digital output lines, four programmable input ranges ($\pm$0.2 to $\pm$10 V) per channel, digital triggering and two counter/timers. The specification of the USB-6211 data acquisition card is shown in table 3.5.

Table 3.5 Specification of the USB-6211 Data acquisition card.

Analog Inputs	Resolution (bits)	Max Rate (kS/s)	Analog Outputs	Resolution (bits)	Max Rate(kS/s)	Digital I/O
16	16	250	2	16	250	4 DI/4 DO

Figure 3.9 USB-6211 Data acquisition card.

3.3.6 Current Sensing Board

For a more advanced motor control, voltages and currents which are applied to armature windings have to be measured. In order to measure the stator current of each armature winding, nine ACS712 current sensors from "Allegro" based on the principle of Hall-Effect shown in figure 3.10 were used. These sensors were chosen based on their current rating of ±30A. The output is an analogue voltage read by the DAQ system. The Specification of the current sensor is shown in table 3.6.

Table 3.6 Current Sensor specification.

Supply Voltage (VCC)	5Vdc Nominal
Measurement Range	-30 to +30 Amps
Voltage at 0A	nominally 2.5VDC
Scale Factor	66mV / A
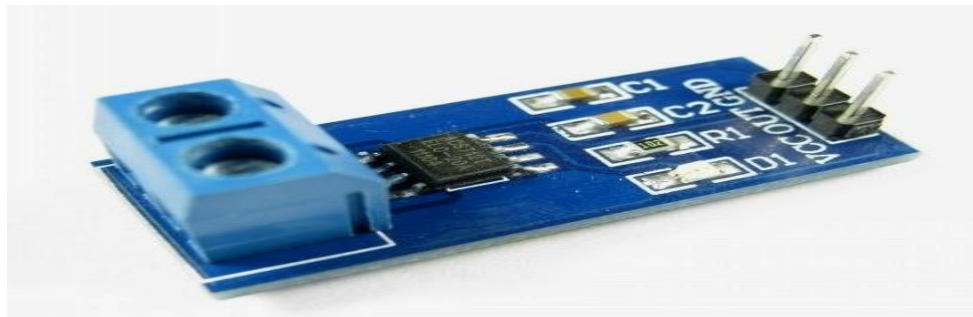
Figure 3.10.Current Sensors.

3.3.7   Power Supplies

A power supply (MAP130-1024 30V) from "Fernell" was used to power the LVDT with 15V and another power supply (E3646A) from "Keysight" capable of delivering a 70 V and 30 A was used to power the H-bridge driver board in order to supply the current to the armature windings.

3.3.8   Fluxmeter

The air-gap flux density (**B**) is determined using the fluxmeter "LakeShore 480" as shown in figure 3.11.

Figure 3.11 Fluxmeter.

3.3.9 Force sensor

In order to measure the actual force output of the motor, a load cell (RS 632-742) shown in figure 3.12 was used. Based on FEM results of the static thrust, it was determined that a 10 kN force sensor would be adequate to measure the output force from the BLDCLM. The output voltage of the load cell is linearly proportional to the applied load and was calibrated with (1 mV = 12.5 N). The sensitivity of the load cell is 2mV. The calibration of the load cell can be found in the appendix B.

Figure 3.12 Force sensor

3.3.10 Thermal camera

Figure 3.13 shows the "FLIR C2" thermal camera from "FLIR" instruments company. It was used to analyse the temperature distribution in the entire section of the motor. Its radiometric image stores 4800 pixels and it has the capability of capturing thermal measurements from -10 °C → 150 °C [77]. The specifications of the FLIR C2 camera is shown in table 3.7.

Figure 3.13 FLIR C2 thermal camera [86].

Table 3.7 Specification of the FLIR C2 camera[86].

Temperature Measurement Range	$-10 \rightarrow +150$ °C
Thermal Sensitivity	0.1°C
Detector Resolution	80 x 60 pixel
Storage Media	Internal memory stores
Image file format	Standard JPEG
Dimensions	Dimensions 125 x 80 x 24mm

3.4   Conclusion

The electrical and mechanical design aspects of the BDCLM, from which the prototype design used in this project are discussed in details. The selection of the appropriate materials for the magnetic circuit and the permanent magnets as well as the reasons for their preference are all discussed. NdFeB magnets were chosen for this project because they can produce a higher energy product and are cheaper than Samarium cobalt magnets [23]. The armature windings used is a 24 AWG enamelled copper wire. A compromise was made between the developed force and the largest current that can pass through the windings without causing any damage.

Chapter 4 : Modelling of brushless DC linear stepping motor

In order to acquire a comprehensive understanding of the machine characteristics and a more precise brushless DC linear motor design, a finite element method (FEM) analysis is initially performed according to the preliminary geometry. A comparison was carried out between the two proposed model designs, in term of the static thrust, air-gap flux density and magnetic flux distribution. The approach adopted for modelling both the magnetic materials and the permanent magnets is explained in detail. This chapter also describes the pre-processing operations involved, including the mesh construction, specified boundary conditions and the excitation sources used.

4.1   Numerical methods for analysing the magnetic field

Different methods are presented in the literature for analysing the magnetic field in machine design. The most important methods are listed as follows [25]:

1. Finite Element Method (FEM)

2. Finite Difference Method (FDM)

3. Boundary Element Method (BEM)

4. Magnetic Equivalent Circuit (MEC)

The FEM is one of most valuable analysis tools used for electrical machine design due to its ability to tackle complex geometries, while taking into account the non-linearity of the magnetic materials used [64]. Therefore, the FEM technique is chosen for this

project. The characteristics of these methods, in terms of geometric approximation and computational cost, are listed in Table 4.1.

Table 4.1 Different numerical methods for solution of the magnetic field [25].

Method	Geometry approximation	Non-Linearity	Computational Cost
FEM	Extremely flexible	Possible	High
FDM	Inflexible	Possible	High
BEM	Extremely flexible	Troublesome	High
MEC	Specific geometries	Possible	Very Low

4.1.1   The finite element method

In order to investigate the static characteristic of a thrust force under the DC current excitation condition, while taking the nonlinear properties of iron materials used into account, two dimensional finite element method (FEM) is carried out using a commercial available software package called "COMSOL Multi-Physics" [65].

The main steps for simulating a motor model while using the FEM technique are shown in figure 4.1. There are three stages involved in the process [16]:

- **Pre-processor Stage**: - As the name indicates, pre-processing is implemented before the analysis stage (processor stage). The Pre-processing involves the preparations of data, such as; choosing an appropriate finite element mesh, assign suitable material properties, and apply boundary conditions. At the end of this stage, the problem is ready to be processed.

- **Processor Stage**: - This stage involves the computation of field variables at the respective nodes, by employing various available processing techniques. The techniques used varies for different software packages.

- **Post-processing Stage**: - This stage involves the representation of the investigation results.
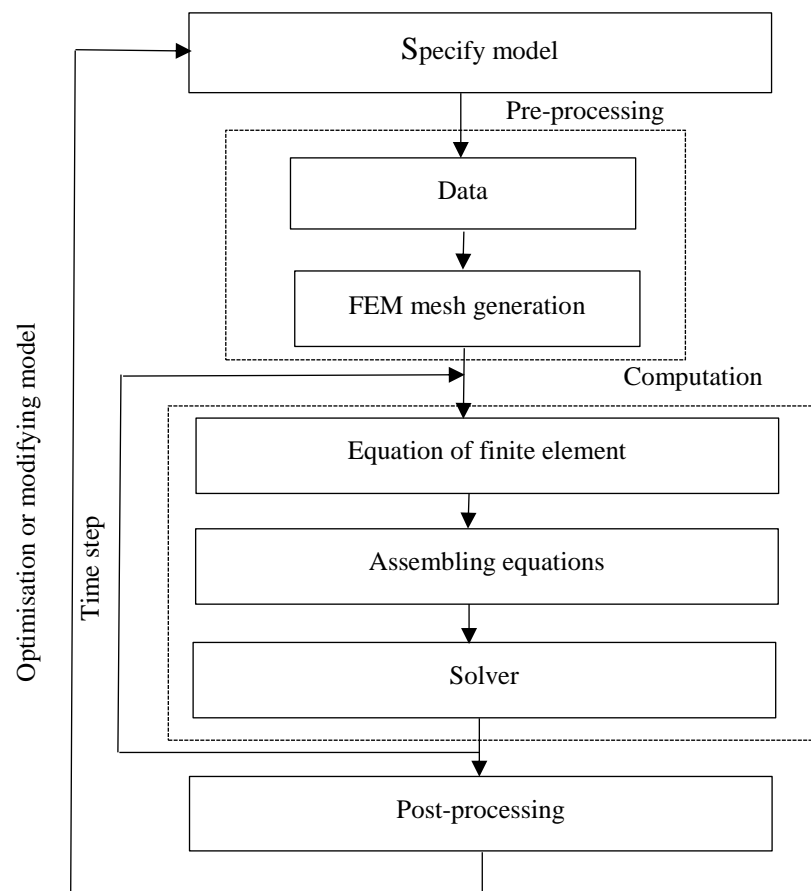
Figure 4.1 Finite element method simulation steps [16].

4.2   Modelling of Brushless DC Linear Stepping Motor

In the past few years, many theoretical and experimental developments regarding the field of low power applications for linear motors as direct drive actuators have been proposed. The motor proposed in this thesis was designed to produce a higher thrust to weight ratio and thrust to input power ratios compared to the already existing designs in literature [62].

Brushless DC Linear motor can be divided into single-side type and double-side type. Single-side plate type linear motor is simple and easy to locate, but the normal force is very large, that is; almost 10 times of the thrust force. Double-side plate type linear motor is difficult to locate, but the thrust is large and the normal force is zero due to its symmetrical structure. In order to design a motor with large thrust, double-sided moving permanent magnet type is adopted in this design.

 The Brushless DC Linear motor in this thesis is considered as a continuous work of Dr. Anayi and Dr.Basak in the field of DC linear motors. As mentioned before in the literature review section 2.12, a DC linear stepping motor was constructed by Basak using sections of triple layer armature winding and the results of the developed thrust was higher than that obtained with a single layer armature winding. The result shows that the effective magnetic flux density was not affected much when the air-gap increases.

According to equation 2.28, where the force produced by the motor is proportional to the number of turns per metre length of the armature, hence, one way of increasing the force is to use multi-layered armature coils. Therefore, in the motor design used in this work, the number of the armature winding is increased in order to increase the motor

thrust without compromising the air-gap flux density and to reduce the power rating of several electronic switching devices. The two proposed models are:

- Brushless and slotless DC linear motor (BSDCLM) which employs a rectangular armature winding.
- Brushless DC linear motor (BDCLM) employs a flat winding.

The modelling and analysis of the linear motor requires the simulation to be done in both time invariant (stationary study) and time variant magnetic fields (transient study). The stationary study is used to obtain the air-gap magnetic flux density and static thrust while the transient study is used to obtain the dynamic behaviour of the motor in terms of speed, varying the magnetic flux with time and to test the commutation algorithm of the armature winding current.

4.3   Modelling of the BSDCLM and BDCLM with "COMSOL Multiphysics"

The BSDCLM and BDCLM have been designed according to the analytical methods, using the FEM analysis, while employing the "COMSOL Multiphysics" software. FEM analysis in "COMSOL" was performed with a magnet remanence of 1.27 T and magnet relative permeability of μr = 1.05. The simulation steps used in "COMSOL Multiphysics" are listed below, while Figure 4.2 shows a clearer illustration of the simulations steps used

a. Geometry description.

b. Material specification (copper, soft iron, air, etc.).

c. Entering of input data (physical properties, boundary and initial

conditions).

    d. Meshing of the geometric domain with finite elements.

    e. Choosing the solver parameter to solve the problem.

    f. Analysis of the results.

The proposed models are made up of the following;

1) The geometrical model of the motor has three main parts, which are; the armature core, moving magnet block and the flat coil domain.

2) The material properties used for the linear motor design are; the armature core and back iron were modelled using mild steel, the armature coil was modeled with copper material, while an empty air space was assigned between the armature and the permanent magnet.

3) The **B-H** curves for the permanent magnet and the mild steel were used to define the motor materials.

4) A triangular shaped mesh was used for the 2D model and a tetrahedral shaped mesh for the 3D model.

4.3.1   Simulation of the BSDCLM

The first proposed model is the Brushless and Slotless DC Linear motor (BSDCLM), employing a rectangular armature winding which produces a uniform flux density in the air-gap. Due to the symmetrical shape of the motor, a two dimensional FEM model based on "COMSOL Multiphysics" software was implemented, according to the motor structure displayed in Figure 4.3. A 288 mm long armature core was used with a dimension of (288 x 30 x 30) mm and only 12 winding sections were modelled. The main parameters and material specification for the BSDCLM model are listed in Table 4.2.
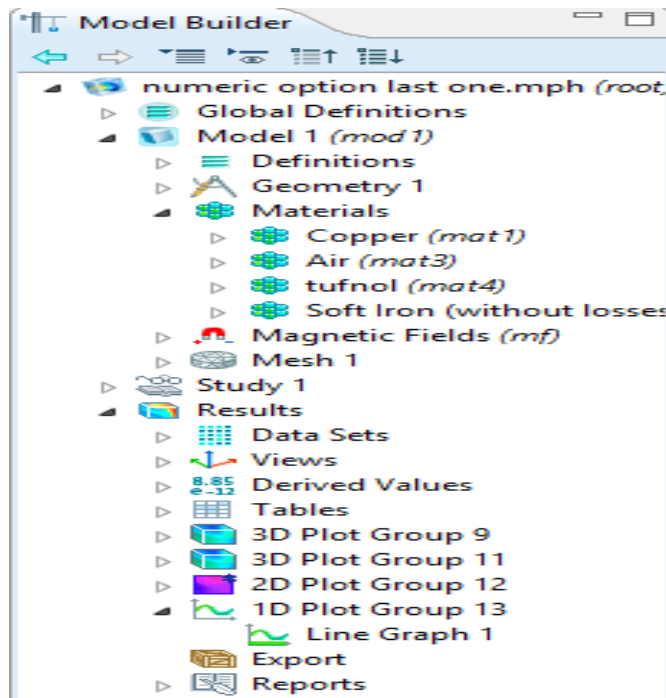
Figure 4.2 COMSOL model builder.

Table 4.2 Dimensions and material specification of the BSDCLM model

Magnet dimensions [mm]	42x 20 x 30
Magnet type	Neodymium Iron Boron
Number of magnets	8
Core dimension [mm]	288 x 30 x 30
Core	Mild steel
Back iron dimension [mm]	99 x 30 x 5
Effective Air gap [mm]	15
Supply Current [A]	2.5
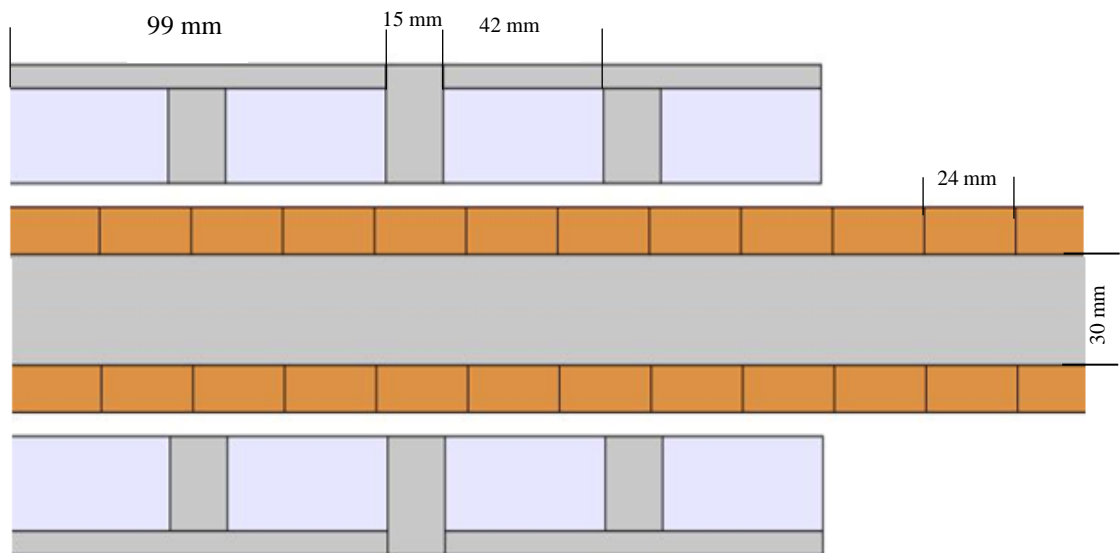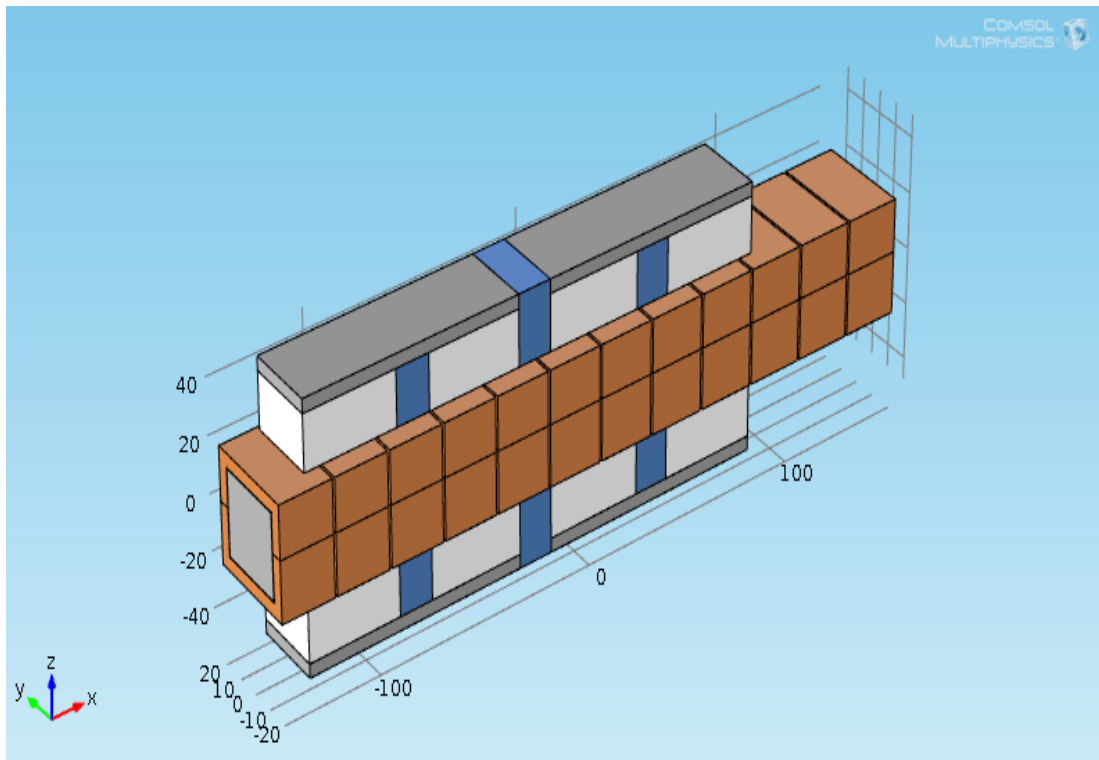
Figure 4.3 Geometry of the BSDCLM.

4.3.2 BSDCLM Mesh Construction

Before the post-processing stage of the simulation, an optimal mesh size has to be selected in order to achieve a better result. A higher mesh size was used in the areas with less changing flux density, however, a much lesser mesh size is used at the area of interest with a rapidly changing flux density, so as to achieve an accurate result. In addition, very fine mesh was created in the air-gap. The properties of the mesh used is clearly displayed in Table 4.3, while a better illustration of the meshed geometry performed in "COMSOL" is presented in figure 4.4.
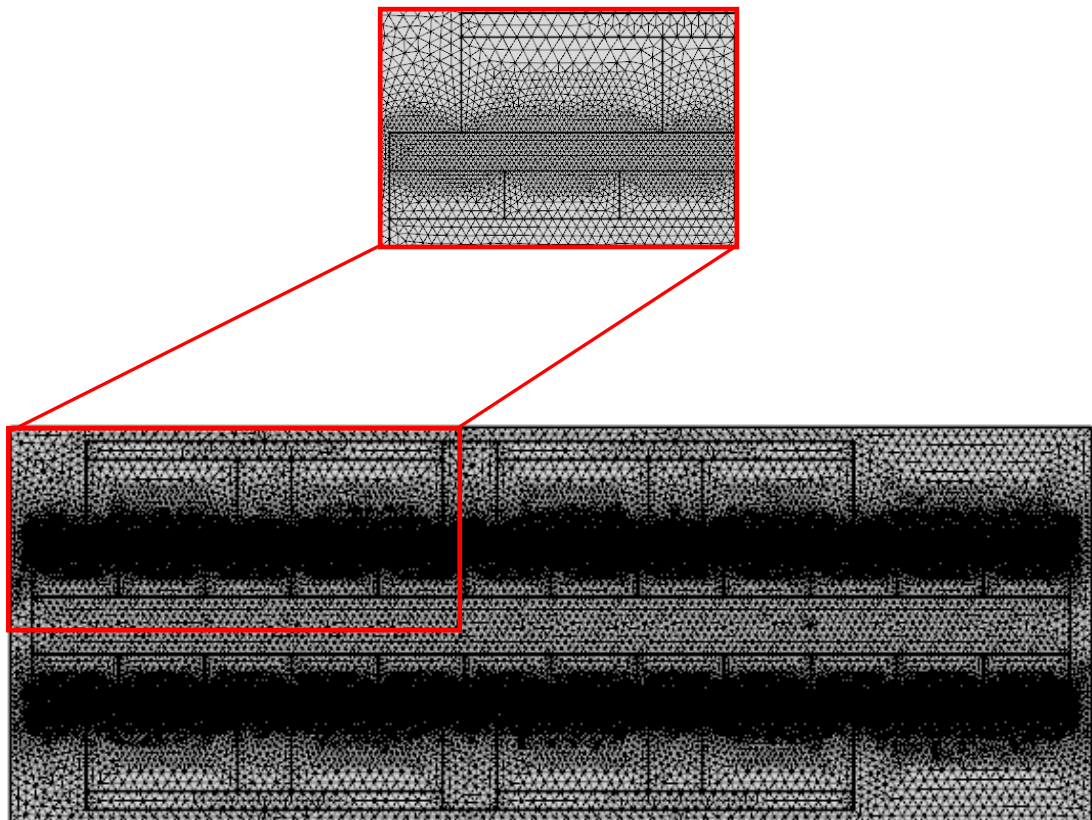
Figure 4.4 Mesh of 2D of the BSDCLM.

Table 4.3 Mesh statistics of the simulation model

Mesh statistics	2D
Mesh type	Triangular
Number of degrees of freedom	104623
Number of elements	61692
Number of boundary elements	3210
Solution time (sec)	23.257

4.3.3 Magnetic flux density of BSDCLM

Magnetic flux is considered one of the most important parameters in analysing the performance of any electrical machine. The distribution of the magnetic flux density throughout the entire cross-section of the motor and the surrounding air space is illustrated in figure 4.5 and the arrows represents the flux direction. The magnetic flux was mostly concentrated in the back iron with a value of 2.5 T and about 1.7 T in the armature core.

 A plot of the computed magnetic vector potential (Wb/m) distribution throughout the cross-section of the motor and airspace is illustrated in figure 4.6. As can be observed, there are three leakage field components from the moving unit. These are the leakage field from the edges of the moving unit, leakage field across the inter-polar space separating the opposite magnet, and the leakage field from the yoke. However, the region between the two opposite magnets produces the highest leakage flux.
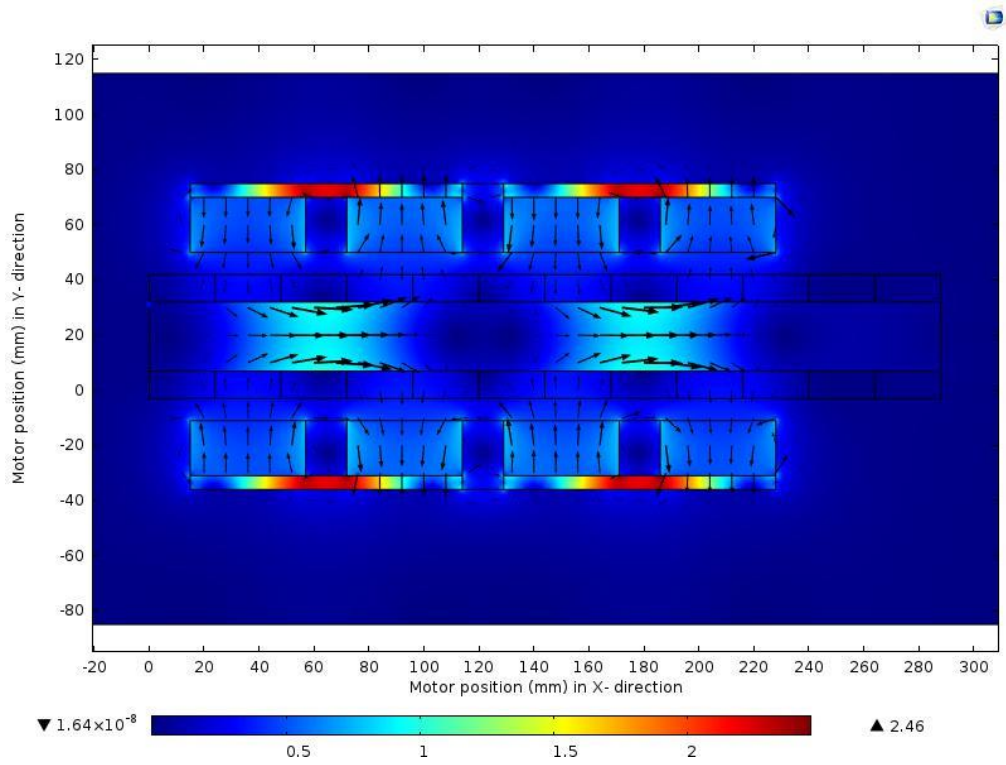
Figure 4.5 Magnetic flux density (T).
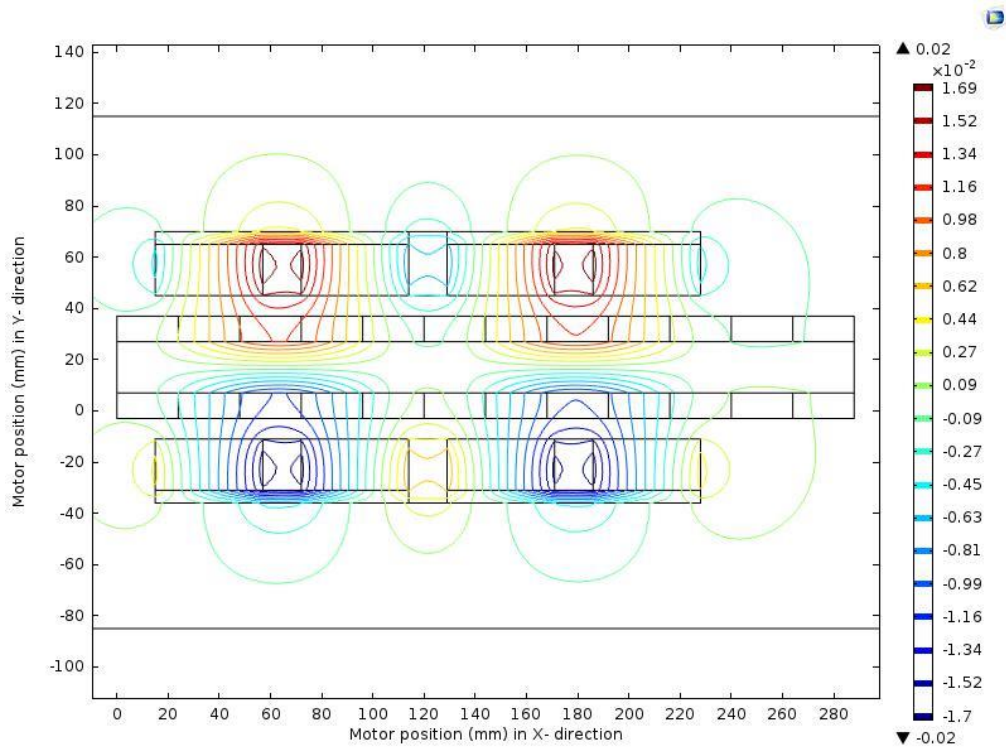
Figure 4.6 Magnetic vector potential (Wb/m).

Figure 3.7 illustrates the computed radial component of the flux density in the air-gap between the armature winding and the magnet. The air-gap is a critical region of the motor with regards to energy transfer and leakage field. As can be seen from the figure 4.7, the peak radial flux density in the air-gap occurs in the area opposite the centre of the magnet. Whereas, radial flux density becomes almost zero in the area opposite the space between the two magnets.
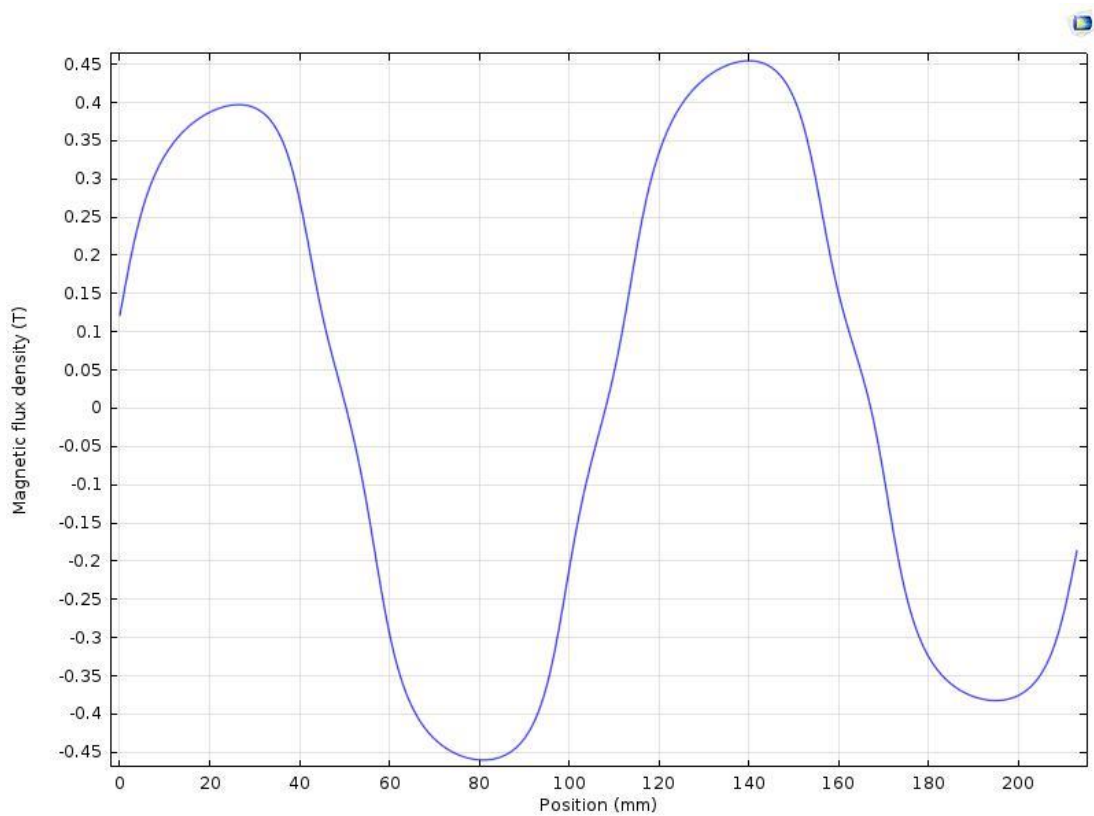
Figure 4.7 Radial magnetic flux distributions.

4.3.4 BSDCLM developed thrust

Figure 4.8 shows the simulated static thrust produced by the motor with different armature current values; 2.5 A, 5 A, 7.5 A, 10 A, 12.5 A and 15 A. The values for the static thrust developed on the slider are shown in Table 4.4.

Table 4.4 Developed static thrust force of BSDCLM

Armature current (A)	BSDCL motor thrust (N)
2.5	123.05
5	242.31
7.5	361.79
10	361.79
12.5	601.2
15	720.95
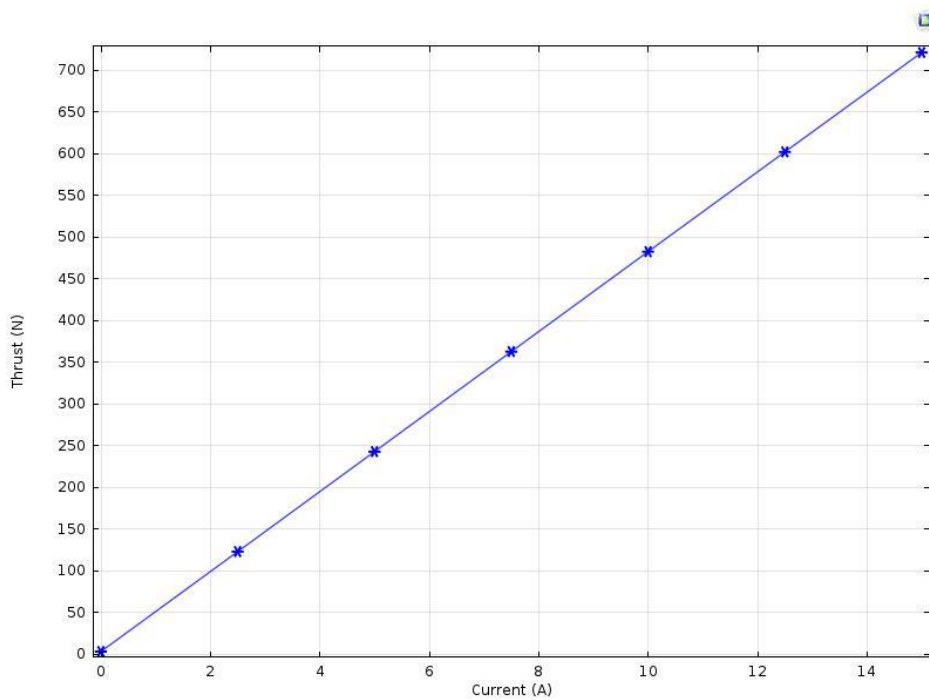
Figure 4.8 Developed thrust BSDCLM.

4.4   Simulation of the BDCLM employing flat winding

The second proposed model is the Brushless DC linear motor (BDCLM) which employs a flat winding. It was designed so that the motor core accommodates twenty-four independent multi-layer coil sections wound with enamelled copper wire, each layer section possessing 470 turns without compromising the effective air gap. Figure 4.9 shows the geometry of the BDCLM. As a result of the asymmetrical shape of the motor geometry, the motor was simulated using the "3D COMSOL Multiphysics". The armature core was chosen to be 288 mm long with dimensions of (288 x 30 x 30) mm and only eight winding sections were modelled. The main parameters and material specification of the BDCLM model are listed in Table 4.5.

Table 4.5 Dimensions and Material specification of the BDC L Motor model

Magnet dimension [mm]	42x 20 x 30
Magnet type	Neodymium Iron Boron
Number of magnets	8
Core dimension [mm]	288 x 30 x 30
Material of the Core	Mild steel
Back iron dimension [mm]	99 x 30 x5
Effective air-gap [mm]	5
Supply current [A]	2.5
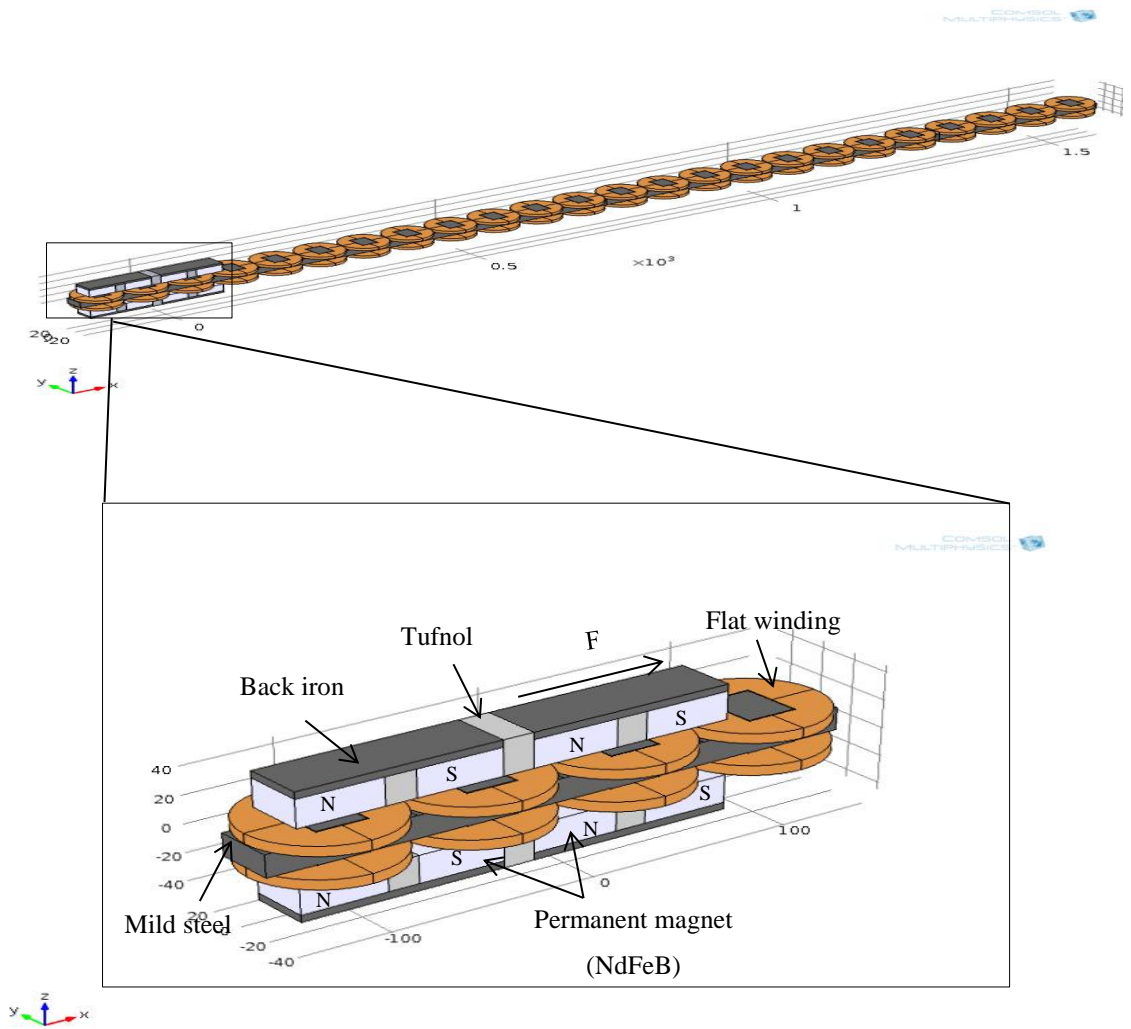
Figure 4.9 Geometry of the BDCLM.

4.4.1 Magnetic flux density of BDCLM

Figure 4.10 illustrates the distribution of the magnetic flux density throughout the entire cross-section of the motor and the surrounding air space. It can be observed that the areas close to the inner-surface of the magnet touching the back iron, and the areas close to the armature facing the magnet have much higher flux density than other areas of the motor.
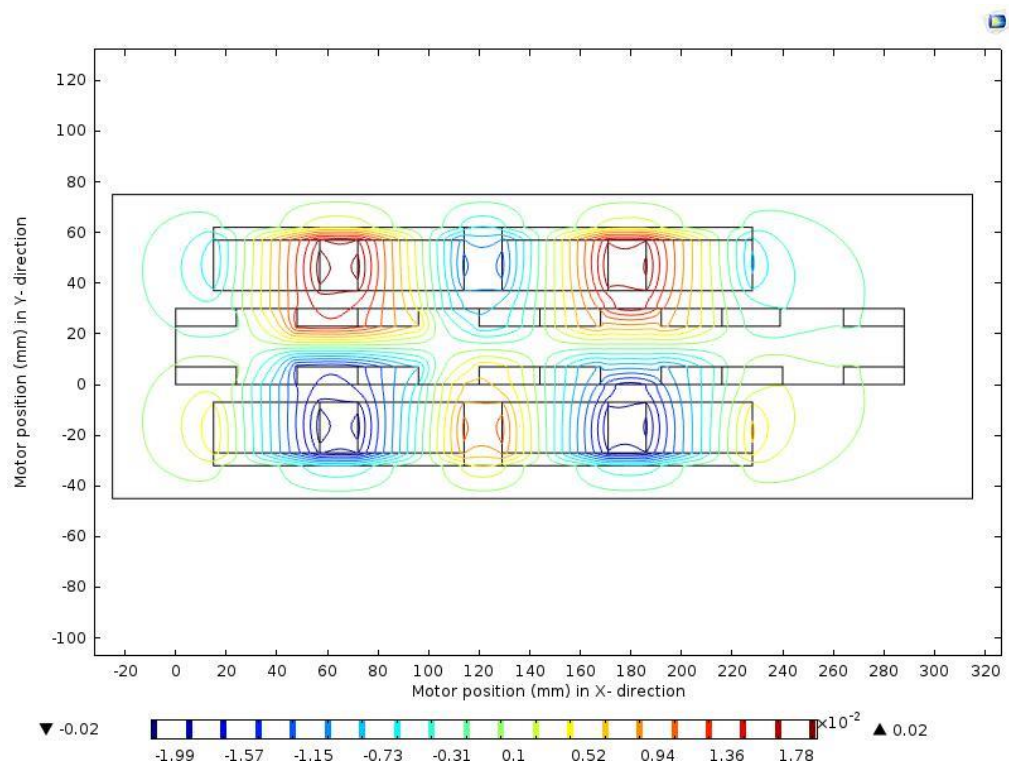
Figure 4.10 Magnetic flux density of BDCLM.

Figure 4.11 illustrates the computed radial component of the flux density in the air-gap of BDCLM. As can be seen, the flux density in the air-gap of the BDCLM is non-uniform due to the slots in the armature core. In the air-gap the peak radial flux is higher than radial flux of the BDCLM because the effective air-gap length in the BDCL motor is less by 5mm.
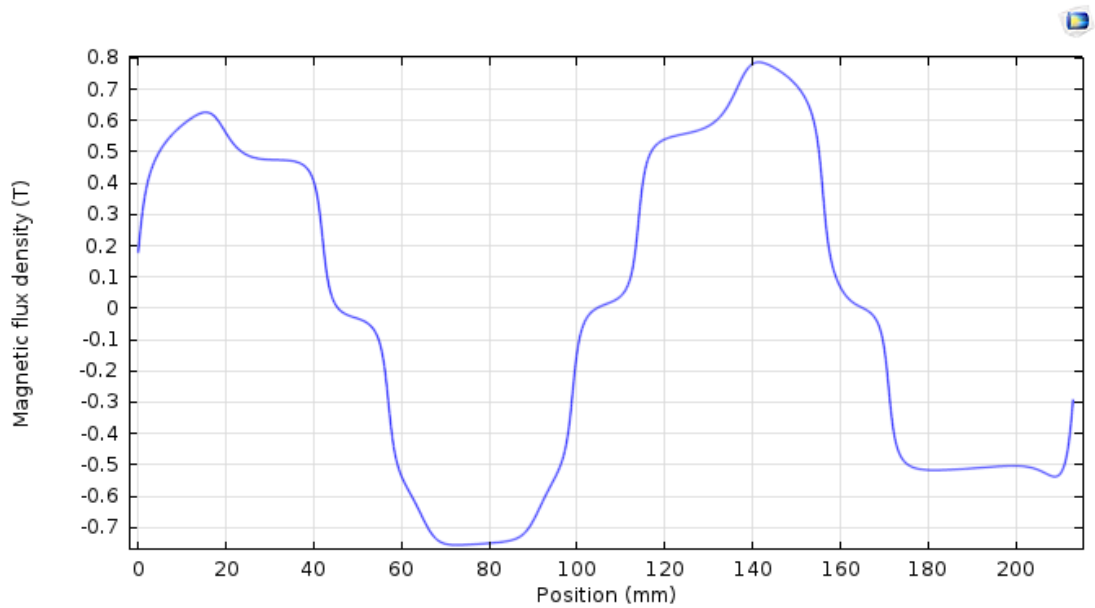
Figure 4.11 Radial magnetic flux distributions.

Figure 4.12 shows the magnetic flux density distribution throughout the motor and the arrows indicates the direction of the current in the armature winding. As can be observed, there is a higher flux concentration at the middle of the back iron which sums up to 1.5 T. The total flux density at the middle of the armature is 0.9 T. The total flux density in the armature core at both ends of the filed unit is 0.45 T. A maximum flux density of about 1.95T was found at the edge of the core teeth and back iron.
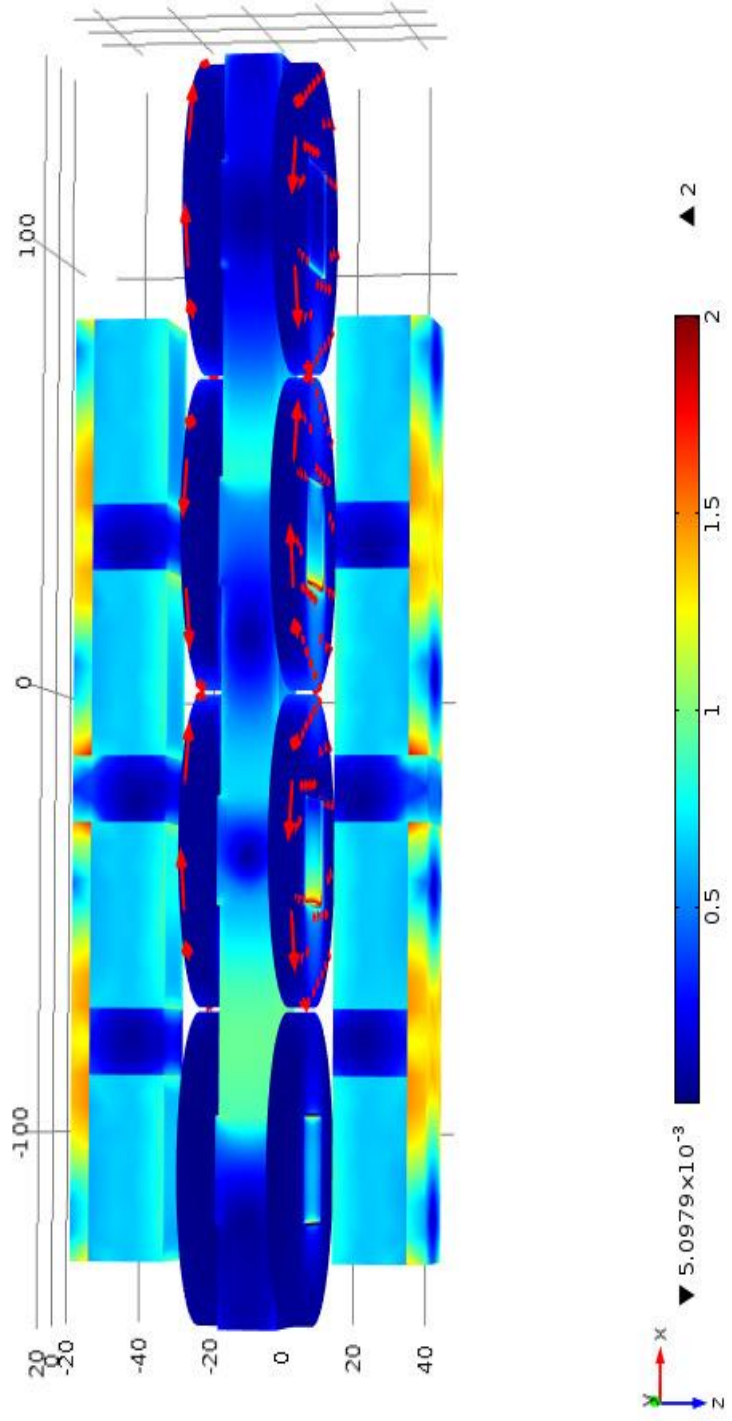
Figure 4.12 Magnetic flux density (T) and Coil current direction.

The arrows in figure 4.13 shows the direction of the magnetic flux throughout the motor while the colours represent the values of the flux density.
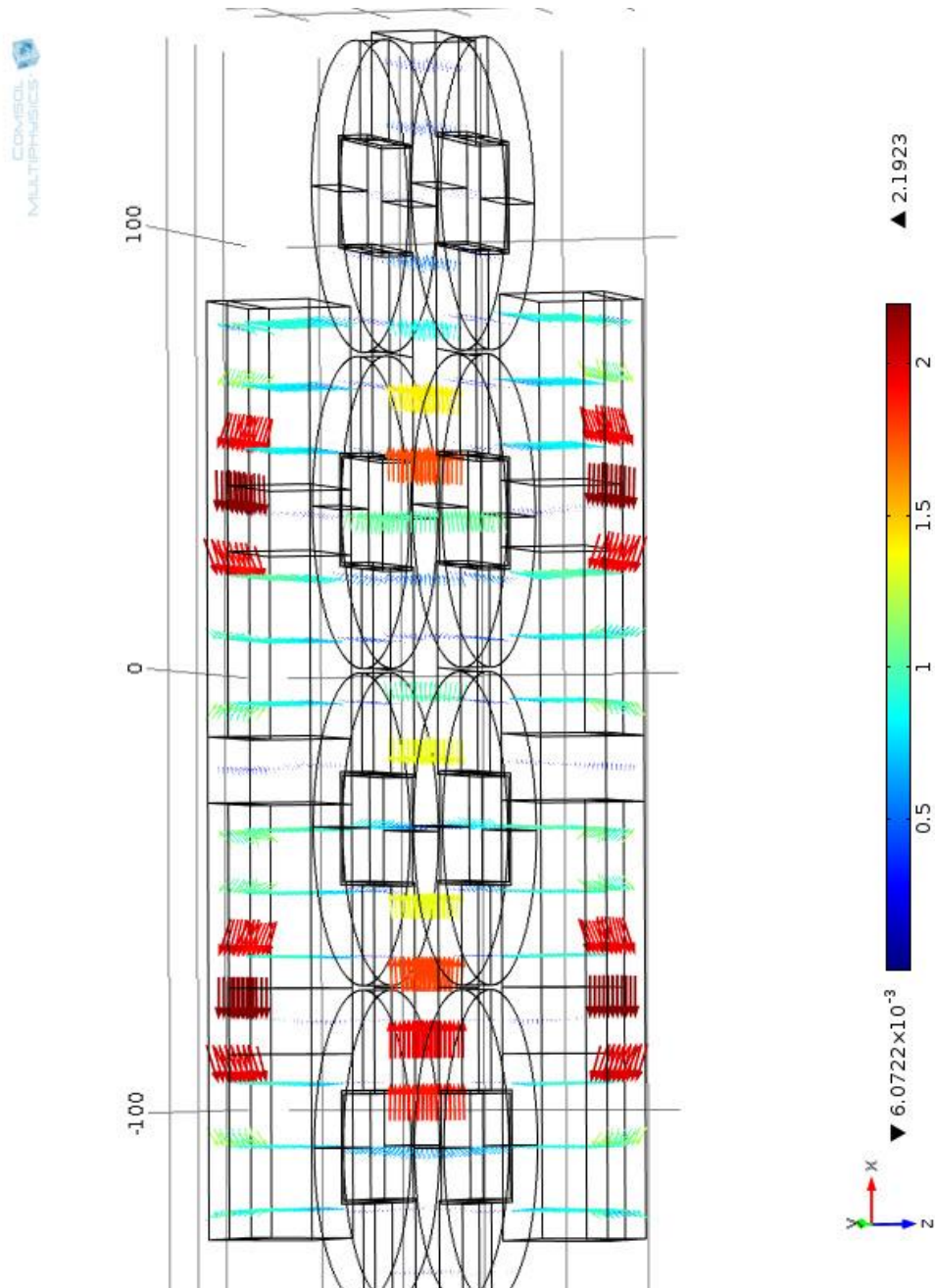
Figure 4.13 Arrows of magnetic flux direction (T).

4.4.2 The thrust analysis of BDLM

Figure 4.14 shows the thrust force produced by the motor with different armature current values; 2.5 A, 5 A, 7.5 A, 10 A, 12.5 A and 15 A. The values of the thrust developed on the slider are shown in Table 3.6.
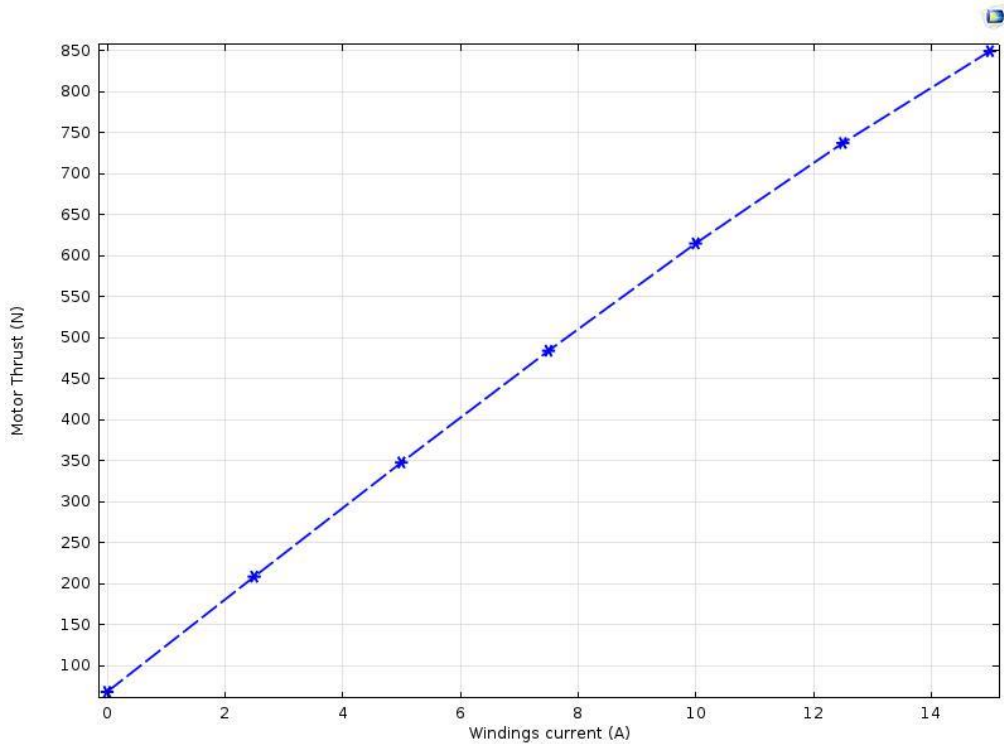
Figure 4.14 Static thrust of BDCLM versus armature current.

Table 4.6 Static thrust of BDCLM with different values of armature current.

Armature current (A)	Thrust (N)
2.5	213.55
5	352.96
7.5	488.02
10	614.33
12.5	726.18
15	824.31

4.5   Comparison between BSDCLM and BDCLM

A comparison was made between the two proposed motors with their specifications listed in tables 3.3 and 3.4, based on the following parameters; (i) Air-gap magnetic flux density (B_g) and (ii) static thrust.

4.5.1 Magnetic flux density variation at the air-gap

Figure 4.7 and figure 4.11 shows the magnetic flux density variation at the air-gap for both the BSDCLM and BDCLM designs. The air-gap flux density (B_g) in the BSDCLM has uniform signal due to absence of the slots compared with the air-gap flux density (B_g) in the BDCLM. The FEM computed peak value for the air-gap flux density (B_g) in the BSDCLM was 0.45 T, However, the computed peak B_g value for the BDCLM was 0.75 T. Thus, the air-gap flux density of the BDCLM was improved by 60 % compared to the BSDCLM.

4.5.2 Static thrust

In order to determine the accuracy and efficiency of the proposed models, the result for both models were compared in terms of the developed thrust as shown in table 4.7. Figure 4.15 compares the thrust produced by both the BSDCLM and BDCLM with different armature current values; 2.5 A, 5 A, 7.5 A, 10 A, 12.5 A and 15 A.

As can be seen from figure 4.15, the values for the static thrust of the BDCLM is higher than that for the BSDCLM with an average difference of 112.4 N and maximum deviation of 63.1 % at armature current of 7.5 A because the air-gap flux density in the BSDCLM is high compared to the air-gap of BDCLM. Hence, the BDCLM was chosen to be constructed.
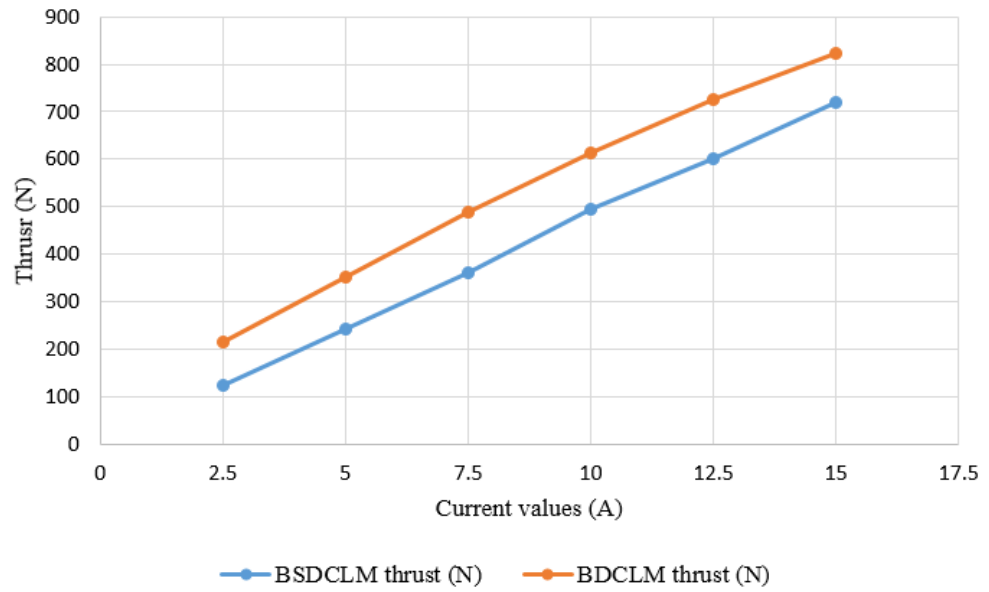
Figure 4.15. Comparison of the developed static thrust of BSDCLM and BDCLM.

Table 4.7 Comparison of the developed static thrust of BSDCLM and BDCLM.

Current (A)	BSDCL thrust (N)	BDCL thrust (N)	Deviation %
2.5	123.05	213.55	45.3
5	242.31	352.96	55.3
7.5	361.79	528	63.1
10	495.78	686	59.3
12.5	601.19	844	62.5
15	720.95	963	51.7

4.6 Effect of the air-gap on the BDCLM thrust

One of the major practical limitations on the performance of linear motors compared with rotary motors is a relatively large air-gap. That is, an increase in the length of the air-gap results in a decrease in the value of the magnetic flux density and the thrust. The air-gap should be as small as possible in order to be considered as a good magnetic circuit. A large air-gap produces an undesirable effect on the behavior of the linear motors. Nevertheless, for practical reasons, the air-gap cannot be designed to the minimum without any limitation (the mechanical clearance between the armature core and the mover).

The parametric sweep function as shown in figure 4.16 was used in order to investigate the effect of the flux density of air-gap on the developed thrust. Parametric sweep function computes the thrust at different air-gap values from 0 mm to 10 mm with different current values from 2.5 A to 15 A.

Figure 4.17 shows the developed thrust of the motor with different values of air-gap from 0 mm to 10 mm at 2.5 A armature current. It can be observed that the thrust decreasing with increasing air-gap. As a result of the mechanical restriction guidance of the moving unit a minimum air-gap of 5 mm was chosen for this model which represents the mechanical clearance between the armature winding and the moving magnets.
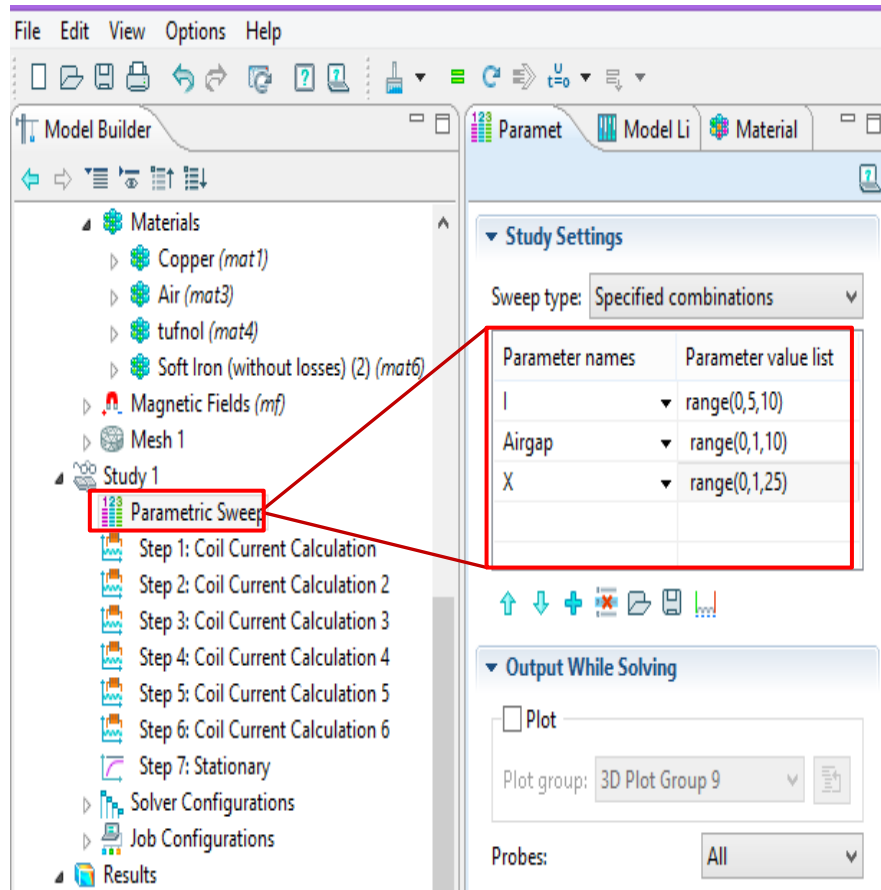
Figure 4.16 Using parameter sweep function in COMSOL model builder.
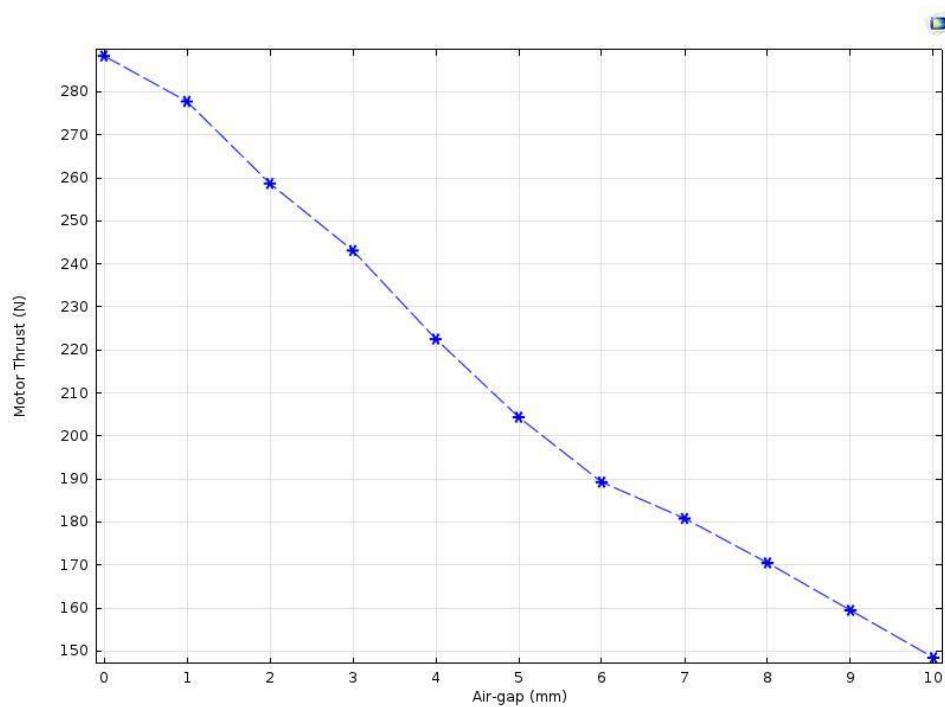
Figure 4.17 BDCLM thrust with different values of air-gap from (0 to 10) mm.

4.7 Armature core and backiron thickness optimisation of the BDCLM

The parametric sweep function as shown in figure 4.18 was used in order to optomise the armature core and backiron thickness without reaching saturation . The parametric sweep function computes the magnatic flux density for different armature core and backiron thicknesses, that is; from 10 mm to 40 mm in steps of 5 mm for the armature core and from 5 mm to 12.5 mm in steps of 2.5 mm for the backiron.
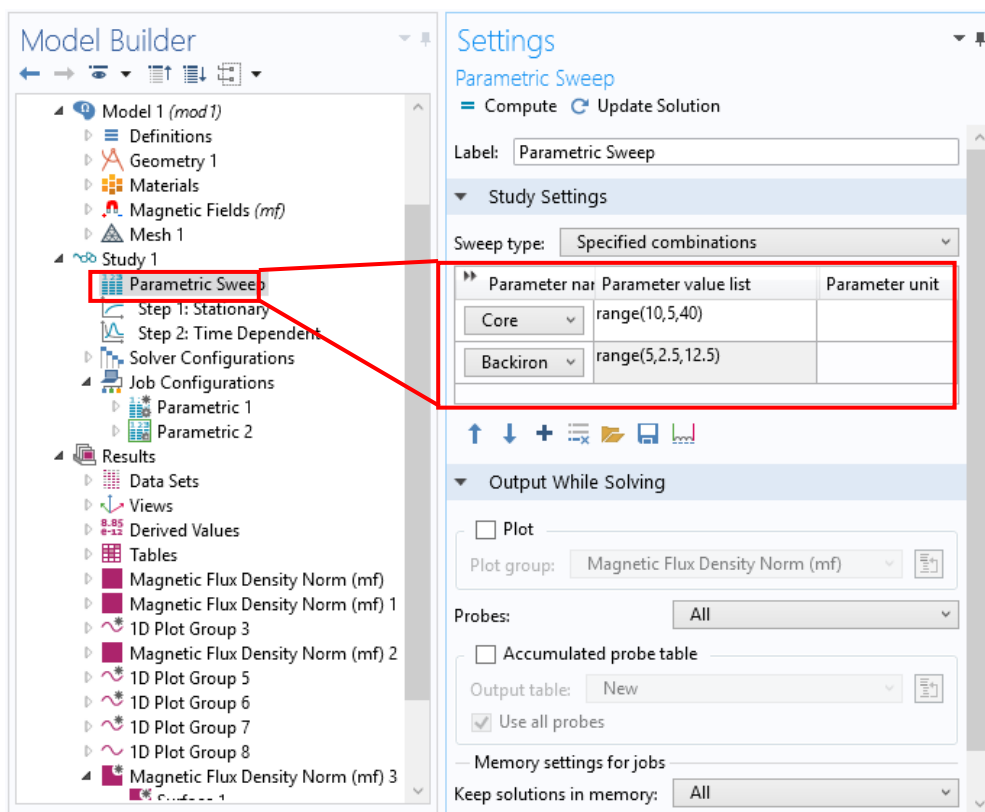
Figure 4.18 Parametric sweep function for the armature core and backiron thickness.

Figure 4.19 and figure 4.20 shows the the magnatic flux density with different armeture core and backiron thicknesses. It can be observed from both plots that the flux density decreases as thickness increases. An armeture core with a thickness of 30 mm was choosen as the optimal armeture core thickness, since it has a maximum magnatic flux density of 0.8 T. Also, the backiron thickness should be as minimum as possible to reduce the size and weight of the moving unit. Hence, a backiron with a thickness of 5 mm was choosen as the optimal backiron thickness.
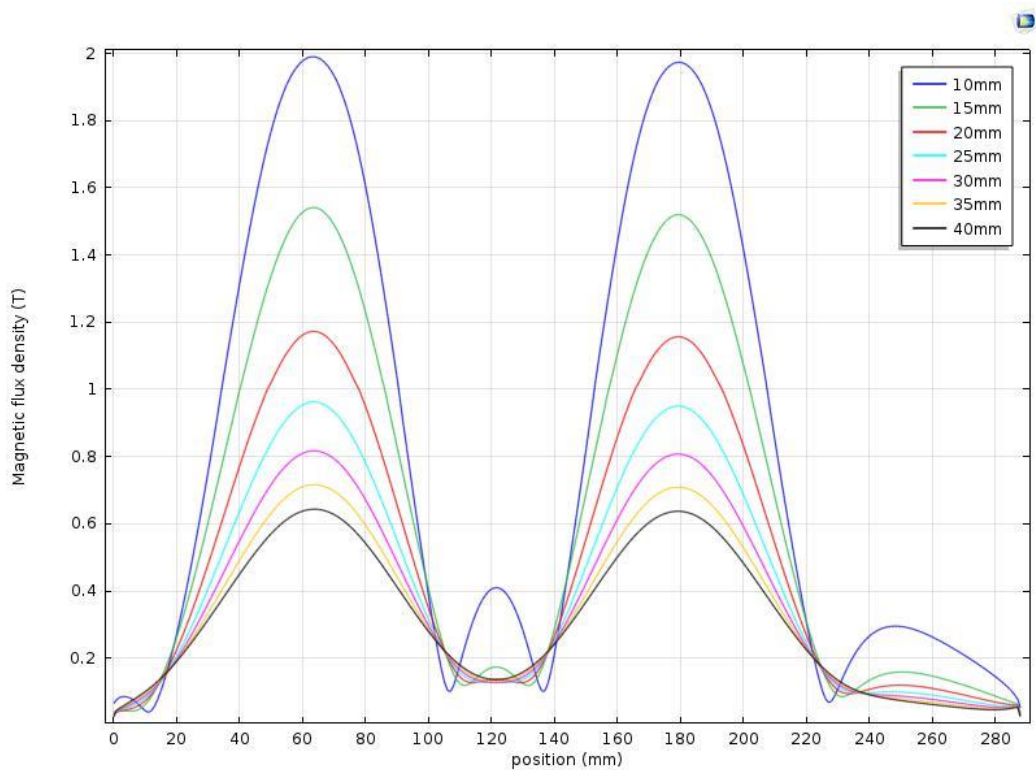
Figure 4.19. Magnetic flux density with different armature core thicknesses.
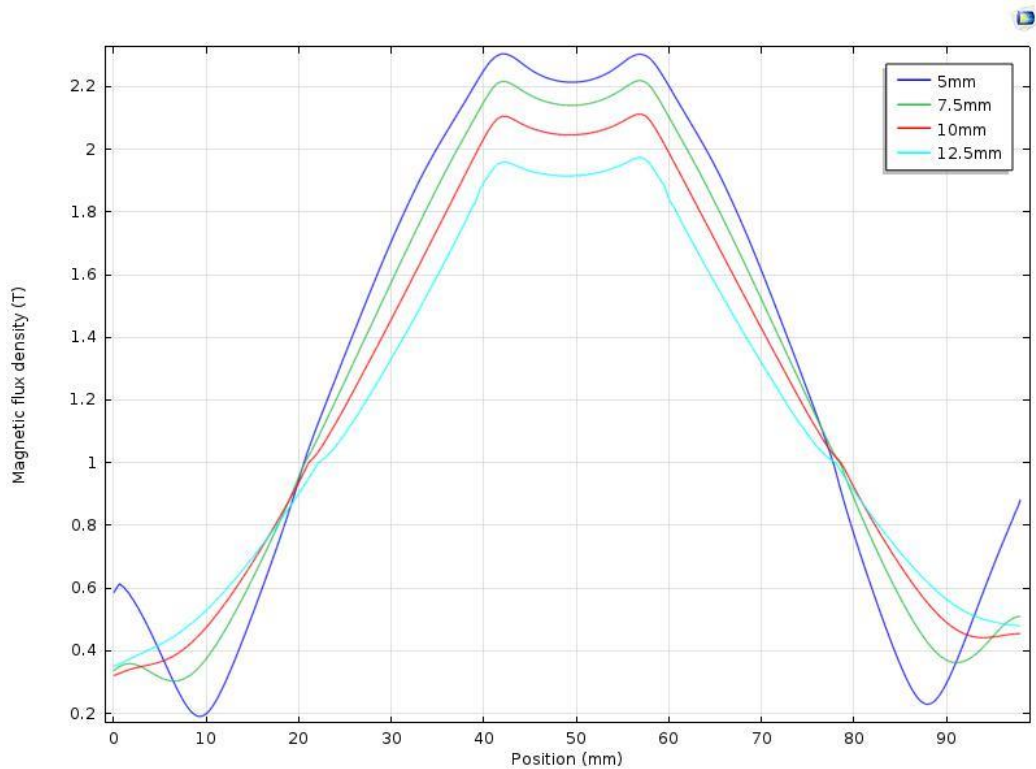
Figure 4.20 Magnetic flux density with different backiron thicknesses.

4.8   Detent force and normal force analysis of the BDCLM

At no supply current condition, the BDCLM experiences two different forces due to the attraction between the PMs and armeture core, which are; the detent force and the normal force.

4.8.1   The Normal Force Analysis of BDCLM

As mentioned earlier in section 2.7, the normal force is generated due to the attraction between the permanent magnets and the iron core of the stator. The normal force problem exists in the single-sided DC linear motor and it affects its running characteristics, stability and control strategy [33].

In a double-sided DC linear motor configuration, when the armature core is centrally located between two sets of permanent magnets, the normal force is zero. Figure 4.21 shows the FEM result of the normal force in the BDCLM with respect to the displacement of the mover at zero current. As can been seen from the graph, the value of the normal force is bigger than that of the thrust force with a maximum value of about 700 N in the single-sided motor.
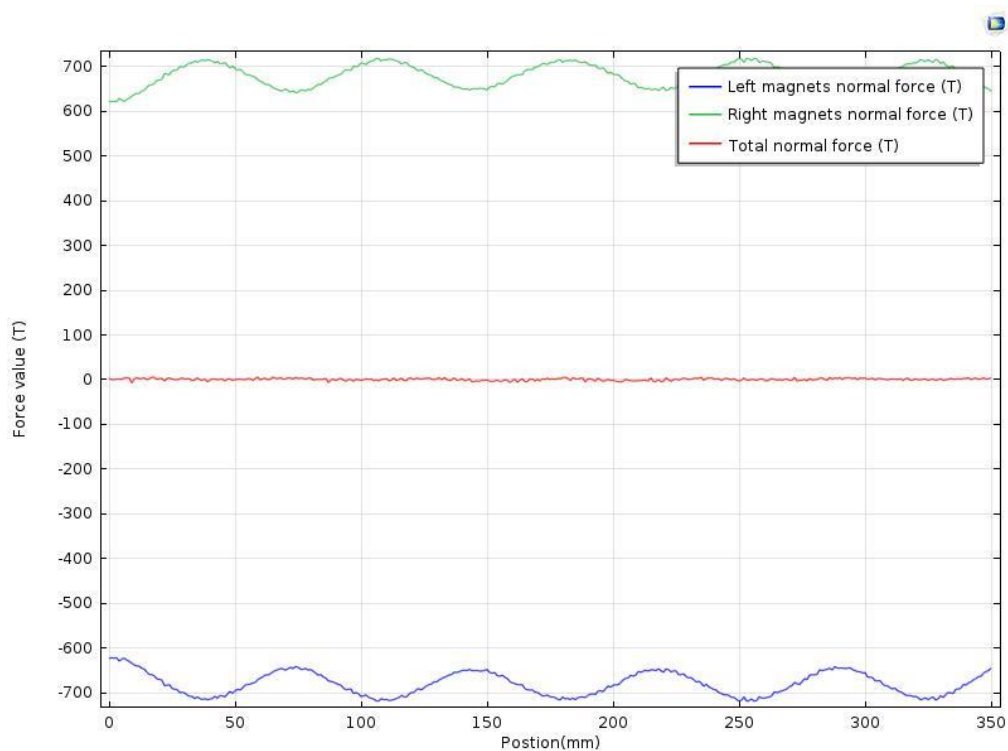
Figure 4.21 Normal Force with respect to the motor displacement.

4.8.2 The Detent Force Analysis of BDCLM

As mentioned earlier in section 2.8.1, there is an additional force excluding the main electromagnetic thrust force in BDCLM, which causes a thrust ripple that affects the motor performance. The detent force is caused by the end effect and the cogging force [54, 55]. The cogging force depends on relative position of the translator and the magnets, and is always present even in the absence of a supply current.

The detent force results in a periodic force oscillation with respect to the mover position. Thus, this periodic force oscillation causes mechanical vibration, acoustic noise and velocity fluctuation, which deteriorates the motor performance [57].

When the input current is zero, the output force is the detent force. The calculated results for the detent force distribution with respect to the relative position between the mover and the stator are shown in Figure 4.22. The detent force has a wavelength of one slot pitch and the peak value of the detent force is almost 20 N, which is almost 10 % of the thrust force 200 N.
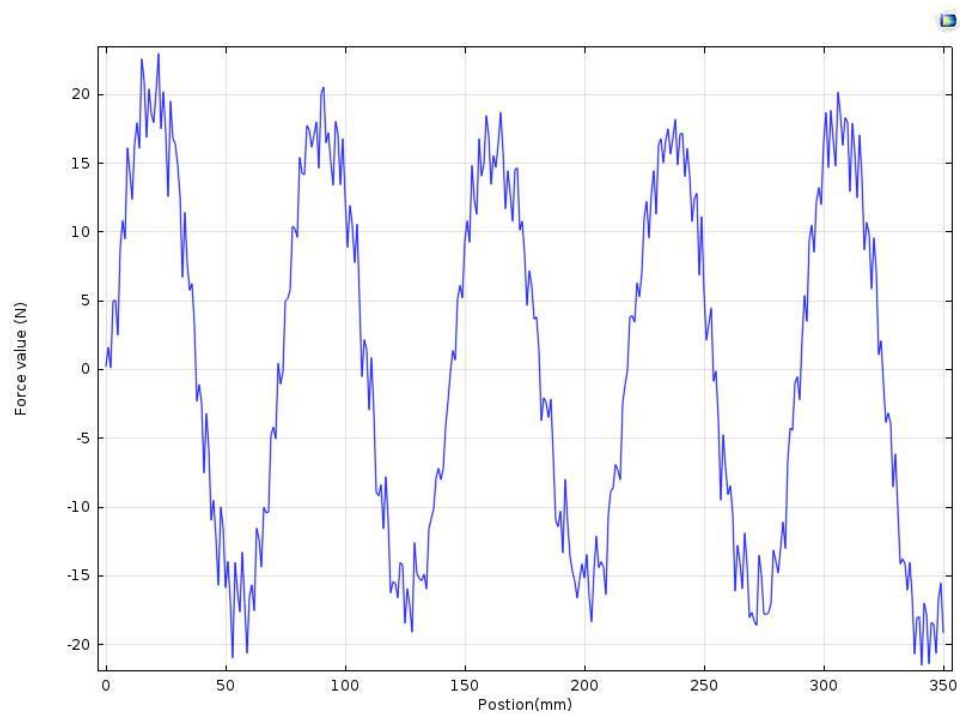
Figure 4.22 Detent Force with respect to the displacement.

4.9   Modelling of the BDCLM in transient

The design and development of a linear motor requires an accurate prediction of both the static and dynamic performance. The static characteristics of the initial prototype design were examined in the modelling of BDCLM section. In this section, the dynamic behaviour of the BDCLM is evaluated by two coupled differential equations; the electrical circuit equation which models the coil winding, and the mechanical motion equation which models the thrust generation and the permanent magnet movement. The two equations should be solved simultaneously [1].

In order to model the translational motion of the BDCLM, time dependent study and moving mesh physics interfaces was added to the stationary study step. The stationary study was used to compute the vector potential field inside and around the stationary permanent magnet as the initial condition to solve a time dependent study step. This step computes the transient response resulting from the slider movement.

The model geometry is designed so that the stator part and the slider part are created as separate unions. These parts are then finalised with the Form Assembly so that the identity pair is automatically created between the stator and the slider in the interface. The moving mesh is also added in order to model the slider's movement.

Since armature current of the BDCLM is a function of slider position, therefore the current was modeled as a piecewise function. Figure 4.23 represents the current function in the third winding with respect to the slider position.
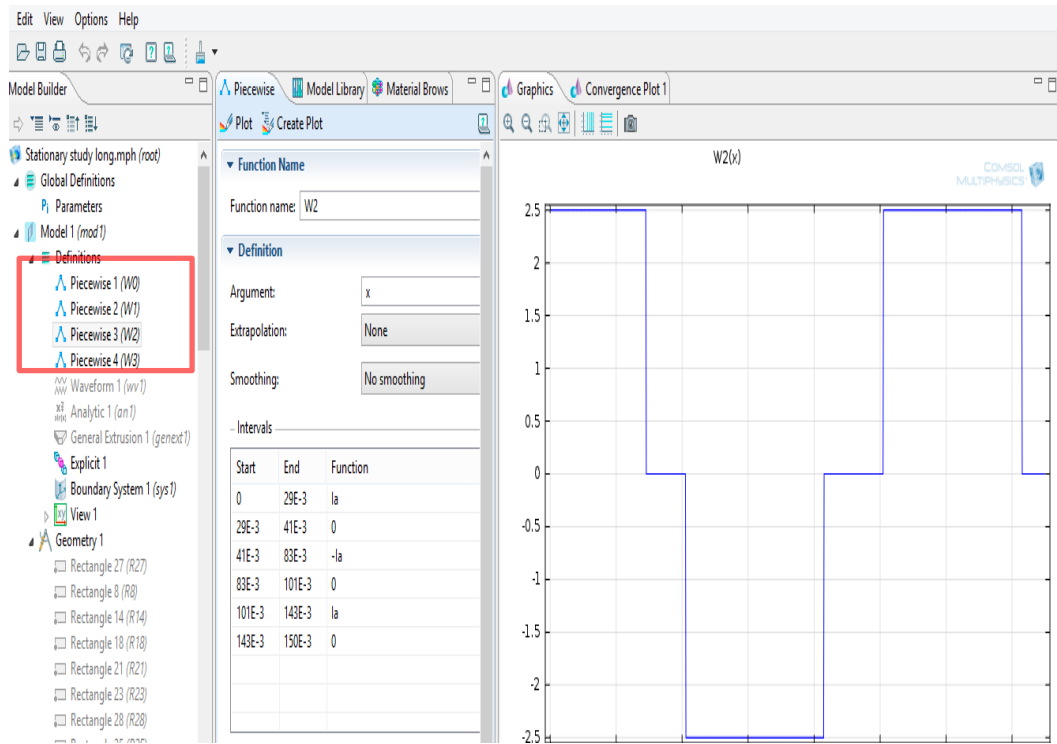
Figure 4.23 waveform of the current function.

4.9.1 Moving Mesh constuction

A moving mesh interface is used to model the 'Translational Motion' of the DC linear motor. The mesh was split into two parts; one for the set of permanent magnets and surrounding air and the other for the armature winding. The stator domains (armature winding) and surrounding air domains were assigned as a fixed mesh, whereas the permanent magnets and surrounding air domains were assigned as a moving mesh. The moving parts were modeled using the prescribed deformation in the x-direction, with a prescribed motion defined by the position variable (p) from the Global **ODEs** and **DAEs** interface. Figure 4.24 shows the settings for the moving mesh interface.
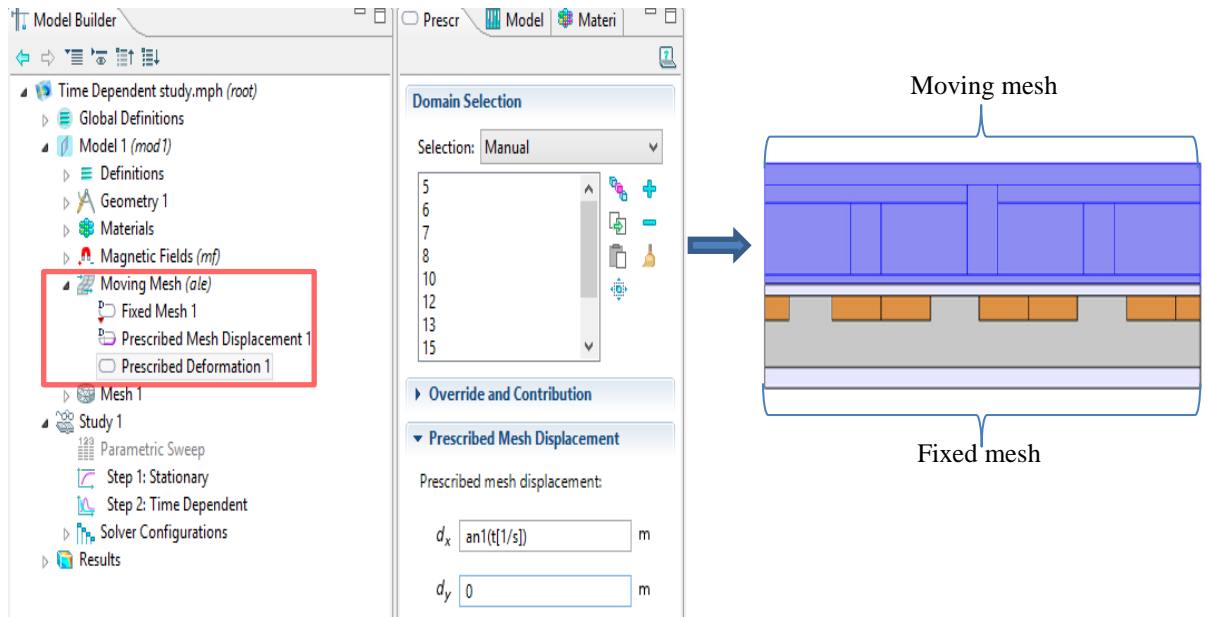
Figure 4.24 Moving Mesh interface settings.

4.9.2 Dynamic behavior of the BSDCLM and BDCLM

The *Global ODEs and DAEs* interface in "COMSOL Multiphysics" is used to accurately predict the dynamic performance of the BSDCLM and BDCLM. The dynamic motion for the BSDCLM and BDCLM are expressed in equation (4.1) and (4.2):

$$M \frac{dv}{dt} - F_x(p, v, t) = 0 \qquad (4.1)$$

$$\frac{dp}{dt} - v = 0 \qquad (4.2)$$

Where p is the mover postion in the x-direction, v is the motor velocity, M is the mover mass and F_x is the thrust force in the x-direction.

Figure 4.25 shows how the dynamic equation of motion for the BSDCLM and BDCLM was implemented using the Global **ODEs** and **DAEs** interface.
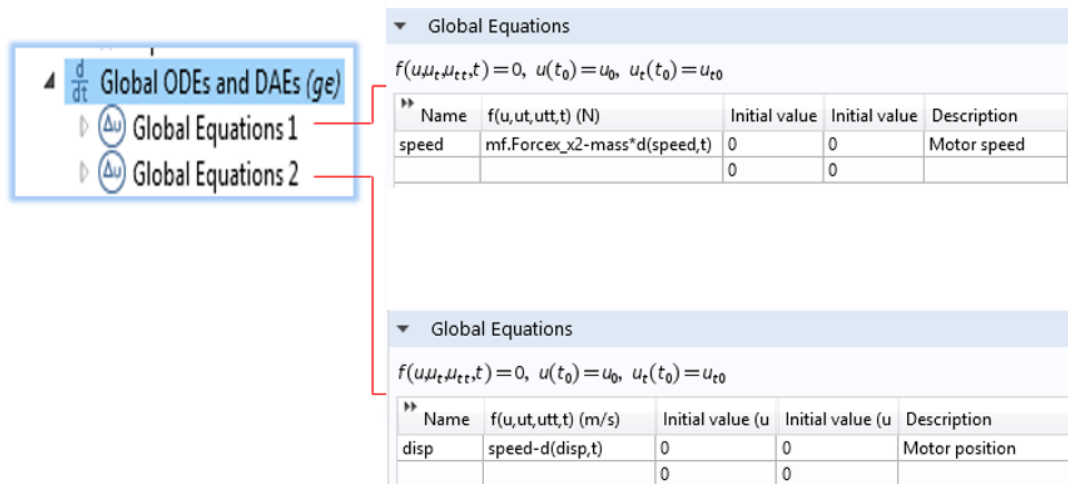
Figure 4.25 Dynamic equation of motion for the BDCLM.

Figures 4.26 shows the distribution pattern of the magnetic flux lines with respect to the mover position (x). As can be seen, the end effect occurs as a result of the open end of the mover.

The dynamic result of the BSDCLM and the BDCLM model in terms of thrust, speed and displacement are shown in figures 4.27, 4.28 and 4.29 respectively. The thrust value of the BSDCLM and the BDCLM model were computed at 2.5A armature winding to be 145 N and 225 N respectively. The motor steady-state speed of the BSDCLM and the BDCLM model were computed to be 0.17 m/sec and 0.25 m/sec respectively. The mover of the BSDCLM and the BDCLM model took about 1.6 secs to reach 272 mm and 365mm respectively. The BSDCLM took about 1.4 secs to reach the steady state while the BDCLM took about 1 sec to reach its steady state.
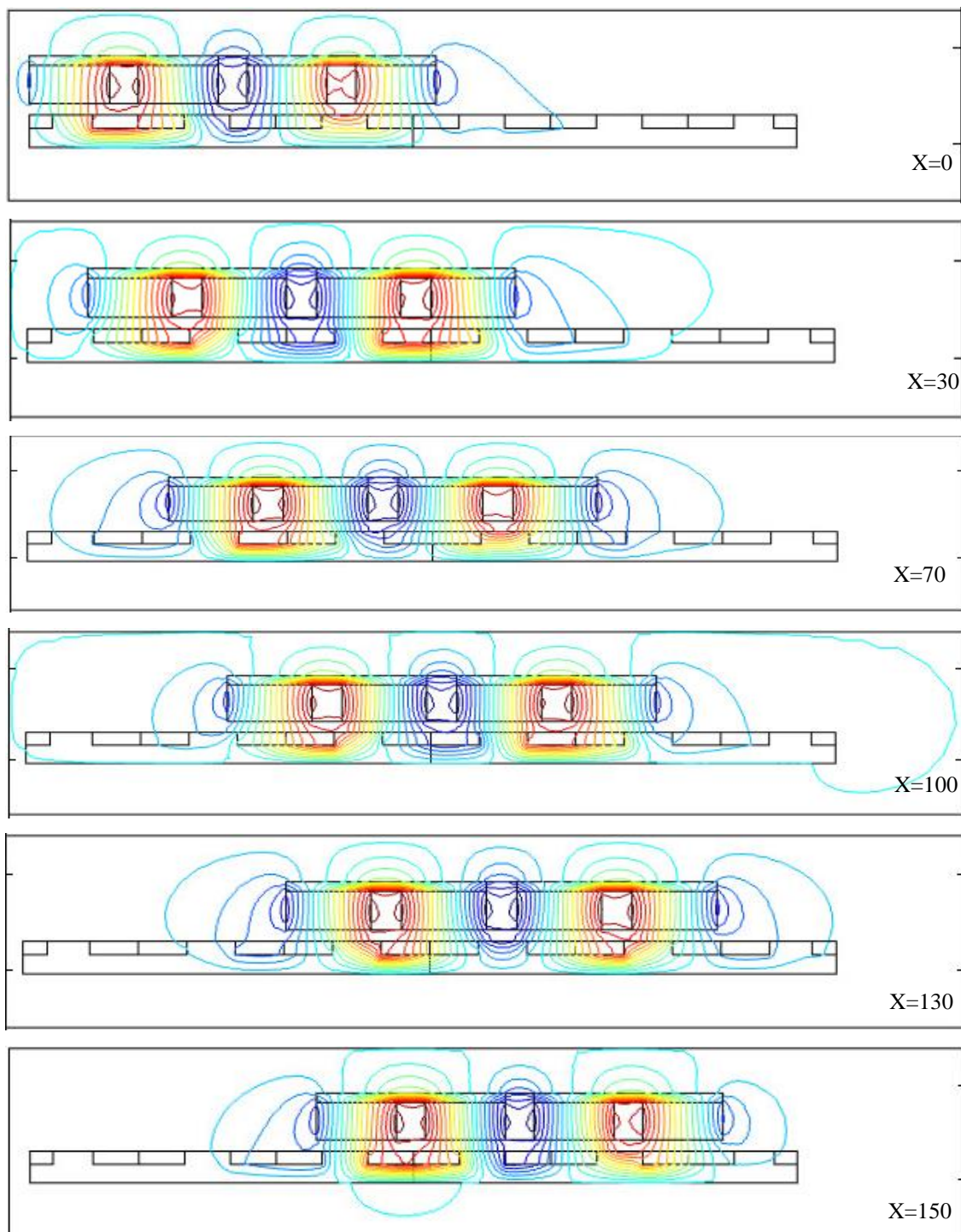
Figure 4.26 Magnetic vector potential for different slider displacement.
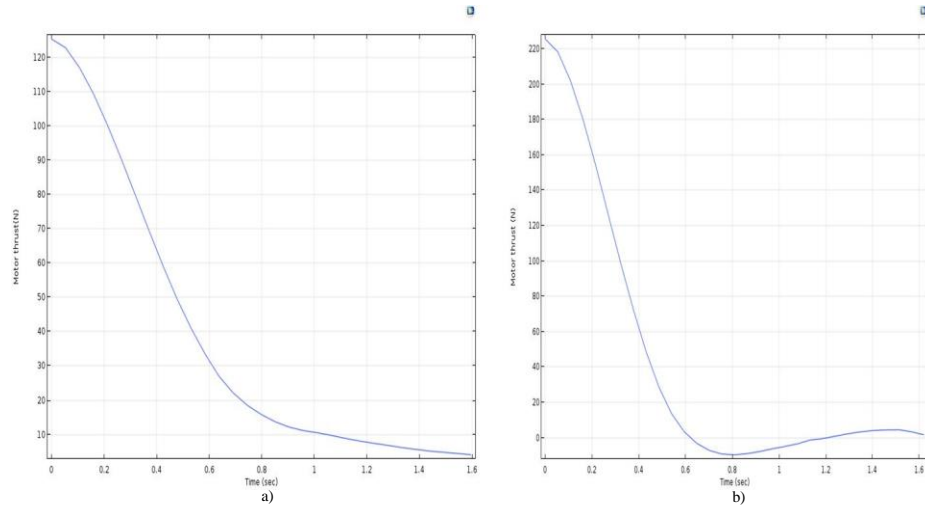
Figure 4.27 Thrust analysis of dynamic model of ; a) the BSDCLM and b) the BDCLM.
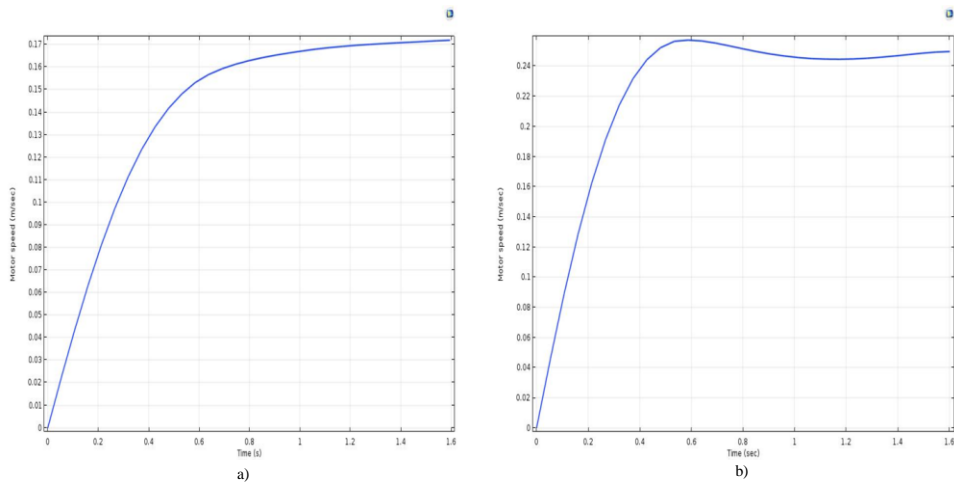
Figure 4.28 Motor speed analysis of dynamic model of ; a) the BSDCLM and b) the BDCLM.
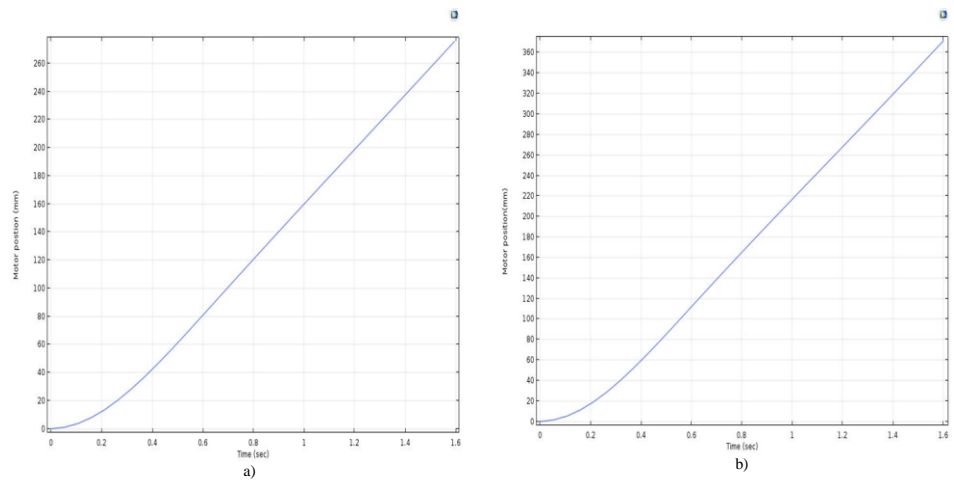
Figure 4.29 Displacement analysis of dynamic model ; a) the BSDCLM and b) the BDCLM.

4.10 Conclusion

A Finite Element Method (FEM) analysis using "COMSOL Multiphysics" was performed to test the motor design. A comparison was made between the two proposed models for the BSDCL and BDCLM in term of the static thrust, air-gap flux density and the static thrust. The result showed that the computed Air-gap flux density value for the BDCLM was improved by 60 % compared to the BSDCLM. The result also showed that the static thrust of the BDCLM is higher than that for the BSDCLM with an average difference of 112.4 N and maximum deviation of 63.1 % at armature current of 7.5 A because the air-gap flux density in the BSDCLM is high compared to the air-gap of BDCLM

The dynamic result of the BSDCLM and the BDCLM model in terms of thrust, speed and displacement were computed at 2.5 A armature winding to be 125 N and 225 N respectively. The motor steady-state speed of the BSDCLM and the BDCLM model were computed to be 0.17 m/sec and 0.25 m/sec respectively. The mover of the BSDCLM and the BDCLM model took about 1.6 secs to reach 272 mm and 365mm respectively. The BSDCLM took about 1.4 secs to reach the steady state while the BDCLM took about 1 sec to reach its steady state.

Chapter 5 : Dynamic Model and Open-loop Transient Response of the BDCLM

The experimental set-up for real time implementation of open-loop velocity and position controllers is presented in this chapter. The static thrust has been measured using a load cell at different slider positions, in order to verify the commutation algorithm. The commutation algorithm was designed to provide a smooth movement of the slider and to obtain a maximum thrust. Also, the measured and FEM predicted air-gap flux density and static thrust are compared.

5.1 Introduction

As the name indicates, no feedback was employed in this system. The open-loop response of any system must be validated before implementing the design of the velocity and position of the motor controller. That is the open-loop velocity, position and current responses of the motor must be measured. The DC linear motor and a personal computer were interfaced with the aid of a "USB-6211" Data Acquisition (DAQ) card integrated with the LabVIEW software by National Instruments. The data acquisition card used has 8 channels with a 16-bit A/D converter. Two channels were used to read the position of the slider and armature current. A system was developed to control the supply of electrical power to each section of the armature winding. A commutation is achieved by energising sections of the armature winding in a sequence, with the aid of a microcontroller (Arduino Mega). A Linear Variable Differential Transformer (LVDT) sensor that can achieve a sensing position up to a 40 cm length

was used to detect the slider position. The velocity of the slider has been calculated by numerically differentiating the position signal.

5.2 Experimental Setup

In order to verify the effectiveness of the proposed BDCLM, experimental tests have been performed. The experimental set-up consists of an assembled brushless DC linear motor, a LVDT position sensor, nine current sensors, two power supplies, an Arduino Mega microcontroller, a data acquisition card and a computer. A schematic diagram illustarating the experimental set-up is shown on Figure 5.1.
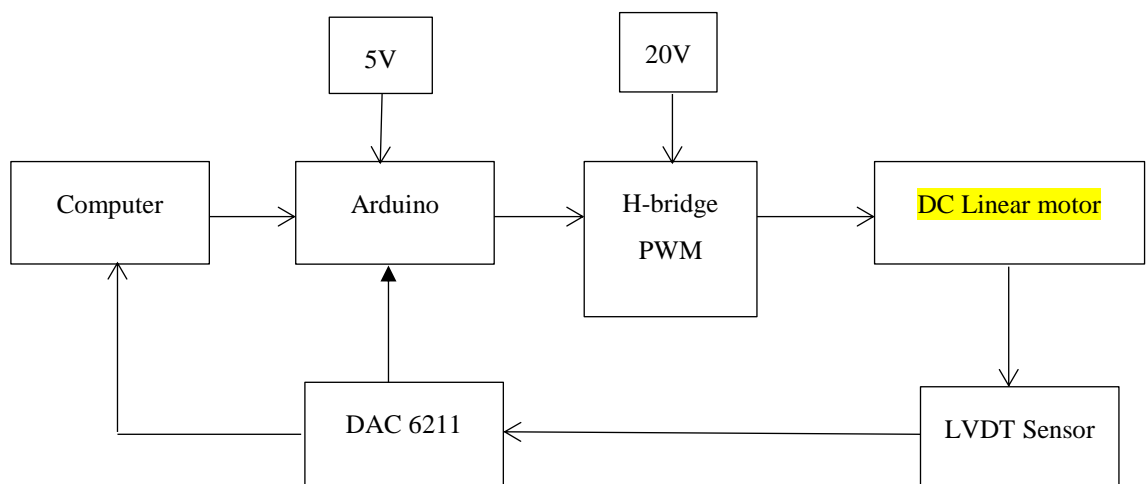
Figure 5.1 A schematic diagram of the experimental set-up.

A picture of the experimental set-up is shown in Figure 5.2. The set-up consists of a Brushless DC-Linear motor (BDCLM) (1), LVDT sensor (2), DAQ 6211 card (3), Arduino Mega board (4),H-bridge board (5), current sensor (6) and portable computer (7).
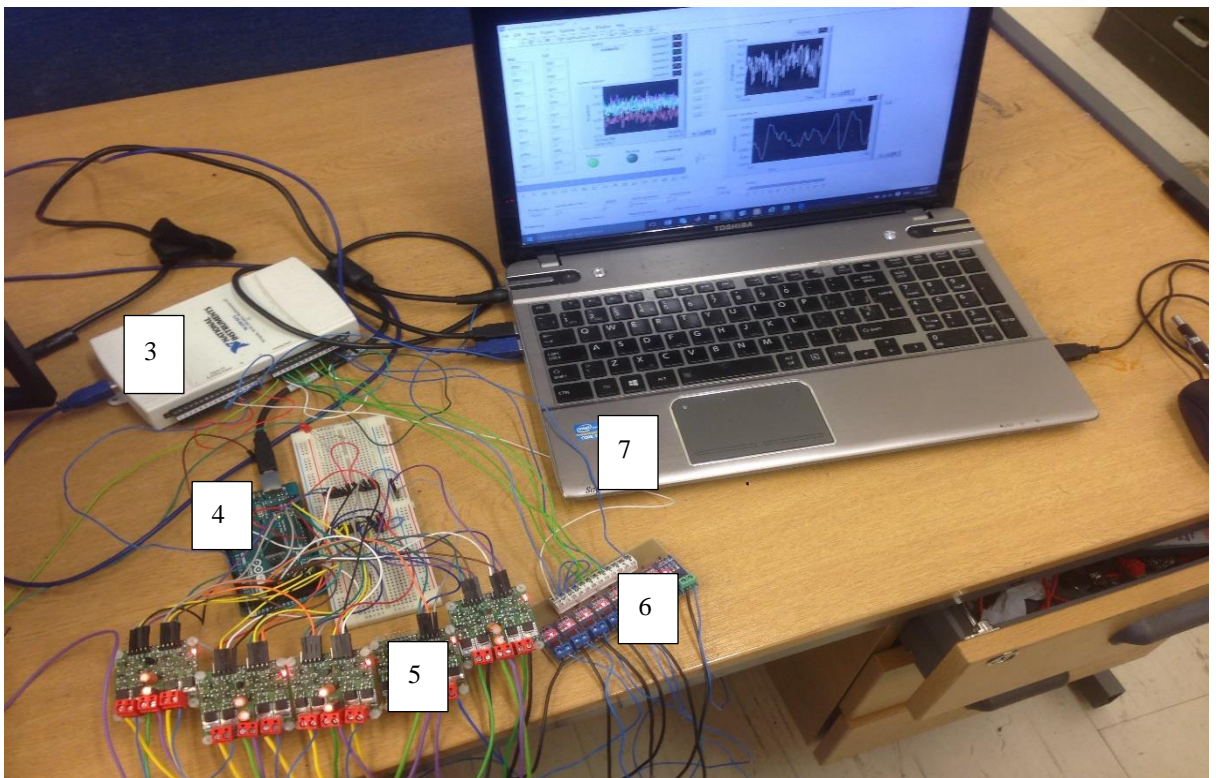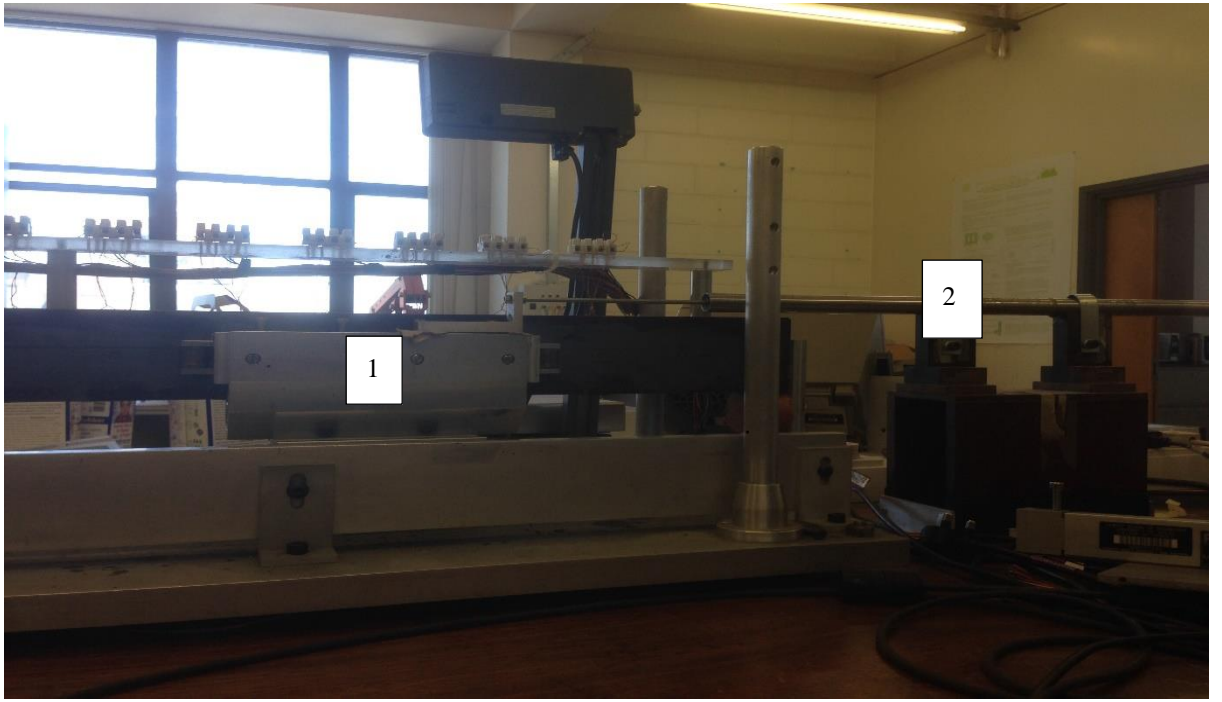
Figure 5.2 Picture of the experimental set-up.

5.3   Commutation strategy design for BDCL motor

In the DC linear machine drive the power switching H-bridge circuit acts as an electronic commutator, which switches the DC current between the windings according to the instantaneous mover position. Commutation strategy is described as the switching sequence of driver voltage across the armature winding section, which is necessary to ensure continuous motion of the slider. The commutation was arranged such that only the coils under the influence of the field at a given moment are carrying current.

The main goal of the commutation is to produce maximum thrust and a continuous motion. For the force to be produced on the slider without ripples, the armature sections just under the magnets must be energised, but other sections should not be energised in order to avoid a reversal force from acting on the moving carriage, thereby causing a brake that decreases the motor speed. The commutation algorithm is presented in appendix C.

The commutation strategy of the BDCLM is position dependent, so the BDCLM requires a position sensor to feedback the position data to the motor control drive system, which determines the next switching sequence.

5.4   Feedback Control

In order to close the control loop, the position of the moving unit of the motor should be measured using the LVDT sensor. The analogue signal output from the LVDT sensor was fed to an A/D channel on the DAQ board as shown if figure 5.1. The slider position is read into the "LabVIEW" program and processed by the controller. The controller then outputs signals through the D/A channels on the DAC board to each of the PWM

amplifiers. The amplifiers in turn power the current-carrying coils, which exert a force on the permanent magnets in the mover, causing a movement.

5.5   Controlling BDCLM using "LabVIEW"

In this experiment the current applied to the armature winding is 2.5 A and the supply voltage is 19.5 V. The armature current was sensed using a Hall-effect current transducer. The motor movement was controlled using the "LabVIEW" programme, for a maximum travel distance of 350 mm and a maximum speed of 0.23m/sec. Also, the movement of the motor was made to be bi-dimensional (i.e. forward and backward movement). The "LabVIEW" programme of controlling the motor was implemented based on Figure 5.1.

The block diagram of the LabVIEW program used to control the DC linear motor is shown in Figure 5.3. The analogue signal output from the LVDT sensor is fed to an A/D channel 1 on the DAQ board. The position was read with the aid of the "LabVIEW" program and processed by the controller. According to the position of the mover, the controller provides the commutation for the armature winding through the "Arduino" board. The "Arduino" then outputs the voltage signals to the H-bridge driver board. The driver board then supplies the current to the coils, which exerts a force on the permanent magnets in the mover, thereby resulting to a movement.

Before turning on the motor, the exact motor position is measured by the LVDT sensor. According to the motor position, the microcontroller sends a control signal to the H-bridge motor drivers to control the armature windings to be energised for continuous movement. The motor was controlled to move forward until it reaches a travel distance

of 350 mm, then it automatically moves backward until it reaches a distance of 15mm

and then it moves forward and so on until the break button is pressed to stop the motor.

5.5.1 Sensor calibration

The calibration of the LVDT sensor and 9 current sensors via the LabVIEW program is

illustrated in Figure 5.4. The output voltage of the LVDT sensor is 5 V at 0 mm position

which was read by DAQ system, then subtracted by **-5** to get 0 V at 0 mm position and

then multiplied by a factor of 39.9 to convert voltage to distance in mm. The voltage

reading of the current sensor was 2.5 V at 0 A, so the output voltage of the current

sensor was subtracted by **-2.5** to measure 0 V at 0 A and then divided by a factor of 0.24

to convert the voltage reading to the actual current value in the armature winding.

5.5.2 Implementation of winding commutation

Figure 5.5 illustrates the implementation of the armature winding commutation

algorithm conducted in "LabVIEW" using the "select case" block. The "select case"

block was also used to choose between the forward and backward movement option.

The armature winding commutation algorithm (current function $f_k(x)$) is shown in

appendix C.

5.5.3 Implementation of BDCLM motion direction controller

Figure 5.6 illustrates the mechanism of choosing between the forward and backward

motor movement. The motor was programed to move forward with a maximum distance

of 350 mm and move backward when it reaches the15 mm position.

Figure 5.3 Block program of LabVIEW motor control.
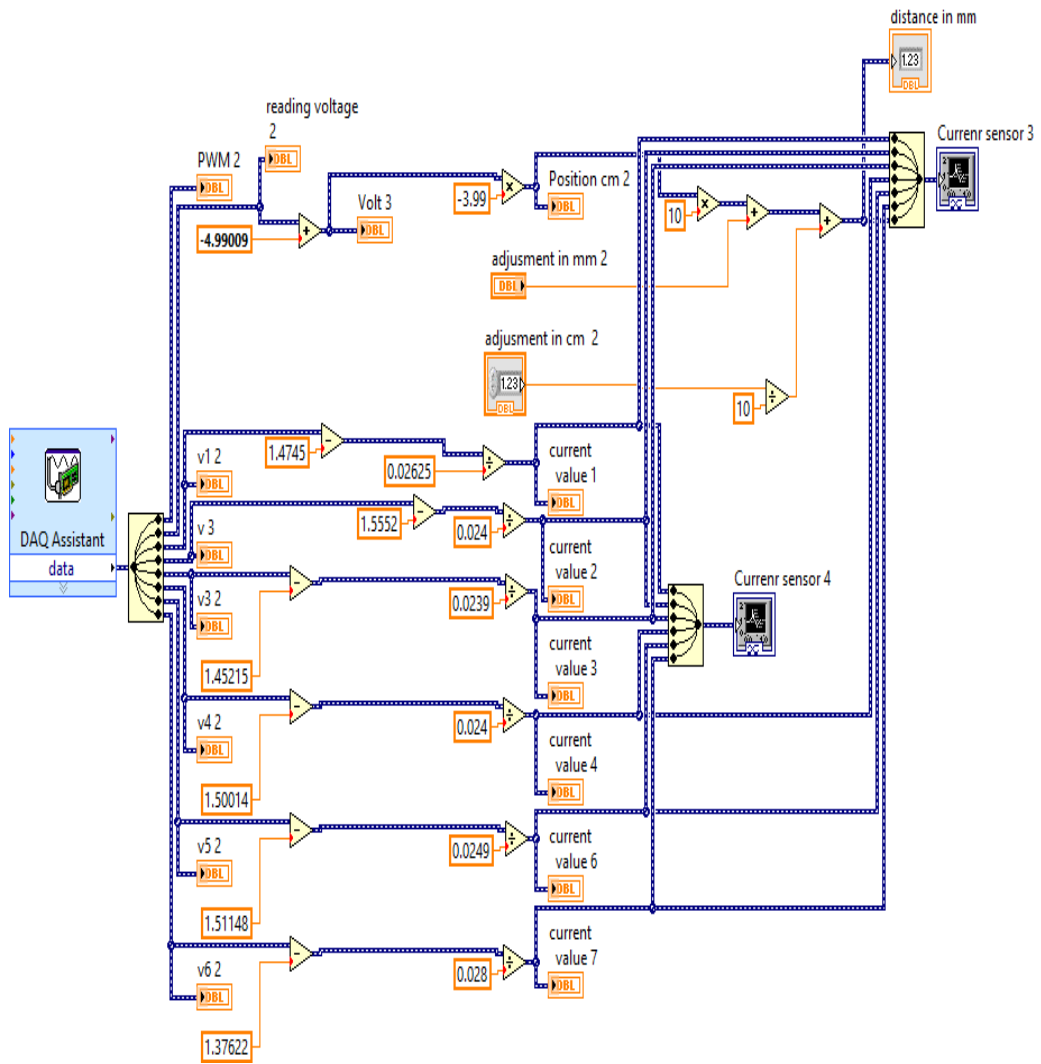
Figure 5.4 Current and distance measurement.
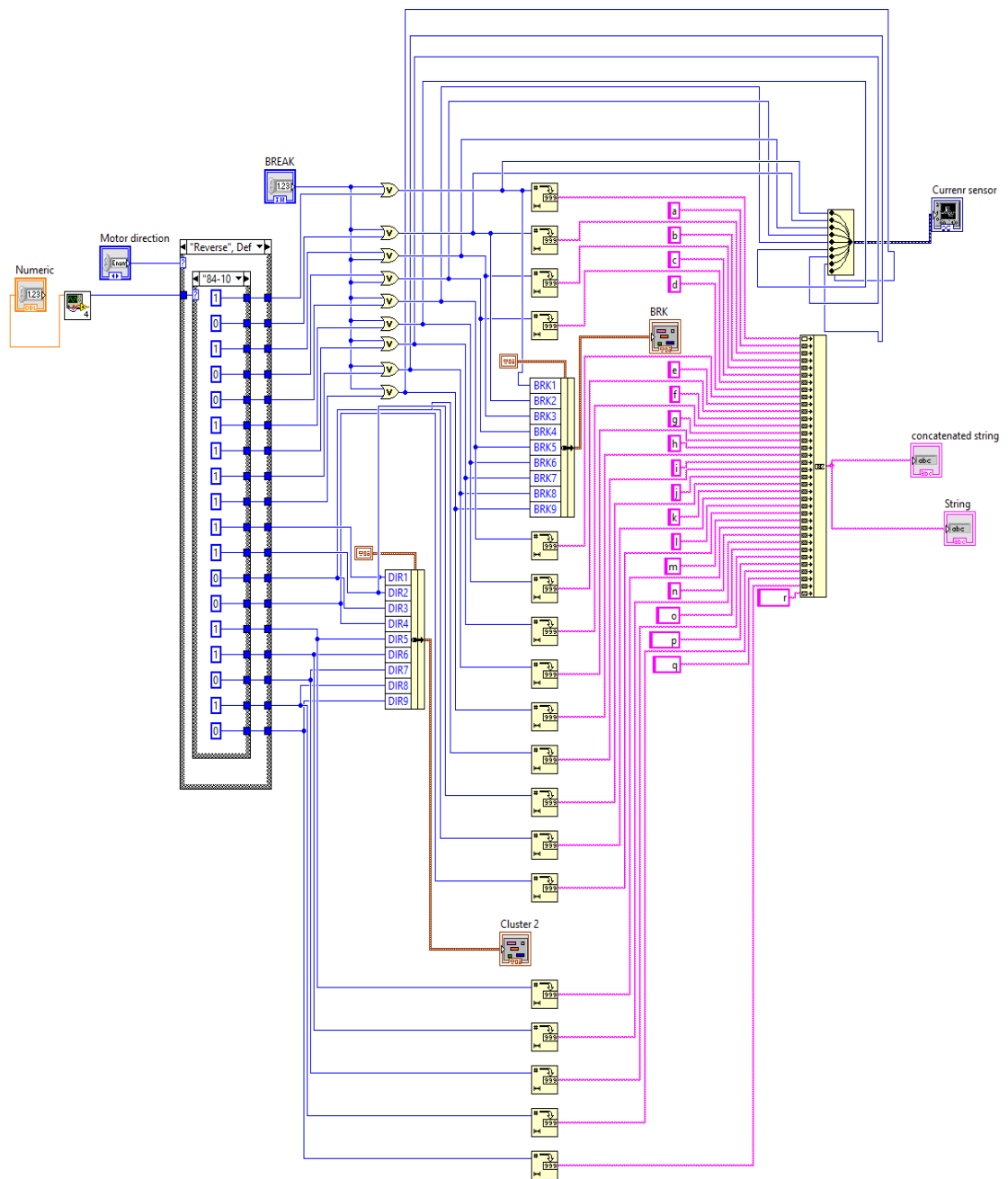
Figure 5.5 Winding commutation.
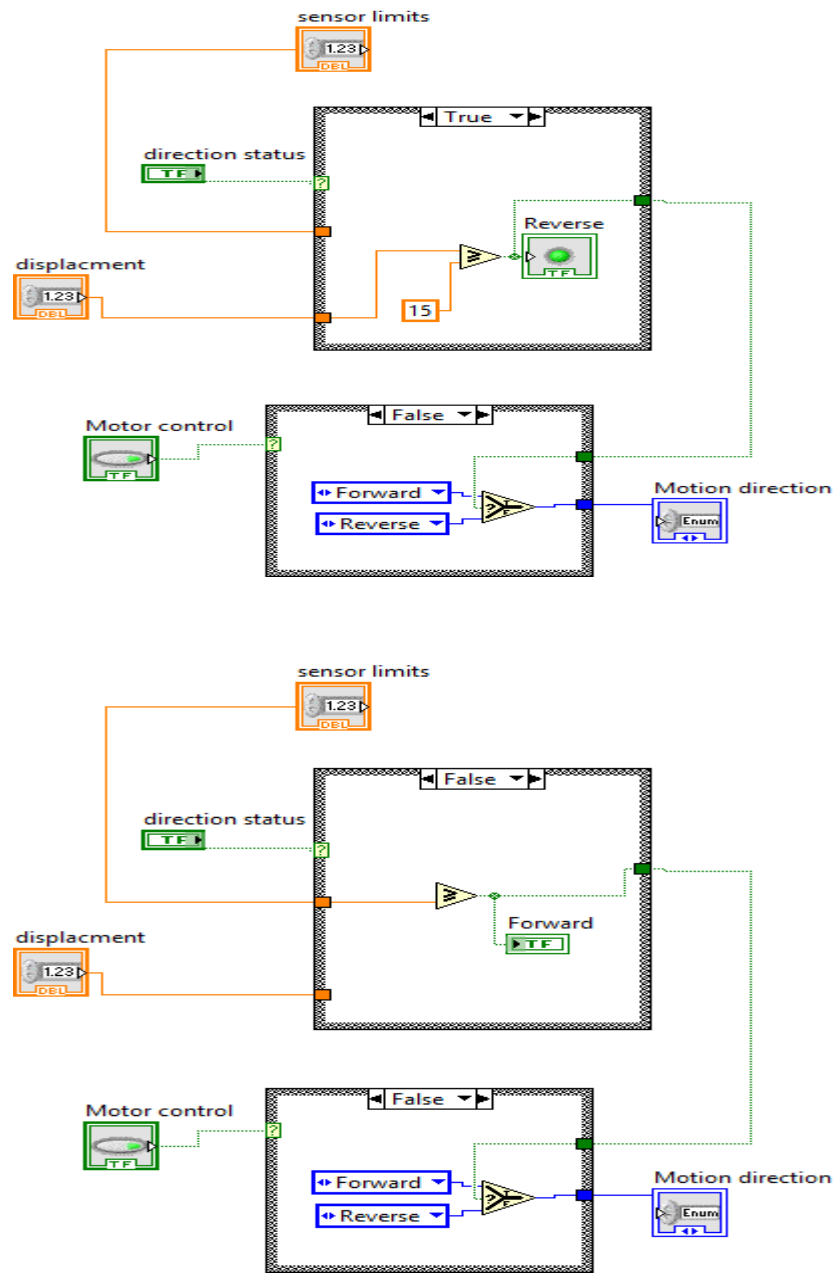
Figure 5.6 Controlling motor motion direction.

5.5.4 Motor speed measurement implementation

Figure 5.7 illustrates motor speed measurement implementation. The velocity of the slider (v) was calculated by numerically differentiating the position signal (x) using the derivative function in "LabVIEW". This procedure was done by subtracting the current position reading from the previous reading and dividing the result by the subtraction of the current time and pervious time. The derivative function in "LabVIEW" is based on:

$$v = \frac{dx}{dt} \qquad (5.1)$$
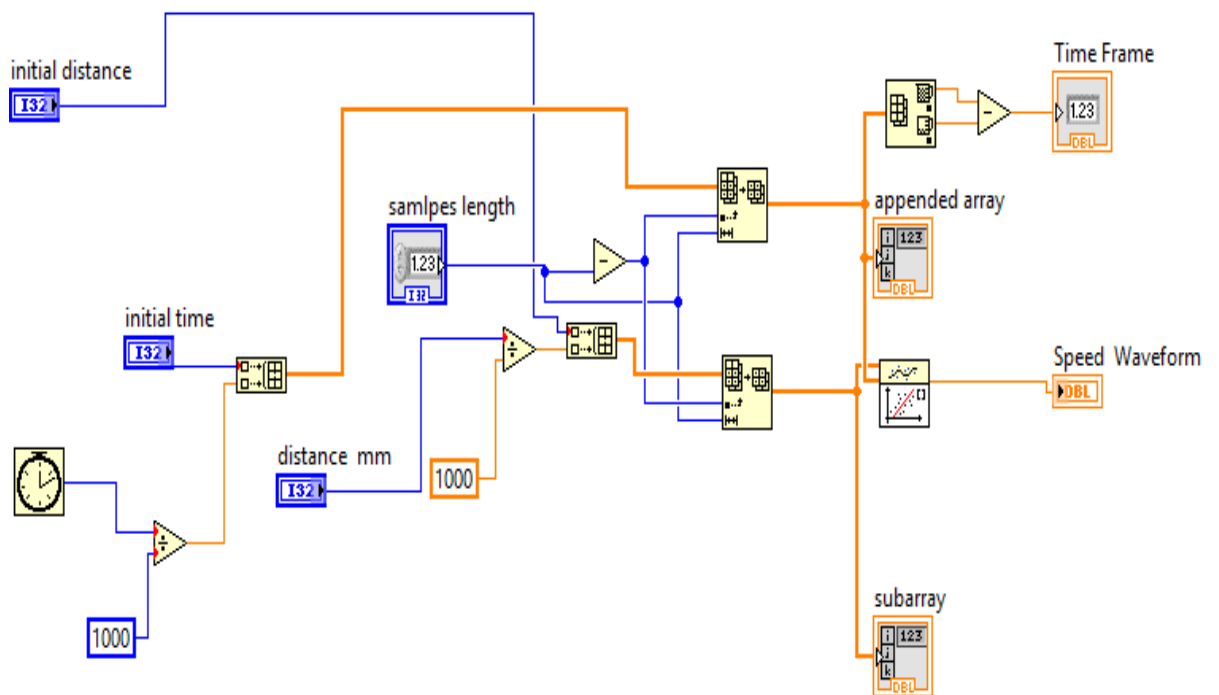
Figure 5.7 Motor speed measurement.

5.6　Experimental Results and Discussions.

In this section, the static and dynamic parameters of the BDCLM are investigated using practical experiments, in order to verify the results obtained via the series of FEM numerical simulations conducted in "COMSOL".

5.6.1　Repeatability test for BDCLM measurements.

The repeatability of the developed BDCLM system was investigated with respect to the measured air-gap flux density, static thrust, armature windings currents, speed and position of the motor. Each of the Measurements were repeated five times in order to confirm the reproducibility of the measurement results, since the success of the motor design is dependent on the satisfactory reproducibility of the results obtained.

The standard error (SE) and percentage error ($\% \ Error$) was calculated using equations 5.2 and 5.3 respectively, where SE is the standard error, S the standard deviation, n the number of iterations and a the average value of the 5 iterations. The maximum percentage error recorded for the air-gap flux density, static thrust, armature windings currents, speed and position measurements were 0.37 %, 0.94 %, 0.5 %, 2.5 % and 2 % respectively.

$$SE = \frac{S}{\sqrt{n}} \qquad\qquad (5.2)$$

$$\% \ Error = \frac{S}{a} \times 100 \qquad (5.3)$$

5.6.2 Measuring the magnetic air-gap flux density

The air-gap flux density of the BDCLM was measured every 10 mm along the length of the mover (213 mm) using a gaussmeter (LakeShore 480), which measured the flux density perpendicular to the probe. The experimental result of the air-gap flux density is shown in figure 5.8. As can be seen from the graph that the measured air-gap flux density is not uniform along the mover length due the flux linkage which agreed with the FEM results.
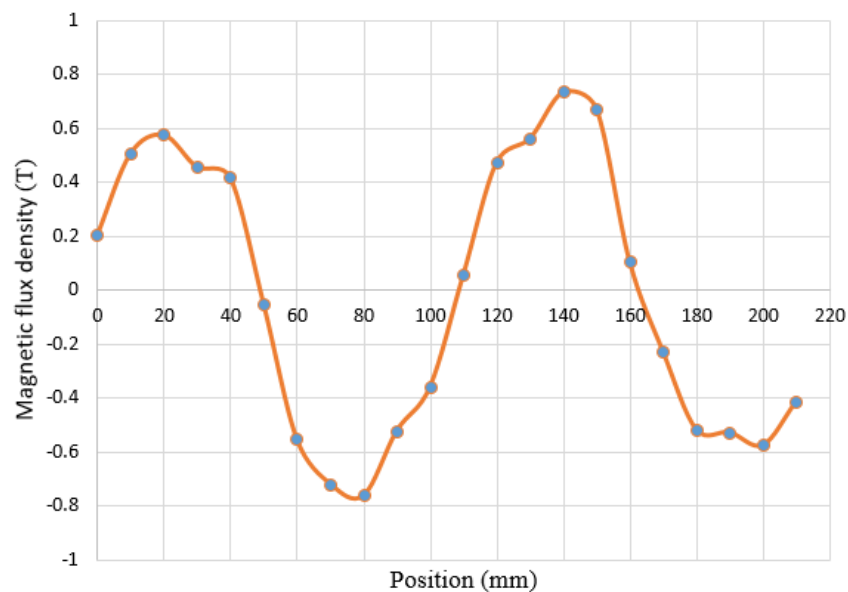
Figure 5.8 Measured air-gap magnetic flux density with different position along the length of the mover.

5.6.3 Measuring the static thrust

In BLDLM machines, the magnetic flux is generated by permanent-magnets and linked with the armature winding to generate a thrust [88]. To fully evaluate the force produced by the motor, the force at each position along the stroke should be measured. In order

to achieve this, a load cell (RS 632-742) was fastened to the moving unit as well as the LVDT sensor. Figure 5.9 shows the set-up for the force measurement. The load cell and LVDT sensor were driven with a current of 2.5A, using a DC power supply (MAP130-1024 30V) from "Fernel".

The output data from the load cell and LVDT position sensor were recorded using a data acquisition (DAQ) card (National Instruments USB-6215) and National Instruments "LabVIEW" software. For all the experiments performed, the DAQ was configured to record 600 samples per milliseconds.
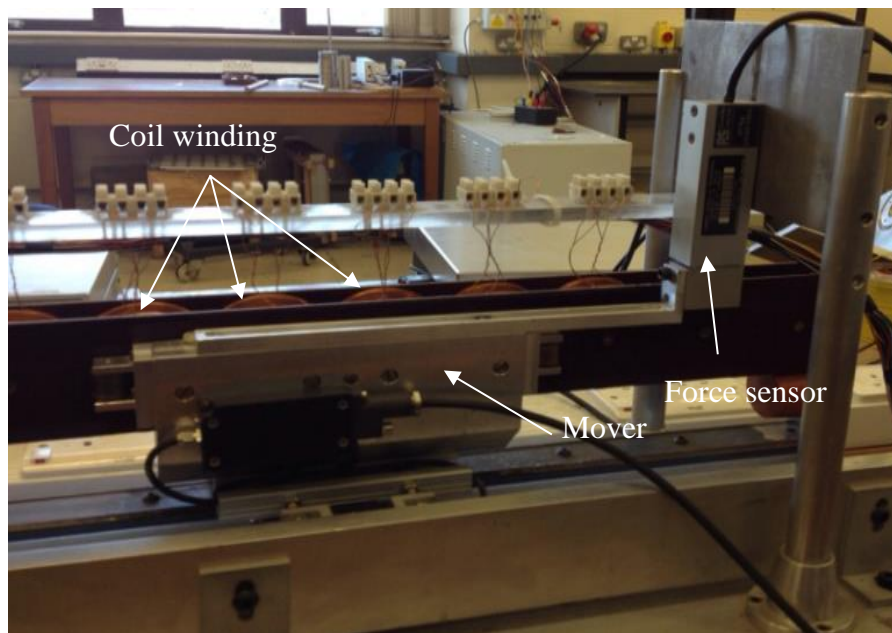
Figure 5.9 Measurement static thrust set-up.

To produce a force, current has to be applied to the motor windings. A DC power supply (E3646A) capable of delivering a 70 V at 30 A was used. A bank of switches was used to assign the current to the motor windings. The current value for each windings was measured using a current sensor and its output was directly recorded by the DAQ. In

order to obtain a smooth movement of the carriage, only three armature winding were energised at a particular time according to the commutation strategy, in order to prevent a reversal force from acting on the moving carriage as a brake, thus decreasing the speed of the mover.

The static thrust was measured using a load cell at different positions of the slider, to verify the algorithm which was designed to provide smooth movement as well as to obtain a maximum thrust. Figure 5.10 shows the measured motor static thrust at 2.5 A armature current with different displacements.

Table 5.1 shows the values of the thrust force at 2.5 A armature current with different displacements (143 mm in length). It also shows which coils should be energised in order to provide smooth motor movement.
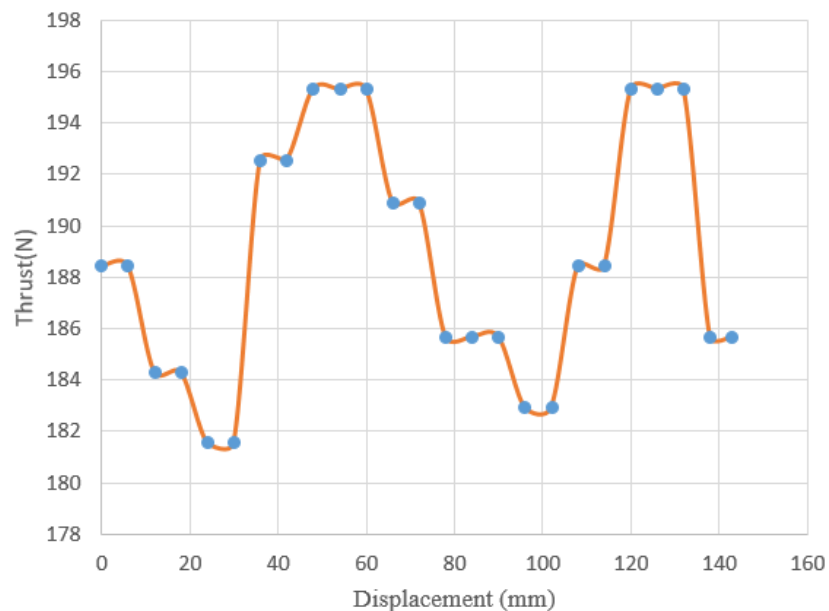
Figure 5.10 Measured thrust force at different displacement.

Table 5.1 The measured thrust with different displacement at armature current 2.5A.

Position	W1	W2	W3	W4	W5	W6	Load cell voltage(mV)	Force (N)
0 -5		-	+	-			15.7	188.4
6 -11		-	+	-			15	187.5
12 -17	-		+	-			14.72	184.25
18 -23	-		+	-			14.78	184.8
24 -29	-		+	-			14.52	181.5
30 -35	-	+		-			14.67	183.4
36 -41	-	+		-			15.4	192.5
42 -47	-	+	-				15.45	193.2
48 -53	-	+	-				15.62	195.25
54 -59		+	-	+			15.57	194.6
60 -65		+	-	+			15.5	193.4
66 -71		+	-	+			15.27	190.85
72 -77			-	+	-		15	187.5
78 -83			-	+	-		14.85	185.63
84 -89		-		+	-		14.74	184.3
90 -95		-		+	-		14.7	183.7
96 -101		-		+	-		14.63	182.87
102-107		-	+		-		14.78	184.75
108-113		-	+		-		15.1	188.37
114-119		-	+	-			15.3	191.46
120 -125		-	+	-			15.62	195.25
126-131			+	-	+		15.54	194.31
132-137			+	-	+		15.33	191.6
138-143			+	-	+		14.85	185.63

5.6.4 Measurement of the armature windings current

The current in the excitation windings are shown in figure 5.11. As can be seen, the current windings are a function of the mover position and only three windings were excited at a time to produce a smooth movement and a maximum thrust. The average of the current for each active armature winding is about 2.5 A.
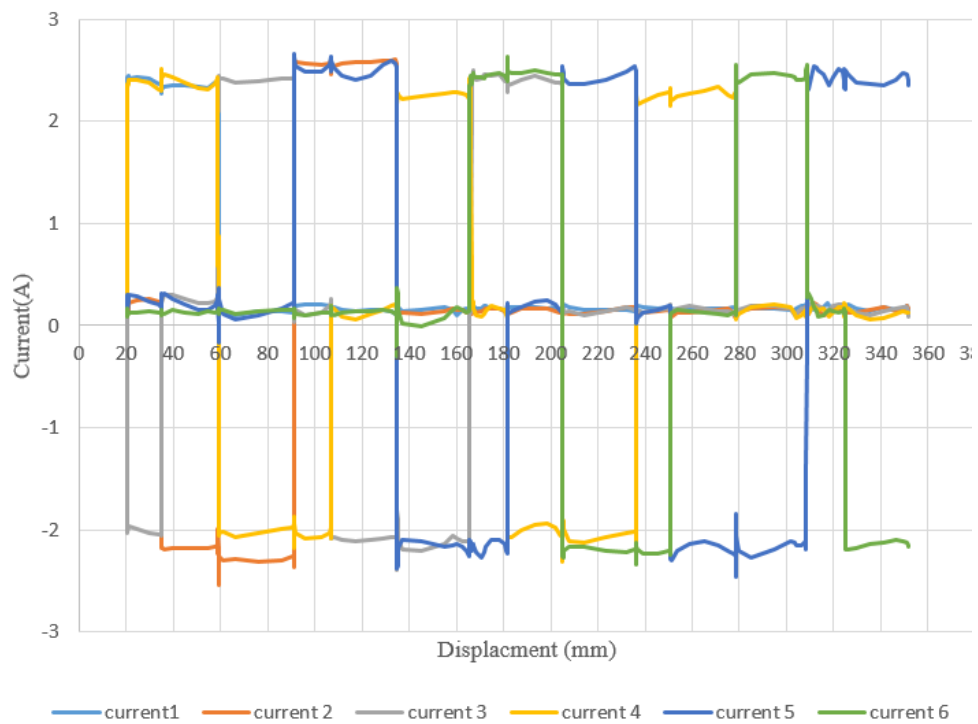
Figure 5.11 Measured windings current.

5.6.5 Measurement of the open loop speed response of BDCLM

Figure 5.12 shows the open loop dynamic response of the BDCLM. The graph obtained from the motor carriage moves forward for a period of 1.6 secs with a current winding of 2.5 A. The motor movement wasn't totally smooth and reached its maximum speed of 0.24 m/sec at 1 sec. The non-uniform of the motor movement occurs due to a small misalignment in double sided the BDCLM and the motor core slots.
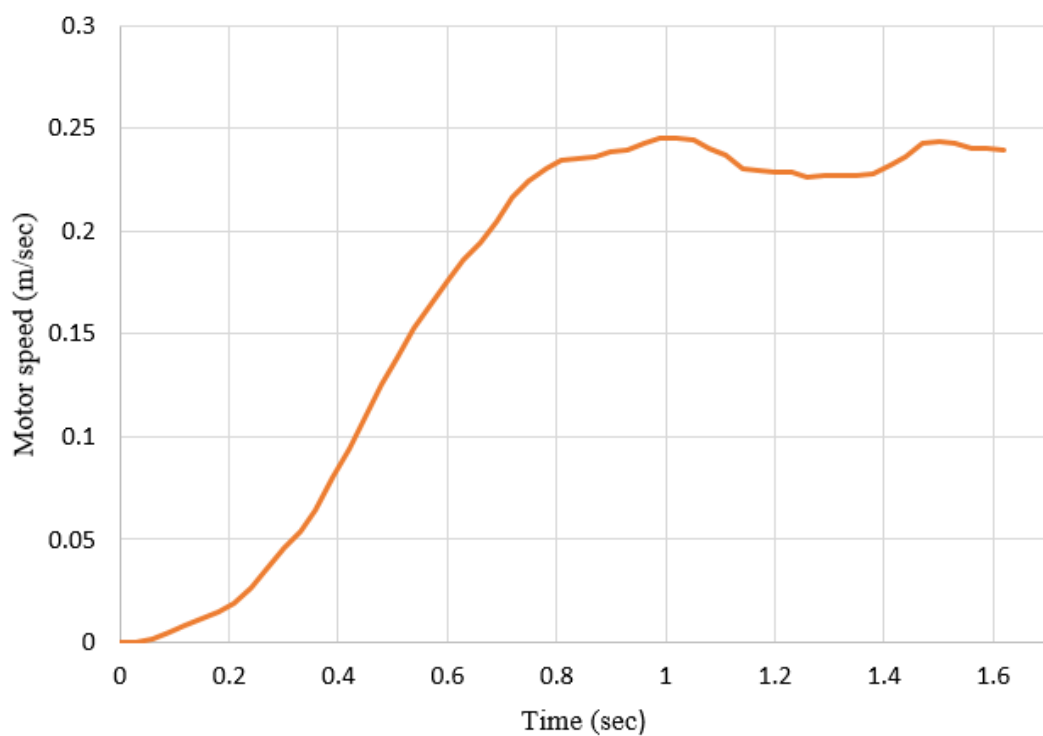
Figure 5.12 Open loop dynamic response of the linear motor.

5.6.6 Measurement of the BDCLM position

Although the total length of the motor is 1.8 m, only 350 mm of the motor can be used, because of the limitation to the length of the LVTD rod and to avoid the slider from hitting the end of the linear motor which would damage the slider. Figure 5.13 shows the motor displacement. The slider starts moving forward from 15 mm position, which is the position where the thrust is maximum until reaching 340 mm and then it automatically moves backward until it reaches a distance of 15mm as programed.
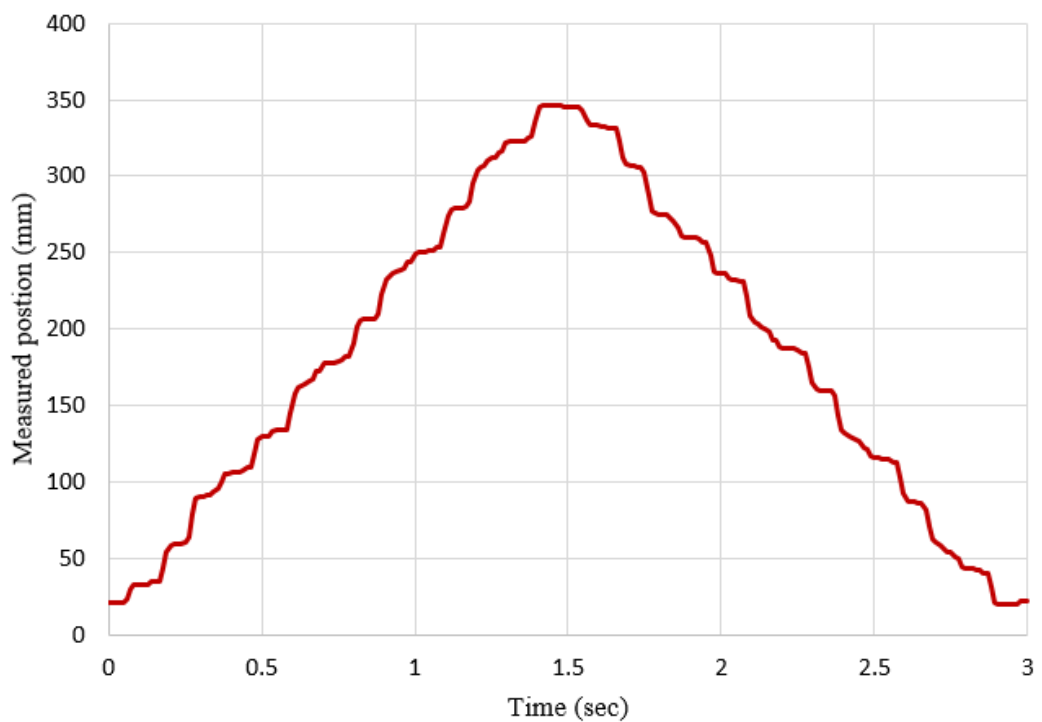
Figure 5.13 Motor displacement.

5.7 Comparison between computed and experimental results

In order to verify the motor design and improve the stability and dynamic performances of the BDCLM, it is necessary to ensure an accurate analysis of the magnetic air-gap flux density and developed thrust. In this section, the characteristics of the thrust and the magnetic air-gap flux density under various excitation currents is compared. The compared results were obtained via FEM simulation and practical experimental measurements.

5.7.1 Comparison between measured and computed magnetic air-gap flux density of the BDCLM.

In this section, the magnetic air-gap flux density of the BDCLM under various exciting currents acquired via FEM simulation and practical experimental measurements was compared. The air-gap flux density of the motor was measured using a digital gauss-meter. Figure 5.14 and Figure 5.15 shows the measured and computed magnetic air-gap flux density of the BDCLM at different armature current values (0 A, 2.5 A, 5 A, 7.5 A, 10 A). As can be seen from the graph, the magnetic air-gap flux density increases with increasing armature current. The non-uniform of the measured and the computed air-gap flux density occurs due to the leakage flux caused by the two adjacent permanent magnets and existence teeth in the armature core.

5.7.2 Comparison between measured and computed thrust of the BDCLM

In this section, the developed static thrust of the BDCLM under various excitation currents acquired via FEM simulation and practical experimental measurements is compared. The developed static thrust of the motor was measured along the length of travel with the use of a load cell attached to the slider. The force characteristic obtained

is the same for both the simulation and experiment investigations. The excitation current values were varied from 2.5 A to 15 A in steps of 2.5 A.
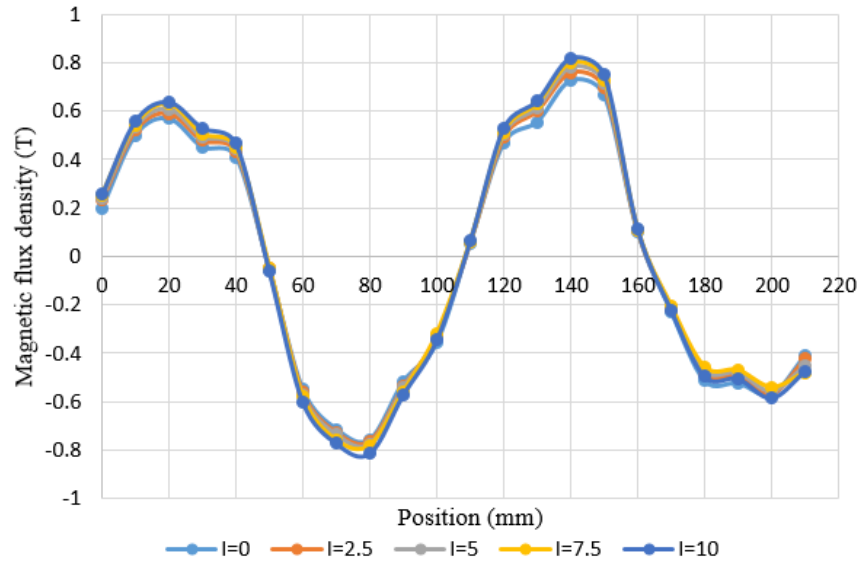
Figure 5.14 Measured magnetic air-gap flux density of the BDCLM.
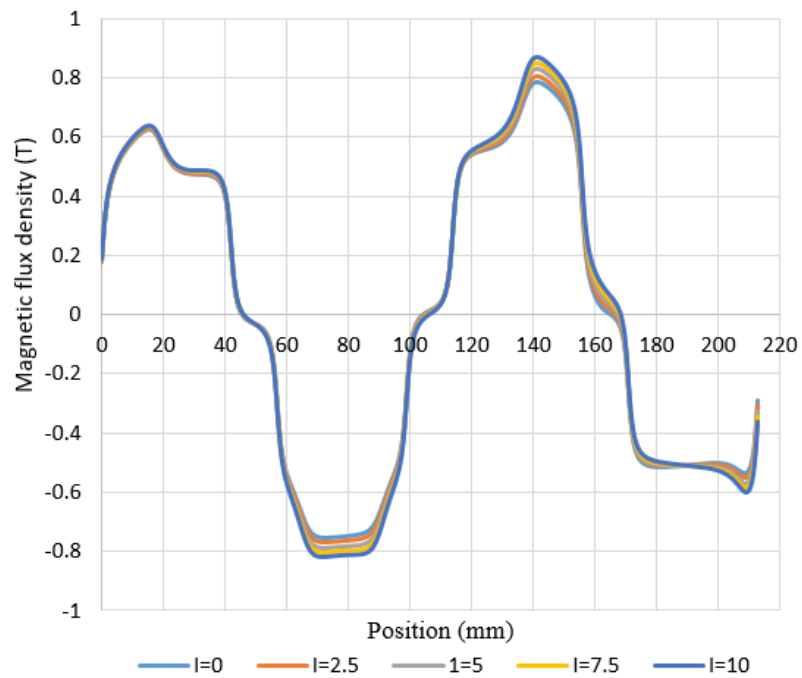
Figure 5.15 Computed magnetic air-gap flux density of the BDCLM.

Figure 5.8 shows the comparison between the experimental and computed static thrust as the armature current is varied. There is a percentage error between the slopes of the simulated and measured values of the static thrust. This is due to the leakage field, frictional force and the normal force produced by the unbalanced force of attraction between the poles and armature core on either side of the motor.

The results indicate that the measured and computed result are in good agreement and that the static thrust is proportional to the exciting current. Based on the results obtained, the maximum deviation between the computed and measured data is 8.9 %. Hence, one can conclude that there is a reasonable agreement between the computed and measured results. The values of the thrust force on the slider are shown in Table 5.2.
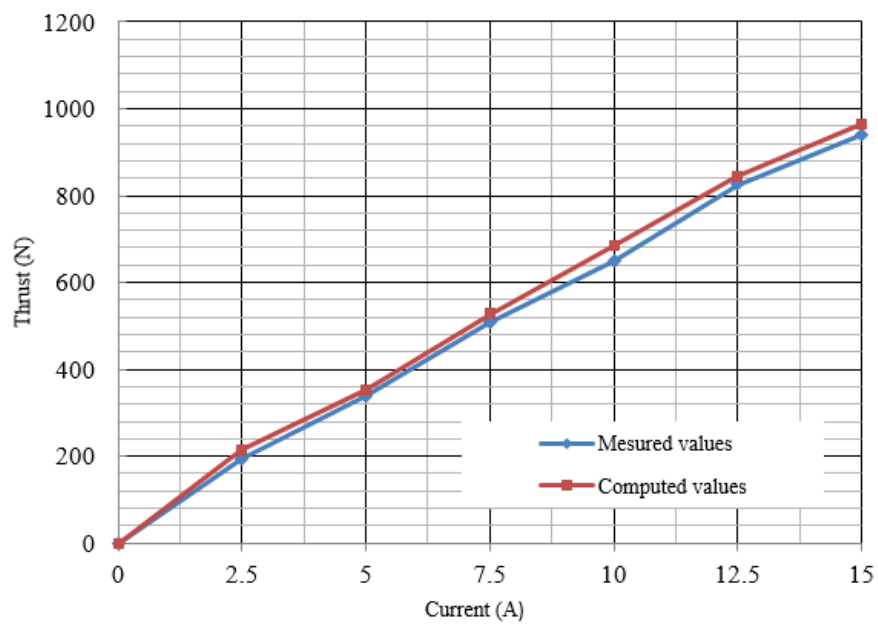
Figure 5.16 Measured and computed static thrust.

Table 5.2 Measured and computed thrust

Current (A)	Measured thrust (N)	Computed thrust (N)	Deviation %
2.5	195	214	8.9
5	340	353	3.6
7.5	510	528	3.4
10	650	686	5.2
12.5	825	844	5.3
15	940	963	2.4

5.8   Conclusion

A low-cost motor control system based on a DAQ system and "Arduino" microcontroller was used to control the motor movement. The DAQ card (USB6211) was used to measure both the current and position signals, which were converted to a digital format for processing, analysis, and storage in a computer. A H-Bridge driver circuit was used to drive the DC linear motor and to control its direction.

A commutation is achieved by energising the sections of the armature winding in a sequence, with the aid of a microcontroller (Arduino Mega). The static thrust was measured using a load cell at different positions of the slider, in order to verify the commutation algorithm, which was designed to provide a smooth movement and a maximum thrust. The velocity of the slider was calculated by numerically differentiating the position signal.

The magnetic air-gap flux density and the static thrust of the BDCLM under various exciting currents (0A, 2.5A, 5A, 7.5A, 10A) acquired via FEM simulation and practical experimental measurements. Based on the results obtained, the maximum deviation between the computed and measured data is 8.9 %. Hence, there is a reasonable agreement between the computed and measured results.

The open loop dynamic response of the BLDCM linear motor were measured in term of motor speed and position. The results showed the mover moves forward for a period of 1.6 sec with a current winding of 2.5 A, the mover reached its maximum speed at 0.24 m/sec.

Chapter 6 : Speed and position control of BDCLM

In this chapter, the modelled BDCLM system and its controller are presented. To predict the dynamic performance of the motor under certain conditions, a model was created using MATLAB/SIMULINK software. The developed model was used to generate a dynamic modelling in which the dynamic performance of the motor could be used to investigate any of the design parameters. Also, this section discusses the speed and position control of the BDCLM using a Proportional-Integral-Derivative (PID) algorithm implemented in an "Arduino" microcontroller. The PID algorithm attempts to reduce the error between the measured (speed and position) and the desired (speed and position) by calculating the error, then it outputs a pulse width modulated voltage that can adjust the speed and position accordingly.

6.1   Mathematical modelling of BDCLM with N-winding.

The mathematical equation for the BDCLM is expressed in Equation (6.1) described [67, 68, 69, and 70]:

$$\begin{pmatrix} E_1 \\ E_1 \\ . \\ . \\ E_N \end{pmatrix} = R \begin{pmatrix} i_1 \\ i_2 \\ . \\ . \\ i_N \end{pmatrix} + (L-M) \begin{pmatrix} \frac{d_{i_1}}{d_t} \\ \frac{d_{i_2}}{d_t} \\ . \\ . \\ \frac{d_{i_N}}{d_t} \end{pmatrix} + \begin{pmatrix} e_1 \\ e_2 \\ . \\ . \\ e_N \end{pmatrix} \tag{6.1}$$

Where N is the number of armature windings, $E_1, E_2, \dots, E_N$ the voltages for the stator windings, R the resistance of the stator winding, $i_1, i_2, \dots, i_N$ the currents for the stator

windings, L the self-inductance, M the mutual inductance between the windings, and $e_1, e_2, \ldots e_K$ the induced back EMF. The instantaneous current of the stator winding and the back EMF in BDCLM is expressed in equations (6.2) and (6.3) respectively:

$$i_K = \left[\frac{1}{Ls + R}(E_K - e_K)\right] f_K(x) \tag{6.2}$$

$$e_K = K_e . v . f_K(x) \tag{6.3}$$

Where, Ls = L-M, v is the slider mechanical speed, x is the slider position and $f_K(x)$ is the windings switching current algorithm with a maximum magnitude of ± 1 and was modelled as a normalized function of the slider position. The mathematical expression of the current function $f_k(x)$ is addressed in appendix E.

The force developed in each phase is the product of the motor constant (K_t) and the current (i) as shown in equation 2.31. For a motor with an N number of windings, the sum of the developed force (T) produced by each winding is expressed as;

$$T = T_1 + T_2 + \ldots + T_N \tag{6.4}$$

The assumption made is that all the windings are perfectly symmetrical, then; $K_t = K_{t1} = K_{t2} \ldots K_{tN}$ and the motor current (i) at any particular position (x), is expressed as; $i_{motor} = i_1 = i_2 \ldots i_N$. Therefore, the total force (T_e) developed is expresses in equation (6.5).

$$T_e = K_t \{f_1(x) \, i_1 + f_2(x) \, i_2 + \ldots + f_N(x) i_N\} \tag{6.5}$$

$$T_e = \sum_{k=1}^{N}[K_k i_K f_K(x)] \tag{6.6}$$

6.2 Modelling DC linear motor with 9-windings.

To predict the performance of the motor under certain conditions, a model was created using MATLAB/SIMULINK based on the mathematical equations as described in section 6.1. The modelled BDCLM with 9-windings is shown in figure 6.1 and 6.2.
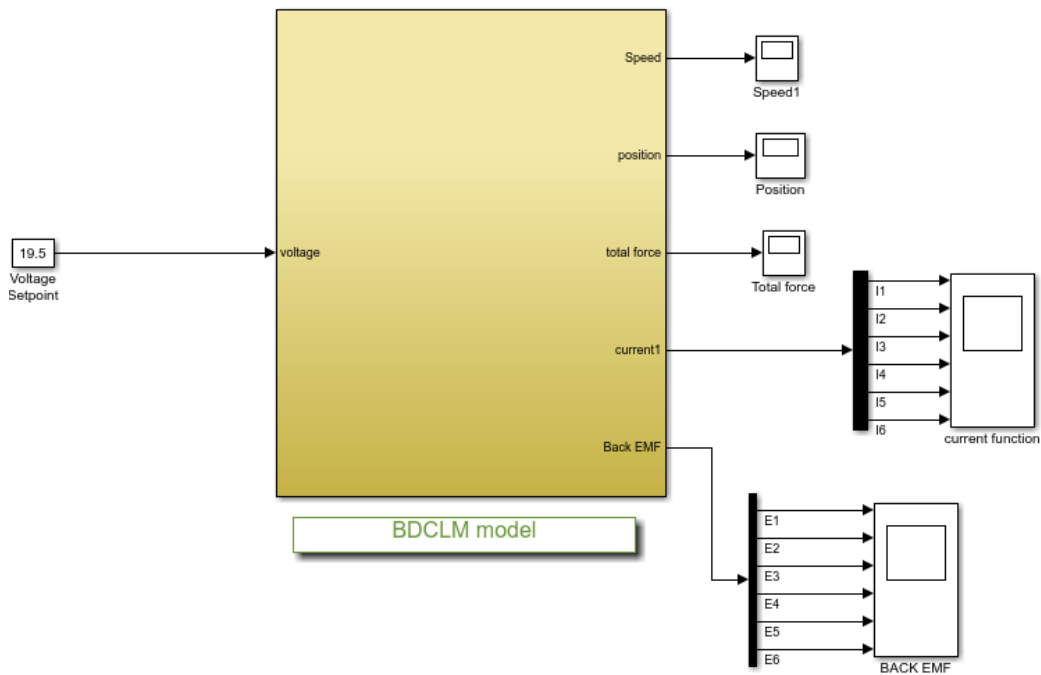
Figure 6.1. MATLAB/SIMULINK block diagram of the BDCLM.
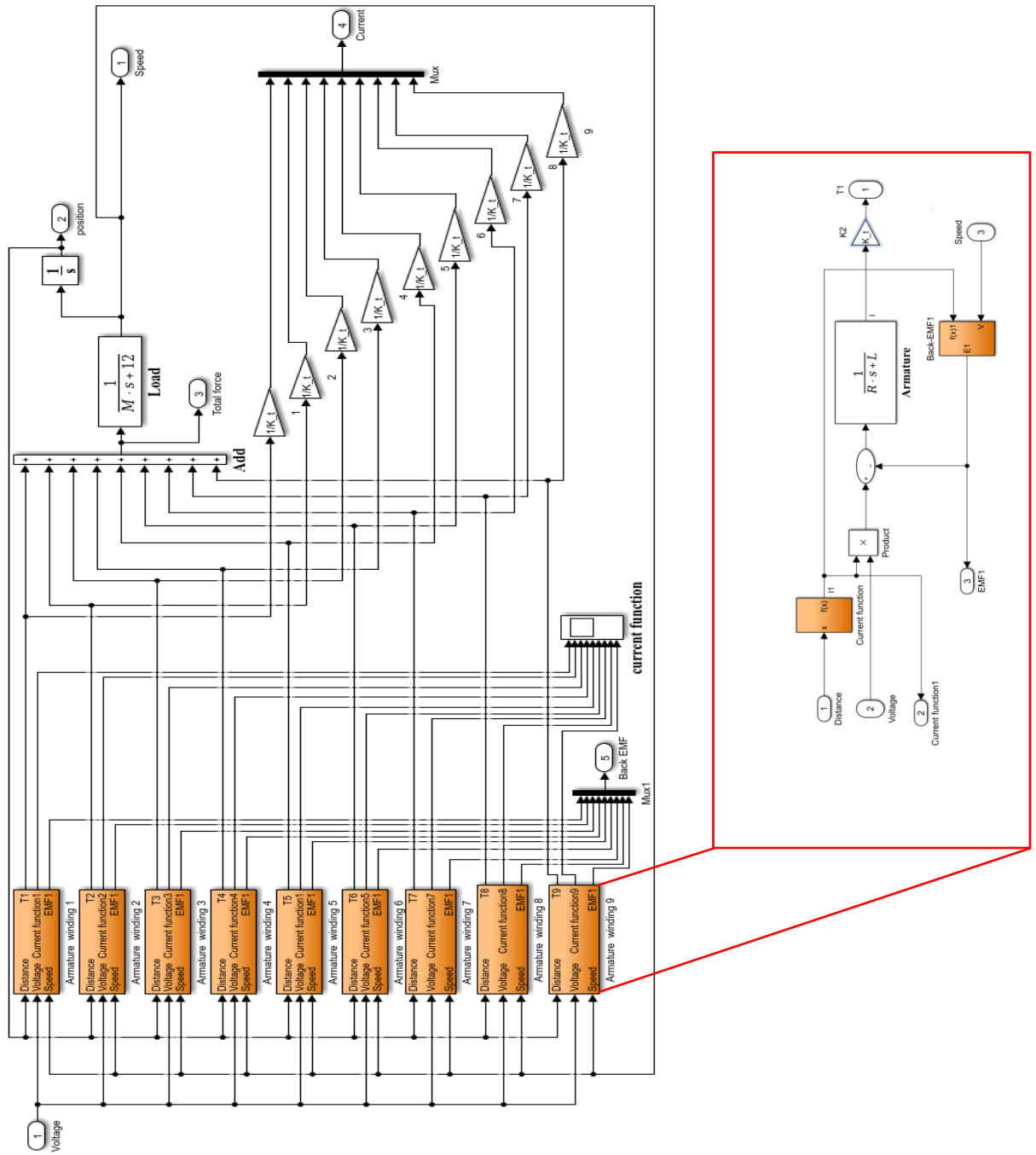
Figure 6.2 MATLAB/SIMULINK of the of the 9-windings BDCLM block diagram.

The modelling of the back EMF was performed with the assumption that all the windings have identical back EMF waveforms. Based on the slider position, the numerical expression for the back EMF can be obtained. Therefore, with the speed command and slider position, the symmetric N-phase back EMF waveforms can be generated at every operating speed. The waveforms of the function $f_K(x)$ for the 9 windings were modelled as a normalized function of the mover position as shown in figure 6.3.
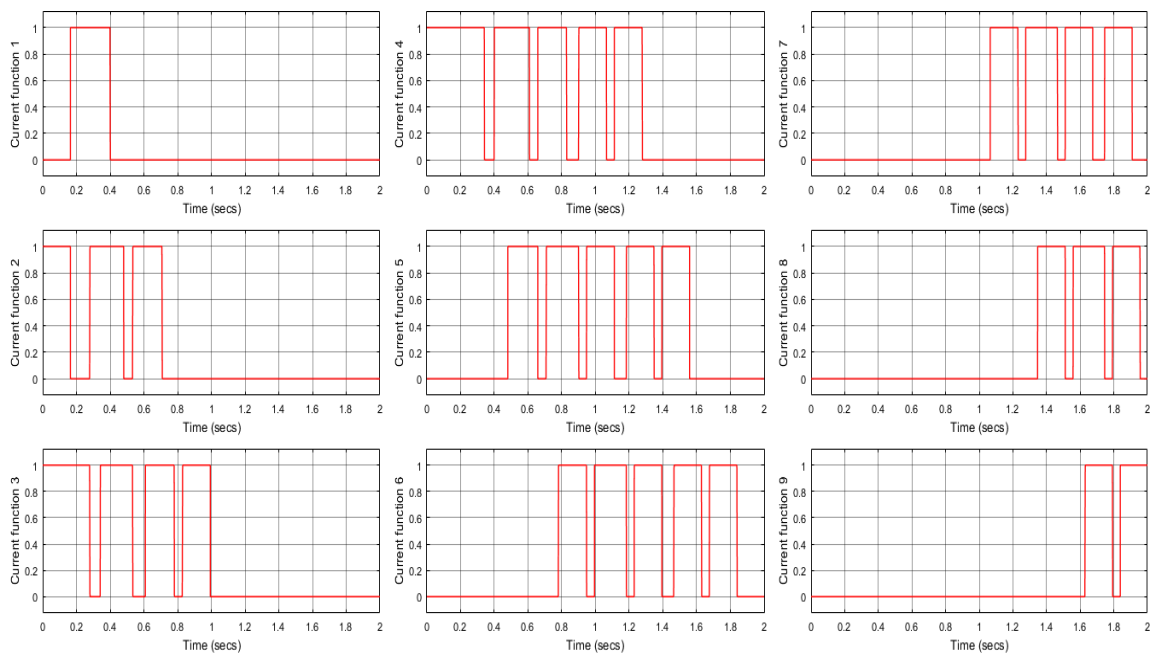
Figure 6.3 The waveform of the function $f_K(x)$ of 9 windings.

The physical parameters of the BDCLM which were listed in table 4.2, were set before running the simulation and these parameters include; M= 6.4 kg, b = 12 N, K = 72, R = 6.1 Ω, L = 7.8 mH and t = 1.5 s. The results in terms of the motor speed, thrust, motor position, back EMF and current winding are shown in figures 6.4, 6.5, 6.6, 6.7and 6.8 respectively. The back EMF signal was determined using equation 6.3. The result shows

that the motor needs about 1 s to reach its steady-state speed of 0.25 m/sec and requires about 1.5 s to reach its maximum position of 0.357 m.
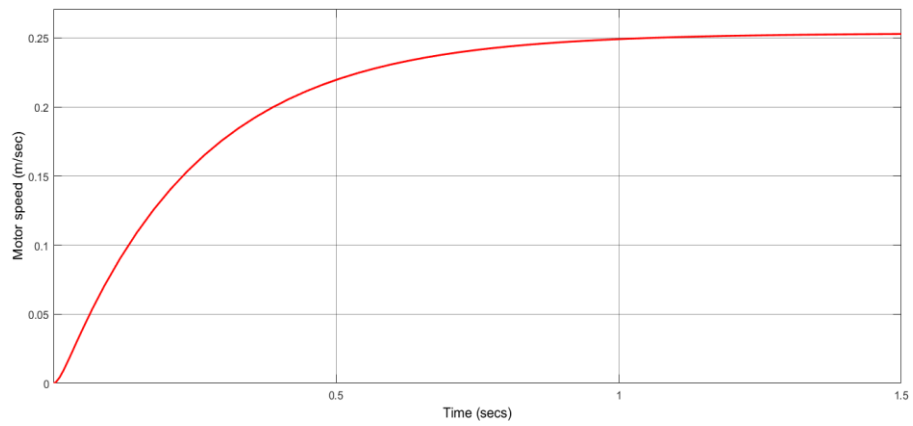
Figure 6.4. Speed response of the 9-winding BDCLM.
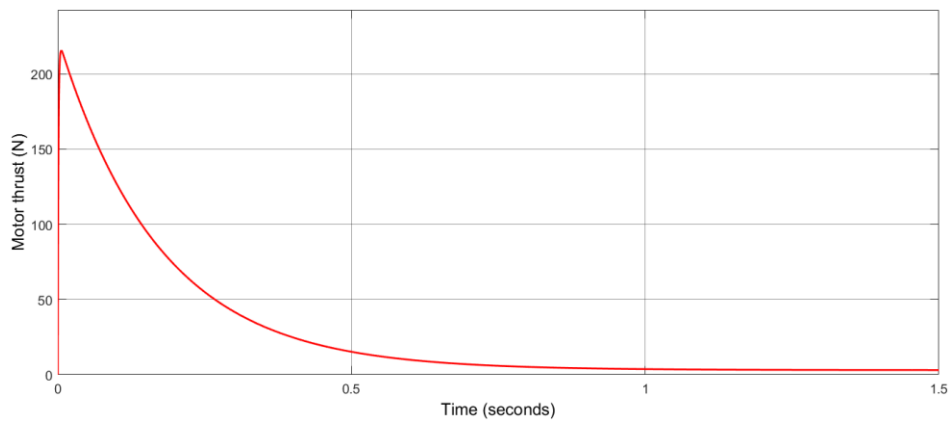
Figure 6.5. The developed force response of the 9-winding BDCLM.
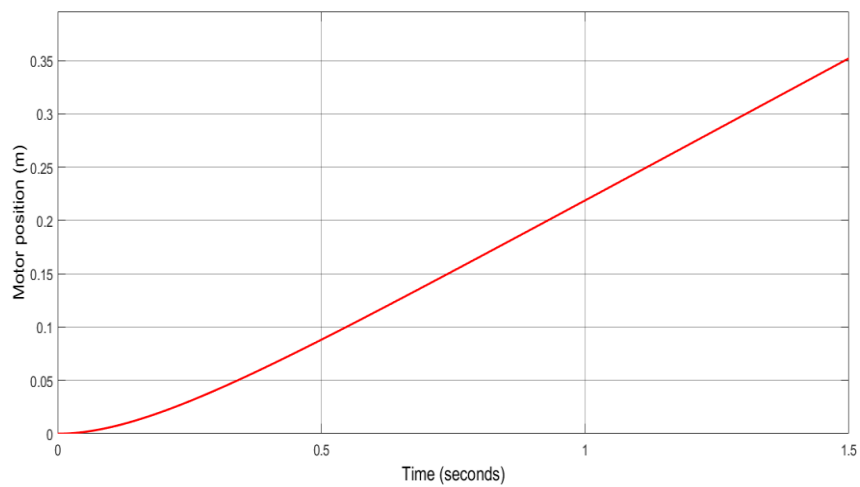
Figure 6.6. Position response of the 9-winding BDCLM.
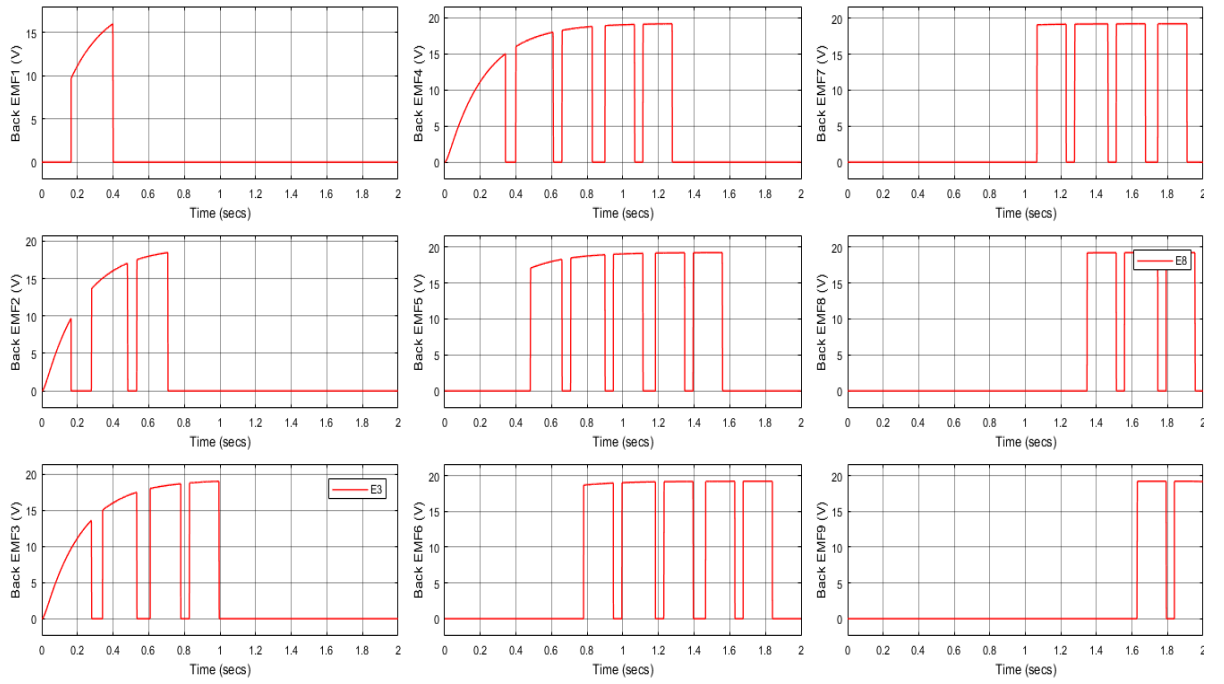
Figure 6.7. Back EMF waveforms of the 9-winding BDCLM.
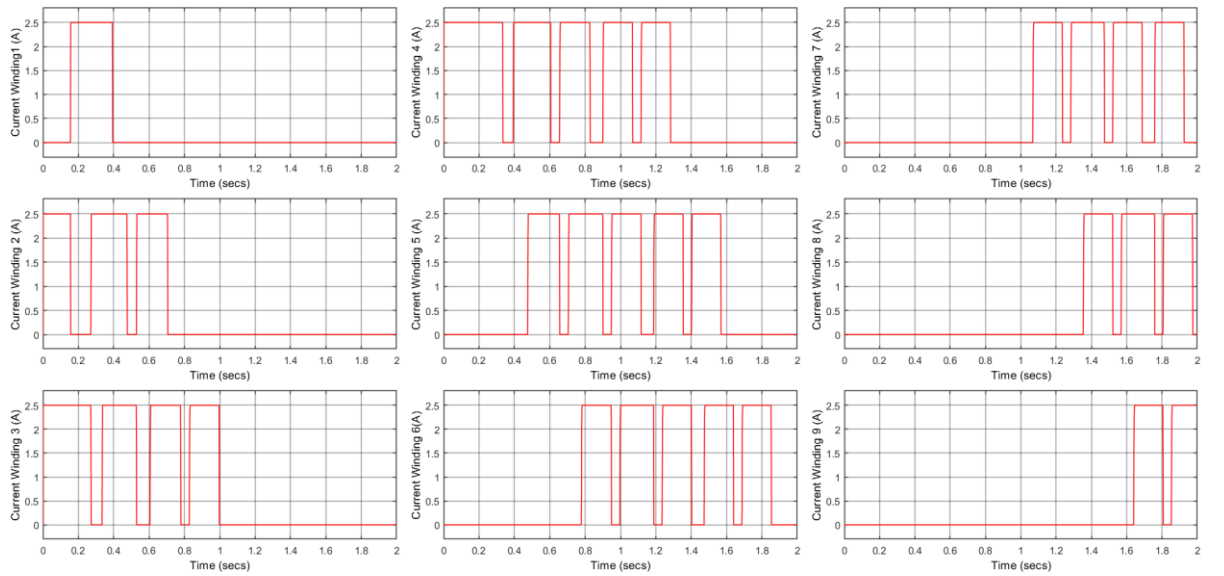
Figure 6.8 Current response of the 9-winding BDCLM.

154

6.3 Using PID controller to control the motor speed and position

Although the speed of the BDCLM is proportional to the applied voltage using the PWM technique in the open loop, the speed obtained may vary with applied load disturbance. A closed-loop speed/position control system can be used to maintain the steady speed, hence, achieving a better speed regulation and a faster response.

The main goal of the control system is to compensate the force oscillations and disturbances in the segmented long stator BDCLM in order to achieve a smooth motion and precise position. The BDCLM system is designed to operate in two modes (i.e. closed loop speed control and closed-loop position control), so as to maintain the motor speed and to stop at a user specified position. The combination of these two modes enables the system to travel fast towards the targeted position and terminate at a precise specified position.

This section discusses the speed and position control of the BDCLM using the Proportional-Integral-Derivative (PID) algorithm implemented on "Arduino" microcontroller. PID attempts to correct the error between the measured (speed, position) and the desired (speed, position) by calculating the error and then outputting a pulse width modulated voltage that can adjust the (speed, position) accordingly.

6.3.1 PID controller

A proportional-Integral-Derivative controller (PID) is a generic controller widely used in industrial systems due to its simplicity, robustness, reliability and easy tuning parameters. The PID control equation involves three different parameters; the proportional K_p, the integral K_i and derivative K_d terms. The corresponding PID control law in continuous form can be expressed as:

$$u(t) = K_p e(t) + K_i \int_0^t e(t)dt + K_d \frac{de(t)}{dt} \qquad\qquad (6.6)$$

The variable $e(t)$ represents the tracking error. The input variable of the PID controller

is the velocity error calculated as the difference between the reference velocity and the

actual velocity. The controller computes both the derivative and the integral of the error

signal. The control signal $u(t)$ is sent to the motor, then the new output is produced.

The new output is sent back and subtracted from the set point signal to obtain a new

error signal $e(t)$.The controller takes the new error signal and computes its derivative

and integral again, this process is repeated in order to eliminate the error signal $e(t)$[71].

The PID controller algorithm is still remaining even the signal error $e(t)$ is zero. The

typical structure of PID control is shown in Figure 6.9. Table 6.1 demonstrates effect of

the PID controller parameters on the rise time, settling time, maximum overshoot, and

steady- state error. The mathematical expression of the rise time, settling time and

overshot are expressed in table 6.3.
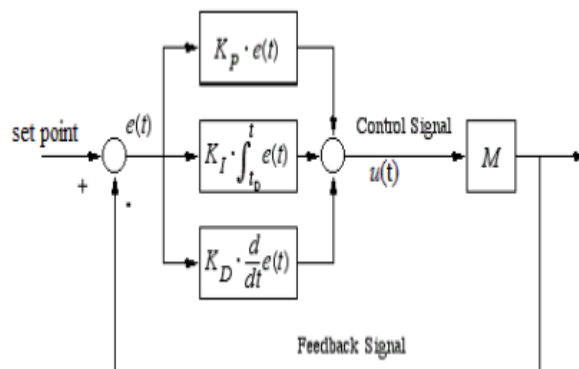
Figure 6.9. Block diagram of PID control system [71].

To design a PID controller the steps below must be followed which are [72]:

- Obtain open loop response from the mathematical model of BDCLM and determine what needs to be improved.

- Add a proportional constant K_p to improve the rise time.

- Add a derivative control K_d to improve the overshoot.

- Add an integral control K_i to eliminate the steady state error.

- Adjust the controller parameters (K_p, K_d, K_i) until the design requirements are met.

Table 6.1 PID controller parameters

Control parameters	Rise time	Settling time	Overshoot	Steady state error
K_p	Decrease	Small change	Increase	Decrease
K_i	Decrease	Increase	Increase	Eliminate
K_d	Small change	Decrease	Decrease	Small change

In general, transfer function of a 2nd order system H(s) can be expressed as

$$G(s) = \frac{K\,\omega_n^2}{S^2 + 2\xi\omega_n S + \omega_n^2} \qquad (6.7)$$

Where ω and ξ are the natural frequency and the damping ratio respectively. The response for such a system and transient response parameters are shown in Figure 6.10. These parameters can be expressed as a function of ω_n and ζ and summarised in the table 6.2.
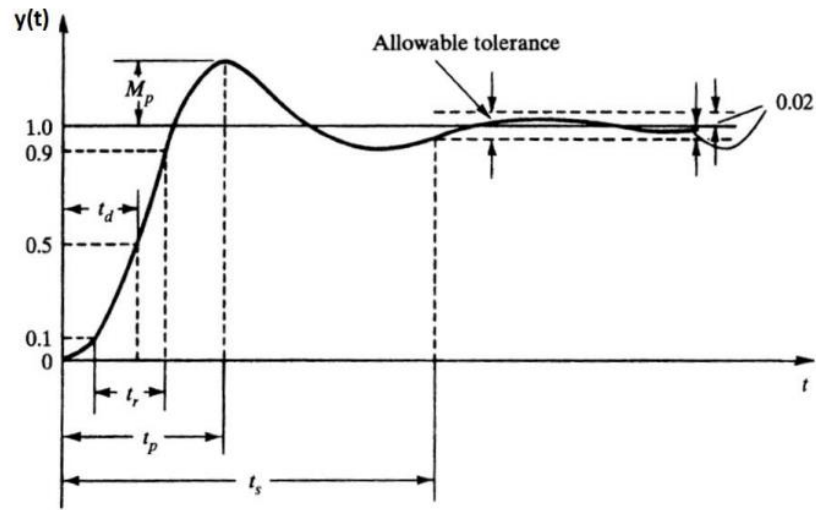
Figure 6.10 Transient characteristics of atypical 2nd order motor response [72].

Table 6.2 Transient system parameters [72].

Parameter	Symbol (unit)	Formula
Rise Time	$t_r(s)$	$\frac{\pi - \beta}{\omega_d}$, where $\beta = tan^{-1}\left(\frac{\sqrt{1 - \zeta^2}}{\zeta}\right)$ $\omega_d = \omega\sqrt{1 - \zeta^2}$
Maximum Overshoot	$M_p(\%)$	$e^{\frac{-\zeta\pi}{\sqrt{1 - \zeta^2}}} \times 100$
Delay Time	$t_d(s)$	$\frac{1 + 0.7\zeta}{\omega_n}$
Settling Time	$t_s(s)$	$\frac{4}{\zeta\omega_n}$ (2 % setting time) $\frac{3}{\zeta\omega_n}$ (5 % settling time)
Peak Time	$t_p(s)$	$\frac{\pi}{\omega_d}$
Steady State Error	e_{ss}	$[\lim_{t \to \infty} y(t)] - y_{des}^{ss}$

6.3.2   PID Controller Tuning

There are different types of PID controller tuning methods. The three most common

methods used are; the Ziegler and Nichols method (ZN), the Chien-Hrones-Reswick

method (CHR) and the Cohen-Coon method (CC). However, the MATLAB software has a built-in PID controller-tuning tool, which is much easier to use for tuning the PID controller parameters and choose the optimum values.

6.3.3 PID speed controller

The PID controller was added to the model in order to control the speed of the motor. Figure 6.11 shows the speed control of BDCLM with PID controller which it's parameters (K_p , K_d , K_i) are tuned using the tuning tool function in "MATLAB/SIMULINK" to obtain the desired speed response. Figure 6.12 illustrates the tuned response of PID controller and table 6.4 shows the PID controller parameters.
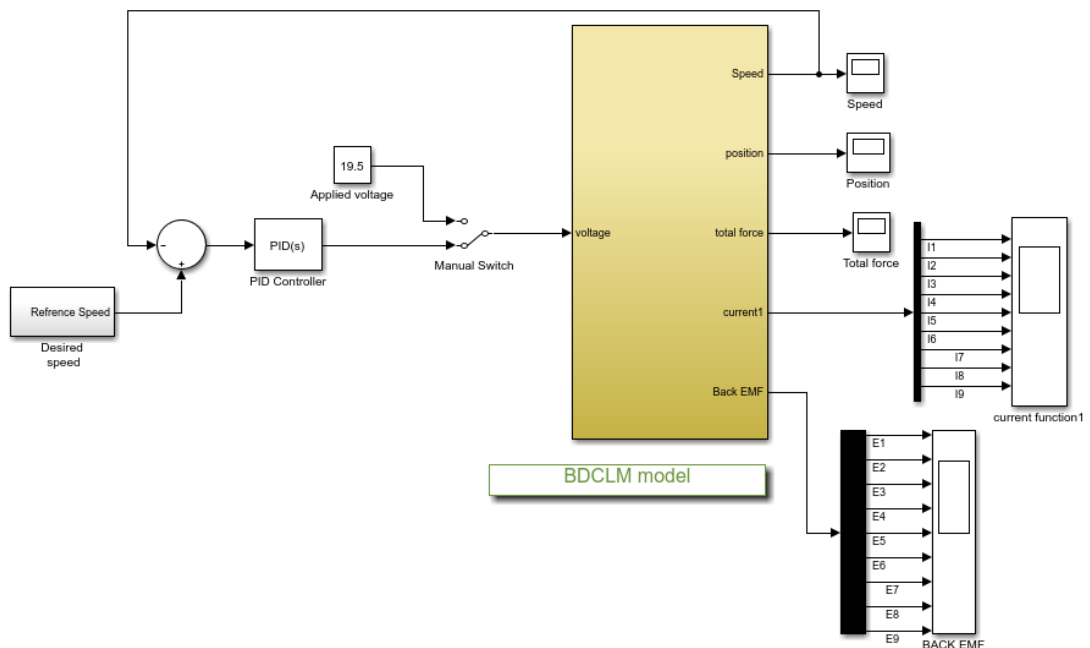
Figure 6.11 PID speed controller of the BDCLM.
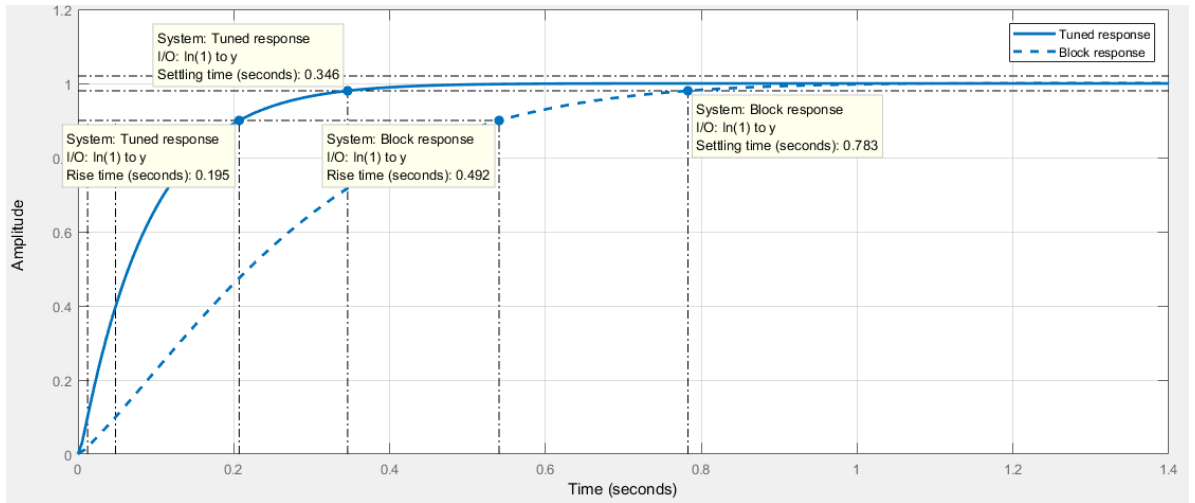
Figure 6.12 Tuned response of PID controller.

Table 6.3 The PID motor speed parameters.

P	37.56
I	65
D	0.0126
Rise time (sec)	0.195
Settling time (sec)	0.346
Overshoot (%)	0.0019

The PID controller attempts to correct the error between the measured speed and the desired speed by calculating the error and then outputting a pulse width modulated voltage that can adjust the speed accordingly.

To demonstrate the system performance, a sudden change is applied to the reference speed. Initially, the reference speed is 0.24 m/sec and then increased to 0.4 m/sec. The speed response illustrated in figure 6.13. The motor almost requires 0.5sec to reach the steady state.
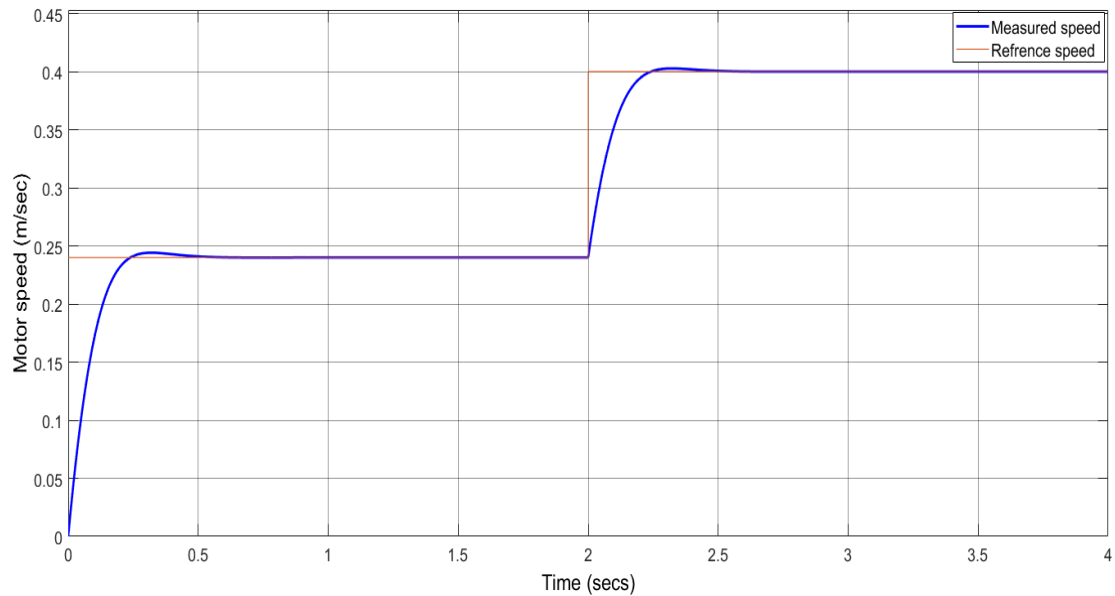
Figure 6.13 Speed response of the motor after using the PID controller.

Figure 6.14 shows the effect of the PID controller with different parameters on the motor speed response.
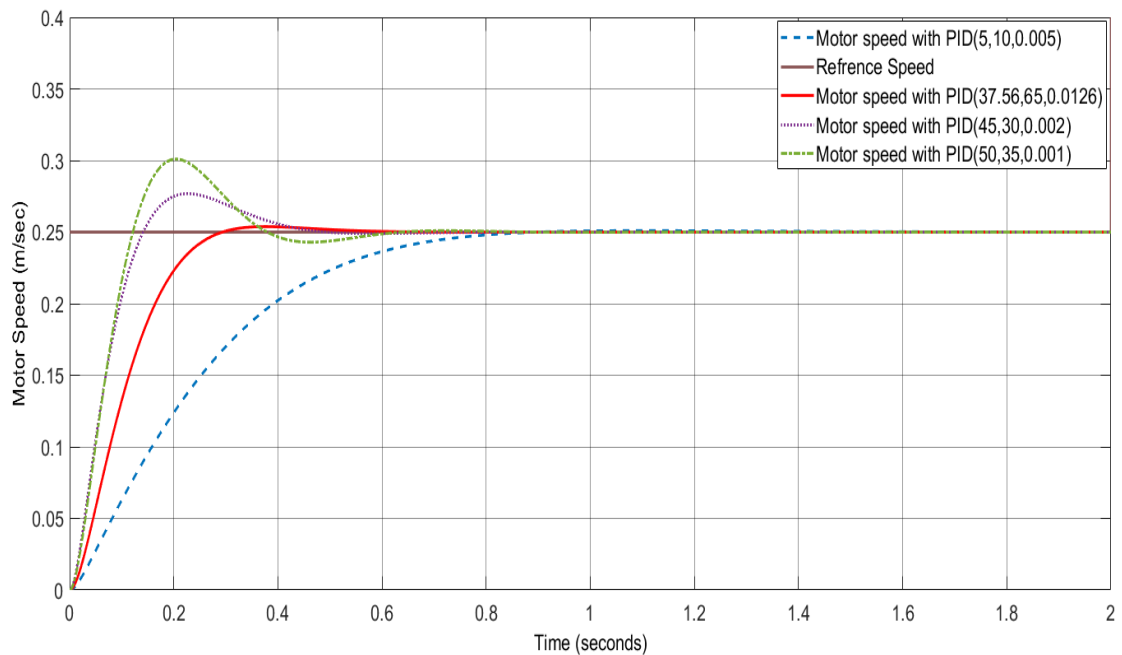
Figure 6.14 Effect of the PID controller parameters on the motor speed response

6.3.4   PID position controller

By taking the output mover position and feeding it back to the input, a closed-loop position control system is achieved. Figure 6.15 shows the position control of BDCLM with PID controller which it's parameters (K_p, K_d, K_i) are tuned using the tuning tools function in "MATLAB" to obtain the desired position.

The PID controller attempts to correct the error between the current position and the desired position by calculating the error and then generating a pulse width modulated voltage which is applied to the motor terminals to make the positional error zero.

The parameters of the PID motor position controller were tuned using the tuning tool function in "MATLAB/SIMULINK" to obtain the desired motor position. The parameters of the PID motor position controller were chosen as shown in table 6.4. The reference position set to be 320 mm, which represent the actual length of the motor displacement. As it can be seen from the graph that the motor needs almost 1.1 secs to reach reference position.

Table 6.4 The PID motor position parameters

K_p	10.8
K_i	17
K_d	0.11
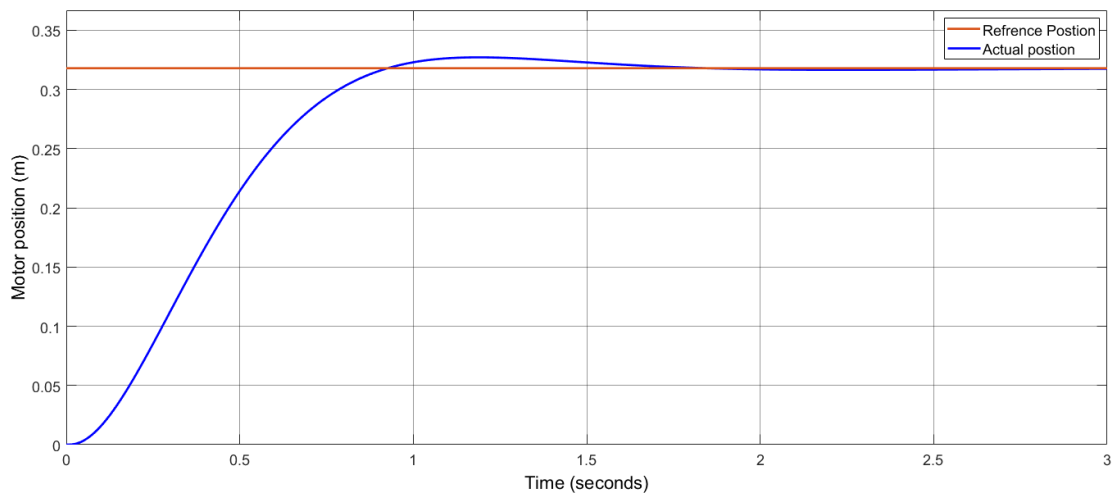
Figure 6.15 Using the PID controller to control the motor position.

6.4   Experimental results of speed and position control

The control system was designed to enable the motor to start moving from any point, in any predetermined direction, over any length along the track. For comparing the accuracy of the real time implementation of the PID controller, it can be compared with the corresponding simulation results. The PID speed and postion control paramerters which is taken from "MATLAB" motor simulation has been implemented in in LabVIEW by using the predefined PID block from the "LabVIEW Control, Design and Simulation Module". The simulation model of PID controller as block diagram in "LabVIEW" is shown in figure 6.16. The PID configuration in Labview consist of of; **Value A** which represents the set point value, **Value B** which represents the process variable, **PID gains** which specifies the normalized PID gain parameters, **PWM High Time** which presents the control action (PWM signal high time) that the PID algorithm calculates, Output range specifies the allowable range of the output [91]. With respect to different reference motor speed, PWM will generate the duty cycle. According to that duty cycle, average voltage value applied to DC motor also varies. Figure 6.17 shows the PWM signal in LabVIEW.
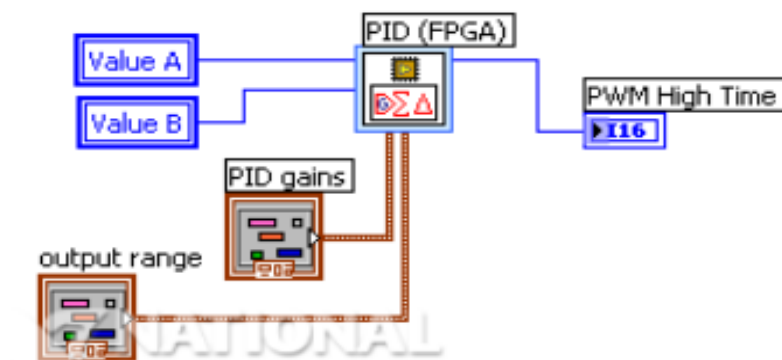
Figure 6.16 the PID configuration in LabVIEW.
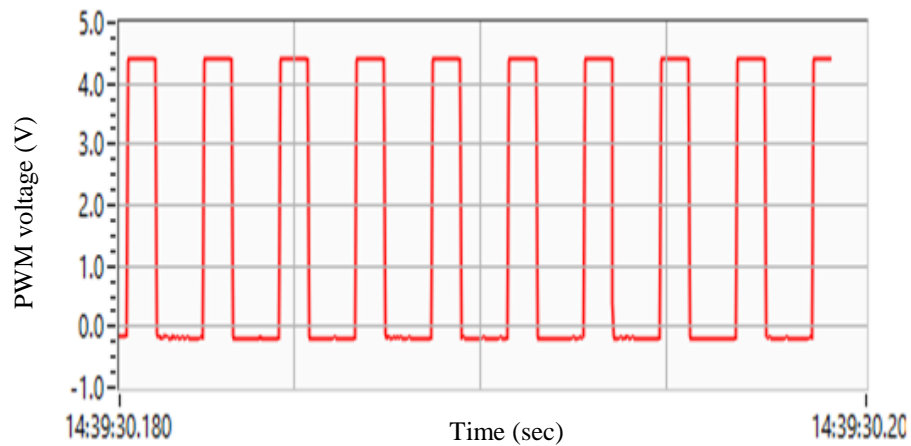
Figure 6.17. PWM signal in LabVIEW.

6.4.1 Repeatability test for BDCLM control measurements.

The repeatability of the developed BDCLM system was investigated with respect to the measured PID controlled speed and position of the motor. Each of the measurements were repeated five times in order to confirm the reproducibility of the measurement results.

The standard error (SE)and percentage error were calculated using equations 5.2 and 5.3 respectively. The maximum percentage error recorded for the speed and position measurement results were 2.5 % and 0.22 % respectively.

6.4.2 Experimental results of PID speed control

The experimental work was executed with 19.5V applied voltege and the curent values for the 9 armeture winding are shown in figure 6.18 . The velocity of the slider, which was calculated by numerically differentiating the position signal is fed to the PID

controller, the controller will compare the measured speed with the reference speed and the output the error will be applied to the PWM driver board to control the speed. The PID parameters from table 6.3 were implemented in LabVIEW and were used as initial values for the PID controller.
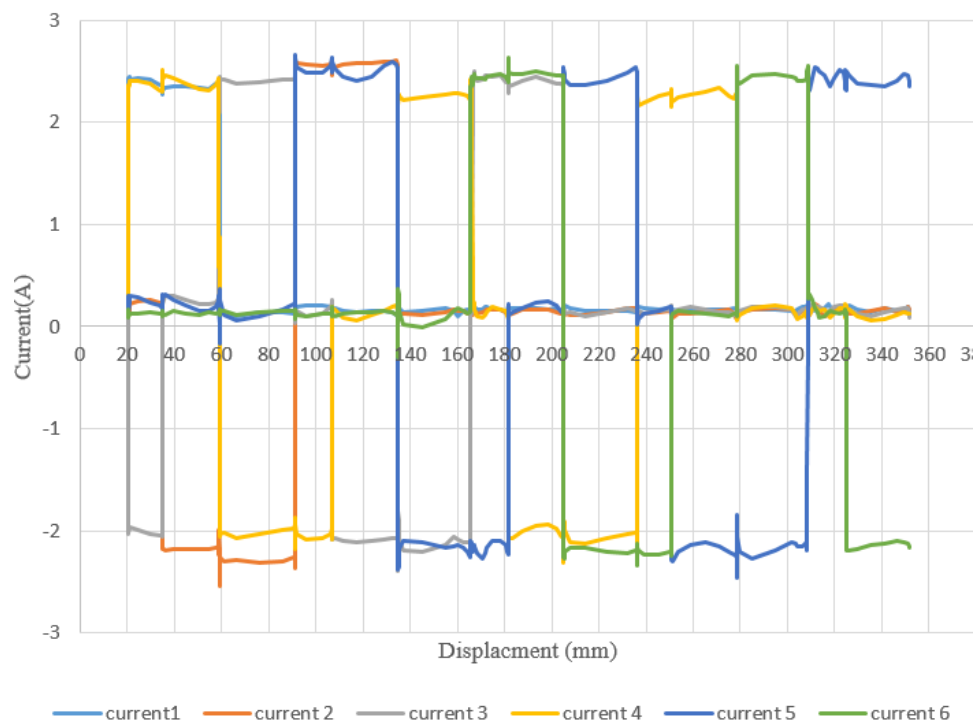
6.18 Measured windings current.

Figure 6.19 shows the PID motor speed control. The motor needs almost 0.7 sec to reach steady state speed of 0.235 secs. The maximum and minimum percentage error between the reference and the measured speed was found to be 1.77% and 1.16% respectively. Figure 6.20 illustrates the PID motor control with different speed (0.11 m/sec, 0.16 m/sec, and 0.24 m/sec). Due to the limitation of the motor driver board which supplies maximum voltage of 20 V to the armature winding, maximum speed of 0.24 m/sec was obtained.
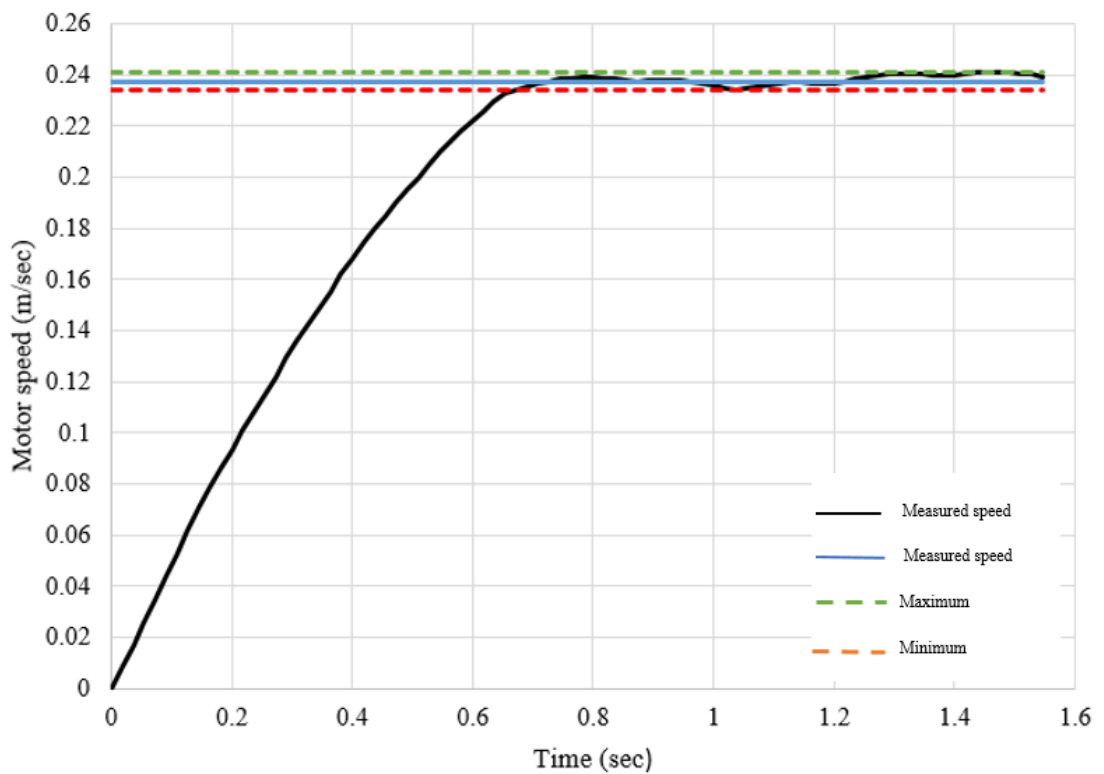
6.19 PID motor speed control.
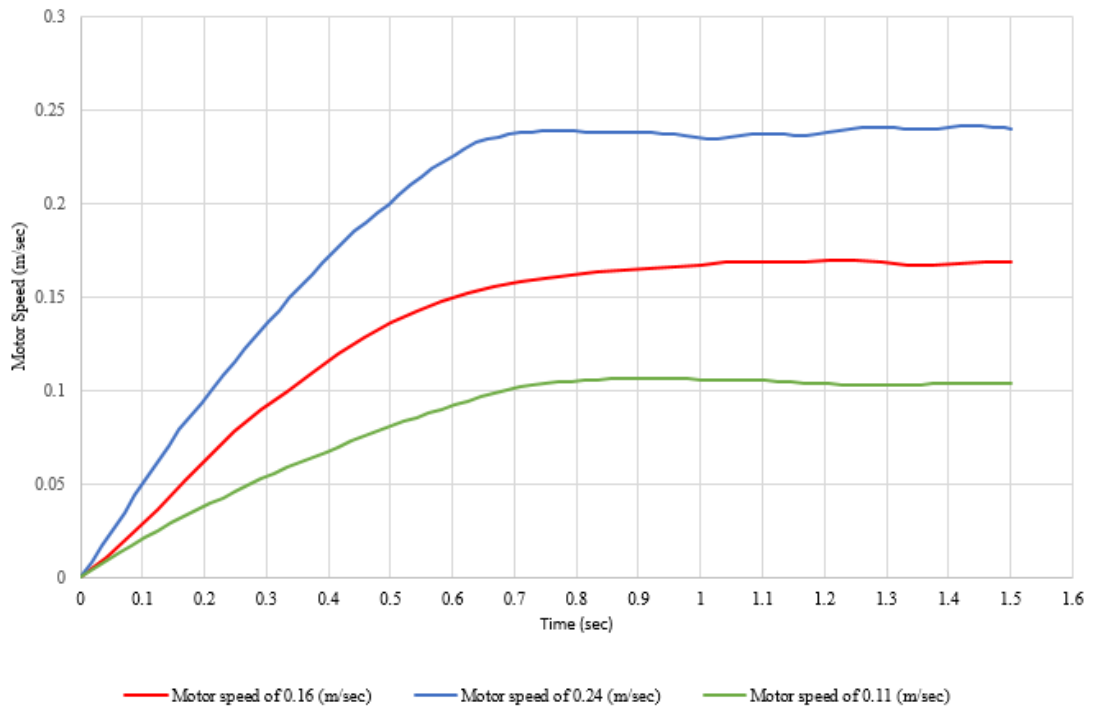
Figure 6.20 PID motor control with different speed (0.11 m/sec, 0.16 m/sec, and 0.24 m/sec)

6.4.3   Experimental results of position control

The aim of the position control is to move the motor from the initial position to the desired point. Therefore, PID position control is implemented in the "LabVIEW" program to control the motor. The PID position control was tested for point–to-point motion requirement. The PID parameters from Table 6.4 were implemented in LabVIEW and were used as initial values for the PID controller.

The reference position is set to be 320 mm, the actual position response of the moving magnets is compared to the reference position and then the tracking error, which is the difference between the actual position and the reference position, is used as input to the controller. A verity of experimental position control tests with different reference position are performed and the average accuracy of the position error is 1mm. Figure

6.20 shows the position control with different reference positions (180 mm ,220 mm 320 mm).
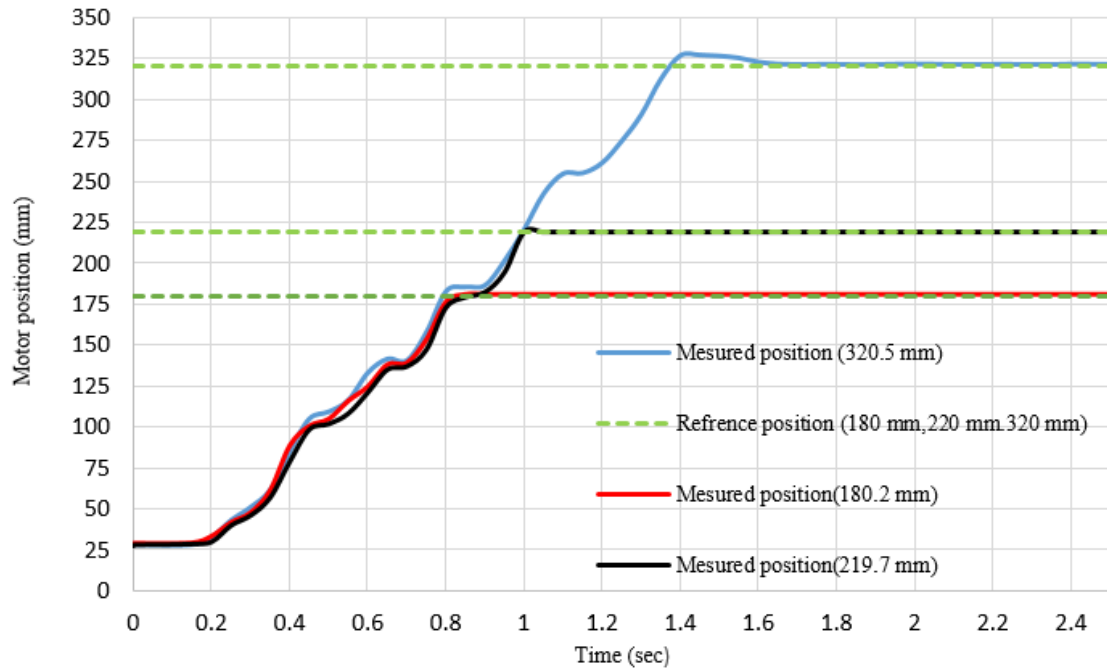
Figure 6.21 Measured motor position control with reference positions (180 mm, 220 mm 320 mm).

6.5   Conclusion

The dynamic behaviour of the motor, using a mathematical model in the form of a set of second-order differential equations that can be solved using numerical techniques is evaluated. A model was created using "MATLAB/SIMULINK" to predict the performance of the motor under certain conditions. An experimental assessment of the motor is presented and compared with the simulated results, to illustrate the effectiveness of the dynamic modelling method. The experimental of the speed and

position control system of the motor are developed using "National Instrument's LabVIEW software", Arduino Mega and Data Acquisition Board.

The parameters of the PID motor speed and position controller was tuned to obtain the optimal values using tuning tool in MATLAB software. The parameters of the PID motor speed and position controller were chosen to be (K_p=37.56, K_i = 65, K_d= 0.0126) and (K_p= 10.8, K_i= 17, K_d= 0.11) respectively.

The experimental was executed within nominal conditions 19.5 V for speed and postion control with refrence speed and postion 0.24 m/sec and 320 mm respectively. The velocity of the slider which was measured to be 0.235 at steady state. The motor needs almost 0.7 sec to reach steady state speed. The maximum and minimum error percentage error between the reference and the measured speed was found to be 1.77% and 1.16% respectively. Verity experimental position control with different reference position are performed and the average accuracy of the position error is 1mm.

The experimental results were within 2 % and 3 % of the modelled results with respect to the motor speed and position. These results demonstrate a good agreement between the two approaches.

Chapter 7   : Thermal Analysis

This chapter discusses the effect of power losses generated in different parts of an electrical machine. During electrical machine operation, certain amount of energy is lost in a form of heat. The heat losses produced in a PM machine are; electrical losses, magnetic losses and mechanical losses. Thermal analysis is an important topic that can affect the electrical machine performance, reliability, lifetime and efficiency. Hence, a range of thermal tests were performed to investigate the temperature distribution within the motor for better understanding of the motor's capability and limitations. The experimental result shows that the temperature level in BDCLM did not exceed the permitted level. Hence, the thermal efficiency of the motor is not affected.

7.1   Introduction

Permanent magnet linear motors (PMLMs) have gained huge attention due to its high thrust, high speed and high acceleration. However, to achieve these merits, PMLMs are usually supplied with high current density, which may generate excessive heat in the windings and could lead to a rapid temperature rise [73]. The problem of temperature rise has attracted more attention, since excessive heat generated in the windings could deteriorate the electromagnetic performance of the motor [74].

 Overheating of permanent magnet (PM) machines can cause degradation of insulation materials, magnet demagnetization and loss of motor efficiency [40]. It could also limit the thrust density output and prevent the machine from reaching its design characteristic [73]. Therefore, it is essential to investigate the thermal behaviour in order to provide a reference temperature level for the motor design and guarantee its secure application.

7.2   Motor losses

The main sources of heating in PM machines are generally divided into three groups, with respect to the areas where they occur. These losses include; copper losses (Joule losses), core losses and hysteresis losses due to eddy currents and mechanical losses due to friction [75]. Figure 7.1 illustrates the main sources of losses in electrical machines. Also, the energy conversion from electrical to thermal energy is discussed in the next section.
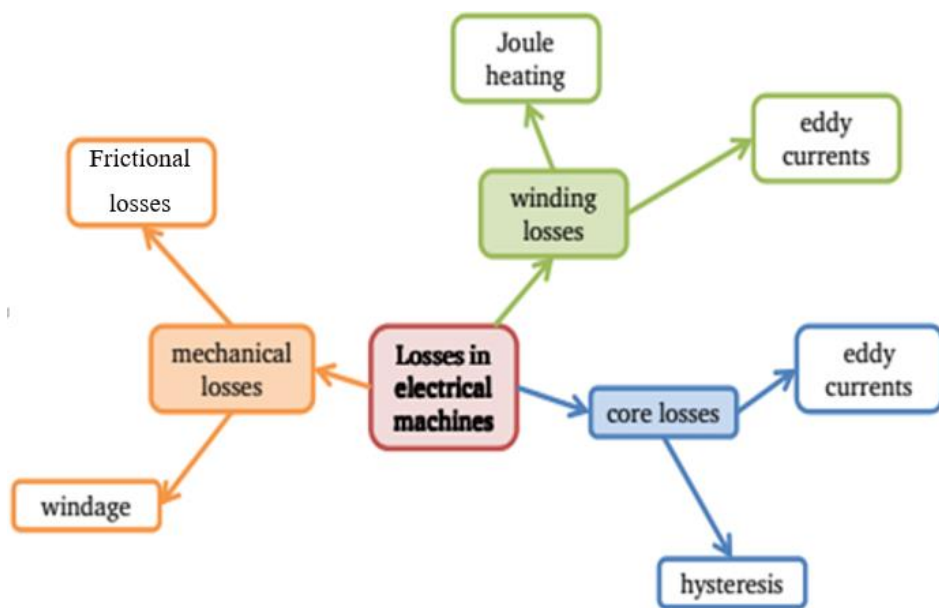
Figure 7.7.1 Main sources of losses in electrical machines [76].

7.2.1   Copper losses

The copper losses (P_c) often contributes the largest amount of the total losses in a PM machine. The copper losses in BDCLM arises due to the current going through the armature windings and can be calculated as shown in Equation 7.1:

$$P_c = m \, I^2 R \qquad (7.1)$$

Where R is the resistance of the armature winding, m is the number of active windings and I is the armature current. The winding resistance is dependent on the total length of the conductor per phase and the area of the conductor as shown in equation 3.1.

Any increase in the developed thrust will increase the armature current that will contribute to the thermal loss of the armature winding. The thermal loss will be converted to heat and will increase both the temperature of the motor winding and its resistance. The copper loss is temperature dependent and it increases proportionally with increasing temperature of the copper. Therefore, the copper loss at any temperature can be determined with equation [79]:

$$R[T] = R_{r(20)}[1 + \alpha_{20}(T-20)] \qquad (7.2)$$

Where,

R: The resistance of the conductor at a given temperature.

R_r: The resistance of the conductor at the reference temperature which is usually 20°C.

The alpha constant (α) is the temperature coefficient of material used for the armature winding.

A thin layer of glass cloth tape (150°C rated) was used as an insulation material between the armature core and the armature windings, thus the operating temperature of the armature winding (T_{Cu}) should not exceed 140 °C with a safety margin of 10 °C, to prevent the insulation material from melting.

$$T_{Cu} \leq 140°C \qquad (7.3)$$

7.2.2 Iron losses

Iron losses arises during the conversion of magnetic energy into thermal energy in the iron core of the machine. The losses occur due to the variation of magnetic flux in the material. The analysis of the iron losses in electric machines have been discussed in many papers [73-85]. The total iron loss (P_{iron}) is made up of two major components, which are the hysteresis loss (P_h) and the eddy current loss (P_e) [68]:

$$P_{iron} = P_h + P_e \qquad (7.4)$$

7.2.3 Hysteresis loss

Hysteresis loss depends on the peak value and the frequency of the flux density variation. The hysteresis loss (P_h) is expressed as shown in equation (7.5):

$$P_h = K_h . B^\beta . f \qquad (7.5)$$

Where K_h is the hysteresis loss coefficient, f frequency, B magnetic flux density and β is the Steinmetz constant which depends on the type of magnetic material used [76].

7.2.4 Eddy current

The variation of magnetic flux in a ferromagnetic material will induce a current in the material. The induced current will generate its own secondary magnetic field which opposes the applied magnetic field. The eddy current loss (P_e) is expressed as shown in equation [79]:

$$P_e = K_e . B^2 . f^2 \qquad (7.6)$$

Where K_e is the eddy current loss coefficient.

7.2.5 Mechanical loss

The mechanical loss occurs due to the mechanical friction and viscous losses. The mechanical loss depends on several factors, such as bearing type, lubrication, motor load and mover speed [25]. The friction force of a bearing is complex to calculate in literature. Also, different formulas exist for calculating the frictional force [80]. The general model for the friction force is shown in figure 7.2.

Since, the friction is a force that must be overcome, in order to enable the movement of the motor. Thus, the static friction (F_s) could be estimated as shown in equation 7.7:

$$F_s = K.I_0 \qquad (7.7)$$

Where K is the thrust constant and I_0 is the value of the armature current required to achieve motion. The static friction was estimated to be12 N.
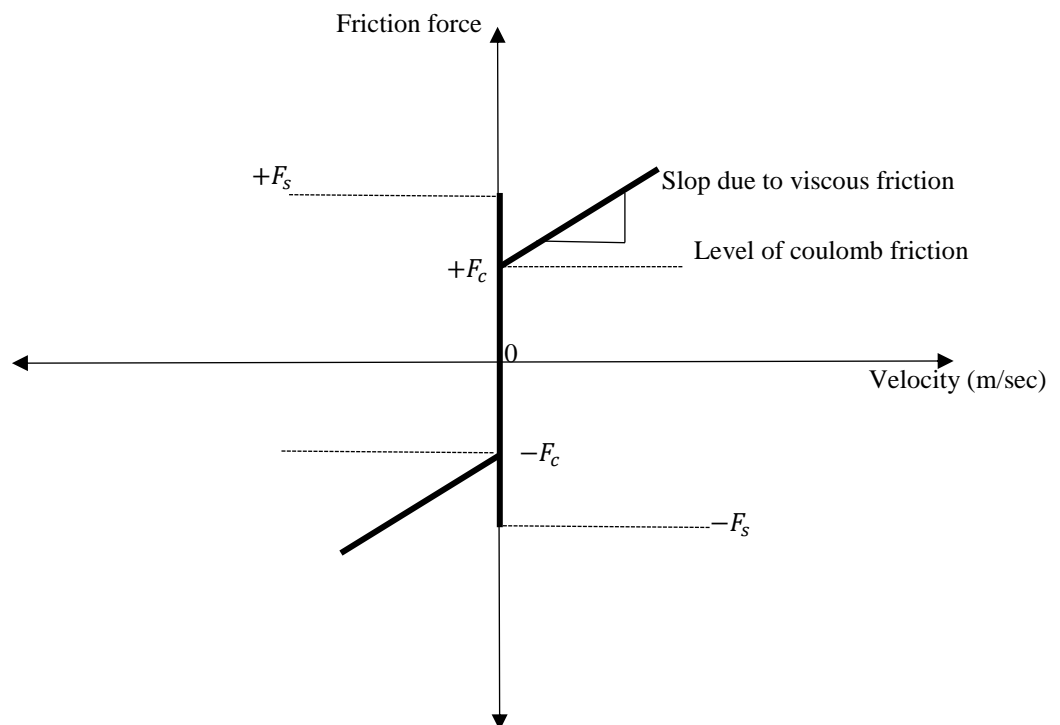
Figure 7.2 Figure 7.2 Linear Motor friction forces.

7.3 Thermal aspects of electrical machines

In any electrical machine, the internal temperature that will be reached at any given operating point must be predicted and analysed during the design, to ensure that the cooling system is sufficient to avoid overheating [76]. It is very important to take temperature rise into account when designing such permanent magnet machines, because the magnetic property of permanent magnets may change, leading to demagnetization. This can deteriorate their electromagnetic performance and limit their thrust output [78]. However, there is little concern about the overheating problem as mentioned in section 4.2.2. Though the armature current was relatively high, it flows for a short period of time, without causing any damage to the insulation of the conductor. Furthermore, the armature windings are in close contact with the armature core. The armature core serves as a good heat sink to dissipate the heat produced by the armature current. However, temperature investigation must be performed to evaluate the design.

The temperature tolerance depends on the materials utilised in the machine. The motor materials, specifically the permanent magnets and insulation polymers, can only withstand a maximum temperature of about 150 °C or less. In permanent magnet machines, the temperature should be kept below the maximum limit to avoid deterioration in the performance of the machine. The effect of temperature on the permanent magnet performance (magnetic properties) is going to be discussed in the next section [76].

7.3.1 Effects of Elevated Temperature on permanent magnets

Permanent magnet materials may lose their magnetic properties if they are heated to a certain high temperature. The maximum operating temperature of a permanent magnet

motor is determined by a combination of the temperature of the armature winding, the demagnetization point of the magnets, and thermal expansion of the motor components. Furthermore, both the electrical conductivity of the coil and the remanent magnetization of the magnets drop at high temperature, reducing the motor performance [61].

The NdFeB permanent magnets are more sensitive to high temperatures, compared to SmCo permanent magnets. Thus, care must be taken when using the NdFeB magnets within electrical motors. In lower temperature applications where high magnetic strength is necessary, NdFeB is a better choice, however, in high temperature applications, SmCo is a better choice. Therefore, special care must be taken to ensure that demagnetization of the permanent magnet does not occur. Demagnetization of the permanent magnet occurs when the temperature of the magent is too high. For practical designs, the magnet must be operated at temperatures significantly lower than the Curie temperature of the permanent magnet [26].

NdFeB has a linear 2nd-quadrant B-H characteristic at 20 °C. However, at higher temperatures, the 2nd-quadrant characteristic becomes non-linear and there is potential for demagnetisation or partial demagnetisation due to the thermal operating environment of the permanent magnet. Figure 7.3 illustrates how the demagnetisation curve of an NdFeB magnet becomes non-linear with an elevated temperature.

The Curie temperature is the temperature at which the magnetization of a magnet is totally destroyed , a typical Curie temperature for an NdFeB magnet is 310 °C and it can only operate up to a maximum temperature of 150 °C. Table 7.1 compares the Curie temperatures and temperature coefficients characteristic for the most commonly used PM materials.

If the final temperature is higher than the threshold temperature, the NdFeB magnet would experience a serious demagnetization [77]. Therefore, a maximum operating temperature (T_{PM}) of 140°C was chosen, with 10°C for safety margin:

$$T_{PM} \leq 140°C \qquad (7.8)$$

Both the remanent magnetic flux density (B_r) and the magnetic coercivity (H_c) are temperature dependent [61]:

$$B_r(T) = B_{r(20)}[1 + \alpha_{Br}(T_{PM}\text{-}20)/100] \qquad (7.9)$$

$$H_c(T) = H_{c(20)}[1 + \alpha_{Hc}(T_{PM}\text{-}20)/100] \qquad (7.10)$$

Where $B_{r(20)}$ is the remanent magnetic flux density at 20 °C, $H_{c(20)}$ is the coercive force at 20 °C, $\alpha_{Br} < 0$ is the temperature coefficient for B_r, $\alpha_{Hc} < 0$ is the temperature coefficient for H_c.
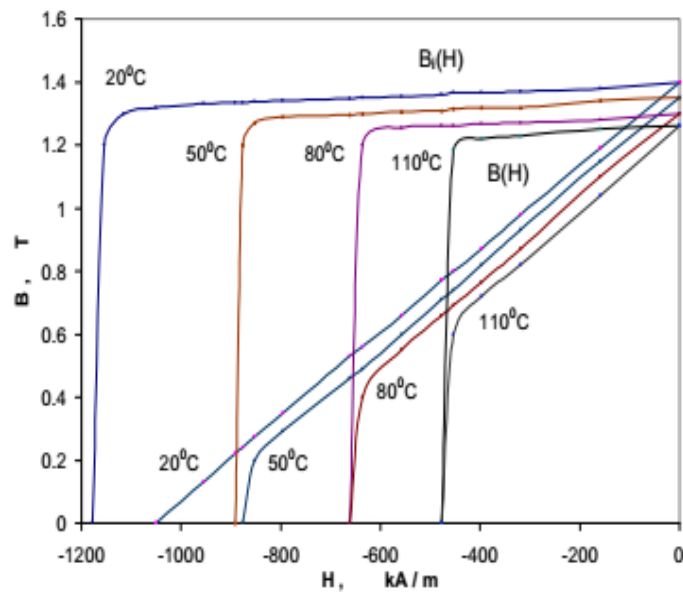
Figure 7.3 Demagnetization curves and their variations with the temperature for NdFeB Magnets [29].

Table 7.7.1Temperature coefficients and Curie temperature for common PM materials [29].

Material	Reversible temperature coefficient for B_r %/^{0}C	Reversible temperature coefficient for $_iH_c$ %/^{0}C	Curie temperature ^{0}C
Alnico 5	−0.02	−0.01	900
Alnico 8	−0.02	−0.01	860
Sm_2Co_{17}	−0.03	−0.20	800
$SmCo_5$	−0.045	−0.40	700
Bonded NdFeB MQP-C (15% Co)	−0.07	−0.40	470
Sintered NdFeB 40 MGOe (0% Co)	−0.10	−0.60	310
Ferrite 8	−0.20	+0.27	450
Plastiform 2401 Ferrite-Neo hybrid	−0.14	−0.04	–

7.4 Experimental evaluation

In order to verify the thermal behaviour of the designed motor, the BLDCM prototype was equipped with a thermal camera. The thermal camera (FLIR C2) from FLIR instruments company was mounted in front of the mover unit. During the experiment all the acquired temperature data were recorded while the motor was moving. A picture of the experimental set-up is shown in figure 7.4.

7.4.1 Repeatability test for the BDCLM thermal measurements.

The repeatability of thermal behaviour of the designed BDCLM system was investigated with respect to the motor temperature. Each of the Measurements were repeated 5 times in order to confirm the reproducibility of the measurement results. The standard error (SE)and percentage error (% $Error$) was calculated using equations 5.2 and 5.3 respectively. The maximum percentage error recorded for the motor temperature was 0.74 %.

7.5   Thermal analysis of BDCLM

Before this stage, only the magnetic and electrical analysis aspects of the motor design was performed, to ensure an efficient delivery of power and thrust at the required speed. Thermal analysis is very importance, because affects between these magnetic and electrical aspects of the motor design [89].

The main objective for performing the thermal analysis of the motor is to ensure the suitability of the machine design, in terms of keeping the temperature of the motor components within certain limits, in order to protect the permanent magnet materials from being demagnetised, as well as to protect the insulation material of the coil from damaging. Hence, the thermal analysis is very important in the electrical machine validation [25]. An observation of the rise in temperature was conducted on the armature winding and as well as the permanent magnet moving unit. The temperature distribution no applied current (I=0) in all parts of the motor is shown in figure 7.5. As can be seen from the graph, the motor temperature at I=0 is below 23.8 °C, which represents the room temperature.

The test was executed within nominal conditions with speed 0.236 m/sec and an applied voltage of 19.5 V. All the acquired temperature data were recorded for 80 mins in steps of 10 mins. As can be seen from figure 7.6, the temperature of the motor increases gradually with time. It increases from the edge to the center of the armeture winding and the maximum temperature appeared near the fourth and fifth armeture windings with a value of about 69.1 °C. The forth and the fifth aramture windings had the maximum temperature because they are both located at the centre of the motor. Therefore, as the motor moves forward and backwards during the experiment the forth and the fifth are more likely to be excited more than the others. Figure 7.7 shows the

maximum temperature of the fifth armature winding at 19.5 V applied voltage for a period of 80 mins.

Figure 7.4 Thermal experimental stand.
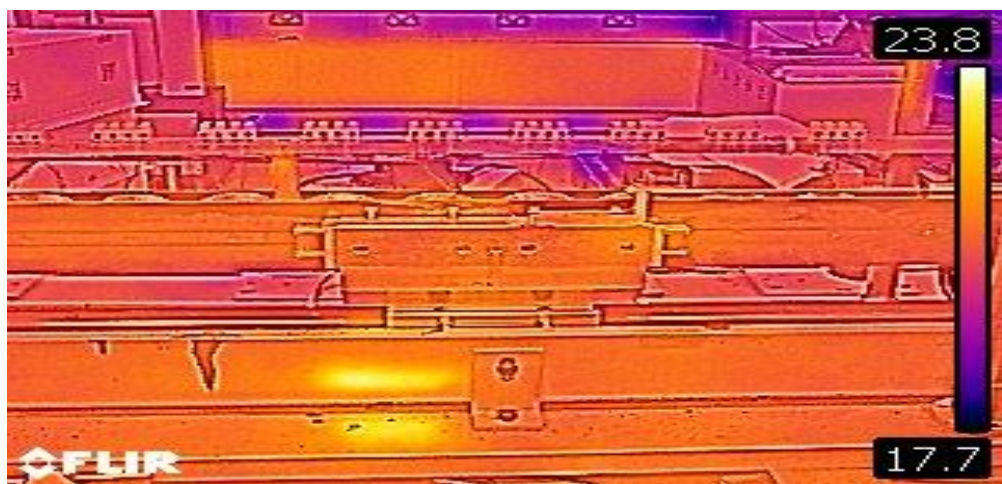
Figure 7.5 The temperature distribution of the motor at no load.
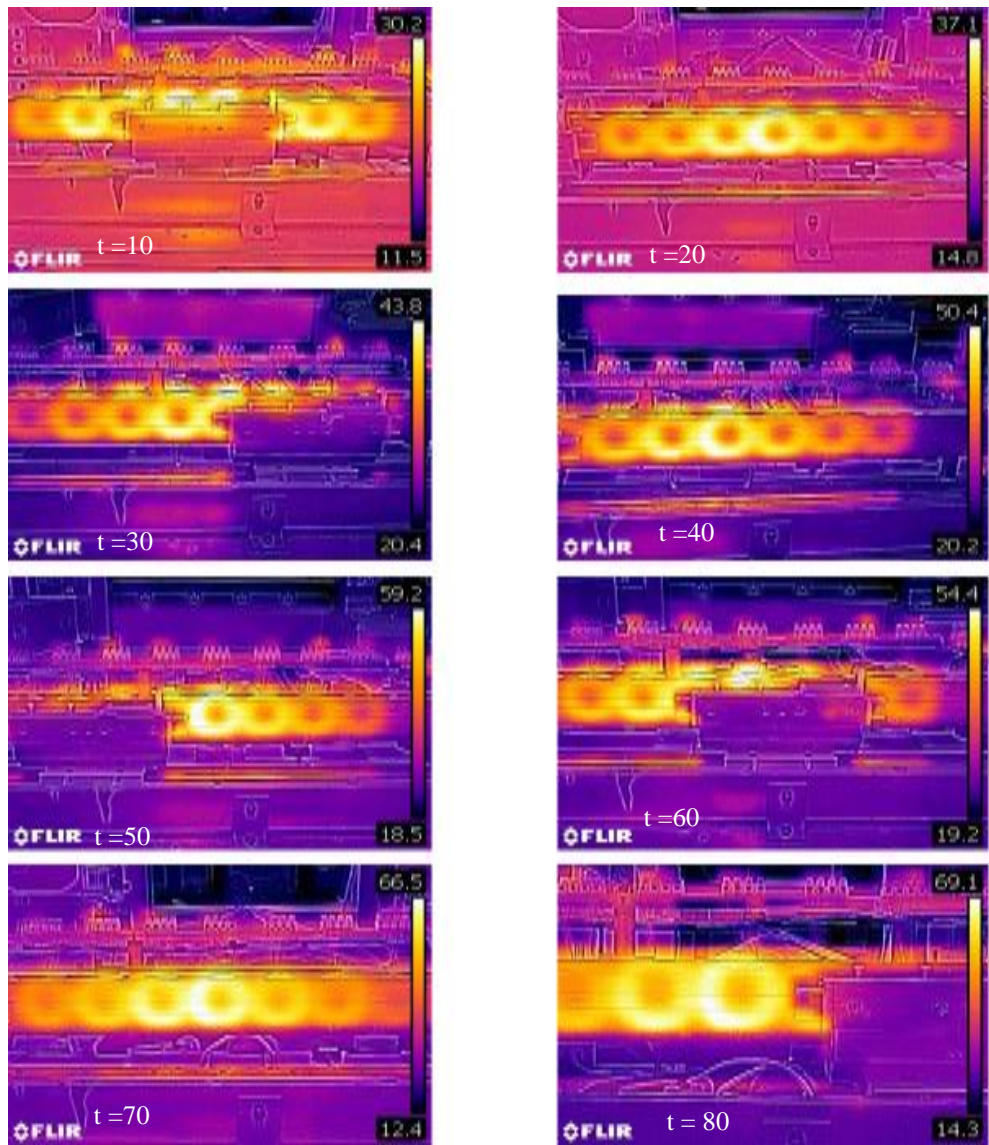
Figure 7.6 Temperature distribution in BDCLM at 19.5V voltage load.
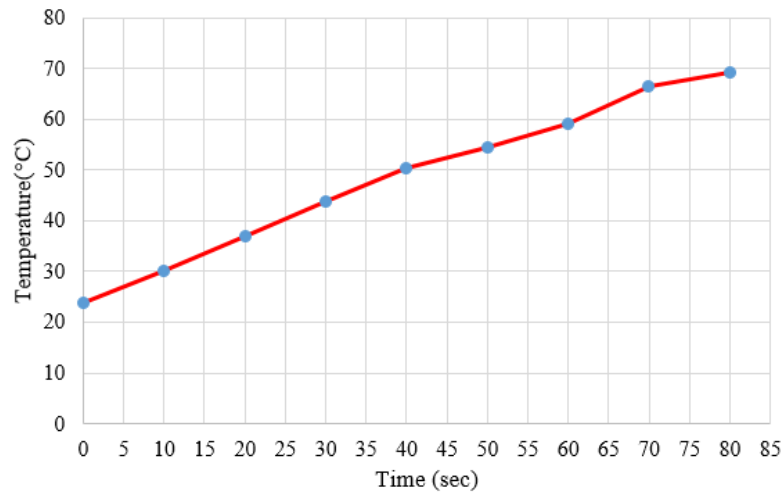
Figure 7.7 Maximum temperature distribution of the fifth armature at 19.5 V applied voltage.

7.6   Conclusion

This chapter discussed   the origin of different electromagnetic power losses in permanent magnet machines. Thermal tests were performed to investigate the temperature distribution within the motor for a better understanding of the motor's capabilities and limitations. The test was executed within nominal conditions with a speed of 0.235 m/sec and an applied voltage of 19.5 V. All the acquired temperature data were recorded every 10 mins for a total period of 80 mins. The experimental result confirmed the efficiency of the motor design, that is, the temperature level in BDCLM did not exceed the permitted level.

Chapter 8   : Conclusion and future work

8.1   Conclusions

The work presented in this thesis focuses on various aspects of the analysis, modelling, and control of a BDCLM. Electric machine design consists of comprehensive electromagnetic, mechanical and thermal tasks that cannot be designed separately. Therefore, the proposed design of the BDCLM has been evaluated using Finite Element Method (FEM). Detailed conclusions have been presented for each chapter while the overall conclusion of the work is summarised below.

- A comparison was made between the two proposed models (BSDCL and BDCLM) using "COMSOL Multiphysics" to test the motor design in term of air-gap flux density and the static thrust. The result showed that the computed Air-gap flux density value for the BDCLM was improved by 60 % compared to the BSDCLM. The result also showed that the static thrust of the BDCLM is higher than that for the BSDCLM with an average difference of 112.4 N and maximum deviation of 63.1 % at armature current of 7.5 A because the air-gap flux density in the BSDCLM is high compared to the air-gap of BDCLM.

- The dynamic results of the BSDCLM and the BDCLM model in terms of thrust, speed and displacement were computed at 2.5A armature winding to be 125 N and 225 N respectively. The motor steady-state speed of the BSDCLM and the BDCLM model were computed to be 0.17 m/sec and 0.25 m/sec respectively. The mover of the BSDCLM and the BDCLM model took about 1.6 secs to reach 272 mm and 365mm respectively. The BSDCLM took about

1.4 secs to reach the steady state while the BDCLM took about 1 sec to reach its steady state.

- The magnetic air-gap flux density and the static thrust of the BDCLM under various exciting currents (0A, 2.5A, 5A, 7.5A, 10A) acquired via FEM simulation and practical experimental measurements. Based on the results obtained, the maximum deviation between the computed and measured data is 8.9 %. Hence, there is a reasonable agreement between the computed and measured results.

- The open loop dynamic response of the BLDCM were measured in term of motor speed and position. The results showed the mover moves forward for a period of 1.6 sec with a current winding of 2.5 A, the mover reached its maximum speed at 0.24 m/sec at 1 sec.

- The experimental for speed and postion control was executed within 19.5 V applied voltage with refrence speed and postion 0.24 m/sec and 320 mm respectively. The velocity of the slider which was measured to be 0.235 at steady state. The parameters of the PID motor speed and position controller were chosen to be (K_p= 37.56, K_i = 65, K_d = 0.0126) and (K_p= 10.8, K_i = 17, K_d = 0.11) respectively. The motor needs almost 0.6 sec to reach steady state speed. The maximum and minimum error percentage error between the reference and the measured speed was found to be 1.77% and 1.16% respectively. Verity experimental position control with different reference position are performed and the average accuracy of the position error is 1 mm.

- It was found that the experimental results of the thermal investigation confirmed the efficiency of the motor design and the temperature level in BDCLM did not exceed the permitted level.

8.2   Further Work

In a double sided DC linear motor, there should be a net zero attraction force between the armature core and the permanent magnets. Any slight misalignment between them would cause a disturbance in the balanced forces acting on the mover. In a practical situation, there is always an existence of a small misalignment in a double sided linear motor, especially with long stators.

Despite the substantial work on modelling and development of the BDCLM presented in this thesis, there are still more areas of interest which can be investigated to improve the motor performance, such as:

- The effect of saturation of the armature core and the back iron on the motor performance.
- The effect of end effect on the motor performance.
- Minimising the force ripple of the motor to improve the motor operation.

Refrence

[1] Evans, S. A. 1996. Deign and optimaisation of a permenent magnet linear reluctance motor for reciprocating electro-mechanical systems. PhD Thesis, Department of Electronic and Electrical Engineering , Loughborough university.

 [2]SAAT, E. H. B. M., 2008. A Sensorless Positioning System for Linear DC Motor , Malaysia: Universiti Putra .

[3]Basak, A., 1996. Permanent Magnet DC Linear Motors. 1st ed. New York: Oxford University Press Inc..

[4]Denirci, R., 2000. Model Reference Adaptive Position Controller , Turkey: Abant Izzet Baysal University.

[5] E. R. Laithwaite, A history of linear electric motors. Basingstoke: Macmillan,

1987. ISBN 978-033339928-6.

[6]Chayopitak, N., 2007. Performance Assessment and Design Optimisation of Linear Synchronous Motors for Manufacturing Applications, Georgia: Georgia Institute of Technology.

[7]Chevailler, S., 2006. comparative study and selection criteria of linear motors, Switzerland: à LA FACULTÉ SCIENCES ET TECHNIQUES DE L'INGÉNIEUR.

[8]Li Xu and Bin Yao, 2001 . Output feedback adaptive robust precision motion control of linear motors. sciencedirect, p. 1029–1039.

[9]N. Navidi ,M. Bavafa and S. Hesami, 2009. A New Approach for Designing of PID Controller for a Linear Brushless DC Motor with Using Ant Colony Search Algorithm. *IEEE,* pp. 1 - 5.

[10] G. R. Slemon, P. E. Burke, and N. Terzis, A linear synchronous motor for

urban transit using rare-earth magnets," IEEE Transactions on Magnetics

14(5): 921.

[11] I. C. Vese, F. Marignetti and M. M. Radulescu, "Multiphysics approach to numerical modelling and analysis of permanent-magnet tubular linear motors," 2008 18th International Conference on Electrical Machines, Vilamoura, 2008, pp. 1-4.

[12]Okonkwo, R. C., 2006. Design and Performance of Permanent-Magnet. *IEEE,* pp. 2179 - 2183.

[13]Barrett, J., 2009. Linear Motors Baiscs. [Online]Available at: http://www.parkermotion.com/whitepages/linearmotorarticle.pdf
[Accessed 25 december 2013].

[14]Aydin, M., 2012. *Brushless Permanent Magnet Servomotors ,* Turkey: Kocaeli University.

[15]SATHYAN, A., 2008. *DIGITAL PWM CONTROL OF BRUSH-LESS DC (BLDC) MOTOR DRIVES ,* Illinois,USA: Illinois Institute of Technology.

[16]M. S. Manna, S. Marwaha, A. Marwaha and C. Vasudeva, "Analysis of Permanent Magnet Linear Induction Motor (PMLIM) Using Finite Element Method," 2009 International Conference on Advances in Recent Technologies in Communication and Computing, Kottayam, Kerala, 2009, pp. 540-542.

[17]Shao, J., 2003. Direct Back EMF Detection Method for Sensorless Brushless DC (BLDC) Motor Drives, Virginia,USA: Virginia Polytechnic Institute and the State University.

[18]Lai, S. H., 2006. Design Optimisation of a Slotless Brushless Permanent Magnet DC Motor with Helically-Wound Laminations for Underwater Rim-Driven Thrusters, Southampton: University of Southampton.

 [19]Sean DeHart, 2006. *Linear Motors.* [Online] Available at: www.ume.gatech.edu/mechatronics_course/Motors_F09.ppt
[Accessed 10 january 2014].

[20]Karacan, C., 2004. Comparison of Performance of Switched Reluctance Motors, Induction Motors and Permenant Mamnet DC Motors, Turkey: Middle East Technical University.

[21] Hamzeh Bahmani, Hamed 2014. Development of novel techniques for the assessment of inter-laminar resistance in transformer and reactor cores. PhD Thesis, Cardiff University.

[22] Magnetic Hysteresis (2016). Electronics-tutorials. [Online]. Available: http://www.electronics-tutorials.ws/ electromagnetism/magnetic-hysteresis.html.

[Accessed 20 July 2015].

[23]Arroyo, E. L. C., 2006. Modeling and Simulation of Permanent Magnet Synchronous Motor Drives, Puerto Rico: Puerto Rico.

[24]Karacan, C., 2004. Comparison of Performance of Switched Reluctance Motors, Induction Motors and Permenant Mamnet *DC Motors,* Turkey: Middle East Technical University.

[25] BRAIWISH, N. (2016). Design Optimisation of Brushless Permanent Magnet Synchronous Motor for Electric Vehicles . Cardiff: Cardiff University .

[26] M. T. Thompson, "Practical Issues in the Use of NdFeB Permanent Magnets in Maglev, Motors, Bearings, and Eddy Current Brakes," in *Proceedings of the IEEE*, vol. 97, no. 11, pp. 1758-1767, Nov. 2009.

[27]Hamid A. Toliyat and Tilak Gopalarathnam, 2002. AC Machines Controlled as DC Machines (Brushless DC Machines/Electronics), Texas: CRC Press LLC.

[28]Islam, M. R., 2009. Cogging Torque, Torque Ripple and Radial Force Alysis of Permenant Magnet Synchronous Machines, s.l.: The Graduate Faculty of The University of Akron.

[29] Gieras, J. F. Permanent Magnet Motor Technology, Design and Applications, Third
Edition. CRC Press Taylor and Francis Group NW. 2010. ISBN: 978-1-4200-6440-7.

[30]Chevailler, S. (2, July 2006). comparative study and selection criteria of linear motors. Switzerland, Switzerland.

[31] Basak, A., "A DC linear motor with sectional armature winding," Stepper Motors and Their Control, IEE Colloquium on , vol., no., pp.9/1,9/4, 25 Jan 1994.

[32]Yu-wu Zhu, Sang-geon Lee and Yun-hyun Cho, 2011. Thrust and normal force characteristics analysis of linear synchronous motor for direct drive conveyer. International Journal of Applied Electromagnetics and Mechanics , 1383-5416(IOS Press), p. 41–48 .

[33] L. Huaiji, Z. Ying and D. Yumei, "Normal force characteristics analysis of single-sided linear induction motor," *2011 International Conference on Electrical Machines and Systems*, Beijing, 2011, pp. 1-6.

[34]Myung J. Chung, Moon G. Lee, Sung Q. Lee, and Dae-Gab Gweon, 2001. Optimal design and development of linear brushless permanent magnet motor. *IEEE,* pp. 436 - 441.

[35]Jaewon Lim and Hyun-Kyo Jung, 2008. Cogging force reduction in permanent magnet linear motor using phase set shift. *IEEE,* 1(Sept 2008), pp. 1 - 4.

[36]K.K. Tan, T.H. Lee, H. Dou and S. Zhao, 2004. Force ripple suppression in iron-core permanent magnet linear motors using an adaptive dither. *sciencedirect,* p. 375–390.

[37] J. Gong, F. Gillon and P. Brochet, "Magnetic and thermal 3D finite element model of a Linear Induction Motor," 2010 IEEE Vehicle Power and Propulsion Conference, Lille, 2010, pp. 1-6.

[38]Ruddy, B. P. (2012). High Force Density Linear Permanent Magnet Motors. Bosten: Massachusetts Institute of Technology.

[39] Duan, Y. (2010, 11 14). METHOD FOR DESIGN AND OPTIMIZATION OF SURFACE. Georgia.

[40]Tan, Zheng et al. "3D Thermal Analysis of a Permanent Magnet Motor with Cooling Fans." Journal of Zhejiang University SCIENCE A 16.8 (2015): 616–621.

[41]Design of an H Bridge(2014). Retrieved from Axotron: http://axotron.se/index_en.php?page=34. [Accessed 15 June 2014].

[42]YU Pei-qiong, L. S., 2004. Techniques for Reducing the Effects of Detent Force in PMLSMs. *IEEE.,* pp. 126-128.

[43] Ratcliff, G. and Griffiths,J., "A linear DC motor", Journal of Scientific Instruments,Vol. 41,pp. 267-268, 1964.

[44] Jones,P.L., "DC linear motor for industrial applications" ,Electrical Times,PP.48-51,JULY 1969.

[45] Griffiths,J. and Jones,P.L.," The direct current linear motor and its applications.4th University Power Engineering Conference scientific instruments, University of Nottingham,pp.98-99,January 1969.

[46] Warnett,K., Linear electric motor, United States Patent No 3581 127 (1971).

[47] Green,C.W. and Jones,P.L.," Application of DC linear machines as short-stroke and static actuators" ,Proc.IEE,Vol.116,NO.4,pp.599-604,April 1969.

[48] Basak,A., "An investigation of DC linear motors" Unpublished PhD. Thesis, university of wales, April 1975.

[49] Dascalescu,L., "Ferrite-Field DC linear motors for Electode-postioning System of Electrostatic Separators", Electric Energy Conference, pp. 473-474,Adelaide,Octoper 1987.

[50] Akmese,R., and Eastham,J.F., "Design of permanent Magnet Flat Linear Motors for Standstill Applications ",IEEE Trans. on Magnetics,vol.28,no.5,pp.3042-3044,septamber 1992.

[51] Anayi, F.J.; Basak, A., 1995. A DC LINEAR MOTOR WITH A SQUARE ARMATURE. IEEE, pp. 462-469.

[52] Filho, A.F.F., An investigation of a double armature homopolar brushless DC linear motors, Unpublished PhD. Thesis, university of wales, April 1996.

[53] Basak, A.; Filho, A.F.F.; Nakata, T.; Takahashi, N., "Three dimensional computation of force in a novel brushless DC linear motor," Magnetics, IEEE Transactions on, vol.33, no.2, pp.2030, 2032, Mar 1997.

[54]In-Soung Jung, Jin Hur and Dong-Seok Hyun, 2001. Performance analysis of skewed PM linear synchronous motor according to various design parameters. *IEEE,* pp. 3653 - 3657.

[55]Junyong LU ,Deliang Liang, Xiangyang FENG, 2003. Simulation of linear brushless dc motor speed-controlled system based on MATLAB/SIMULINK. *IEE,* pp. 696 - 698 vol.2.

[56]A. A. Aboulnaga and A. Emadi , 2004. Design of High Performance Linear Brushless DC Motor with Ironless Core. *IEEE*, pp. 502 - 507.

[57]Shuhua Wang, Xudong Wang, Xiaozhuo Xu and Juanjuan Cao, 2008. Study on minimizing the detent force of PM linear brushless DC motors. *IEEE,* pp. 3430 - 3434.

 [58]Gyu-Hong Kang, Jung-Pyo Hong, and Gyu-Tak Kim, 2001. A novel design of an air-core type permanent magnet linear brushless motor by space harmonics field analysis. *IEEE,* pp. 3732 - 3736.

[59]Nicola Bianchi, Silverio Bolognani, and Alessandro Dalla Francesca Cappello, 2004. Back EMF improvement and force ripple reduction in PM linear motor drives. *IEEE,* pp. 3372 - 3377 Vol.5.

[60]Wenmei Huang, Yajie Xue, Guiying Song, Ying Sun, 2012. Analysis of End Force and Optimization Design for Linear Permanent Magnet Brushless DC Motor. *IEEE,* pp. 1 - 4.

[61]C.H. Lim, Y.K. Tan, S.K.Panda and J X Xu, 2004. Position control of linear permanent magnet BLDC servo using iterative learning contro. *IEEE,* pp. 1936 - 1941 Vol.2.

[62]S. J. Imen and M. Shakeri, 2007. Feed forward adaptive control of a linear brushless DC motor. *IEEE,* pp. 2200 - 2204.

[63]Mehdi Nasri, Hossein Nezamabadi-pour, and Malihe Maghfoori , 2007. A PSO-Based Optimum Design of PID Controller for a Linear Brushless DC Motor. World Academy of Science, Engineering and Technology, 2(Jan. 17, 2007), pp. 211-215.

[64]K. R. Cho, T. S. Hwang, J. K. Seek and D. H. Kim, "Initial position estimation for closed-loop linear hybrid stepping motor drives using DC current excitation," 2006 37th IEEE Power Electronics Specialists Conference, Jeju, 2006, pp. 1-6.

[65] Y. W. Zhu and Y. H. Cho, "Detent force reduction in permanent-magnet linear synchronous motor utilizing auxiliary poles," 2009 8th International Symposium on

Advanced Electromechanical Motion Systems & Electric Drives Joint Symposium, Lille, 2009, pp. 1-6.

[66] Xiaonan Xin, Yangrui Luo, Hexiu Xu and Huijuan Zhang, "A new method of brushless DC motor control system simulation," 2011 2nd International Conference on Artificial Intelligence, Management Science and Electronic Commerce (AIMSEC), Deng Leng, 2011, pp. 3667-3670.

[67] M. F. Tsai, T. P. Quy, B. F. Wu and C. S. Tseng, "Model construction and verification of a BLDC motor using MATLAB/SIMULINK and FPGA control," 2011 6th IEEE Conference on Industrial Electronics and Applications, Beijing, 2011, pp. 1797-1802.

[68] B. Tibor, V. Fedák and F. Durovský, "Modeling and simulation of the BLDC motor in MATLAB GUI," 2011 IEEE International Symposium on Industrial Electronics, Gdansk, 2011, pp. 1403-1407.

[69] Immaneni, H. (2013). Mathematical Modelling and Position Control of Brushless Dc (Bldc) Motor. International Journal of Engineering Research and Applications, pp.1050-1057.

[70]F. H. Ali, H. Mohammed Mahmood and S. M. B. Ismael, "LabVIEW FPGA implementation of a PID controller for D.C. motor speed control," 2010 1st International Conference on Energy, Power and Control (EPC-IQ), Basrah, 2010, pp. 139-144.

[71] Samadhi Manasa, Swapna Rani.T , M. Veda chary, 2015 . POSITION CONTROL OF A DC MOTOR USING PID CONTROLLER. International Journal of Scientific Engineering and Applied Science (IJSEAS) , Vol.1(3, June 2015), pp. 2395-3470 .

[72] Y. Chen, Y. Yao, Q. Lu, Y. Ye and X. Huang, "Electromagnetic and thermal coupling analysis of a water-cooled double-sided permanent magnet linear synchronous

motor," 2015 18th International Conference on Electrical Machines and Systems (ICEMS), Pattaya, 2015, pp. 1136-1140.

[73] Q. Lu, X. Zhang, Y. Chen, X. Huang, Y. Ye and Z. Q. Zhu, "Modelling and Investigation of Thermal Characteristics of a Water-Cooled Permanent-Magnet Linear Motor," in IEEE Transactions on Industry Applications, vol. 51, no. 3, pp. 2086-2096, May-June 2015.

[74] N. Chayopitak and D. G. Taylor, "Thermal analysis of linear variable reluctance motor for manufacturing automation applications," IEEE International Conference on Electric Machines and Drives, 2005., San Antonio, TX, 2005, pp. 866-873.

[75] Howey, D. A. (2010, March 10). Thermal design of air-cooled axial flux permanent magnet machines. London, UK.

[76] Othman, N. B. (2010, September). Design and evaluation of high power density brushless DC permanent magnet machines. Nottingham, UK.

[77] J.Junak,G.Ombach & D.Staton. (2008). Permanent Magnet DC Motor Brush Transient Thermal Analysis,UK.

[78]R. Ibtiouen, S. Mezani, O. Touhami, N. Nouali, and M. Benhaddadi, "Application of lumped parameters and finite element methods to the thermal modeling of an induction motor", IEEE International on Electric Machines and Drives (IEMDC 2001), 2001.

[79] D. Staton, A. Boglietti, and A. Cavagnino, "Solving the More Difficult Aspects of Electric Motor Thermal Analysis in Small and Medium Size Industrial Induction Motors", IEEE Transaction on Energy Conversion, Vol. 20, pp. 620-628, 2005.

[80] A. Boglietti, A. Cavagnino, and D. A. Staton, "TEFC induction motors thermal models: a parameter sensitivity analysis", IEEE Transactions on Industry Applications, Vol. 41, pp. 756-763, 2005.

[81] E. Belicova and V. Hrabovcova, "Analysis of an Axial Flux Permanent Magnet

Machine (AFPM) Based on Coupling of Tow Separated Simulation Models (Electrical and Thermal Ones)", Journal of Electrical Engineering, Vol. 58, No. 1, 2007.

[82] M. M. Baggu, H. L. Hess, and K. Rink, "Thermal modelling of direct lamination cooling (DLC) induction motor for hybrid electric vehicle applications", IEEE Conference on Vehicle Power and Propulsion (VPPC'05), 2005.

[83] A. M. El-Refaie, N. C. Harris, T. M. Jahns, and K. M. Rahman, "Thermal analysis of multibarrier interior PM synchronous Machine using lumped parameter model", IEEE Transaction on Energy Conversion, Vol. 19, pp. 303-309, 2004.

[84] Pudji Irasari, Hilman Syaeful A, and Muhammad Kasim. (May 2011). Thermal Analysis on Radial Flux. The Journal for Technology and Science, Vol. 22, No. 2.

[87] FLIR C2 Thermal Imaging Camera. (2017, 09 05). Retrieved from RS Components Ltd: http://uk.rs-online.com/web/p/thermal-imaging-cameras/8668124/. [Accessed 22 january 2016].

[86]Zhu ZQ, Howe D. "Electrical machines and drives for electric, hybrid, and fuel cell vehicles", Proceedings of the IEEE 2007; 95(4): 746–65.

[87]C. Blache and D. Paccard, "Magnetic structure design method," IEEE Transactions on Magnetics, vol. 29, pp. 2228-31, Sep. 1993.

[88]K. Hameyer and R. Belmans, Numerical Modelling and Design of Electrical Machines and Devices, WIT Press, 1999.

[89]T. Sebastian, G. R. Slemon, and M. A. Rahman, "Modelling of permanent magnet synchronous motors," IEEE Trans. Magn., vol. 22, no. 5, pp.1069-1071, Sep. 1986.

[90]Miller, Tim, "Brushless permanent-magnet motor drives," in Power Engineering Journal, vol.2, no.1, pp.55-60, Jan 1988

[91]S. Thieblin, "Analysis and modelling of thermal behaviour of an electric motor under variable loads and speeds. Application to an electric vehicle motor," Ph.D. dissertation, Univ. Poitiers, Poitiers, France, 1997.

[92]W. Ouyang, D. Zarko and T. A. Lipo, "Permanent Magnet Machine Design Practice and Optimization," 2006 IEEE conference on Industrial Applications, pp.1905-11, Tampa,FL, 2006

[93] F. H. Ali, H. Mohammed Mahmood and S. M. B. Ismael, "LabVIEW FPGA implementation of a PID controller for D.C. motor speed control," *2010 1st International Conference on Energy, Power and Control (EPC-IQ)*, Basrah, 2010, pp. 139-144.

Appendix A- Publication

Conference paper:

A. Ismael and F. J. Anayi, "Modelling of a prototype brushless permanent magnet DC linear stepping motor employing a flat-armature winding configuration," *2016 Third International Conference on Electrical, Electronics, Computer Engineering and their Applications (EECEA)*, Beirut, 2016, pp. 88-92.

Appendix B- Arduino code

The Arduino was program to control the voltage of the armature winding;

```
  AnalogReadSerial

  Reads an analog input on pin 7 to 44, prints the result to the serial monitor.  Attach
the output signal of LVDT to pin A0.

int T1 = 7;int T2 = 8;int T3 = 9;int T4 = 10;int T5 = 11;int T6 = 12;int T7 = 22;int T8
= 24;int T9 = 26;int T10 = 28;int T11 = 30;int T12 = 32;int T13 = 34;int T14 = 36;int
T15 = 38;int T16 = 40;int T17 = 42;int T18 = 44;

int i1;int i2;int i3;int i4;int i5;int i6;int i7;int i8;int i9;int i10;int i11;int i12;int i13;int
i14;int i15;int i16;int i17;int i18;

int v1;int v2;int v3;int v4;int v5;int v6;int v7;int v8;int v9;int v10;int v11;int v12;int
v13;int v14;int v15;int v16;int v17;int v18;

void setup() {

  // initialize serial communication at 9600 bits per second:

  Serial.begin(9600);

  Serial.setTimeout(10);

  pinMode(T1, OUTPUT);  pinMode(T2, OUTPUT);  pinMode(T3, OUTPUT);

   pinMode(T4, OUTPUT);  pinMode(T5, OUTPUT);  pinMode(T6, OUTPUT);

   pinMode(T7, OUTPUT);  pinMode(T8, OUTPUT);  pinMode(T9, OUTPUT);

    pinMode(T10, OUTPUT);  pinMode(T11, OUTPUT);  pinMode(T12, OUTPUT);
pinMode(T13, OUTPUT);  pinMode(T14, OUTPUT);  pinMode(T15, OUTPUT);
pinMode(T16, OUTPUT);  pinMode(T17, OUTPUT);  pinMode(T18, OUTPUT);
pinMode(3, OUTPUT);

}
// the loop routine runs over and over again forever:

void loop() {

  // Reading the sensor value and output on pin A0

  int sensorValue = analogRead(A0);

  // print out the value you read:

  Serial.println(sensorValue);
```

```
// Receive Transistor Voltages

String FETVoltage = Serial.readString();   // Read String of Voltages

//String FETVoltage = "";   // Read String of Voltages

 i1 = FETVoltage.indexOf('a');          //

 i2 = FETVoltage.indexOf('b');          //

 i3 = FETVoltage.indexOf('c');          //

 i4 = FETVoltage.indexOf('d');          //

 i5 = FETVoltage.indexOf('e');          //

 i6 = FETVoltage.indexOf('f');          //

 i7 = FETVoltage.indexOf('g');          //

 i8 = FETVoltage.indexOf('h');          //

 i9 = FETVoltage.indexOf('i');          //

 i10 = FETVoltage.indexOf('j');         //

 i11 = FETVoltage.indexOf('k');           //

 i12 = FETVoltage.indexOf('l');          //

 i13 = FETVoltage.indexOf('m');            //

 i14 = FETVoltage.indexOf('n');          //

 i15 = FETVoltage.indexOf('o');          //

 i16 = FETVoltage.indexOf('p');          //

 i17 = FETVoltage.indexOf('q');           //

 i18 = FETVoltage.indexOf('r');          //

// output the voltage signal

v1 = FETVoltage.substring(0, i1+1).toInt();

v2 = FETVoltage.substring(i1+1, i2+1).toInt();

v3 = FETVoltage.substring(i2+1, i3+1).toInt();

v4 = FETVoltage.substring(i3+1, i4+1).toInt();

v5 = FETVoltage.substring(i4+1, i5+1).toInt();
```

```
v6 = FETVoltage.substring(i5+1, i6+1).toInt();

v7 = FETVoltage.substring(i6+1, i7+1).toInt();

v8 = FETVoltage.substring(i7+1, i8+1).toInt();

v9 = FETVoltage.substring(i8+1, i9+1).toInt();

v10 = FETVoltage.substring(i9+1, i10+1).toInt();

v11 = FETVoltage.substring(i10+1, i11+1).toInt();

v12 = FETVoltage.substring(i11+1, i12+1).toInt();

v13 = FETVoltage.substring(i12+1, i13+1).toInt();

v14 = FETVoltage.substring(i13+1, i14+1).toInt();

v15 = FETVoltage.substring(i14+1, i15+1).toInt();

v16 = FETVoltage.substring(i15+1, i16+1).toInt();

v17 = FETVoltage.substring(i16+1, i17+1).toInt();

v18 = FETVoltage.substring(i17+1, i18+1).toInt();

 if (v1 == 1);     v1 = HIGH;

else

   v1 = LOW;

 // output the voltage signal

digitalWrite(T1, v1);  digitalWrite(T2, v2);  digitalWrite(T3, v3);

digitalWrite(T4, v4);  digitalWrite(T5, v5);  digitalWrite(T6, v6);

digitalWrite(T7, v7);  digitalWrite(T8, v8);  digitalWrite(T9, v9);

digitalWrite(T10, v10);  digitalWrite(T11, v11);  digitalWrite(T12, v12);

digitalWrite(T13, v13);  digitalWrite(T14, v14);  digitalWrite(T15, v15);

digitalWrite(T16, v16);  digitalWrite(T17, v17);  digitalWrite(T18, v18);

 analogWrite(3,sensorValue/4);

 delay(3);

}.
```

Appendix C-Armature winding energising algorithm

Position	W1	W2	W3	W4	W5	W6	W7	W8	W9	W10	W11	W12
0 -5		-	+	-								
6 -11		-	+	-								
12 -17	-		+	-								
18 -23	-		+	-								
24 -29	-		+	-								
30 -35	-	+		-								
36 -41	-	+		-								
42 -47	-	+	-									
48 -53	-	+	-									
54 -59		+	-	+								
60 -65		+	-	+								
66 -71		+	-	+								
72 -77			-	+	-							
78 -83			-	+	-							
84 -89		-		+	-							
90 -95		-		+	-							
96 -101		-		+	-							
102-107		-	+		-							
108-113		-	+		-							
114-119		-	+	-								
120 -125		-	+	-								
126-131			+	-	+							
132-137			+	-	+							
138-143			+	-	+							
144-149				-	+	-						
150-155				-	+	-						
156-161			-		+	-						
162-167			-		+	-						
168-173			-		+	-						
174-179			-	+		-						
180-185			-	+		-						

186-191			-	+	-						
192-197			-	+	-						
198-203				+	-	+					
204-209				+	-	+					
210-215				+	-	+					
216-221					-	+	-				
222-227					-	+	-				
228-223				-		+	-				
234-239				-		+	-				
240-245				-		+	-				
246-251				-	+		-				
252-257				-	+		-				
258-263				-	+	-					
264-269				-	+	-					
270-275					+	-	+				
276-281					+	-	+				
282-287					+	-	+				
288-293						-	+	-			
294-299						-	+	-			
300-305					-		+	-			
306-311					-		+	-			
312-317					-		+	-			
318-323					-	+		-			
324-329					-	+		-			
330-335					-	+	-				
336-341					-	+	-				
342-347						+	-	+			
348-353						+	-	+			
354-359						+	-	+			
360-365							-	+	-		
366-371							-	+	-		
372-377						-		+	-		
378-383						-		+	-		
384-389						-		+	-		
390-395						-	+		-		
396-401						-	+		-		

402-407						-	+	-				
408-413						-	+	-				
414-419							+	-	+			
420-425							+	-	+			
426-431							+	-	+			
432-437								-	+	-		
438-443								-	+	-		
444-449							-		+	-		
450-455							-		+	-		
456-461							-		+	-		
462-467							-	+		-		
468-473							-	+		-		
374-479							-	+	-			
480-485							-	+	-			
486-491								+	-	+		
492-497								+	-	+		
498-503								+	-	+		
504-509									-	+	-	
510-515									-	+	-	
516 -521mm								-		+	-	
522-527								-		+	-	
528-533								-		+	-	
534-539								-	+		-	
540-545								-	+		-	
546-551								-	+	-		
552-557								-	+	-		
558-563									+	-	+	
564-569									+	-	+	
570-575									+	-	+	
576-581										-	+	-
582-587										-	+	-
588-593									-		+	-
594-599									-		+	-
600-605									-		+	-
606-611									-	+		-
612-617									-	+		-

Position	W10	W11	W12	W13	W14	W15	W16	W17	W18	W19	W20	W21
618-623									-	+	-	
624629									-	+	-	
630-635										+	-	+
636-641										+	-	+
642-647										+	-	+
648-653		-	+	-								
654-659		-	+	-								
660-665	-		+	-								
666-671	-		+	-								
672-677	-		+	-								
678-683	-	+		-								
684-689	-	+		-								
690-695		-	+	-								
696-701		-	+	-								
702-707		+	-	+								
708-713		+	-	+								
714-719		+	-	+								
720-725		-	+	-								
726-731		-	+	-								
732-737		-		+	-							
738-743		-		+	-							
744-749		-		+	-							
750-755		-	+		-							
756-761		-	+		-							
762-767		-	+	-								
768-773		-	+	-								
774-779			+	-	+							
780-785			+	-	+							
786-791			+	-	+							
792-797				-	+	-						
798-803				-	+	-						
804-809			-		+	-						

810-815			-		+	-						
816-821			-		+	-						
822-827			-	+		-						
828-833			-	+		-						
834-839				-	+	-						
840-845				-	+	-						
846-851				+	-	+						
852-857				+	-	+						
858-863				+	-	+						
864-869					-	+	-					
870-875					-	+	-					
876-881				-		+	-					
882-887				-		+	-					
888-893				-		+	-					
894-899				-	+		-					
900-905				-	+		-					
906-911				-	+	-						
912-917				-	+	-						
918-923					+	-	+					
924-929					+	-	+					
930-935					+	-	+					
936-941						-	+	-				
942-947						-	+	-				
948-953					-		+	-				
954-959					-		+	-				
960-965					-		+	-				
966-971					-	+		-				
972 -977					-	+		-				
978-983					-	+	-					
984 -989					-	+	-					
990-995						+	-	+				
996-1001						+	-	+				
1002-1007						+	-	+				
1008 -1013							-	+	-			
1014-1019							-	+	-			
1020 -1025						-		+	-			

1026 -1031						-		+	-			
1032 -1037						-		+	-			
1038 -1043						-	+		-			
1044 -1049						-	+		-			
1050-1055						-	+	-				
1056 -1061						-	+	-				
1062 -1067							+	-	+			
1068 -1073							+	-	+			
1074 -1079							+	-	+			
1080-1085								-	+	-		
1086 -1091								-	+	-		
1092 -1097							-		+	-		
1098 -1103							-		+	-		
1104 -1109							-		+	-		
1110 -1115							-	+		-		
1116 -1121							-	+		-		
1122 -1127							-	+	-			
1128 -1133							-	+	-			
1134 -1139								+	-	+		
1140 -1145								+	-	+		
1146 -1151								+	-	+		
1152-1157									-	+	-	
1158 -1163									-	+	-	
1164-1169								-		+	-	
1170 -1175								-		+	-	
1176 -1181								-		+	-	
1182 -1187								-	+		-	
1188 -1193								-	+		-	
1194 -1199								-	+	-		
1200 -1205								-	+	-		
1206-1211									+	-	+	
1212 -1217									+	-	+	
1218-1223									+	-	+	
1224 -1229										-	+	-
1230 -1235										-	+	-
1236 -1241									-		+	-

Position	W13	W14	W15	W16	W17	W18	W19	W20	W21	W22	W23	W24
1242 -1247									-		+	-
1248 -1253									-		+	-
1254 -1259									-	+		-
1260-1265									-	+		-
1266 -1271									-	+	-	
1272 -1277									-	+	-	
1278 -1283										+	-	+
1248 -1289										+	-	+
1290 -1295										+	-	+
1296 -1301								-	+	-		
1302 -1307								-	+	-		
1308-1313							-		+	-		
1314 -1319							-		+	-		
1320 -1325							-		+	-		
1326-1331							-	+		-		
1332 -1337							-	+		-		
1338 -1343							-	+	-			
1344-1349							-	+	-			
1350-1355								+	-	+		
1356 -1361								+	-	+		
1362-1367								+	-	+		
1368-1373									-	+	-	
1374 -1379									-	+	-	
1380 -1385								-		+	-	
1386 -1391								-		+	-	
1392 -1397								-		+	-	
1398 -1403								-	+		-	
1404 -1409								-	+		-	
1410-1415								-	+	-		
1416 -1421								-	+	-		
1422 -1427									+	-	+	
1428 -1433									+	-	+	

1434 -1439									+	-	+	
1440-1445										-	+	-
1546 -1451										-	+	-
1452 -1457									-		+	-
1458 -1463									-		+	-
1464 -1469									-		+	-
1470 -1475									-	+		-
1476 -1481									-	+		-
1482-1487									-	+	-	
1488 -1493									-	+	-	
1494 -1499										+	-	+
1500 -1505										+	-	+
1506 -1511										+	-	+

Appendix D- Measurements

1. Load cell calibration

| Weight(Kg)	Voltage (mV)	Force (N)	Force per voltage (N/mV)
4.0965	3.1	40.1457	12.95022581
5.144	3.9	50.4112	12.92594872
5.6065	4.3	54.9437	12.77760465
5.9605	4.6	58.4129	12.69845652
6.414	5	62.8572	12.57144
6.89	5.4	67.522	12.50407407
7.4615	5.9	73.1227	12.39367797
7.82	6.2	76.636	12.36064516
8.2445	6.6	80.7961	12.24183333
8.825	7	86.485	12.355
9.128	7.3	89.4544	12.2540274
9.709	7.8	95.1482	12.19848718
10.185	8.2	99.813	12.17231707
10.6095	8.6	103.9731	12.08989535
11.0645	9	108.4321	12.04801111
11.5815	9.4	113.4987	12.07432979
12.0905	9.8	118.4869	12.0905
12.3005	10	120.5449	12.05449
12.882	10.5	126.2436	12.0232
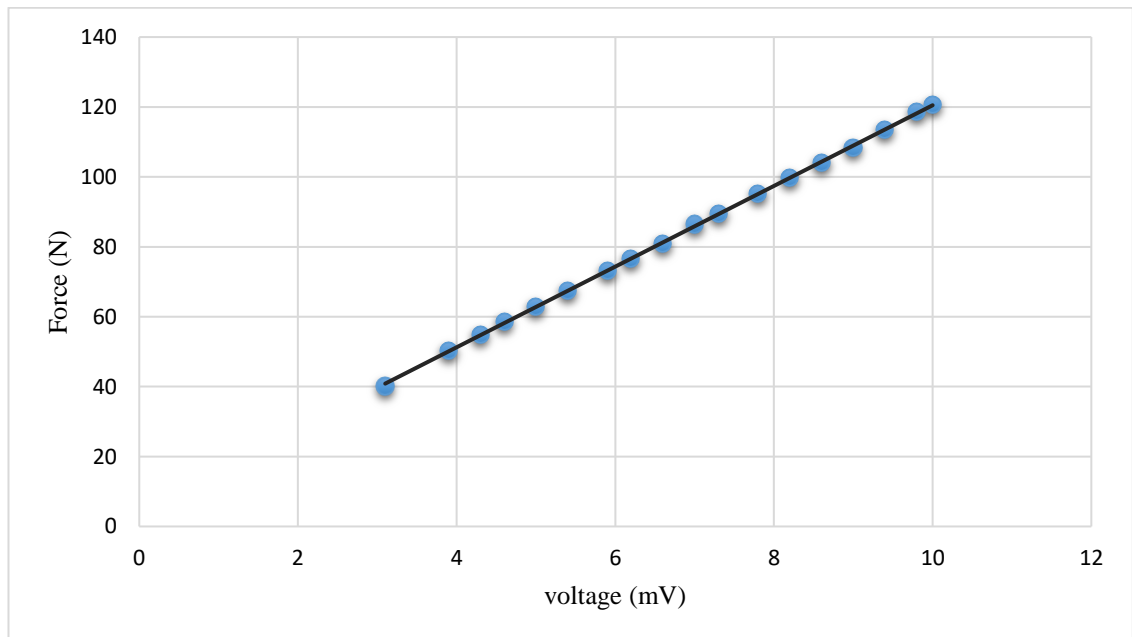
Figure D.1Load cell calibration.

2. Measured magnetic air-gap flux density of the BDCLM

Position(mm)	Magnetic flux density (T) at I=0	Magnetic flux density (T) at I=2.5	Magnetic flux density (T) at I=5	Magnetic flux density (T) at I=7.5	Magnetic flux density (T)at I=10
0	0.2	0.233	0.243	0.254	0.25515
10	0.5	0.52	0.533	0.543	0.55965
20	0.568	0.591	0.608	0.628	0.6384
30	0.45	0.478	0.491	0.502	0.53
40	0.411	0.432	0.444	0.448	0.4662
50	-0.053	-0.0498	-0.057	-0.047	-0.05985
60	-0.55	-0.561	-0.572	-0.58	-0.6006
70	-0.713	-0.725	-0.734	-0.76	-0.7707
80	-0.756	-0.761	-0.773	-0.781	-0.81165
90	-0.518	-0.537	-0.543	-0.559	-0.57015
100	-0.356	-0.33	-0.328	-0.319	-0.3444
110	0.056	0.058	0.061	0.062	0.06405
120	0.468	0.491	0.505	0.513	0.53025
130	0.555	0.601	0.613	0.629	0.64365
140	0.726	0.759	0.781	0.798	0.82005
150	0.664	0.695	0.715	0.73	0.75075
160	0.101	0.106	0.109	0.11	0.11445
170	-0.228	-0.214	-0.21	-0.205	-0.2205
180	-0.514	-0.481	-0.471	-0.458	-0.49455
190	-0.524	-0.491	-0.479	-0.471	-0.50295
200	-0.5703	-0.567	-0.555	-0.541	-0.58275
210	-0.41	-0.422	-0.4503	-0.48	-0.47282

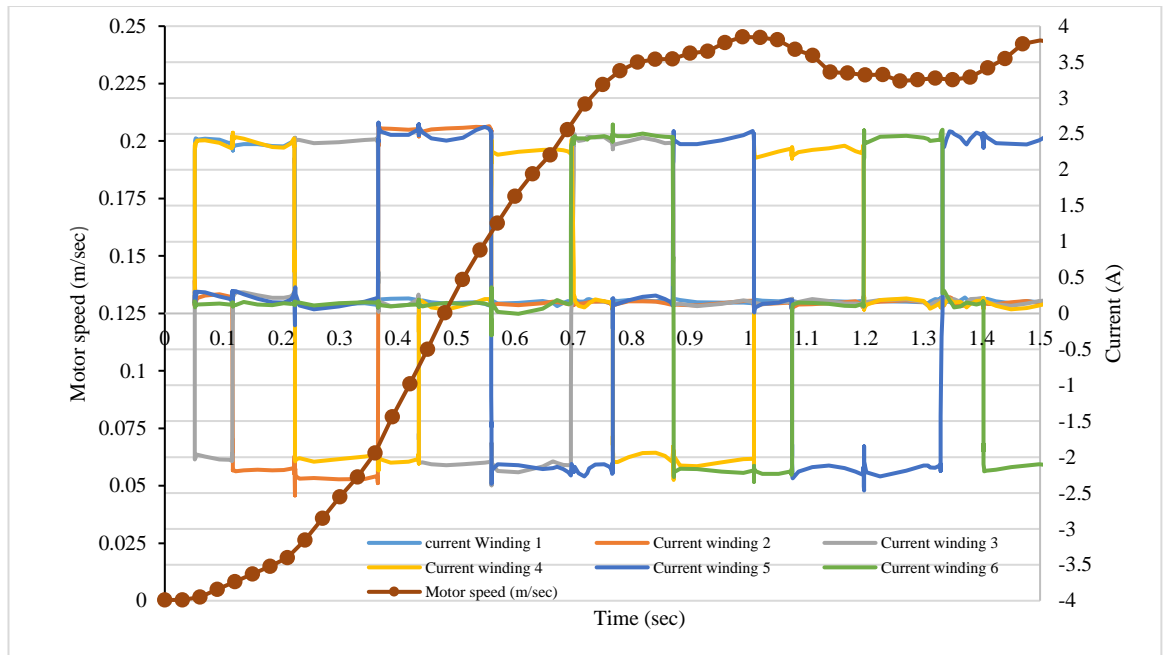## 2. Measured open loop dynamic response of the BDCLM

Figure D.2 Measured open loop dynamic response of the BDCLM.
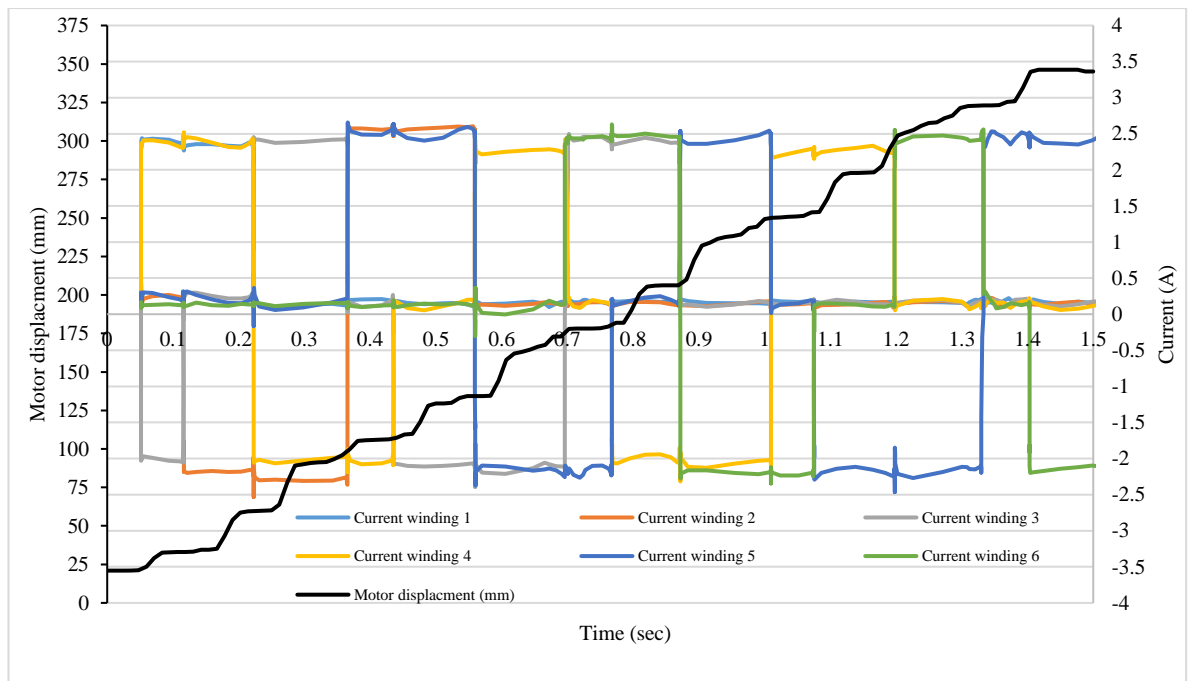
3. Measured open loop BDCLM displacement

Figure D.3 Measured open loop BDCLM displacement

Appendix E- The current function $f_k(x)$

The mathematical expression of the 9-windings switching current function $f_k(x)$ as a function of the slider position is expressed as follows:

$$f_1(x) = \begin{cases} I_1 = 0 & at\ x = 0\ to\ 11\ mm \\ I_1 = -1 & at\ x = 12\ to\ 53\ mm \\ I_1 = 0 & at\ x = 71\ to\ 400\ mm \end{cases}$$

$$f_2(x) = \begin{cases} I_2 = -1 & at\ x = 0\ to\ 11\ mm \\ I_2 = 0 & at\ x = 12\ to\ 29\ mm \\ I_2 = +1 & at\ x = 30\ to\ 71\ mm \\ I_2 = 0 & at\ x = 72\ to\ 83\ mm \\ I_2 = -1 & at\ x = 84\ to\ 125\ mm \\ I_2 = 0 & at\ x = 126\ to\ 400\ mm \end{cases}$$

$$f_3(x) = \begin{cases} I_3 = +1 & at\ x = 0\ to\ 29\ mm \\ I_3 = 0 & at\ x = 30\ to\ 41\ mm \\ I_3 = -1 & at\ x = 42\ to\ 83\ mm \\ I_3 = 0 & at\ x = 84\ to\ 101\ mm \\ I_3 = +1 & at\ x = 102\ to\ 143\ mm \\ I_3 = 0 & at\ x = 144\ to\ 155\ mm \\ I_3 = -1 & at\ x = 156\ to\ 197\ mm \\ I_3 = 0 & at\ x = 198\ to\ 400\ mm \end{cases}$$

$$f_4(x) = \begin{cases} I_4 = -1 & at\ x = 0\ to\ 41\ mm \\ I_4 = 0 & at\ x = 42\ to\ 53\ mm \\ I_4 = +1 & at\ x = 54\ to\ 101\ mm \\ I_4 = 0 & at\ x = 102\ to\ 113\ mm \\ I_4 = -1 & at\ x = 114\ to\ 155\ mm \\ I_4 = 0 & at\ x = 156\ to\ 173\ mm \\ I_4 = +1 & at\ x = 174\ to\ 215\ mm \\ I_4 = 0 & at\ x = 216\ to\ 400\ mm \end{cases}$$

$$f_5(x)= \begin{cases} I_5 = 0 & at\ x = 0\ to\ 71\ mm \\ I_5 = -1 & at\ x = 72\ to\ 113\ mm \\ I_5 = 0 & at\ x = 114\ to\ 129\ mm \\ I_5 = +1 & at\ x = 126\ to\ 173\ mm \\ I_5 = 0 & at\ x = 174\ to\ 185\ mm \\ I_5 = -1 & at\ x = 186\ to\ 227\ mm \\ I_5 = 0 & at\ x = 228\ to\ 245\ mm \\ I_5 = +1 & at\ x = 246\ to\ 287\ mm \\ I_5 = 0 & at\ x = 288\ to\ 299\ mm \\ I_5 = -1 & at\ x = 300\ to\ 341\ mm \\ I_5 = 0 & at\ x = 342\ to\ 400\ mm \end{cases}$$

$$f_6(x)= \begin{cases} I_6 = 0 & at\ x = 0\ to\ 143\ mm \\ I_6 = -1 & at\ x = 144\ to\ 185mm \\ I_6 = 0 & at\ x = 186\ to\ 197\ mm \\ I_6 = +1 & at\ x = 198\ to\ 245\ mm \\ I_6 = 0 & at\ x = 246\ to\ 257mm \\ I_6 = -1 & at\ x = 258\ to\ 299\ mm \\ I_6 = 0 & at\ x = 300\ to\ 317\ mm \\ I_6 = +1 & at\ x = 318\ to\ 359\ mm \\ I_6 = 0 & at\ x = 360\ to\ 371\ mm \\ I_6 = -1 & at\ x = 272\ to\ 400\ mm \end{cases}$$

$$f_7(x)= \begin{cases} I_7 = 0 & at\ x = 0\ to\ 215\ mm \\ I_7 = -1 & at\ x = 216\ to\ 257\ mm \\ I_7 = 0 & at\ x = 258\ to\ 269\ mm \\ I_7 = +1 & at\ x = 270\ to\ 317\ mm \\ I_7 = 0 & at\ x = 318\ to\ 329\ mm \\ I_7 = -1 & at\ x = 330\ to\ 371\ mm \\ I_7 = 0 & at\ x = 372\ to\ 389\ mm \\ I_7 = +1 & at\ x = 290\ to\ 400mm \end{cases}$$

$$f_8(x)= \begin{cases} I_8 = 0 & at\ x = 0\ to\ 287\ mm \\ I_8 = -1 & at\ x = 288\ to\ 329\ mm \\ I_8 = 0 & at\ x = 330\ to\ 341\ mm \\ I_8 = +1 & at\ x = 342\ to\ 389\ mm \\ I_8 = 0 & at\ x = 390\ to\ 400\ mm \end{cases}$$

$$f_9(x)= \begin{cases} I_9 = 0 & at\ x = 0\ to\ 359\ mm \\ I_9 = -1 & at\ x = 360\ to\ 400\ mm \end{cases}$$